MEASUREMENT OF DIRECT CP ASYMMETRY IN $B^{\pm} \to J/\psi K^{\pm}$ DECAYS PRODUCED IN $P\bar{P}$ COLLISIONS AT $\sqrt{S} = 1.96$TEV

BY

GREGORY ANDREW THOMPSON

DISSERTATION

Submitted in partial fulfillment of the requirements
for the degree of Doctor of Philosophy in Physics
in the Graduate College of the
University of Illinois at Urbana-Champaign, 2011

Urbana, Illinois

Doctoral Committee:

Professor Tony Liss, Chair
Professor Kevin Pitts, Director of Research
Professor Gary Gladding
Professor John Stack

ProQuest LLC.
789 East Eisenhower Parkway
P.O. Box 1346
Ann Arbor, MI 48106 - 1346

Abstract

A measurement of direct CP asymmetry is performed using $6fb^{-1}$ of $p\bar{p}$ collisions at $\sqrt{s} = 1.96$TeV from the CDF detector at the Fermi National Accelerator Laboratory. Approximately 80,000 $B^- \rightarrow J/\psi K^-$ (and charge conjugate) events were selected on the dimuon trigger and the yields were determined using a simultaneous mass and lifetime fit. After corrections, a measurement of $A_{CP} = 0.0034 \pm 0.0043(stat.) \pm 0.0060(syst.)$ is obtained, which is consistent with the SM prediction and previous measurements at DØ and the B factories.

For my wife, Tessa.

Acknowledgements

This thesis was supported by the United States Department of Energy grant DE-FG02-91ER40677.

I would like to thank the University of Illinois for providing me with the opportunity to pursue and complete this doctoral thesis. Thanks to Wendy Wimmer and Melodee Schweighart for their patience and immense abilities to navigate the University regulations. Thanks to Donna Guzy, Tonya Ayers and Rene Dunham for all of their help and advice. Thanks to Jim Kraus, Christopher Marino, Ed Rogers and Ben Carls who have all provided help and sympathy related to the myriad software and hardware idiosyncrasies that come with being fellow CDF graduate students. I would also like to thank Heather Gerberich and Olga Norniella who were both fantastic resources throughout the completion of this thesis.

My advisor, Kevin Pitts, was a steady source of insight and encouragement throughout this journey. Especially considering his wide variety of responsibilities, the amount of time and energy he was able to reserve for contemplating this surprisingly complex analysis deserves great recognition. It is largely to his credit that I was able to maintain confidence that this work could be completed.

I would like to thank Eiko Yu who provided the guidance necessary to allow me to take on the COT calibration responsibilities. Also, I would like to thank Bob Wagner for his leadership and insight related to my continuing COT responsibilities.

Thank you to my parents, Carolynne and Andy Thompson, for providing immense support and encouragement throughout my extended education. Their enthusiasm for my work, even when it was outside of their understanding was a great source of comfort. Thanks to my brother, Jeff Thompson, whose personal interest in science is a great source of motivation. I would also like to thank my wife's parents, Julie and Gary Ballard, who were another great source of support through these challenges.

My incredible wife Tessa deserves great recognition for her contribution to this doctoral thesis. She has been a wonderful source of strength through some incredibly trying and uncertain times. Her confidence, patience, and love has been the foundation on which the work was completed.

Table of Contents

List of Figures viii

List of Tables xi

Chapter 1 Introduction 1

Chapter 2 Theory 2
2.1 The Standard Model of Particle Physics 2
2.2 CKM Matrix 3

Chapter 3 CP Violation 8
3.1 Indirect CP Violation 8
3.2 Direct CP Violation 8
3.2.1 Direct CP Violation in $B^- \to J/\psi K^-$ 8

Chapter 4 Semileptonic Charm Decays 12

Chapter 5 Roadmap 15

Chapter 6 Experimental Apparatus 17
6.1 Overview 17
6.2 The Tevatron Accelerator Complex 17
6.2.1 Cockcroft-Walton 17
6.2.2 Linac and Booster 18
6.2.3 Main Injector 18
6.2.4 Tevatron 19
6.3 Collider Detector at Fermilab 20
6.3.1 Tracking 21
6.3.2 Silicon 22
6.3.3 COT 23
6.3.4 Calorimeters 24
6.3.5 Time of Flight 25
6.3.6 Cherenkov Luminosity Counters 25
6.3.7 Muon Systems 26

Chapter 7 COT Calibration 29
7.1 COT Signal 29
7.2 Calibration Overview 31
7.3 Calibration Hardware 32

Chapter 8 Trigger 34
8.1 CDF Trigger System 34
8.2 J/ψ Trigger 35
8.3 8 GeV/c CMUP Trigger 37

Chapter 9 Datasets . . . **38**
9.1 Overview . . . 38
9.2 Raw Datasets . . . 38
9.3 B-STntuples . . . 39
9.4 Skims . . . 39
9.5 Datasets Used . . . 39

Chapter 10 Monte Carlo . . . **41**

Chapter 11 Analysis . . . **42**
11.1 Overview . . . 42
11.2 $B^- \to J/\psi K^-$ . . . 43
11.2.1 $B^- \to J/\psi \pi^-$ . . . 44
11.2.2 Other Potential Backgrounds . . . 44

Chapter 12 Likelihood Fit . . . **47**
12.1 Likelihood Function . . . 47
12.2 Mass Probability Density Function . . . 47
12.3 Proper Decay Time Probability Density Function . . . 48
12.3.1 Signal Events . . . 48
12.3.2 Background Events . . . 49

Chapter 13 Results from $B^- \to J/\psi K^-$ . . . **51**
13.1 $B^- \to J/\psi K^-$ Fits . . . 51
13.2 Raw $A_{CP}(B^- \to J/\psi K^-)$ . . . 54

Chapter 14 Semileptonic D^{*+} Decays . . . **55**
14.1 K^- Efficiency Ratio . . . 55
14.1.1 Sources of charge bias . . . 56
14.2 Determination of $\frac{\epsilon_{K^+}}{\epsilon_{K^-}}$ . . . 56
14.3 π^+ Efficiency Ratio . . . 57
14.4 μ^+ Efficiency Ratio . . . 57
14.5 Method . . . 58
14.6 $D^{*+} \to D^0\pi^+$ Monte Carlo . . . 62
14.7 $D^{*+} \to D^0\pi^+, D^0 \to \mu^+K^-\nu_\mu$ Results . . . 63

Chapter 15 Results . . . **69**
15.1 Measurement of $A_{CP}(B^- \to J/\psi K^-)$ . . . 69

Chapter 16 Systematic Uncertainties . . . **71**
16.1 Systematics from $B^- \to J/\psi K^-$ . . . 71
16.1.1 $B^- \to J/\psi K^-$ Candidate Reconstruction . . . 71
16.1.2 Background Modeling in $B^- \to J/\psi K^-$ . . . 71
16.1.3 $B^- \to J/\psi \pi^-$ Contribution . . . 72
16.2 Systematics from $D^{*+} \to D^0\pi^+, D^0 \to \mu^+K^-\nu_\mu$ . . . 73
16.2.1 μ^+ vs. μ^- Efficiency . . . 73
16.2.2 Background Modeling in $D^{*+} \to D^0\pi^+, D^0 \to \mu^+K^-\nu_\mu$ . . . 74
16.2.3 Signal Modeling . . . 74
16.2.4 Fake Muon Rate . . . 74
16.2.5 π^+ as K^- Rate . . . 75
16.2.6 η Dependence . . . 75
16.2.7 Mismeasured π Efficiency Ratio . . . 76
16.2.8 Summary of Systematics . . . 76

Chapter 17 Summary . . . **78**

Chapter 18 Conclusion **79**

Appendix A $B^- \to J/\psi K^-$ Fits **80**
A.1 Mass Lifetime Fits 80
A.2 Mass Fits with $L_{xy} > 0.015$cm 93

Appendix B $D^{*+} \to D^0\pi^+, D^0 \to \mu^+K^-\nu_\mu$ Fits **102**
B.1 Yields 102
B.2 RS Fits 106
B.3 WS Fits 142

Appendix C Monte Carlo Decay Tables **178**

Glossary **179**

References **181**

List of Figures

2.1 $b \to c\,(u)$ Weak Decay . . . 5
2.2 Unitarity condition of the CKM matrix as a triangle representation . . . 6
2.3 Current state of global CKM fit . . . 7

3.1 Tree Diagram for $B^- \to J/\psi K^-$ . . . 9
3.2 Penguin Diagram for $B^- \to J/\psi K^-$ . . . 10
3.3 Exotic Penguin Diagram for $B^- \to J/\psi K^-$ with a charged Higgs and $\tilde{t}$ loop. . . . 10

4.1 Tree Diagram for $D^{*+} \to D^0\pi^+$ . . . 12
4.2 Tree Diagram for $D^0 \to \mu^+ K^- \nu_\mu$ . . . 13

6.1 Schematic of the Fermilab Tevatron Accelerator Complex . . . 18
6.2 Instantaneous Luminosity at beginning of stores of CDF Run II . . . 20
6.3 Isometric view of the CDF Detector (schematic) . . . 21
6.4 Schematic view of the CDF detector, with subsystem volumes labeled . . . 22
6.5 Schematic of SVX geometry as viewed along the beam direction . . . 23
6.6 1/6 section of the COT with number of cells, wire orientation (stereo (S) or axial(A)) and radius given for each superlayer. An enlarged section also shows detailed geometry of field and sense planes. . . . 24
6.7 Cross-section view of one quadrant of the CDF tracking volume. The PEM, PHA and WHA are visible. The location of the TOF system is also shown. . . . 26
6.8 $\eta - \phi$ coverage for the CDF muon systems . . . 27

7.1 Schematic of the COT front end electronics . . . 30
7.2 ASDQ block diagram . . . 31
7.3 ASDQ Signal in four stages (top to bottom): Input to preamplifier, output of preamplifier, output of tail cancellation, output of baseline restorer, output of discriminator . . . 31
7.4 Simplified schematic of calibration hardware. Left section describes the hardware in the control room, while the right hand side describes the hardware on the detector. . . . 33

8.1 Schematic of the CDF DAQ and Trigger System . . . 35
8.2 Schematic of the various paths through the Level 1 and Level 2 trigger systems. . . . 36

11.1 $B^- \to J/\psi\pi^-$ MC Templates . . . 45
11.2 $B_s \to J/\psi X$ MC subject to the analysis cuts and reconstructed as a $B^- \to J/\psi K^-$ to test for peaking backgrounds under the signal region . . . 46

13.1 $B^- \to J/\psi K^-$ Mass Fits for the entire data set . . . 52
13.2 $B^- \to J/\psi K^-$ Mass Fits for the entire data set with $L_{xy} > 0.015$cm . . . 53

14.1 Soft pion efficiency as a function of $p_T(\pi^+)$. The red line shows the $p_T(\pi^+)$ distribution from the $D^{*+} \to D^0\pi^+, D^0 \to \pi^+\pi^-$ decays. A bin by bin p_T correction is applied to account for any differences in p_T spectra. . . . 58
14.2 Example plots showing the RS, SS and WS distributions from the semileptonic D^{*+} decays. . 61
14.3 Example plots showing the RS, SS and WS with scaling to demonstrate SS as combinatoric background template . . . 61
14.4 Fake μ^+ MC templates . . . 64
14.5 Signal (K^-) and π^- MC templates . . . 65
14.6 D^{*+} $\delta(M(\mu^+K^-\pi^+), M(\mu^+K^-))$ distributions for RS and WS to demonstrate the size of the sample. . . . 68

15.1 A_{CP} is displayed as a function of proper decay length (ct). . . . 70

16.1 Kinematic fit quality distribution for $B^- \to J/\psi K^-$ and $B^+ \to J/\psi K^+$ . . . 72
16.2 η distribution for K^+ and K^- . . . 76

A.1 $M(B^+ \to J/\psi K^+), 2.0\text{GeV}/c < p_T(K^+) \leq 3.0\text{GeV}/c$ . . . 81
A.2 $M(B^- \to J/\psi K^-), 2.0\text{GeV}/c < p_T(K^-) \leq 3.0\text{GeV}/c$ . . . 82
A.3 $M(B^+ \to J/\psi K^+), 3.0\text{GeV}/c < p_T(K^+) \leq 4.0\text{GeV}/c$ . . . 83
A.4 $M(B^- \to J/\psi K^-), 3.0\text{GeV}/c < p_T(K^-) \leq 4.0\text{GeV}/c$ . . . 84
A.5 $M(B^+ \to J/\psi K^+), p_T(K^+) \geq 4.0\text{GeV}/c$ . . . 85
A.6 $M(B^- \to J/\psi K^-), p_T(K^-) \geq 4.0\text{GeV}/c$ . . . 86
A.7 $ct(B^+ \to J/\psi K^+), 2.0\text{GeV}/c < p_T(K^+) \leq 3.0\text{GeV}/c$ . . . 87
A.8 $ct(B^- \to J/\psi K^-), 2.0\text{GeV}/c < p_T(K^-) \leq 3.0\text{GeV}/c$ . . . 88
A.9 $ct(B^+ \to J/\psi K^+), 3.0\text{GeV}/c < p_T(K^+) \leq 4.0\text{GeV}/c$ . . . 89
A.10 $ct(B^- \to J/\psi K^-), 3.0\text{GeV}/c < p_T(K^-) \leq 4.0\text{GeV}/c$ . . . 90
A.11 $ct(B^+ \to J/\psi K^+), p_T(K^+) \geq 4.0\text{GeV}/c$ . . . 91
A.12 $ct(B^- \to J/\psi K^-), p_T(K^-) \geq 4.0\text{GeV}/c$ . . . 92
A.13 $M(B^+ \to J/\psi K^+), 2.0\text{GeV}/c < p_T(K^+) \leq 3.0\text{GeV}/c$ . . . 94
A.14 $M(B^- \to J/\psi K^-), 2.0\text{GeV}/c < p_T(K^-) \leq 3.0\text{GeV}/c$ . . . 97
A.15 $M(B^+ \to J/\psi K^+), 3.0\text{GeV}/c < p_T(K^+) \leq 4.0\text{GeV}/c$ . . . 98
A.16 $M(B^- \to J/\psi K^-), 3.0\text{GeV}/c < p_T(K^-) \leq 4.0\text{GeV}/c$ . . . 99
A.17 $M(B^+ \to J/\psi K^+), p_T(K^+) \geq 4.0\text{GeV}/c$ . . . 100
A.18 $M(B^- \to J/\psi K^-), p_T(K^-) \geq 4.0\text{GeV}/c$ . . . 101

B.1 $D^{*+}Fits : \delta(M(\mu K\pi), M(\mu K)), 2.0\text{GeV}/c < p_T(K^-) \leq 3.0\text{GeV}/c, -\frac{\pi}{12} < \phi(K^-) \leq \frac{3\pi}{12}$ . . . 106
B.2 $D^{*+}Fits : \delta(M(\mu K\pi), M(\mu K)), 2.0\text{GeV}/c < p_T(K^-) \leq 3.0\text{GeV}/c, \frac{3\pi}{12} < \phi(K^-) \leq \frac{7\pi}{12}$ . . . 107
B.3 $D^{*+}Fits : \delta(M(\mu K\pi), M(\mu K)), 2.0\text{GeV}/c < p_T(K^-) \leq 3.0\text{GeV}/c, \frac{7\pi}{12} < \phi(K^-) \leq \frac{11\pi}{12}$ . . . 108
B.4 $D^{*+}Fits : \delta(M(\mu K\pi), M(\mu K)), 2.0\text{GeV}/c < p_T(K^-) \leq 3.0\text{GeV}/c, \frac{11\pi}{12} < \phi(K^-) \leq \frac{15\pi}{12}$ . . . 109
B.5 $D^{*+}Fits : \delta(M(\mu K\pi), M(\mu K)), 2.0\text{GeV}/c < p_T(K^-) \leq 3.0\text{GeV}/c, \frac{15\pi}{12} < \phi(K^-) \leq \frac{19\pi}{12}$ . . . 110
B.6 $D^{*+}Fits : \delta(M(\mu K\pi), M(\mu K)), 2.0\text{GeV}/c < p_T(K^-) \leq 3.0\text{GeV}/c, \frac{19\pi}{12} < \phi(K^-) \leq \frac{23\pi}{12}$ . . . 111
B.7 $D^{*+}Fits : \delta(M(\mu K\pi), M(\mu K)), 3.0\text{GeV}/c < p_T(K^-) \leq 4.0\text{GeV}/c, -\frac{\pi}{12} < \phi(K^-) \leq \frac{3\pi}{12}$ . . . 112
B.8 $D^{*+}Fits : \delta(M(\mu K\pi), M(\mu K)), 3.0\text{GeV}/c < p_T(K^-) \leq 4.0\text{GeV}/c, \frac{3\pi}{12} < \phi(K^-) \leq \frac{7\pi}{12}$ . . . 113
B.9 $D^{*+}Fits : \delta(M(\mu K\pi), M(\mu K)), 3.0\text{GeV}/c < p_T(K^-) \leq 4.0\text{GeV}/c, \frac{7\pi}{12} < \phi(K^-) \leq \frac{11\pi}{12}$ . . . 114
B.10 $D^{*+}Fits : \delta(M(\mu K\pi), M(\mu K)), 3.0\text{GeV}/c < p_T(K^-) \leq 4.0\text{GeV}/c, \frac{11\pi}{12} < \phi(K^-) \leq \frac{15\pi}{12}$ . . . 115
B.11 $D^{*+}Fits : \delta(M(\mu K\pi), M(\mu K)), 3.0\text{GeV}/c < p_T(K^-) \leq 4.0\text{GeV}/c, \frac{15\pi}{12} < \phi(K^-) \leq \frac{19\pi}{12}$ . . . 116
B.12 $D^{*+}Fits : \delta(M(\mu K\pi), M(\mu K)), 3.0\text{GeV}/c < p_T(K^-) \leq 4.0\text{GeV}/c, \frac{19\pi}{12} < \phi(K^-) \leq \frac{23\pi}{12}$ . . . 117
B.13 $D^{*+}Fits : \delta(M(\mu K\pi), M(\mu K)), p_T(K^-) > 4.0\text{GeV}/c, -\frac{\pi}{12} < \phi(K^-) \leq \frac{3\pi}{12}$ . . . 118
B.14 $D^{*+}Fits : \delta(M(\mu K\pi), M(\mu K)), p_T(K^-) > 4.0\text{GeV}/c, \frac{3\pi}{12} < \phi(K^-) \leq \frac{7\pi}{12}$ . . . 119
B.15 $D^{*+}Fits : \delta(M(\mu K\pi), M(\mu K)), p_T(K^-) > 4.0\text{GeV}/c, \frac{7\pi}{12} < \phi(K^-) \leq \frac{11\pi}{12}$ . . . 120
B.16 $D^{*+}Fits : \delta(M(\mu K\pi), M(\mu K)), p_T(K^-) > 4.0\text{GeV}/c, \frac{11\pi}{12} < \phi(K^-) \leq \frac{15\pi}{12}$ . . . 121
B.17 $D^{*+}Fits : \delta(M(\mu K\pi), M(\mu K)), p_T(K^-) > 4.0\text{GeV}/c, \frac{15\pi}{12} < \phi(K^-) \leq \frac{19\pi}{12}$ . . . 122
B.18 $D^{*+}Fits : \delta(M(\mu K\pi), M(\mu K)), p_T(K^-) > 4.0\text{GeV}/c, \frac{19\pi}{12} < \phi(K^-) \leq \frac{23\pi}{12}$ . . . 123
B.19 $D^{*-}Fits : \delta(M(\mu K\pi), M(\mu K)), 2.0\text{GeV}/c < p_T(K^-) \leq 3.0\text{GeV}/c, -\frac{\pi}{12} < \phi(K^-) \leq \frac{3\pi}{12}$ . . . 124

B.20 $D^{*-} Fits : \delta(M(\mu K\pi), M(\mu K)), 2.0\text{GeV}/c < p_T(K^-) \leq 3.0\text{GeV}/c,\ \frac{3\pi}{12} < \phi(K^-) \leq \frac{7\pi}{12}$ 125
B.21 $D^{*-} Fits : \delta(M(\mu K\pi), M(\mu K)), 2.0\text{GeV}/c < p_T(K^-) \leq 3.0\text{GeV}/c,\ \frac{7\pi}{12} < \phi(K^-) \leq \frac{11\pi}{12}$ 126
B.22 $D^{*-} Fits : \delta(M(\mu K\pi), M(\mu K)), 2.0\text{GeV}/c < p_T(K^-) \leq 3.0\text{GeV}/c,\ \frac{11\pi}{12} < \phi(K^-) \leq \frac{15\pi}{12}$ 127
B.23 $D^{*-} Fits : \delta(M(\mu K\pi), M(\mu K)), 2.0\text{GeV}/c < p_T(K^-) \leq 3.0\text{GeV}/c,\ \frac{15\pi}{12} < \phi(K^-) \leq \frac{19\pi}{12}$ 128
B.24 $D^{*-} Fits : \delta(M(\mu K\pi), M(\mu K)), 2.0\text{GeV}/c < p_T(K^-) \leq 3.0\text{GeV}/c,\ \frac{19\pi}{12} < \phi(K^-) \leq \frac{23\pi}{12}$ 129
B.25 $D^{*-} Fits : \delta(M(\mu K\pi), M(\mu K)), 3.0\text{GeV}/c < p_T(K^-) \leq 4.0\text{GeV}/c,\ -\frac{\pi}{12} < \phi(K^-) \leq \frac{3\pi}{12}$ 130
B.26 $D^{*-} Fits : \delta(M(\mu K\pi), M(\mu K)), 3.0\text{GeV}/c < p_T(K^-) \leq 4.0\text{GeV}/c,\ \frac{3\pi}{12} < \phi(K^-) \leq \frac{7\pi}{12}$ 131
B.27 $D^{*-} Fits : \delta(M(\mu K\pi), M(\mu K)), 3.0\text{GeV}/c < p_T(K^-) \leq 4.0\text{GeV}/c,\ \frac{7\pi}{12} < \phi(K^-) \leq \frac{11\pi}{12}$ 132
B.28 $D^{*-} Fits : \delta(M(\mu K\pi), M(\mu K)), 3.0\text{GeV}/c < p_T(K^-) \leq 4.0\text{GeV}/c,\ \frac{11\pi}{12} < \phi(K^-) \leq \frac{15\pi}{12}$ 133
B.29 $D^{*-} Fits : \delta(M(\mu K\pi), M(\mu K)), 3.0\text{GeV}/c < p_T(K^-) \leq 4.0\text{GeV}/c,\ \frac{15\pi}{12} < \phi(K^-) \leq \frac{19\pi}{12}$ 134
B.30 $D^{*-} Fits : \delta(M(\mu K\pi), M(\mu K)), 3.0\text{GeV}/c < p_T(K^-) \leq 4.0\text{GeV}/c,\ \frac{19\pi}{12} < \phi(K^-) \leq \frac{23\pi}{12}$ 135
B.31 $D^{*-} Fits : \delta(M(\mu K\pi), M(\mu K)), p_T(K^-) > 4.0\text{GeV}/c,\ -\frac{\pi}{12} < \phi(K^-) \leq \frac{3\pi}{12}$ 136
B.32 $D^{*-} Fits : \delta(M(\mu K\pi), M(\mu K)), p_T(K^-) > 4.0\text{GeV}/c,\ \frac{3\pi}{12} < \phi(K^-) \leq \frac{7\pi}{12}$ 137
B.33 $D^{*-} Fits : \delta(M(\mu K\pi), M(\mu K)), p_T(K^-) > 4.0\text{GeV}/c,\ \frac{7\pi}{12} < \phi(K^-) \leq \frac{11\pi}{12}$ 138
B.34 $D^{*-} Fits : \delta(M(\mu K\pi), M(\mu K)), p_T(K^-) > 4.0\text{GeV}/c,\ \frac{11\pi}{12} < \phi(K^-) \leq \frac{15\pi}{12}$ 139
B.35 $D^{*-} Fits : \delta(M(\mu K\pi), M(\mu K)), p_T(K^-) > 4.0\text{GeV}/c,\ \frac{15\pi}{12} < \phi(K^-) \leq \frac{19\pi}{12}$ 140
B.36 $D^{*-} Fits : \delta(M(\mu K\pi), M(\mu K)), p_T(K^-) > 4.0\text{GeV}/c,\ \frac{19\pi}{12} < \phi(K^-) \leq \frac{23\pi}{12}$ 141
B.37 $D^{*+} Fits : \delta(M(\mu K\pi), M(\mu K)), 2.0\text{GeV}/c < p_T(K^-) \leq 3.0\text{GeV}/c,\ -\frac{\pi}{12} < \phi(K^-) \leq \frac{3\pi}{12}$ 142
B.38 $D^{*+} Fits : \delta(M(\mu K\pi), M(\mu K)), 2.0\text{GeV}/c < p_T(K^-) \leq 3.0\text{GeV}/c,\ \frac{3\pi}{12} < \phi(K^-) \leq \frac{7\pi}{12}$ 143
B.39 $D^{*+} Fits : \delta(M(\mu K\pi), M(\mu K)), 2.0\text{GeV}/c < p_T(K^-) \leq 3.0\text{GeV}/c,\ \frac{7\pi}{12} < \phi(K^-) \leq \frac{11\pi}{12}$ 144
B.40 $D^{*+} Fits : \delta(M(\mu K\pi), M(\mu K)), 2.0\text{GeV}/c < p_T(K^-) \leq 3.0\text{GeV}/c,\ \frac{11\pi}{12} < \phi(K^-) \leq \frac{15\pi}{12}$ 145
B.41 $D^{*+} Fits : \delta(M(\mu K\pi), M(\mu K)), 2.0\text{GeV}/c < p_T(K^-) \leq 3.0\text{GeV}/c,\ \frac{15\pi}{12} < \phi(K^-) \leq \frac{19\pi}{12}$ 146
B.42 $D^{*+} Fits : \delta(M(\mu K\pi), M(\mu K)), 2.0\text{GeV}/c < p_T(K^-) \leq 3.0\text{GeV}/c,\ \frac{19\pi}{12} < \phi(K^-) \leq \frac{23\pi}{12}$ 147
B.43 $D^{*+} Fits : \delta(M(\mu K\pi), M(\mu K)), 3.0\text{GeV}/c < p_T(K^-) \leq 4.0\text{GeV}/c,\ -\frac{\pi}{12} < \phi(K^-) \leq \frac{3\pi}{12}$ 148
B.44 $D^{*+} Fits : \delta(M(\mu K\pi), M(\mu K)), 3.0\text{GeV}/c < p_T(K^-) \leq 4.0\text{GeV}/c,\ \frac{3\pi}{12} < \phi(K^-) \leq \frac{7\pi}{12}$ 149
B.45 $D^{*+} Fits : \delta(M(\mu K\pi), M(\mu K)), 3.0\text{GeV}/c < p_T(K^-) \leq 4.0\text{GeV}/c,\ \frac{7\pi}{12} < \phi(K^-) \leq \frac{11\pi}{12}$ 150
B.46 $D^{*+} Fits : \delta(M(\mu K\pi), M(\mu K)), 3.0\text{GeV}/c < p_T(K^-) \leq 4.0\text{GeV}/c,\ \frac{11\pi}{12} < \phi(K^-) \leq \frac{15\pi}{12}$ 151
B.47 $D^{*+} Fits : \delta(M(\mu K\pi), M(\mu K)), 3.0\text{GeV}/c < p_T(K^-) \leq 4.0\text{GeV}/c,\ \frac{15\pi}{12} < \phi(K^-) \leq \frac{19\pi}{12}$ 152
B.48 $D^{*+} Fits : \delta(M(\mu K\pi), M(\mu K)), 3.0\text{GeV}/c < p_T(K^-) \leq 4.0\text{GeV}/c,\ \frac{19\pi}{12} < \phi(K^-) \leq \frac{23\pi}{12}$ 153
B.49 $D^{*+} Fits : \delta(M(\mu K\pi), M(\mu K)), p_T(K^-) > 4.0\text{GeV}/c,\ -\frac{\pi}{12} < \phi(K^-) \leq \frac{3\pi}{12}$ 154
B.50 $D^{*+} Fits : \delta(M(\mu K\pi), M(\mu K)), p_T(K^-) > 4.0\text{GeV}/c,\ \frac{3\pi}{12} < \phi(K^-) \leq \frac{7\pi}{12}$ 155
B.51 $D^{*+} Fits : \delta(M(\mu K\pi), M(\mu K)), p_T(K^-) > 4.0\text{GeV}/c,\ \frac{7\pi}{12} < \phi(K^-) \leq \frac{11\pi}{12}$ 156
B.52 $D^{*+} Fits : \delta(M(\mu K\pi), M(\mu K)), p_T(K^-) > 4.0\text{GeV}/c,\ \frac{11\pi}{12} < \phi(K^-) \leq \frac{15\pi}{12}$ 157
B.53 $D^{*+} Fits : \delta(M(\mu K\pi), M(\mu K)), p_T(K^-) > 4.0\text{GeV}/c,\ \frac{15\pi}{12} < \phi(K^-) \leq \frac{19\pi}{12}$ 158
B.54 $D^{*+} Fits : \delta(M(\mu K\pi), M(\mu K)), p_T(K^-) > 4.0\text{GeV}/c,\ \frac{19\pi}{12} < \phi(K^-) \leq \frac{23\pi}{12}$ 159
B.55 $D^{*-} Fits : \delta(M(\mu K\pi), M(\mu K)), 2.0\text{GeV}/c < p_T(K^-) \leq 3.0\text{GeV}/c,\ -\frac{\pi}{12} < \phi(K^-) \leq \frac{3\pi}{12}$ 160
B.56 $D^{*-} Fits : \delta(M(\mu K\pi), M(\mu K)), 2.0\text{GeV}/c < p_T(K^-) \leq 3.0\text{GeV}/c,\ \frac{3\pi}{12} < \phi(K^-) \leq \frac{7\pi}{12}$ 161
B.57 $D^{*-} Fits : \delta(M(\mu K\pi), M(\mu K)), 2.0\text{GeV}/c < p_T(K^-) \leq 3.0\text{GeV}/c,\ \frac{7\pi}{12} < \phi(K^-) \leq \frac{11\pi}{12}$ 162
B.58 $D^{*-} Fits : \delta(M(\mu K\pi), M(\mu K)), 2.0\text{GeV}/c < p_T(K^-) \leq 3.0\text{GeV}/c,\ \frac{11\pi}{12} < \phi(K^-) \leq \frac{15\pi}{12}$ 163
B.59 $D^{*-} Fits : \delta(M(\mu K\pi), M(\mu K)), 2.0\text{GeV}/c < p_T(K^-) \leq 3.0\text{GeV}/c,\ \frac{15\pi}{12} < \phi(K^-) \leq \frac{19\pi}{12}$ 164
B.60 $D^{*-} Fits : \delta(M(\mu K\pi), M(\mu K)), 2.0\text{GeV}/c < p_T(K^-) \leq 3.0\text{GeV}/c,\ \frac{19\pi}{12} < \phi(K^-) \leq \frac{23\pi}{12}$ 165
B.61 $D^{*-} Fits : \delta(M(\mu K\pi), M(\mu K)), 3.0\text{GeV}/c < p_T(K^-) \leq 4.0\text{GeV}/c,\ -\frac{\pi}{12} < \phi(K^-) \leq \frac{3\pi}{12}$ 166
B.62 $D^{*-} Fits : \delta(M(\mu K\pi), M(\mu K)), 3.0\text{GeV}/c < p_T(K^-) \leq 4.0\text{GeV}/c,\ \frac{3\pi}{12} < \phi(K^-) \leq \frac{7\pi}{12}$ 167
B.63 $D^{*-} Fits : \delta(M(\mu K\pi), M(\mu K)), 3.0\text{GeV}/c < p_T(K^-) \leq 4.0\text{GeV}/c,\ \frac{7\pi}{12} < \phi(K^-) \leq \frac{11\pi}{12}$ 168
B.64 $D^{*-} Fits : \delta(M(\mu K\pi), M(\mu K)), 3.0\text{GeV}/c < p_T(K^-) \leq 4.0\text{GeV}/c,\ \frac{11\pi}{12} < \phi(K^-) \leq \frac{15\pi}{12}$ 169
B.65 $D^{*-} Fits : \delta(M(\mu K\pi), M(\mu K)), 3.0\text{GeV}/c < p_T(K^-) \leq 4.0\text{GeV}/c,\ \frac{15\pi}{12} < \phi(K^-) \leq \frac{19\pi}{12}$ 170
B.66 $D^{*-} Fits : \delta(M(\mu K\pi), M(\mu K)), 3.0\text{GeV}/c < p_T(K^-) \leq 4.0\text{GeV}/c,\ \frac{19\pi}{12} < \phi(K^-) \leq \frac{23\pi}{12}$ 171
B.67 $D^{*-} Fits : \delta(M(\mu K\pi), M(\mu K)), p_T(K^-) > 4.0\text{GeV}/c,\ -\frac{\pi}{12} < \phi(K^-) \leq \frac{3\pi}{12}$ 172
B.68 $D^{*-} Fits : \delta(M(\mu K\pi), M(\mu K)), p_T(K^-) > 4.0\text{GeV}/c,\ \frac{3\pi}{12} < \phi(K^-) \leq \frac{7\pi}{12}$ 173
B.69 $D^{*-} Fits : \delta(M(\mu K\pi), M(\mu K)), p_T(K^-) > 4.0\text{GeV}/c,\ \frac{7\pi}{12} < \phi(K^-) \leq \frac{11\pi}{12}$ 174
B.70 $D^{*-} Fits : \delta(M(\mu K\pi), M(\mu K)), p_T(K^-) > 4.0\text{GeV}/c,\ \frac{11\pi}{12} < \phi(K^-) \leq \frac{15\pi}{12}$ 175
B.71 $D^{*-} Fits : \delta(M(\mu K\pi), M(\mu K)), p_T(K^-) > 4.0\text{GeV}/c,\ \frac{15\pi}{12} < \phi(K^-) \leq \frac{19\pi}{12}$ 176
B.72 $D^{*-} Fits : \delta(M(\mu K\pi), M(\mu K)), p_T(K^-) > 4.0\text{GeV}/c,\ \frac{19\pi}{12} < \phi(K^-) \leq \frac{23\pi}{12}$ 177

List of Tables

2.1 Elementary Particles in the Standard Model . . . 3

3.1 Current $A_{CP}\,(B^- \to J/\psi K^-)$ Measurements . . . 11

9.1 Dimuon Datasets for $B^- \to J/\psi K^-$ . . . 39
9.2 Dimuon Datasets for $D^{*+} \to D^0\pi^+, D^0 \to \mu^+ K^- \nu_\mu$ . . . 40

11.1 Cuts on $B^- \to J/\psi K^-$ . . . 43

12.1 Summary of $B^- \to J/\psi K^-$ mass fit parameters . . . 49
12.2 Summary of $B^- \to J/\psi K^-$ lifetime fit parameters . . . 50

13.1 $B^- \to J/\psi K^-$ Yields from the Mass Only Fit . . . 51
13.2 $B^- \to J/\psi K^-$ Yields from the Mass Only Fit with $L_{xy} > 0.015$cm . . . 53
13.3 $A_{CP}^{raw}(B^- \to J/\psi K^-)$ . . . 54

14.1 Cuts on μ^+ . . . 59
14.2 Cuts on K^- . . . 59
14.3 Cuts on π^+ . . . 59
14.4 Sign Combinations . . . 60
14.5 Ratio of RS : WS events from fake μ^+ from MC . . . 63
14.6 Ratio of π^- : K^- events from MC . . . 63
14.7 Signal and WS Yields for the entire D^{*+} dataset . . . 67
14.8 K^+ efficiency ratio $\frac{\epsilon_{K^+}}{\epsilon_{K^-}}$ . . . 67

15.1 $A_{CP}(B^- \to J/\psi K^-)$ . . . 69

16.1 Systematic Uncertainties on $A_{CP}(B^- \to J/\psi K^-)$ . . . 77

17.1 Updated $A_{CP}\,(B^- \to J/\psi K^-)$ Measurements . . . 78

A.1 $B^- \to J/\psi K^-$ Yields for $2.0\text{GeV}/c < p_T(K^-) \leq 3.0\text{GeV}/c$ . . . 93
A.2 $B^+ \to J/\psi K^+$ Yields for $2.0\text{GeV}/c < p_T(K^-) \leq 3.0\text{GeV}/c$ . . . 93
A.3 $B^- \to J/\psi K^-$ Yields for $3.0\text{GeV}/c < p_T(K^-) \leq 4.0\text{GeV}/c$ . . . 93
A.4 $B^+ \to J/\psi K^+$ Yields for $3.0\text{GeV}/c < p_T(K^-) \leq 4.0\text{GeV}/c$ . . . 93
A.5 $B^- \to J/\psi K^-$ Yields for $p_T(K^-) > 4.0\text{GeV}/c$ . . . 95
A.6 $B^+ \to J/\psi K^+$ Yields for $p_T(K^-) > 4.0\text{GeV}/c$ . . . 95
A.7 $B^- \to J/\psi K^-$ Fitted Lifetime for $2.0\text{GeV}/c < p_T(K^-) \leq 3.0\text{GeV}/c$ . . . 95
A.8 $B^+ \to J/\psi K^+$ Fitted Lifetime for $2.0\text{GeV}/c < p_T(K^+) \leq 3.0\text{GeV}/c$ . . . 95
A.9 $B^- \to J/\psi K^-$ Fitted Lifetime for $3.0\text{GeV}/c < p_T(K^-) \leq 4.0\text{GeV}/c$ . . . 95
A.10 $B^+ \to J/\psi K^+$ Fitted Lifetime for $3.0\text{GeV}/c < p_T(K^+) \leq 4.0\text{GeV}/c$ . . . 96
A.11 $B^- \to J/\psi K^-$ Fitted Lifetime for $p_T(K^-) > 4.0\text{GeV}/c$ . . . 96
A.12 $B^+ \to J/\psi K^+$ Fitted Lifetime for $p_T(K^+) > 4.0\text{GeV}/c$ . . . 96

B.1 $D^{*+} \to D^0\pi^+, D^0 \to \mu^+K^-\nu_\mu$ Yields 102

C.1 Muonic D^{*+} MC Decay Table 178

Chapter 1

Introduction

In 1977, the first observation of the b quark was made with the discovery of the Υ meson, the bound state of a b quark and its corresponding anti quark $\bar{b}$, at the Fermi National Acceleration Laboratory (Fermilab) [1]. B decays are generally interesting in that the b quark is both quite massive and long lived compared to the other upper generation quarks. It cannot decay within its generation since the t quark is more massive, thus must decay via the weak interaction which is the reason for the long and observable lifetime.

The eigenstates of the weak interaction are linear combinations of the strong (quark) eigenstates. The Cabibbo-Kobayashi-Maskawa (CKM) matrix provides the linear transformation between the strong and weak eigenstates. Since the b quark must decay via the weak interaction, B meson decays provide information about five of the nine elements of the CKM matrix. Imaginary components in these matrix elements can lead to CP violation in weak decays, which has been observed in several B decays.

The B^- meson is the bound state of a b quark and a $\bar{u}$ quark. This thesis presents a measurement of Direct CP Asymmetry in $B^- \to J/\psi K^-$ at the Collider Detector at Fermilab (CDF). CDF is one of two mulltipurpose detectors which collect data from $p\bar{p}$ collisions at $\sqrt{s} = 1.96$ GeV/c in the Tevatron accelerator. CP violation is not expected to be large in this decay[2], and a measurement of a large CP violating asymmetry would be anomalous.

Chapter 2

Theory

2.1 The Standard Model of Particle Physics

The first idea of a universe comprised of irreducible building blocks is largely attributed to the ancient greek philosopher Democritus and atomic hypothesis. Almost 2500 years later the first observation of a fundamental particle was achieved. The observation of the electron[3] in 1897 by J. J. Thomson could be labeled as the birth of modern elementary particle physics, and was part of the work which earned him the Nobel Prize in 1906. In 1920, Paul A.M. Dirac calculated the coefficient of spontaneous emission of an atom [4], which employed the first formulation of a quantum field theory, and provided the basis for quantum electrodynamics. Later, the integration of special relativity and quantum mechanics led to the prediction of anti-matter, specifically the positron (anti-electron), which was quickly confirmed by Carl D. Anderson [5].

During the initial growth period of particle physics, new particles were observed in cosmic ray experiments and cloud chambers. The development of particle accelerators and improved detector technologies came with the 1950s. With this improved technology came more and more discoveries of elementary particles which cast doubt on their fundamental nature. This led Murray Gell-Mann[6] and George Zweig to hypothesize that many of these particles were in fact composed of yet to be observed particles. Gell-Mann coined these newly fundamental particles as quarks[7]. This hypothesis predicted the existence of the Ω^- baryon which was observed later that year at Brookhaven National Laboratory [8]. Deep inelastic scattering experiments at the Stanford Linear Accelerator Complex (SLAC) provided further evidence of the quark substructure in the nucleon [9].

As the experimental discoveries continued, weak interaction mediated by the $W^{\pm}$ and Z^0 bosons was unified with the electromagnetic interaction mediated by the photon into quantum electrodynamics(QED)[10]. Further, the strong interaction mediated by the gluon was formulated in quantum chromodynamics (QCD)[11]. These formulations, in concert with the observation of the fundamental particles, provide the framework for the Standard Model of Particle Physics (SM). The SM posits that all matter is comprised of twelve elementary particles and all interactions between these particles are governed by four fundamental forces.

The elementary particles are subdivided into two types (six quarks and six leptons) and three generations with a pair of quarks and leptons each in every generation. All of the elementary particles are spin $\frac{1}{2}$ fermions. The first generation lepton pair is the electron (e^-) and electron neutrino (ν_e). The carries a negative electrical charge which is defined as the basic unit of charge while the ν_e is electrically neutral. The first generation quarks are the up (u) and down (d) which carry fractional charges of $\frac{2}{3}$ and $\frac{-1}{3}$ respectively. The next two generations of fundamental particles follow the same pattern, but carry increasing mass as summarized in Table 2.1. Each of these particles also has a corresponding anti-particle with opposite electrical charge for a total of 24 fundamental particles.

Table 2.1: Elementary Particles in the Standard Model

Type	Charge	1st Generation	2nd Generation	3rd Generation
quarks	$\frac{2}{3}$	up (u)	charm (c)	top (t)
	$-\frac{1}{3}$	down (d)	strange (s)	bottom (b)
leptons	-1	electron (e^-)	muon (μ^-)	tau (τ^-)
	0	electron neutrino (ν_e)	muon neutrion (ν_μ)	tau neutrino (ν_τ)

The interactions between these particles are all governed by the four fundamental forces: electromagnetic, weak, strong and gravity. The standard model describes the mediation of these forces through gauge boson force carriers. The mediators of electroweak QED is the photon for electromagnetic interaction and the massive $W^\pm$ and Z^0 bosons for the weak interaction. The strong force, is described by QCD, and mediated with gluons. A gauge theory for gravity does not, as of yet, fit into the SM.

The SM has been wildly successful in tests performed of it in the laboratory over the past decades. However, there are issues that have not been resolved. Of particular interest to this thesis is the obvious matter-antimatter imbalance in the universe which cannot be accounted for from within the SM. This is the strongest motivation to search for new sources of CP asymmetry beyond the SM.

2.2 CKM Matrix

In general, the weak eigenstates are not equivalent to the flavor eigenstates. Therefore, when dealing with weak interactions, as seen in the neutral kaon system, a change of basis is required. This transformation is performed using the Cabibbo-Kobayashi-Maskawa (CKM) matrix. CP violation arises as imaginary components in this matrix. The matrix elements also arise as the coupling constant of the $W^\pm$ to the

quarks. An imaginary component in the coupling can lead to a decay rate asymmetry through an interference between amplitudes. This imaginary component is often referred to as a CP violating phase. In the case of the K^0 system, this creates an imbalance in the likelihood that the system will decay as a K^0 or $\bar{K^0}$ in a given mode. In the B^- system, the branching fraction for a given mode may be charge asymmetric as a result of the imaginary phase. It is important to note that CPT symmetry (which is conserved in the SM) dictates that the inclusive decay rate for a particle-antiparticle pair is identical. These points will be discussed further in the next chapter.

The CKM matrix is a 3×3 unitary matrix and as such can be defined uniquely by three real and one complex parameter. The unitarity of the matrix constrains the matrix to four free parameters. The most common choice of parameterizations[12] describes the matrix in terms of three mixing angles $(\theta_{12}, \theta_{13}, \theta_{23})$ and the complex phase (δ).

$$\begin{pmatrix} V_{ud} & V_{us} & V_{ub} \\ V_{cd} & V_{cs} & V_{cb} \\ V_{td} & V_{ts} & V_{tb} \end{pmatrix} = \begin{pmatrix} c_{12}c_{13} & a_{12}c_{13} & s_{13}e^{-i\delta} \\ -s_{12}c_{23} - c_{12}s_{23}s_{13}e^{-i\delta} & c_{12}c_{23} - s_{12}s_{23}s_{13}e^{-i\delta} & s_{23}c_{13} \\ s_{12}s_{23} - c_{12}c_{23}s_{13}e^{-i\delta} & -c_{12}s_{23} - s_{12}c_{23}s_{13}e^{-i\delta} & c_{23}c_{13} \end{pmatrix} \tag{2.1}$$

where c_{ij} and s_{ij} are short hand for $cos\theta_{ij}$ and $sin\theta_{ij}$ respectively. The components V_{ij} refer to the coupling constant for a W^+ vertex between i and j quark. An experimentally motivated parameterization is the Wolfenstein parameterization[13],

$$\begin{pmatrix} V_{ud} & V_{us} & V_{ub} \\ V_{cd} & V_{cs} & V_{cb} \\ V_{td} & V_{ts} & V_{tb} \end{pmatrix} = \begin{pmatrix} 1 - \lambda^2/2 & \lambda & A\lambda^3(\rho - i\eta) \\ -\lambda & 1 - \lambda^2/2 & A\lambda^2 \\ A\lambda^3(1 - \rho - i\eta) & -A\lambda^2 & 1 \end{pmatrix} + \mathcal{O}(\lambda^4) \tag{2.2}$$

where each of the four parameters (A, ρ, λ, η) are of order 1. The expansion is carried out in powers of λ which is the sine of the Cabibbo angle (θ_c), with $\sin(\theta_c) \approx 0.2272$ [14]. This expansion is accurate to order λ^3.

The CP violating phase is seen in V_{ub} as well as V_{td}, and will arise in more terms at higher orders of λ. Each component of the matrix shows the required admixture to go from the flavor eigenstates to the weak eigenstates, but it is also a coupling constant that factors into the amplitude of weak processes.

An example is shown in Fig. 2.1 where the b quark decays to a c quark by emitting a W^- which decays leptonically. The leptonic decay is immaterial to this subject, but demonstrates how V_{cb} will contribute

to the amplitude. [1] To order λ^3, this amplitude carries no CP violating phase in the standard model. However, in the similar example where the b quark decays to a u quark, the CKM element that is introduced is V_{ub} which does in fact carry a complex phase at order λ^3. CP Violation can then be introduced through interference between this diagram and another diagram with the same initial and final states.

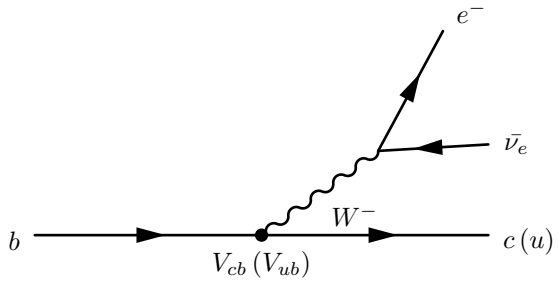

Figure 2.1: $b \to c\,(u)$ Weak Decay

The unitarity of the CKM matrix ($V^{\dagger}_{CKM}V_{CKM} = 1$) provides strong constraints which can be used to generate a geometric visualization in terms of a unitary triangle. One example of a constraint is:

$$V_{ud}V^*_{ub} + V_{cd}V^*_{cb} + V_{td}V^*_{tb} = 0. \tag{2.3}$$

Dividing by $V_{cd}V^*_{cb}$ gives a formulation of a triangle with base of unit length as shown in Fig. 2.2. The upper vertex is resides at the point (ρ, η) which are the values found in the Wolfenstein parameterization. The characteristics of this triangle can be constrained by theoretical and experimental results. A recent global fit of various results is shown in Fig. 2.3. The fact that η is non-zero is the reason CP violation is observed in the standard model.

[1] There is also a leptonic version of the CKM matrix which contributes to this process at the $W^- - \nu_e - e^-$ vertex, but the off-diagonal elements are all zero aside from a small correction to facilitate neutrino mixing.

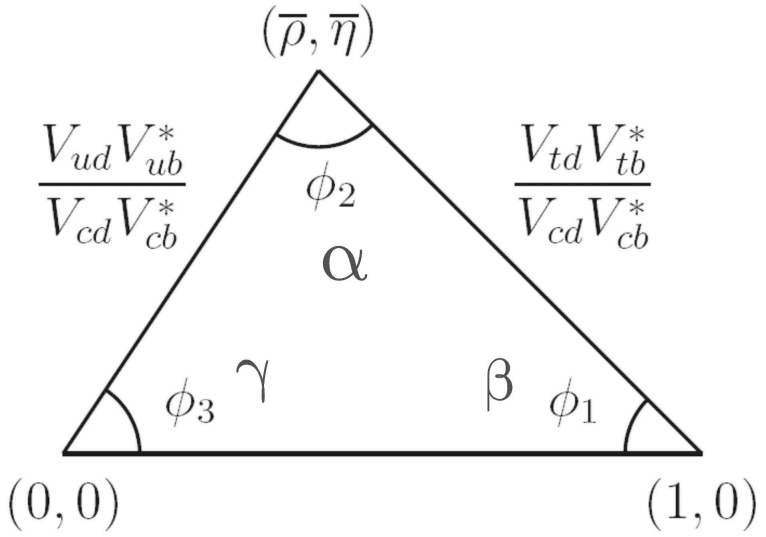

Figure 2.2: Unitarity condition of the CKM matrix as a triangle representation

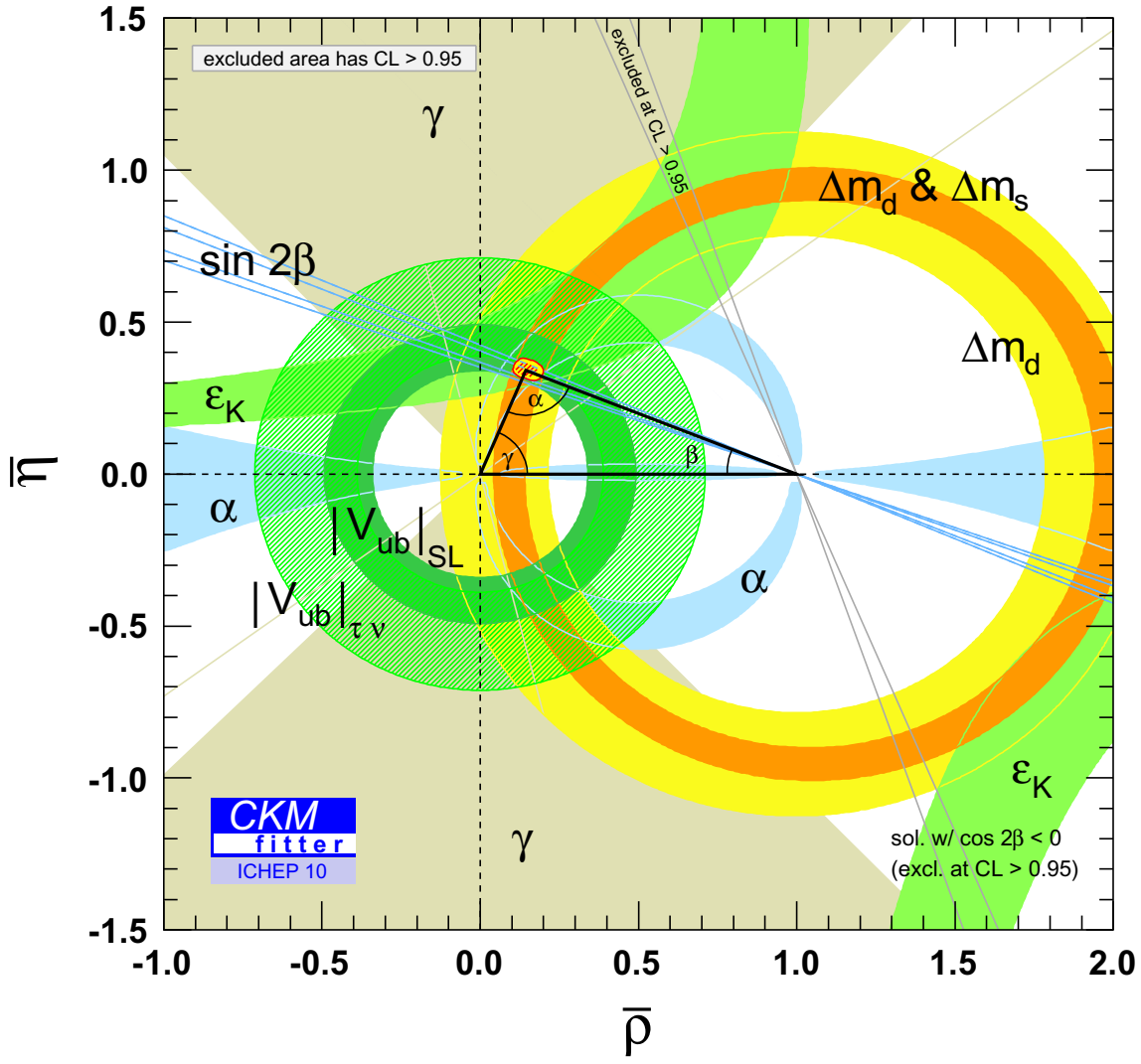

Figure 2.3: Current state of global CKM fit

Chapter 3

CP Violation

The observable universe demonstrates a massive matter-antimatter asymmetry. The mechanism for this asymmetry is referred to as baryogenesis and has CP violation as one of its necessary conditions[15]. While the SM describes CP violation as observed in the B meson and K system with great success, it falls well short of accounting for the observed asymmetry on the cosmological scale[16].

3.1 Indirect CP Violation

Indirect CP violation occurs during the propagation of a particle. If a particle is an admixture of CP eigenstates, indirect CP violation occurs as a variation of the admixture over time. The first observation of indirect CP violation occurred in the neutral K system[17]. The weak eigenstates of the K^0 system are referred to as K_L and K_S where L and S refer to long and short respectively in reference to the decay length of the two particles. Initially, these weak eigenstates were assumed to be CP eigenstates. This was disproven when the weak "eigenstate" K_L with $CP = +1$ was observed to decay to a $\pi^+\pi^-$ final state with $CP = -1$.

3.2 Direct CP Violation

If CP symmetry is conserved in a decay, the branching fractions for the decay are identical for the particle-antiparticle pair. When this symmetry is broken, there is some variation between the branching fraction which represents a CP asymmetry. The goal of this thesis is to measure the Direct CP Asymmetry in the decay $B^- \to J/\psi K^-$.

3.2.1 Direct CP Violation in $B^- \to J/\psi K^-$

Violation of charge conservation has never been observed in any system. It is clear then that a B^+ meson at production decays as a B^+ meson without any flavor oscillation. However it is possible for direct CP

violation to manifest in this system as an imbalance in partial widths for the particle-antiparticle couplet. It is the aim of this analysis to probe such an imbalance in the decay channel $B^{\pm} \to J/\psi K^{\pm}$. The quantity defined to be measured is the direct CP asymmetry:

$$A_{CP} = \frac{\Gamma\left(B^- \to J/\psi K^-\right) - \Gamma\left(B^+ \to J/\psi K^+\right)}{\Gamma\left(B^- \to J/\psi K^-\right) + \Gamma\left(B^+ \to J/\psi K^+\right)}. \tag{3.1}$$

The partial width Γ in this expression is defined as:

$$\Gamma\left(B^- \to J/\psi K^-\right) = \frac{N\left(B^- \to J/\psi K^-\right)}{N\left(B^-\right)}, \tag{3.2}$$

where $N\left(B^-\right)$ is the inclusive number of B^- mesons produced in the collisions and $N\left(B^- \to J/\psi K^-\right)$ is the number of those B^- mesons that decay in the $J/\psi K^-$ channel. The same is true for $B^+ \to J/\psi K^+$, and for the remainder of the document, charge conjugation is generally applied.

CP violation is present in the SM in general and is expected to be present in this process, albeit at a small level. The amplitude of this process is expected to be dominated by the lowest order feynman diagrams. The tree level diagram (Fig. 3.1) has the b weakly decaying to a c by emitting a W^-. The decay also proceeds via a penguin diagram (Fig. 3.2) with a W^- loop dominated by a t quark by virtue of its mass. Since gauge bosons are colorless, the tree level diagram is color suppressed since the $\bar{c}s$ must be the same color-anticolor pair as the $b\bar{u}$ in the B^- meson to form the $J/\psi K^-$ final state. The penguin diagram has no color requirements by construction but the Z meson must decay as a $c\bar{c}$ pair to form the $J/\psi K^-$ final state. These factors compete and result in a estimated $\frac{P}{T}$ ratio on the order of 10^{-3}.

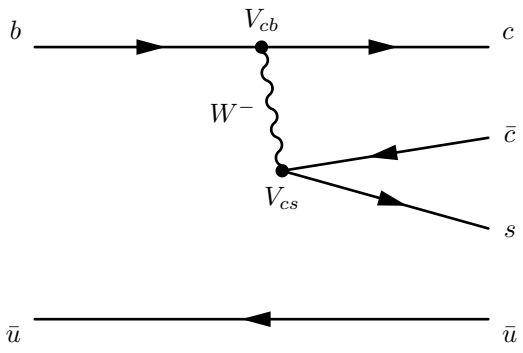

Figure 3.1: Tree Diagram for $B^- \to J/\psi K^-$

The interference term between these two diagrams in the amplitude results in a prediction of a small but

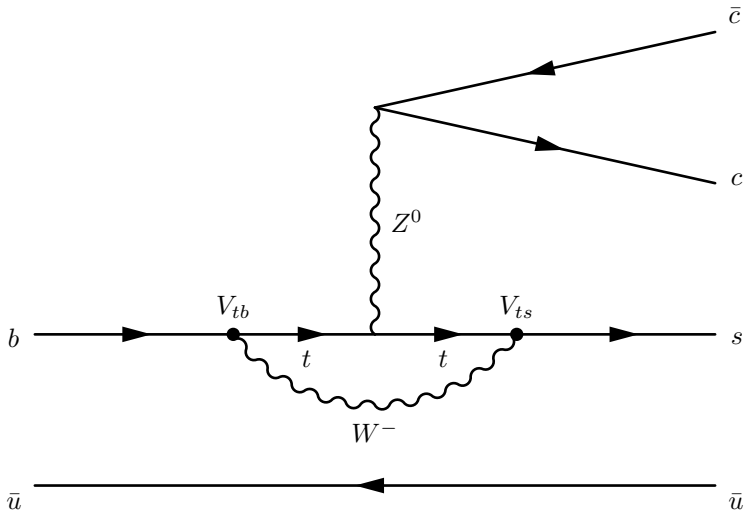

Figure 3.2: Penguin Diagram for $B^- \rightarrow J/\psi K^-$

potentially observable amount of CP violation at ($A_{CP} \approx 0.003$) [2]. The imaginary phase is introduced at λ^4 through V_{cb} and V_{ts}[18]. Exotic models beyond the SM could introduce diagrams that may increase A_{CP}. These models include an extra $U(1)'$ gauge boson or certain Higgs doublet models. A significant measurement that shows A_{CP} in excess of 1% would be a strong indication of new physics. On the other hand, since by definition, we are ignorant of any masses or couplings involved in any new physics process, any interference terms could suppress the SM level of A_{CP}. For this reason, a measurement consistent with expectation does not eliminate any of these exotic models.

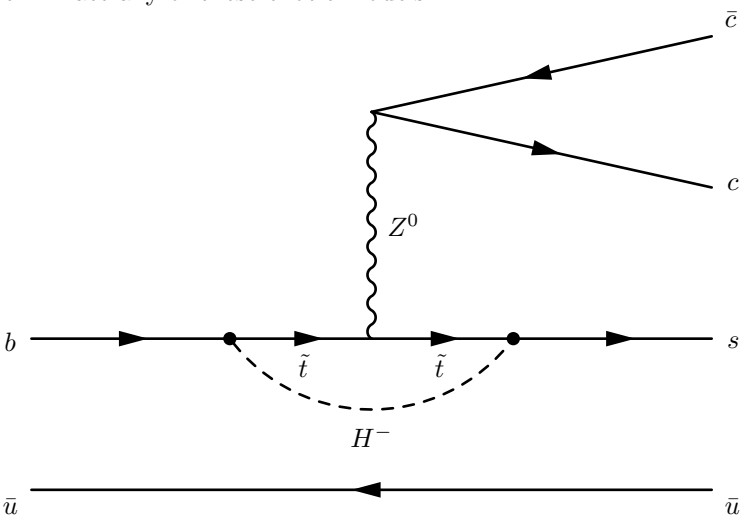

Figure 3.3: Exotic Penguin Diagram for $B^- \rightarrow J/\psi K^-$ with a charged Higgs and $\tilde{t}$ loop.

Measurements of $A_{CP}\,(B^- \rightarrow J/\psi K^-)$ have been performed at the b-factories CLEO, BaBar, [14] and Belle[19] as well as at DØ[20]. An unofficial average is also included since the Belle measurement was not included in the PDG calculation at the time of this thesis.

Table 3.1: Current $A_{CP}\,(B^- \to J/\psi K^-)$ Measurements

Experiment	Result		(stat.)		(syst.)	Year	Sample
CLEO	0.018	$\pm$	0.043	$\pm$	0.004	2000	$e^+e^- \to \Upsilon(4S)$
Babar	0.030	$\pm$	0.014	$\pm$	0.010	2005	$e^+e^- \to \Upsilon(4S)$
DØ	0.0075	$\pm$	0.0061	$\pm$	0.0030	2008	$p\bar{p}$ at 1.96TeV
Belle	-0.0076	$\pm$	0.0050	$\pm$	0.0022	2010	$e^+e^- \to \Upsilon(4S)$
Average	0.0003	$\pm$ 0.0041					

Chapter 4

Semileptonic Charm Decays

In order to measure the charge bias, a large sample with equal numbers of K^+ and K^- at production is required. Since the measurement of the K^- in $B^- \to J/\psi K^-$ reconstruction is limited to tracking, with no trigger requirements, it is instructive to find a similar decay that is collected with minimal influence from the K^- . Further, it is important to select a channel that is void of any inherent charge asymmetry. These requirements are largely met by the decay $D^{*+} \to D^0\pi^+, D^0 \to \mu^+ K^- \nu_\mu$, this is also the general technique employed in the $A_{CP}(B^- \to J/\psi K^-)$ measurement at DØ[20].

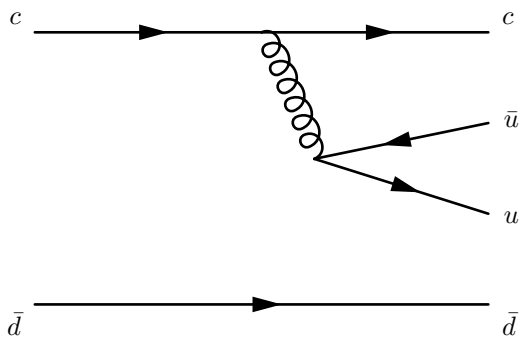

Figure 4.1: Tree Diagram for $D^{*+} \to D^0\pi^+$

The detector is insensitive to the weakly interacting neutrinos making it impossible to fully reconstruct this decay. However, since the difference between the mass of the D^{*+} and D^0 is just above the mass of the π^+ , which limits the phase space of the decay, allows for signal discrimination in a mass difference variable. The proper masses (M) of the parent particles are determined by the minkowski norm of the four-momenta (P) of the daughter particles.

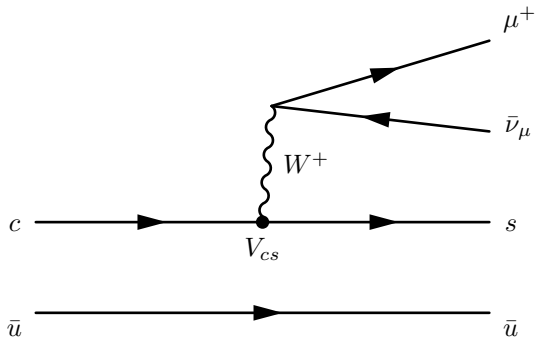

Figure 4.2: Tree Diagram for $D^0 \rightarrow \mu^+ K^- \nu_\mu$

$$M(D^{*+})^2 = -||P\left(D^0\right) + P\left(\pi^+\right)|| \tag{4.1}$$

$$M(D^0)^2 = -||P\left(\mu^+\right) + P\left(K^-\right) + P\left(\nu_{mu}\right)|| \tag{4.2}$$

Further, according to momentum conservation:

$$P\left(D^0\right) = P\left(\mu^+\right) + P\left(K^-\right) + P\left(\nu_{mu}\right) \tag{4.3}$$

$$M(D^{*+})^2 = -||P\left(\mu^+\right) + P\left(K^-\right) + P\left(\nu_{mu}\right) + P\left(\pi^+\right)||^2 \tag{4.4}$$

Assuming we have no information about the neutrino:

$$M(D^0) = \sqrt{-||P\left(\mu^+\right) + P\left(K^-\right)||^2} + \delta_\nu(D^0) \tag{4.5}$$

$$M(D^{*+}) = \sqrt{-||P\left(\mu^+\right) + P\left(K^-\right) + P\left(\pi^+\right)||^2} + \delta_\nu(D^{*+}) \tag{4.6}$$

Where the δ_{nu} indicates the error associated with ignoring the neutrino momentum in the mass calculation. Since the minkowski norm is calculated as:

$$-||P||^2 = E^2 - |\vec{p}|^2 \tag{4.7}$$

and the neutrino rest mass is close to zero, the main contribution of the neutrino to the mass arises from its kinetic energy. There is also a contribution from lost cross terms in the magnitude calculation. But, since the same kinetic energy is lost from both $M(D^{*+})$ and $M(D^0)$ with the missing neutrino:

$$\delta_\nu(D^0) \approx \delta_\nu(D^{*+}) \tag{4.8}$$

If it were possible to fully reconstruct the decay, a histogram of the quantity $M(D^{*+}) - M(D^0)$ would result in a strong peak just above $M(\pi^+)$. Since this is out of the reach of the detector, the next best alternative is the quantity:

$$M(\mu^+K^-\pi^+) - M(\mu^+K^-) = M(D^{*+}) - M(D^0) + \delta_\nu(D^{*+}) - \delta_\nu(D^0) \tag{4.9}$$

which should also result in a peak above $M(\pi^+)$, but with poorer resolution due to the lack of information from the neutrino. This resolution deficiency will be proportional to the neutrino momentum, which can be crudely approximated by $M(\mu^+K^-) - M(D^0)$. Given this, it is expected that histograms of $M(\mu^+K^-\pi^+) - M(\mu^+K^-)$ in varying bins of $M(\mu^+K^-)$ will contain peaks above $M(\pi^+)$ with widths that are proportional to $M(\mu^+K^-)$.

Chapter 5

Roadmap

The goal of this analysis is to measure the Direct CP Asymmetry in the decay $B^- \rightarrow J/\psi K^-$. CP violation does not occur in strong interactions, which accounts for most of the $B^{\pm}$ meson production. As a consequence, B^+ and B^- are produced at an equal rate at the Tevatron. Any CP asymmetry occurs in the weak decay, and manifests as an imbalance in the branching ratios for the particle-antiparticle pair. This analysis explores specifically the $B^- \rightarrow J/\psi K^-$ decay due to its convenient trigger signature. There is also theoretical motivation that a significant measurement of A_{CP} in this channel could point to exotic physics models. In order to accomplish this goal, we must identify a large sample of $B^- \rightarrow J/\psi K^-$ decays and quantify any charge bias introduced by the detector.

To measure the yields, we collect data on the $J/\psi \rightarrow \mu^+\mu^-$ trigger and perform a kinematic fit on the muon pairs with another track to create $B^- \rightarrow J/\psi K^-$ candidates. A variety of track quantity cuts are applied to maximize the statistical power of the signal.

Since each candidate event contains both a μ^+ and a μ^-, any charge bias must be introduced from the K. The detector based charge asymmetry ratio for K is determined by analyzing the semileptonic D decay: $D^{*+} \rightarrow D^0\pi^+, D^0 \rightarrow \mu^+K^-\nu_\mu$. Since CP violation has never been observed in the charm sector, any surplus of D^{*+} or D^{*-} can be attributed to detector effects for μ, K or π. This quantity has already been measured for μ and π in previous analyses which allows for the extraction of a K efficiency ratio.

The final measurement is constructed from the above quantities according to the following formula:

$$A_{CP} = \frac{N\left(B^-\right)\frac{\epsilon\left(K^+\right)}{\epsilon\left(K^-\right)} - N\left(B^+\right)}{N\left(B^-\right)\frac{\epsilon(K^+)}{\epsilon(K^-)} + N\left(B^+\right)} \tag{5.1}$$

The yields are extracted using a combined likelihood fit of the lifetime and mass of the $B^- \rightarrow J/\psi K^-$ candidates.

The remainder of the thesis will discuss various aspects of the analysis in greater detail. First an overview of the experimental apparatus will be presented, with a separate chapter describing the tracking chamber with more precision. The datasets that are used in this analysis will be described and the method of the

analysis will be described in detail. The results will be presented with the charge bias measurement from the $D^{*+} \to D^0\pi^+, D^0 \to \mu^+K^-\nu_\mu$ decays first, followed by the yields from $B^- \to J/\psi K^-$. The CP asymmetry will then be extracted and finally any systematic uncertainties will be accounted for.

Chapter 6

Experimental Apparatus

6.1 Overview

The data used in this analysis was collected by the Collider Detector at Fermilab (CDF) which records collisions produced by the Fermilab Tevatron. There exists extensive documentation for both the detector and accelerator elsewhere that this chapter does not attempt to reproduce. It will provide an overview and describe in further detail the components that are essential to the analysis.

6.2 The Tevatron Accelerator Complex

The Tevatron at Fermilab is a 2 km diameter circular synchotron that accelerates proton and antiproton beams and collides them at two interaction points on the ring. With a center of mass energy of $\sqrt{s} = 1.96$ TeV, the Tevatron was the highest energy particle physics collider until the Large Hadron Collider (LHC) at CERN recorded collisions at $\sqrt{s} = 7$ TeV on March 30, 2010. The protons and antiprotons are contained in 36 bunches with a spacing of 396 ns. Collisions occur when the beams are squeezed at two interaction points on the ring: B0 and D0, where CDF and DØ respectively are located. The protons and antiprotons are produced in a staged accelerator complex before being introduced into the Tevatron. In the following subsections, a overview of the accelerator chain are presented.

6.2.1 Cockcroft-Walton

The accelerator chain begins with hydrogen gas contained in the Cockcroft-Walton pre-accelerator. The gas is ionized into H^- and separated from other species by a magnetic field. The ions are then accelerated to 750 keV by a diode-capacitor voltage multiplier. This process occurs every 66 ms to create bunches for injection into the linear accelerator(Linac) for the the next stage.

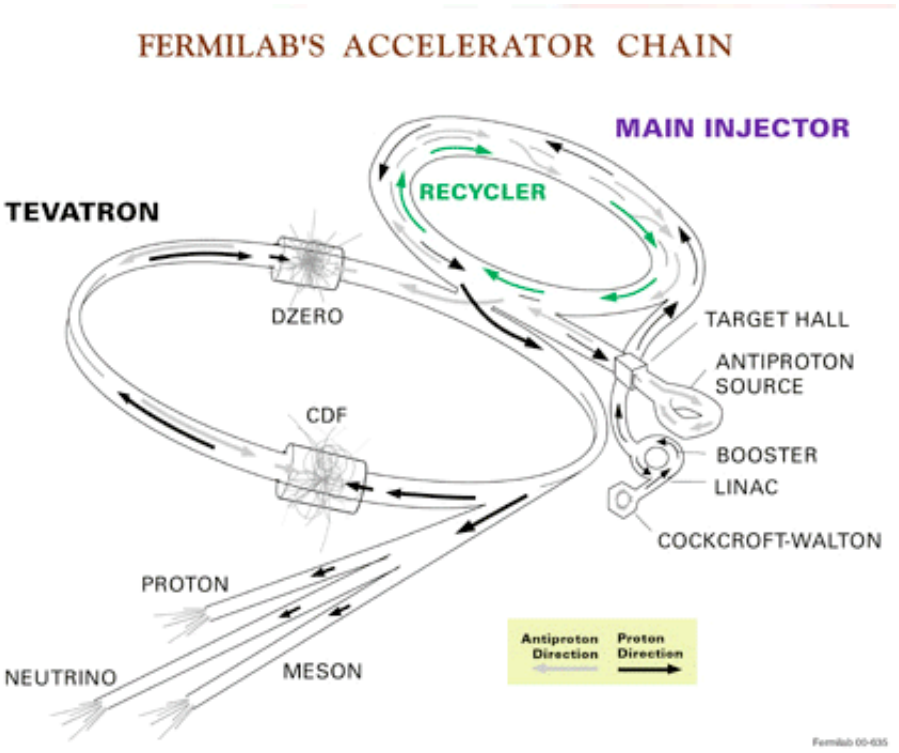

Figure 6.1: Schematic of the Fermilab Tevatron Accelerator Complex

6.2.2 Linac and Booster

The Linac is a 150m long linear accelerator which accelerates the beam bunches to 400 MeV and injects them into the Booster which is a 150 m diameter synchotron. The ions pass through a thin carbon foil during the injection to strip the electrons. The bare proton beams are collected in the Booster to increase the intensity. The beam reaches maximum intensity every 10-12 revolutions and are subsequently accelerated to 8 GeV for injection into the Main Injector.

6.2.3 Main Injector

The Main Injector was a part of the major upgrade to the Tevatron in 1994. It serves several functions in the accelerator chain. It functions under two modes: collider accumulation mode and collider injection mode. In accumulation mode, if receives 84 bunches of protons from the Booster every 2 seconds. The protons are accelerated to 120 GeV then directed to a nickel alloy target in the Target Hall. This produces a shower of particles which is focused into a parallel beam by a cylindrical lithium lens. The bunch structure of the incident proton beam persists through to this particle beam. This beam is passed through a pulsed dipole magnet which serves to separate negatively charged particles with about 8 GeV of energy. For every 10^6

incident protons on the target, 20 antiprotons are produced and collected in the Antiproton Source. Here, the antiprotons are debunched into a continuous beam and the momentum spectrum is narrowed through stochastic cooling. The antiprotons are stored in the Antiproton source as well as the Recycler Ring which is located in the same tunnel as the Main Injector. The Recycler Ring was added in 2004 because limiting the number of antiprotons stored in the Antiproton Source allows for greater optimization of the antiproton accumulation rate.

A sufficient number of antiprotons are accumulated for a physics collision run after 10-20 hours. At this point, the Main Injector enters injection mode. Seven bunches of protons are collected directly from the Booster and accelerated to 150 GeV, coalesced into a single bunch and injected into the Tevatron. Thirty-six of these proton bunches are injected into the Tevatron at 12 seconds intervals. The protons are separated into 3 trains of 12 bunches. The bunches have a spacing of 396 ns at 980 GeV, while the trains have a spacing of about 2.62 μs. This large train spacing allows for injection of the antiprotons without disturbance of the beam and provides an abort gap for safe disposal of the beam. Antiprotons are extracted from the Antiproton Source and Recycler and injected in sets of four bunches. The anti-proton bunch structure mirrors the proton bunch structure and the beam travels in the opposite direction as both species share the magnet and vacuum systems of the Tevatron.

6.2.4 Tevatron

The beams travel in opposite directions following helical orbits with beam interactions minimized by electrostatic separators. The beams are accelerated to the full energy of 980 GeV. At full energy, the particles circle the ring with a period of 21 μs at a speed of 0.9999996 c. Collisions are produced by focusing the beams with quadrapole magnets at the two interaction points on the ring.

The performance of the Tevatron is quantified by the instantaneous luminosity, which is the coefficient between the rate and cross-section of $p\bar{p}$ collisions.

$$rate = \mathcal{L} \times \sigma \tag{6.1}$$

The instantaneous luminosity can be approximated as

$$\mathcal{L} = \frac{f N_B N_p N_{\bar{p}}}{2\pi \left(\sigma_p^2 \sigma_{\bar{p}}^2\right)} \times H\left(\frac{\sigma_\mu}{\beta^*}\right), \tag{6.2}$$

where f is the revolution frequency, N_B is the number of bunches, $N_{p/\bar{p}}$ is the number of protons/antiprotons, and σ_p is the beam size at the collision point. H is the correction factor that accounts for non-zero crossing

angles and the bunch shapes. This approximation is reached by summing across each of the bunches since N_p and $N_{\bar{p}}$ can vary by as much as 20%. The beam size can also vary in principle, but in practice are generally uniform.

The instantaneous luminosity decreases exponentially as the number of protons and anti-protons decrease because of the collisions and interactions between the beams. As collisions are recorded, more anti-protons are being generated and stored in the Antiproton Source and Recycler. When a sufficient stack is available, the remaining beam is dumped from the Tevatron and replaced with this new stack. Continual improvements to the storage, cooling and transfer methods from the Beam Division at Fermilab has resulted in a steady improvement of the instantaneous luminosity over the course of Run II (Fig. 6.2).

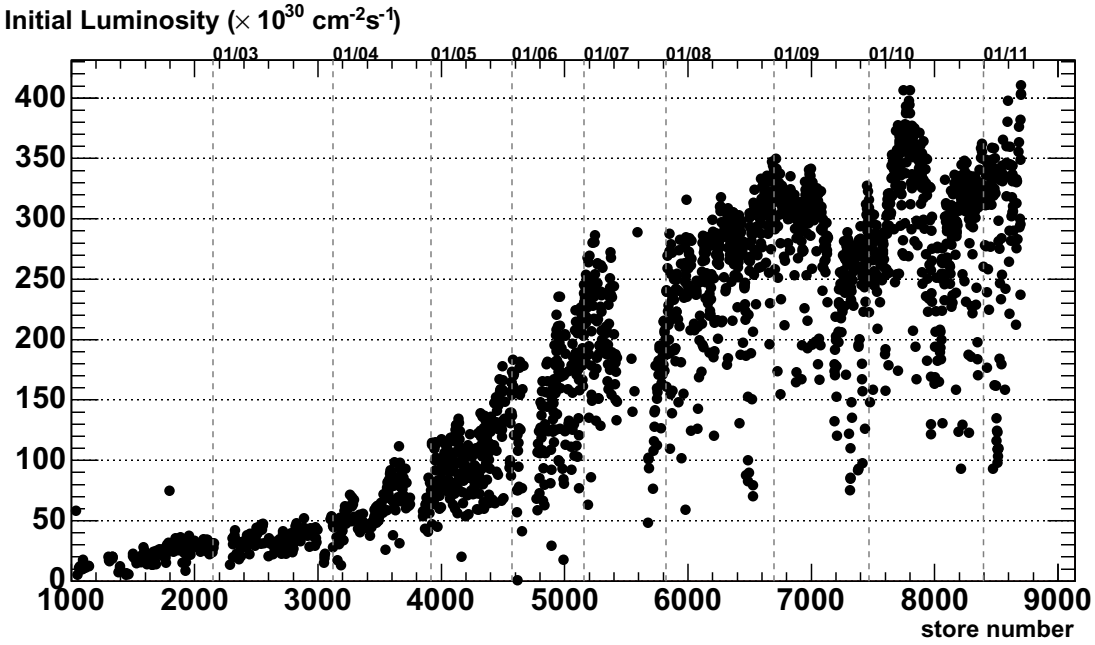

Figure 6.2: Instantaneous Luminosity at beginning of stores of CDF Run II

6.3 Collider Detector at Fermilab

The Collider Detector at Fermilab (CDF) is a general purpose detector to study to collisions produced by the Tevatron. It has been collecting data at interaction point B0 on the Tevatron ring since the first collisions in October of 1985. Following increases in accelerator performance and major upgrades during the 1996 shutdown, almost every subsystem of the detector has been upgraded or rebuilt. The detector consists of a tracking system, calorimetry system and muon detection system.

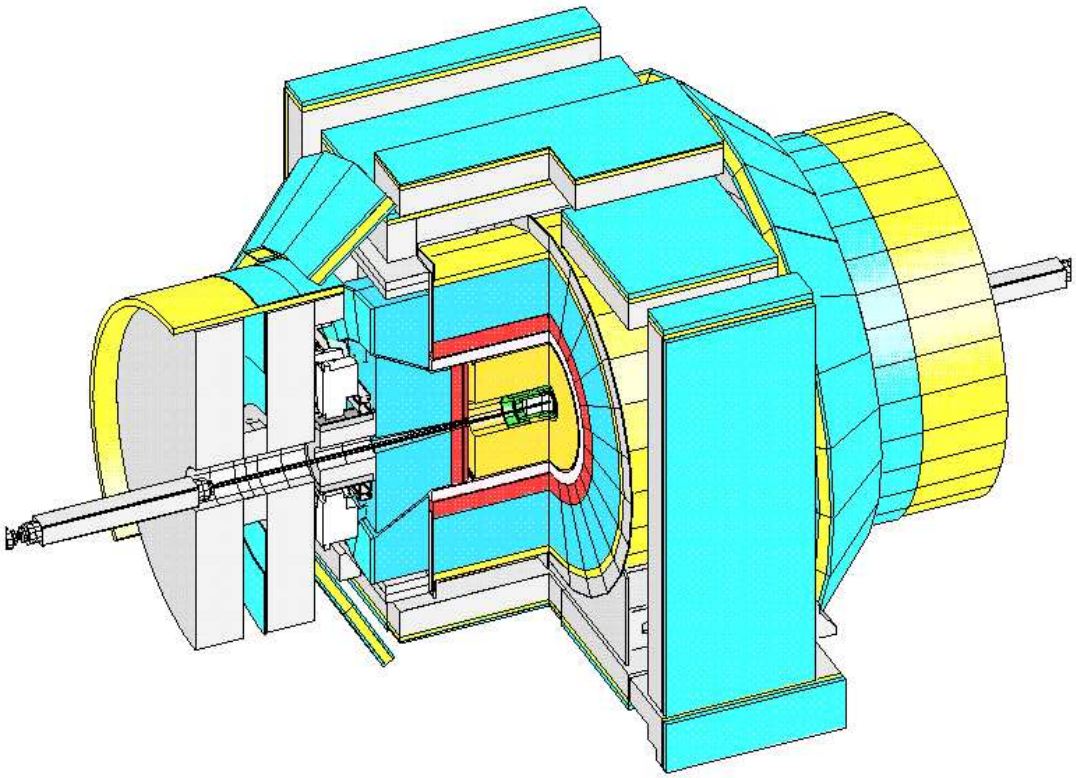

Figure 6.3: Isometric view of the CDF Detector (schematic)

6.3.1 Tracking

The CDF detector is approximately cylindrically symmetric and charged particles travel on a helical path due to the immersion of the tracking volume in a solenoidal magnetic field. The CDF coordinate system defines the proton direction as $\hat{z}$, this is opposite the magnetic field direction. The coordinate system is right-handed with the $\hat{y}$ axis pointing up.

Pseudorapidity is an important quantity in the CDF experiment and is defined as:

$$\eta = -\log\left(\tan\frac{\theta}{2}\right) \tag{6.3}$$

where θ is the polar angle measured from the positive $\hat{z}$ axis.

The helical path for the charged particle can be uniquely described by 5 tracking parameters. At CDF, these parameters are:

$$\vec{\alpha} = \{\lambda, C, z_0, d_0, \phi_0\} \tag{6.4}$$

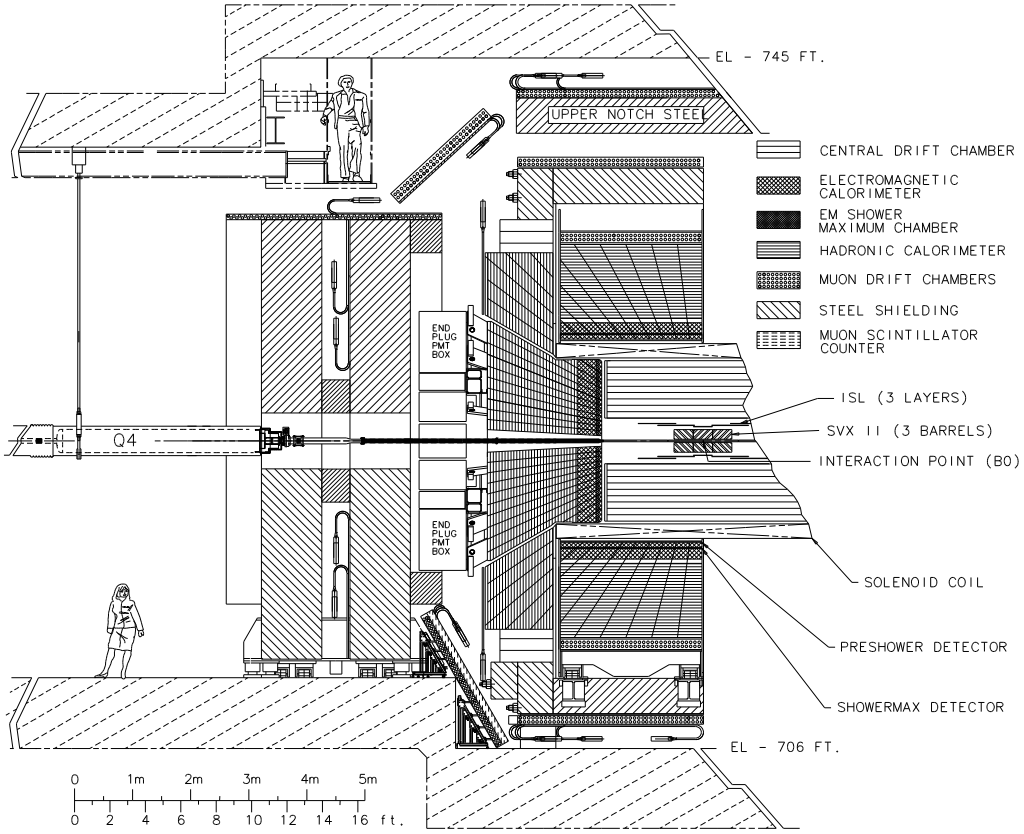

Figure 6.4: Schematic view of the CDF detector, with subsystem volumes labeled

λ is $\cot\theta$. C is the half curvature of the track and carries the sign of the charge. z_0 and ϕ_0 are the z position and azimuthal angle at minimum approach to the beam line. Finally, d_0 is the track impact parameter, with magnitude equal to the distance of closest approach to the beam line. The impact parameter also carries a sign defined by the following normalized scalar triple product:

$$d_0 = \frac{\hat{z}\cdot(\vec{r}\times\vec{p}_T)}{\vec{p}_T} \tag{6.5}$$

where $\vec{r}$ is the vector to the point of minimum approach.

6.3.2 Silicon

CDF employs three different Silicon based tracking systems close to the beam pipe. The innermost is Layer 00 (L00), which is surrounded by the Silicon Vertex Detector (SVX II) and the Intermediate Silicon Layer (ISL). The geometry of the entire silicon detector can be seen in Fig. 6.5.

L00 is a single sided, radiation hard silicon layer which resides immediately outside the beam pie and

greatly improves track impact parameter resolution.

SVX II, the main silicon detector in CDF, is built in three cylindrical sections which lay end to end. Each section, or barrel, is 29 cm long and consists of five layers of staggered silicon. Each layer is made up of 12 overlapping wedges in ϕ. Each layer consists of double sided silicon microstrip detectors.

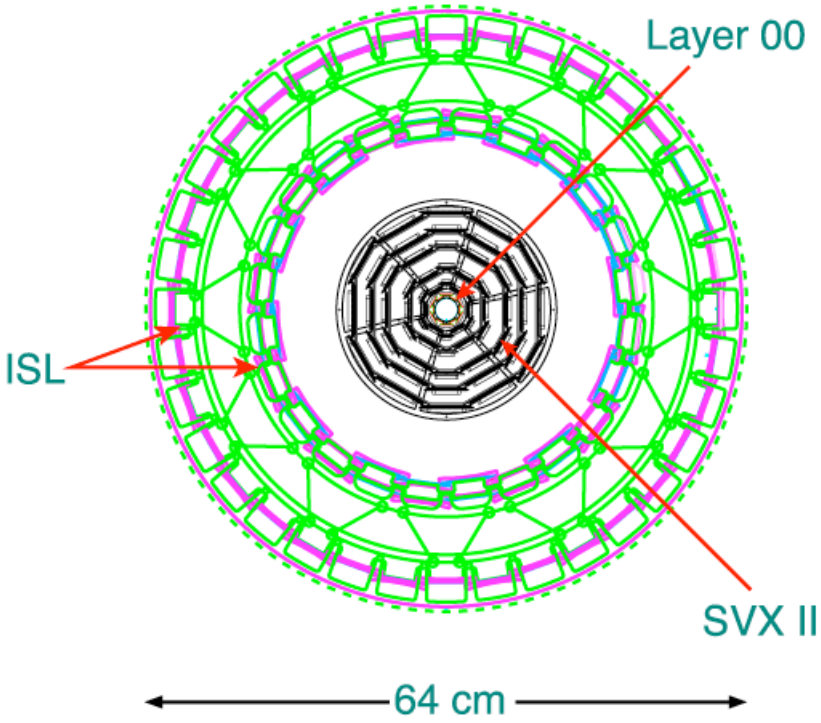

Figure 6.5: Schematic of SVX geometry as viewed along the beam direction

6.3.3 COT

The Central Outer Tracker (COT) is an open-cell drift chamber providing charge particle tracking information in the region of $|z| < 155$ cm from radius 44 cm to 132 cm. The entire chamber contains 30,240 gold plated tungsten sense wires. The wires are arranged in 8 super layers containing cells of 12 wires each. Superlayers contain increasing number of cells with increasing radial distance. The innermost superlayer containing 168 cells, the outermost containing 480. Four of the superlayers are axial, with wires parallel to the beamline providing sensitivity in the $\hat{r} - \hat{\phi}$ plane. These axial superlayers are alternated with stereo superlayers which which have a 2° tilt with respect to the beam. In collaboration with the axial layers, this provides limited sensitivity in the $\hat{z}$ direction. Every superlayer contains potential wires and are separated by cathode field panels to immerse the chamber in an electric field. The geometry is shown in Fig. 6.6.

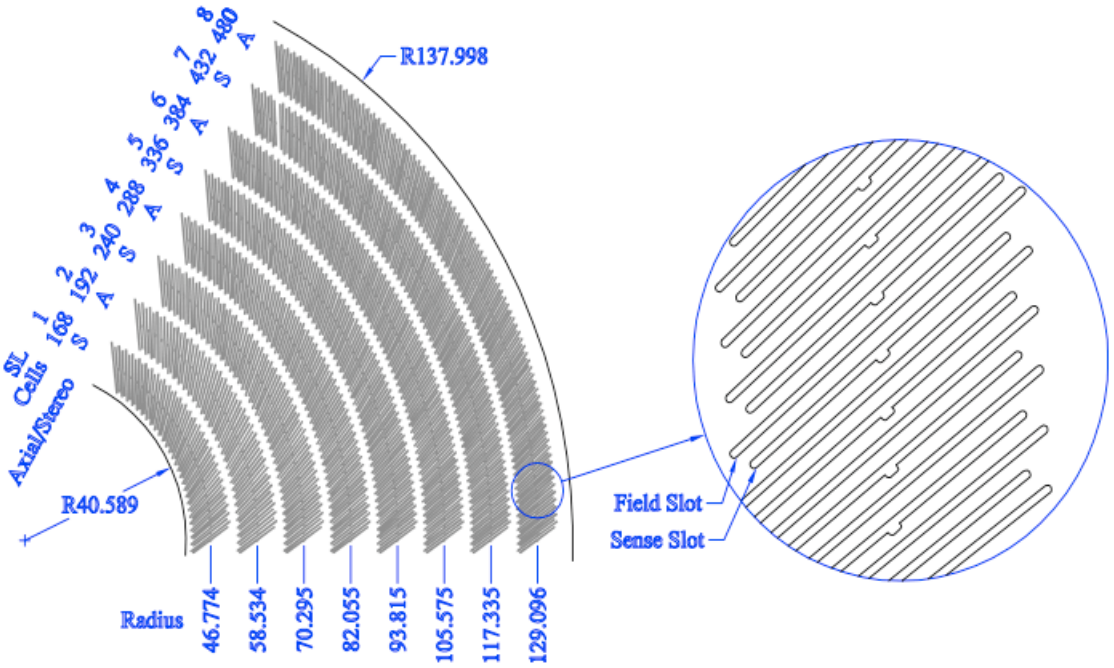

Figure 6.6: 1/6 section of the COT with number of cells, wire orientation (stereo (S) or axial(A)) and radius given for each superlayer. An enlarged section also shows detailed geometry of field and sense planes.

The chamber is filled with a 50:50 Argon:Ethane gas mixture. This gas is ionized by charged particles that travel through the chamber leaving a trail of electrons to drift toward the sense wires. The path of these electrons is influenced by both the electric field in the chamber and a magnetic field produced by a solenoid that immerses the tracking systems. This arrangement results in a Lorentz Angle of 35° which is matched by the tilt of the cells in the COT.

As an electron left in the ionizing trail of the charged particle moves towards the sense wire, the electric field increases and accelerates the charge, resulting in a charge avalanche. This amplifies the signal by a factor of 10^4. This pulse of charge is collected on the sense wire and recorded as a hit and read out with timing information. As a charged particle passes through the entire chamber, hits are collected from up to 96 layers providing information to recreate a helical track for use in analysis.

6.3.4 Calorimeters

The CDF calorimetry system is subdivided into several electromagnetic and hadronic scintillator calorimeters. There are five subsystems in total providing total coverage out to $|\eta| < 3.6$. They consist of a uniform pattern of towers segmented evenly in ϕ and η which point back to the interaction region. These systems

are:

- Central Electromagnetic (CEM), $|\eta| < 1.1$
- Central Hadron (CHA), $|\eta| < 0.9$
- Wall Hadron (WHA) $0.7 < |\eta| < 1.3$
- Plug Electromagnetic (PEM), $1.1 < |\eta| < 3.6$
- Plug Hadron (PHA), $0.7 < |\eta| < 1.3$

some of which are displayed in Figure 6.7. The calorimetry systems use photomultiplier tubes to sample the deposited energy by measuring light produced in polystyrene based scintillators. The scintillators produce light when excited by ionizing radiation. These scintillator layers are alternated with an absorber material. The CEM and PEM use lead sheets, the CHA and WHA use steel and the PHA uses iron. When a particle passes through an absorber layer, it produces a shower as it interacts with the nuclei. This produces a shower of energy that is deposited in the scintillators. Hadronic showers are produced via strong interactions with the nuclei, producing showers of charged particles. The EM calorimetry measures the energy of electrons via Bremsstrahlung radiation and the energy of photons through conversions. Electrons and photons are differentiated by detectors embedded in the EM detectors at about 6 radiation lengths.

6.3.5 Time of Flight

Time of flight is an important quantity for particle identification. The COT allows for excellent momentum resolution through precise measurement of the track curvature in the magnetic field. With time of flight information, an estimate of the particle velocity can be made, which can be used to extract the mass for particle identification.

The Time of Flight Detector (TOF) consists of 216 scintillating bars in a cylindrical geometry located just outside the COT as seen in Figure 6.7. Each bar is 300 cmin length with a 4cm × 4cm cross-section. The time of flight information is extracted as the arrival time relative to the beam crossing. This system is especially effective for discriminating between low momentum K^- and π^+ .

6.3.6 Cherenkov Luminosity Counters

The luminosity ($\mathcal{L}$) at CDF is determined through the rate of inelastic $p\bar{p}$ collisions according to the following formula:

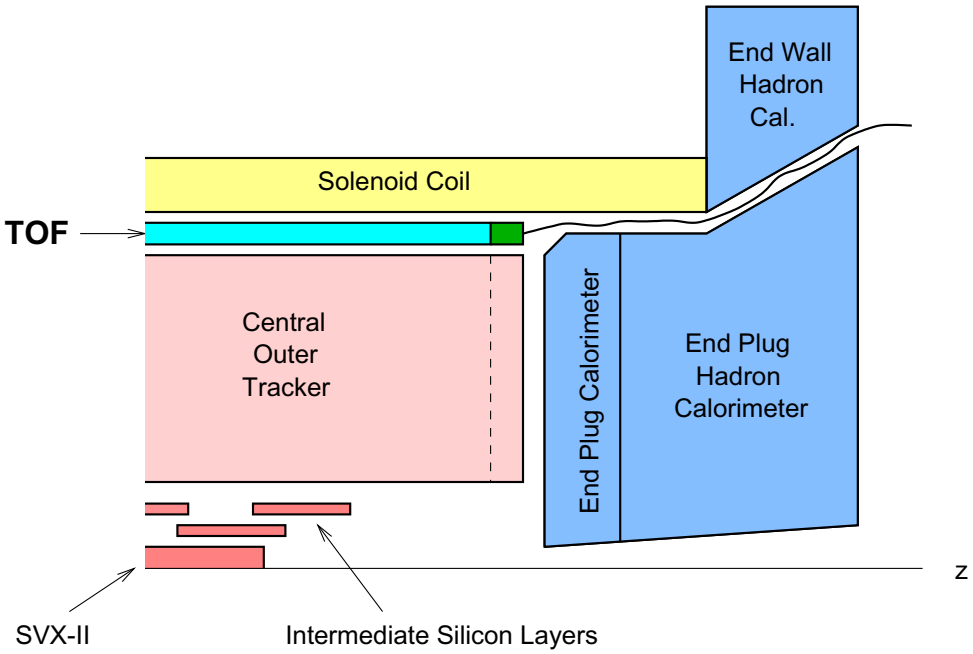

Figure 6.7: Cross-section view of one quadrant of the CDF tracking volume. The PEM, PHA and WHA are visible. The location of the TOF system is also shown.

$$< N > f = \sigma_{in} \mathcal{L} \tag{6.6}$$

where $< N >$ is the average number of interactions per beam crossing, f is the beam crossing frequency, and σ_{in} is the inelastic cross-section. The Cherenkov Luminosity Counters (CLC) are two detectors which reside in 3 degree holes inside the end-plug calorimeters. Each detector consists of three concentric layers of 16 counters each. Each counter is a long gas filled tube (180 cm in the outer layer, 110cm in the inner layers) which points towards the primary interaction point. A PMT sits at the far end of the tube to collect Cherenkov light generated by charged particles moving above the speed of light in the gas. A particle that originates at the interaction point will traverse the entire length of the tube and generate a large signal, while particles produced in secondary interactions will yield a much smaller signal. This allows for a measurement of the mean number of interactions. The bunch crossing rate is known by construction and the inelastic cross-section has been measured which allows for extraction of the instantaneous luminosity.

6.3.7 Muon Systems

Generally, the only particles that live long enough to exit the tracking system are protons, electrons, pions, kaons and muons. π^+ , K^- , e^- and p lose energy quickly in the dense calorimeter systems due to a combi-

nation of Bremsstrahlung radiation and nuclear interactions. Muons are less susceptible to bremsstrahlung than electrons since they are about 200 times more massive, and are immune to strong interactions as leptons. For these reasons, muons with significant energy tend to escape the detector. For this reason, CDF is surrounded by several muon detection systems. There is even addtional steel between the muon systems and the rest of the detector to minimize any non-muon pollution.

The muon system consists of four systems of drift chambers much like the COT. They cover a range of $|\eta| < 1.5$. The separate systems are the Central Muon Detector (CMU), Central Muon Upgrade (CMP), Central Muon Extension (CMX) and Intermediate Muon Detector. These drift chambers measure short track stubs that are extrapolated to match COT tracks in order to reduce background from noise in the electronics. The coverage of the various muon systems is shown in Figure 6.8.

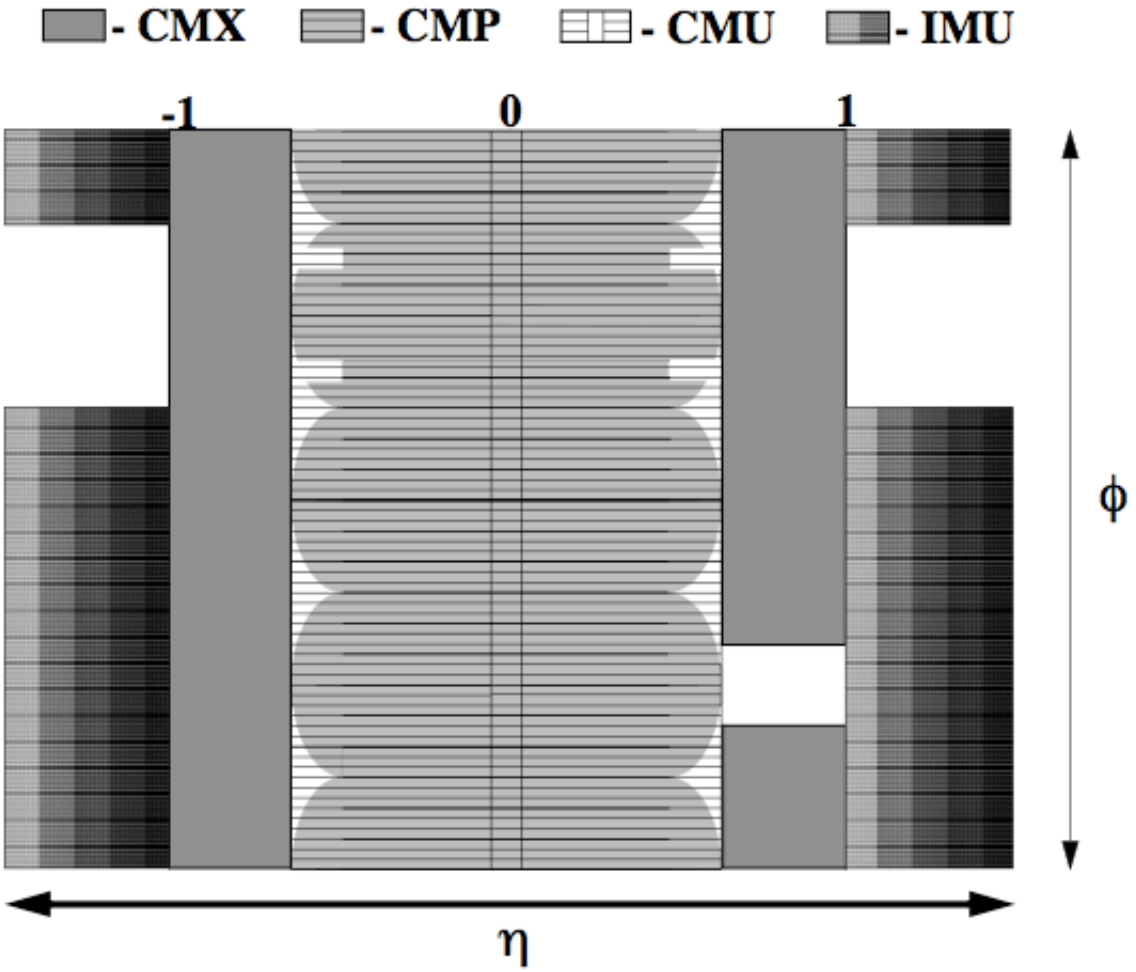

Figure 6.8: $\eta - \phi$ coverage for the CDF muon systems

Background can also be produced if hadrons (K^- , π^+) reach the muon chambers, but this is largely

suppressed by the amount of material shielding. However, this material introduces a complication due to Columb scattering. This is the elastic scattering of point particles on a massive charge. When a muon traverses dense material, it passes near many massive nuclei and undergoes small-angle deflections. This complicates COT track-muon stub matching, but is well understood and accounted for in processing.

Chapter 7

COT Calibration

This section describes the Central Outer Tracker (COT) in increasing detail, specifically a description of the calibration system employed for this subsystem of the detector. The COT is the drift chamber that is responsible for detecting tracks that are one of the building blocks that make up events at CDF. The COT was a Run II upgrade to the Central Tracking Chamber (CTC). It consists of 30240 channels divided into 2520 cells. Each cell consists of 13 potential wires and 12 sense wires, and is enclosed by gold-plated Mylar sheets which serve as cathode panels. The front-end electronics chain starts with the ASDQ (Amplifier Shaper Discriminator with Charge Encoding) daughterboards. Each daughterboard holds 2 ASDQ ASICs (24 channels) and connect via a microcoaxial cable to a TDC. The signal passes through a Repeater board which compensates for any shaping through the microcoaxial cable. Each TDC takes signals from 4 ASDQ daughterboards (96 channels).

The COT is designed with a maximum drift time of 220 ns with a maximum drift distance of 0.9 cm. The chamber is filled with a 50:50 mixture of Argon-Ethane gas which has drift velocity of 50 μm/ns.

7.1 COT Signal

A charged particle that traverses through the 50:50 Ar-Ethane leaves an ionization trail. The electrons that left in the ionization trail travel towards a sense wire in the cell at the gas drift velocity of $\approx 50\mu$m/ns. As the electron approaches the sense wire, the large gradient in electric field accelerates the electrons which initiates a limited avalanche of secondary ionizations. The mean number of secondary ionizations produced per incident primary electron is referred to as the gas gain (G), and is a function of the potential of the sense wire. In the case of the COT $G \approx 2 \times 10^4$.

A minimum ionizing particle will produce, on average, 20 electrons which travel towards the sense wire. The amount of charge that is deposited on the sense wire is approximated by

$$Q \approx N \cdot G \tag{7.1}$$

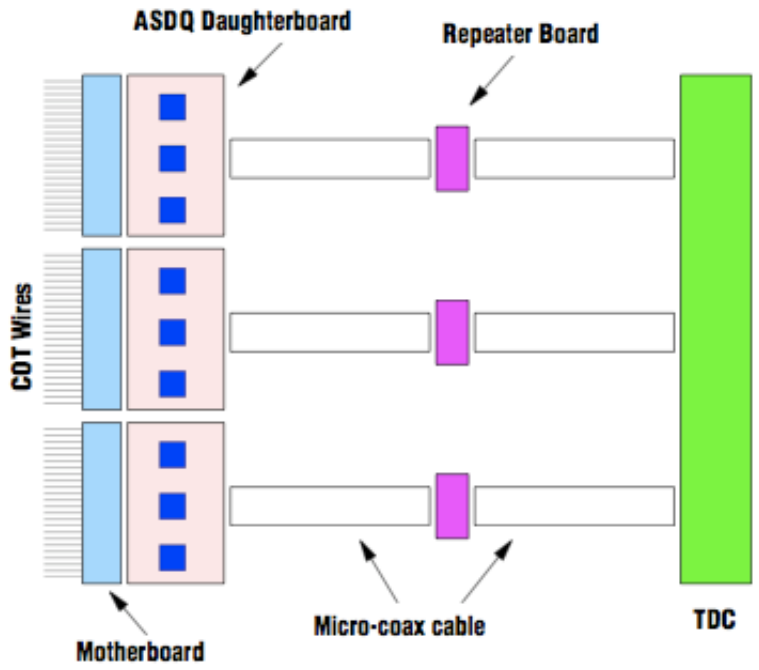

Figure 7.1: Schematic of the COT front end electronics

which corresponds to about 4×10^5 electrons or 64fC. The secondary ionization electrons are already at the potential of the sense wire, and thus make a minor contribution to the signal. The main source of signal on the wire is that which is induced by the positive ions produced in the avalanche drifting away from the wire. The slow drift of the massive ions results in a large tail which must be accounted for to generate the pulse resolution required for the potential high hit frequency.

A block diagram of the ASDQ is shown in Figure 7.2. The signal from the wire enters an input protection circuit which buffers the preamplifier from large external spikes. The preamplifier then amplifies the signal and converts it from the charge input to a voltage output. The tail from the ion drift is canceled by a circuit element which produces a mirror image of the tail. A baseline restorer then brings the signal back to a nominal zero. Finally a discriminator circuit is used to generate a digital pulse, which is sent to the TDC as a hit. The shape of a typical signal through these stages is show in Figure 7.3.

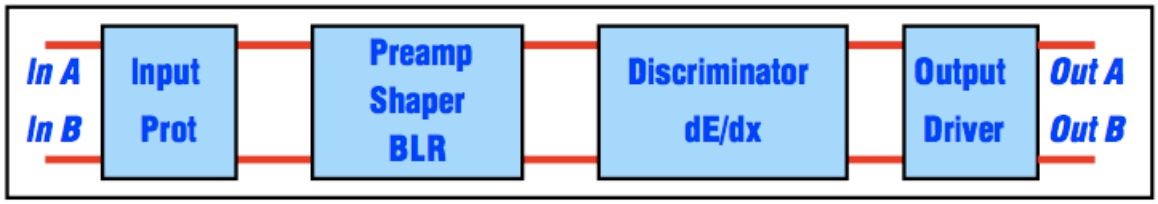

Figure 7.2: ASDQ block diagram

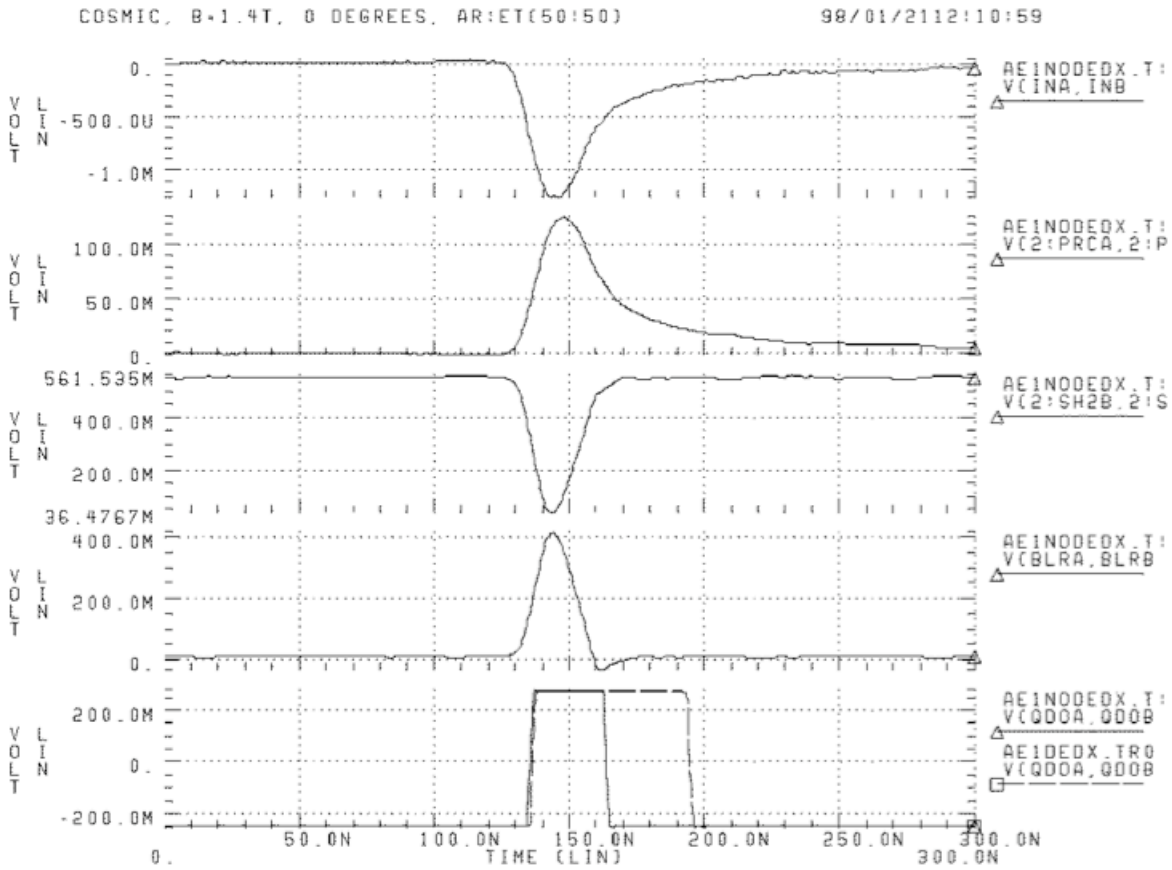

Figure 7.3: ASDQ Signal in four stages (top to bottom): Input to preamplifier, output of preamplifier, output of tail cancellation, output of baseline restorer, output of discriminator

7.2 Calibration Overview

The COT is used to produce tracks based on timing and hit information. Between stores at CDF the ACE performs an "online" timing calibration to measure the channel-level variance in the readout times of the 30240 channels. Channel to channel differences are compensated by offsets that are applied in software.

These differences arise mainly due to differences in cable-length between the COT and the crates that house the TDCs. They will also drift due to changes in the readout electronics. Each time a calibration is taken, it is checked against the database that contains the most recent set of offsets. Any changes that are seen are then uploaded to the database and used by the L3 trigger and the production farm to correct the raw start times recorded with each COT hit to improve the tracking resolution.

A diagnostic calibration is also taken each time work is done on the COT or neighbouring subsystems. This calibration provides information about hit times as well as pulse width and channel occupancy. The signals are generated in the same fashion but the readout collects more information. This allows for greater discrimination about the nature of any issue that may arise. For example a blown resistor at the ASDQ input will result in an impedance mismatch and generate reflections in the readout. This will be indicated by occupancies greater than one.

7.3 Calibration Hardware

The calibration starts with a pulse generated by the TRACER which sends a signal to a Digital Delay Generator (DDG) which generates a calibration pulse. This pulse is sent to a 1-to-8 fanout board and sends an identical signal to each of the 8 COT racks that are housed on the detector. Each rack contains a 1-to-3 fanout board on one of its crates. This signal is sent to the TRACER that lives in each crate and generates a calibration pulse on the backplane that is sent out the front plane of each TDC, along the microcoax cables, through the repeater and to the ASDQ cards mounted on the face of the COT. Each ASDQ contains calibration circuity that, upon receiving this signal, generates a pulse of charge on each of the 24 channels. This is equivalent to receiving a dose of charge from the COT and the readout electronics now treat this as a signal and the measurement at the TDC provides the timing information that is required to determine the offsets.

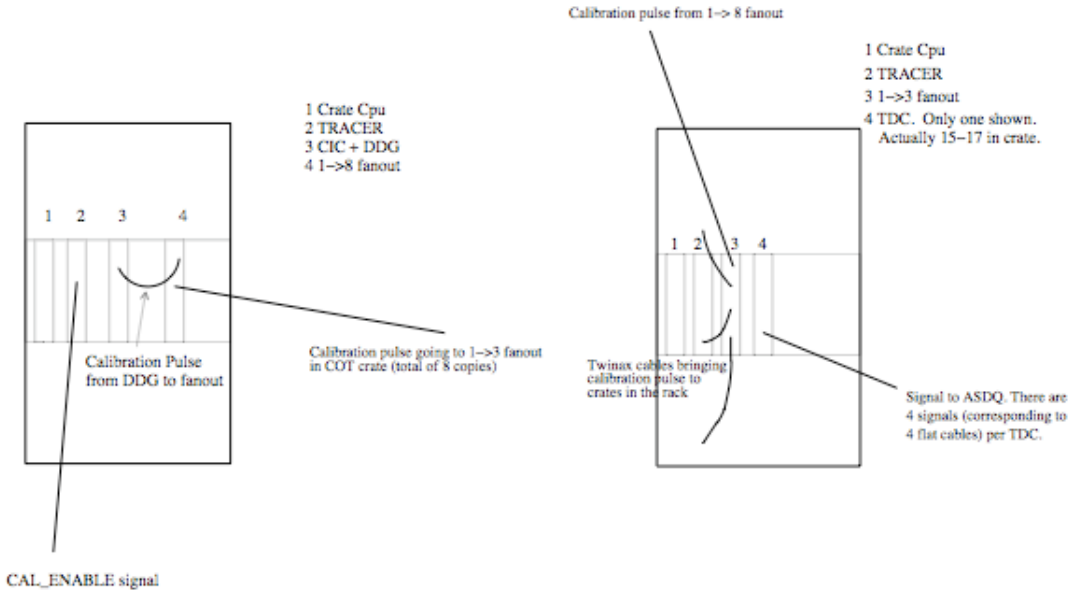

Figure 7.4: Simplified schematic of calibration hardware. Left section describes the hardware in the control room, while the right hand side describes the hardware on the detector.

Chapter 8

Trigger

8.1 CDF Trigger System

The beam crossing rate at CDF far exceeds the available bandwidth for recording events. It is necessary to judiciously select events to maximize the physics information that can be extracted. This is accomplished at CDF through the implementation of a three level trigger system. Each level selects a subset of events based on physics motivations and feeds these events to the next level, until the raw data is written to tape after the Level-3 selection. The goal of the trigger system is to maximize physics acceptance, while minimizing deadtime.

The Level-1 system consists of dedicated hardware for finding physics objects including clusters in calorimeter and track stubs in the muon systems. The eXtremely Fast Tracker (XFT)[21], a part of the CDF II upgrade, allows for track reconstruction from the COT. The track extraplation system (XTRP)[22] provides the ability to match tracks from the COT to stubs in the muon chamber or clusters in the calorimeter. This allows for improved electron and muon identification, as well as increased momentum resolution. The Muon Matchbox (TCMD) is the system where the XTRP tracks are compared to muon stubs. The XTRP is also employed in the two-track trigger which provides hadronic events largely from B-decays. The Level-1 trigger accept rate is about 30 KHz.

The Level-2 trigger accepts events from Level-1 at a maximum rate of 30 KHz. This system includes four asynchronous event buffers and accepts additional information from the central shower-max detector and the silicon tracking system. The CES allows from improved discrimination of photons and electrons. The SVX II works in concert with the XFT to provide precise measurement of the track impact parameter. This allows for quick identification of displaced vertices, which are a common B-physics signature. The Level-2 accept rate was originally $\sim$ 300Hz, but the system has since been upgraded to handle $\sim$ 800Hz.

The Level-3 trigger is a PC farm consisting of about 500 machines running the Level 3 trigger software. Data from the full detector are read to the farm via optical fibers. The rejection criteria are similar to that at Level 2, but full event reconstruction is performed. The output is written to permanent storage with a

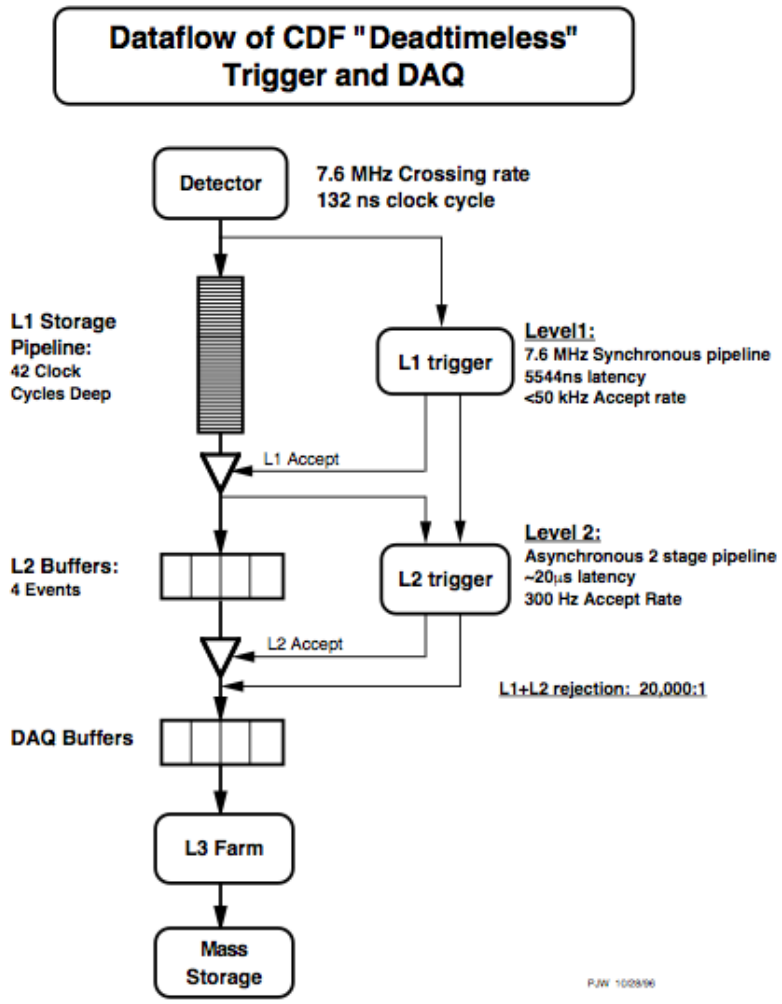

Figure 8.1: Schematic of the CDF DAQ and Trigger System

maximum rate of 150 Hz.

8.2 J/ψ Trigger

The dimuon decay of the J/ψ provides a strong signature for many physics processes. There are a group of trigger paths that exploit this signature. These are the JPSIMUMU trigger paths, and generally require 2 CMU and/or CMX muon candidates. At Level-1, two stubs are found in the muon systems and matched with extrapolated tracks from the XTRP in the Muon Matchbox. Various p_T cuts are required depending on the specific trigger path.

Many of these triggers are prescaled to minimize dead time. A prescale factor of X implies that on

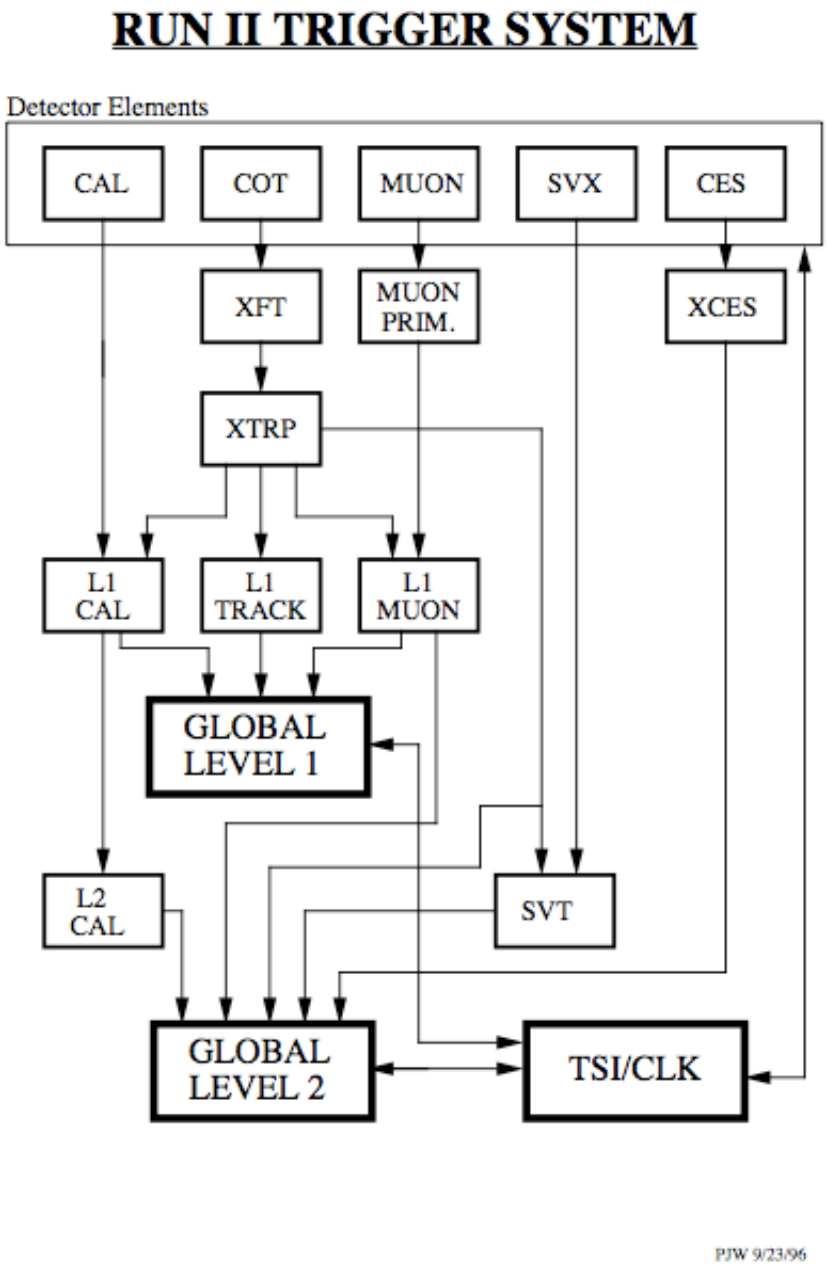

Figure 8.2: Schematic of the various paths through the Level 1 and Level 2 trigger systems.

average one event is accepted for every X events. Trigger paths can be prescaled with a static or dynamic factor. In a dynamically prescaled trigger, the prescaling factor varies with luminosity.

8.3 8 GeV/c CMUP Trigger

The 8 GeV/c CMUP Trigger provides a sample of high p_T muons with minimum bias introduced from detector components. The selection criteria requires tracks with $p_T > 8$GeV/c matching stubs in both the CMU and CMP muon chambers.

Chapter 9

Datasets

9.1 Overview

The interaction rate at CDF far exceeds the maximum rate of data-taking. This is necessary to extract any decent sized sample for the variety of physics programs since the vast majority of events are inelastic collisions with low q^2 and provide very little physics insight. Potentially interesting events must pass through several layers of discrimination before being written to the inclusive CDF dataset.

After being written to tape, the raw data is repackaged in various ways for use by different physics groups. The B-physics group which facilitated this analysis, employs a standard data container called the B Standard Ntuple (B-STntuple). This data format contains various pre-defined decays which are relevant to B physics analyses. The event contains decays with fit information and links to stable tracks that make up the decay. The stable tracks contain important physics information, but lack the information required to perform a full fit. Any fitting to be completed must be done before the B-STntuple stage.

Although the B-STntuple provides a light dataset compared to the raw data, there is still significant overhead involved in carrying decays that may not be relevant to a particular analysis. Skimming provides a framework for creating minimal datasets that include only that information that is to be used in a particular analysis. This provides great benefits for analyses that adapt and demand that the data be analyzed many times.

9.2 Raw Datasets

The raw datasets are generally grouped by the trigger path that the event traversed to be written to disk. An event that passes more than one trigger will find itself in more than one dataset. In this analysis, two types of triggers are used for two purposes. The $\mu\mu$ triggers provide the $B^- \rightarrow J/\psi K^-$ events and the $CMUP8$ trigger is used to extract the K^- charge efficiency ratio. The raw datasets contain all relevant detector and event information to perform full analyses.

9.3 B-STntuples

B-STntuples are generated from the raw data according to standard or custom instructions. The first step is to generate a list of tracks. These tracks are then filtered into potential stable particles: π^+ , K^- , μ^+ , etc. Low-level decay particles that may be candidates for B daughters are generated from these stable collections. Then B candidates are built from the low level decay collections and stable collections. Full vertex fitting is performed and the results of these fits including quality metrics are stored. The covariance matrix, which is required to perform full fits are abandoned in interest of storage efficiency. Every track is included in the π^+ collection by default. All other stable and low-level decay collections are pruned to only include those that are included in a B candidate that passed all of the quality cuts.

9.4 Skims

B-STntuples are much more efficient method of storage compared to the raw datasets, but will generally contain much superfluous information for a specific analysis. This puts excessive strain on data storage and processing. There exists a framework in the CDF software to produce skims that are user-generated and will contain only the tracks and information deemed relevant to a given analysis. The skims are generally produced to store a particular decay candidate including the daughter tracks, while abandoning all other tracks stored in the event. Further, some loose analysis cuts can be applied at the skimming stage to further increase resource efficiency.

9.5 Datasets Used

The raw datasets are defined by the trigger which was collected the events. This analysis took advantage of the B-STntuple framework. These ntuples are generated with a comprehensive decay table based on the trigger signature of the raw dataset. The B-STntuples used in this analysis include those summarized in Table 9.1.

Table 9.1: Dimuon Datasets for $B^- \rightarrow J/\psi K^-$

Dataset	Location	Data Period	Run Numbers
0d	$cdfpbnt/xpmmgd$	0	138425-186598
0h	$cdfpbnt/xpmmgh$	$1-4$	190697-203799
0i	$cdfpbnt/xpmmhi$	$5-10$	203819-212133
0j	$cdfpbnt/xpmmij$	$11-14$	233133-254686
0k	$cdfpbnt/xpmmik$	$15-17$	254800-261005
0m	$cdfpbnt/xpmmfm$	$18-28$	261119-289197

There did not exist a B-STntuple for the 8 GeV/c CMUP trigger, so it was necessary to generate custom datasets which would include these triggers. The raw 8 GeV/c CMUP trigger dataset was processed into a B-STntuple which is now available for use by other CDF analyses. The locations and vital information are summarized in Table 9.2.

Table 9.2: Dimuon Datasets for $D^{*+} \to D^0\pi^+, D^0 \to \mu^+K^-\nu_\mu$

Dataset	Location	Data Period	Run Numbers
0d	$cdfpbnt/hiptfd$	0	138425-186598
0h	$cdfpbnt/hiptfh$	$1-4$	190697-203799
0i	$cdfpbnt/hiptfi$	$5-10$	203819-212133
0j	$cdfpbnt/hiptfj$	$11-14$	233133-254686
0k	$cdfpbnt/hiptfk$	$15-17$	254800-261005
0m	$cdfpbnt/hiptfm$	$18-28$	261119-289197

Chapter 10

Monte Carlo

Simulated samples of B^- and D^{*+} decays are used to optimize event selection, model signal and background distributions, and assess systematic uncertainties. Monte Carlo simulation (MC) samples are generated to model the $B^- \to J/\psi\pi^-$ mass template. Single b hadrons are generated according to the predicted next-to-leading order QCD calculation [23] with momentum and rapidity spectra measured by CDF [24]. These hadrons are then decayed using the EVTGEN package [25], with the requirement that they decay as a $B^- \to J/\psi\pi^-$, and fed into a GEANT simulation of the CDF detector [26]. The simulated data are then processed and reconstructed in the same manner as the detector data.

Two samples of D^{*+} decays are generated. Both with power law $(p_T)^-7$ distributions to match the data sample. The rapidity spectra matches that measured at CDF. The first sample is the inclusive $D^{*+} \to D^0\pi, D^0 \to X$ is generated to study systematic detector biases. The second sample includes only D^{*+} decays with a muon to model the signal shape. In all of the MC samples generated it is assumed that there is no CP violation in D^{*-} production or decay.

Chapter 11

Analysis

11.1 Overview

The goal of this thesis is to determine the direct CP asymmetry in the decay $B^- \to J/\psi K^-$. This is accomplished by collecting $B^- \to J/\psi K^-$ events on the $\mu^+\mu^-$ trigger from the CDF detector on the Tevatron Accelerator at Fermi National Accelerator Laboratory. Direct CP asymmetry (A_{CP}) is defined as:

$$A_{CP} = \frac{\Gamma\left(B^- \to J/\psi K^-\right) - \Gamma\left(B^+ \to J/\psi K^+\right)}{\Gamma\left(B^- \to J/\psi K^-\right) + \Gamma\left(B^+ \to J/\psi K^+\right)} \tag{11.1}$$

Where Γ is the partial width for the process in question. In detector quantities, $\Gamma(B^- \to J/\psi K^-)$ can be written as:

$$\Gamma(B^- \to J/\psi K^-) = \frac{N\left(B^- \to J/\psi K^-\right)}{2\mathcal{L}\sigma_{b\bar{b}} f_u \epsilon_{J/\psi K} A_{J/\psi K}}, \tag{11.2}$$

where $N(B^- \to J/\psi K^-)$ is the number of $B^- \to J/\psi K^-$ decays produced in the collisions. The luminosity ($\mathcal{L}$), cross-section ($\sigma_{b\bar{b}}$), and fragmentation function (f_u) are all charge independent, so the expression for A_{CP} simplifies to:

$$A_{CP} = \frac{N\left(B^- \to J/\psi K^-\right)\frac{\epsilon_{J/\psi K+} A_{J/\psi K+}}{\epsilon_{J/\psi K-} A_{J/\psi K-}} - N\left(B^+ \to J/\psi K^+\right)}{N\left(B^- \to J/\psi K^-\right)\frac{\epsilon_{J/\psi K+} A_{J/\psi K+}}{\epsilon_{J/\psi K-} A_{J/\psi K-}} + N\left(B^+ \to J/\psi K^+\right)} \tag{11.3}$$

Making the assumption that the efficiency ($\epsilon_{J/\psi K}$) and acceptance ($A_{J/\psi K}$) both factorize, this expression simplifies further:

$$A_{CP} = \frac{N\left(B^- \to J/\psi K^-\right)\frac{\epsilon_{K+} A_{K+}}{\epsilon_{K-} A_{K-}} - N\left(B^+ \to J/\psi K^+\right)}{N\left(B^- \to J/\psi K^-\right)\frac{\epsilon_{K+} A_{K+}}{\epsilon_{K-} A_{K-}} + N\left(B^+ \to J/\psi K^+\right)} \tag{11.4}$$

where efficiency refers to the fraction of tracks which pass through the detector that are reconstructed. Acceptance refers to the fraction of tracks which pass through the a portion of the detector where it could

be reconstructed. Since the efficiency (ϵ) and acceptance (A) both account for a loss of events, ϵ is redefined as the product for sake of simplicity.

$$\epsilon \equiv \epsilon A \tag{11.5}$$

The final expression is:

$$A_{CP} = \frac{N\left(B^- \to J/\psi K^-\right)\frac{\epsilon_{K^+}}{\epsilon_{K^-}} - N\left(B^+ \to J/\psi K^+\right)}{N\left(B^- \to J/\psi K^-\right)\frac{\epsilon_{K^+}}{\epsilon_{K^-}} + N\left(B^+ \to J/\psi K^+\right)} \tag{11.6}$$

This shows that the three necessary ingredients to extract $A_{CP}\left(B \to J/\psi K\right)$ include the yields of $B^+ \to J/\psi K^+$ and $B^- \to J/\psi K^-$ and the detector induced charge bias for K, expressed as $\frac{\epsilon_{K^+}}{\epsilon_{K^-}}$. It is important to note that only the relative ratio of $\frac{\epsilon_{K^+}}{\epsilon_{K^-}}$ is required.

11.2 $B^- \to J/\psi K^-$

Aside from complications due to detector effects, the core of this analysis is to measure an asymmetry between the yields for $B^- \to J/\psi K^-$ and $B^+ \to J/\psi K^+$. This section will discuss the methods employed to reconstruct the candidates and any complications that arise, including contributions from the Cabibbo-suppressed $B \to J/\psi \pi^+$.

The $B^- \to J/\psi K^-$ events are collected on the dimuon trigger. The $\mu^+\ \mu^-$ trigger pair are kinematically fit with another track to generate the $B^- \to J/\psi K^-$ candidate. A host of loose quality cuts (Table 11.1) are applied to maximize the signal quality. Also, a good run list is applied to ensure all the data used was collected while all relevant subsystems of the detector were properly functional.

Table 11.1: Cuts on $B^- \to J/\psi K^-$

	Units	Requirement
$p_T(B^-)$	GeV/c	≥ 6.0
$M(B^-)$	GeV/c^2	≥ 5.6
$M(B^-)$	GeV/c^2	≤ 5.0
$M(J/\psi)$	GeV/c^2	≥ 3.05
$M(J/\psi)$	GeV/c^2	≤ 3.15
$p_T(K^-)$	GeV/c	≥ 2.0
Num Si Hits (μ^+)	–	≥ 3
Num Si Hits (μ^-)	–	≥ 3

An unbinned likelihood fit is performed simultaneously on the mass and proper decay time to extract the yields. The fit is performed in 3 bins of $p_T(K^-)$ and 6 bins of $\phi(K^-)$ for both $B^- \to J/\psi K^-$ and

$B^+ \to J/\psi K^+$. The binning is performed in order to properly account for $\frac{\epsilon_{K^+}}{\epsilon_{K^-}}$ which is expected to vary with $p_T(K^-)$ and $\phi(K^-)$ as further discussed in section 14.7.

The fact that the events are collected on a diumon trigger provide the added benefit that no charge bias can arise from the μ^+ tracking. Both the $B^- \to J/\psi K^-$ and $B^+ \to J/\psi K^+$ require a μ^+ μ^- pair from a neutral resonance, so any bias should contribute equally to $B^- \to J/\psi K^-$ and $B^+ \to J/\psi K^+$.

11.2.1 $B^- \to J/\psi \pi^-$

In the mass window, the main source of background is simply combinatoric (three random tracks) and is modeled well with a linear function. However, there is another source of background which provides a slight complication. The Cabibbo-suppressed decay $B^- \to J/\psi \pi^-$ will arise as a reflection above the $B^- \to J/\psi K^-$ mass peak when the π^+ is misassigned as a K^-.

This is accounted for by generating $B^- \to J/\psi \pi^-$ MC and assigning the K^- mass to the π^+ to create a template for this effect to be fit in the data. The shape of the template is fixed from MC while the amplitude relative to the $B^- \to J/\psi K^-$ signal peak is allowed to float in the final fit. The shape is determined by the kinematics of the decay, which the MC models quite well. The template was fit using the sum of three Gaussians in each of the three $p_T(K^-)$ bins (Figs. 11.1(a),11.1(b),11.1(c))as well as one fit across all $p_T(K^-)$ bins (Fig. 11.1(d)).

11.2.2 Other Potential Backgrounds

There are potential sources of background from other B meson decays that are worth investigating. B^0 decays are not an issue since at least one track must be missing from the B^0 to be reconstructed as a B^+ candidate due to the difference in charge. The maximum mass for a B^0 with a missing track would be:

$$M(B^0) - M(\pi^+) \approx 5.13\text{GeV}/c^2 \tag{11.7}$$

which is below the signal region and outside of the $B^- \to J/\psi K^-$ mass resolution.

It is possible that there is a contribution from B_s due to its higher mass. Again, since the B_s is neutrally charged, a daughter particle must be missing which could result in a reflection into the B^+ signal region since the maximum mass in this situation would be:

$$M(B_s) - M(\pi^+) \approx 5.22\text{GeV}/c^2 \tag{11.8}$$

which is beginning to leak into the signal region. The main concern is the potential for a background which

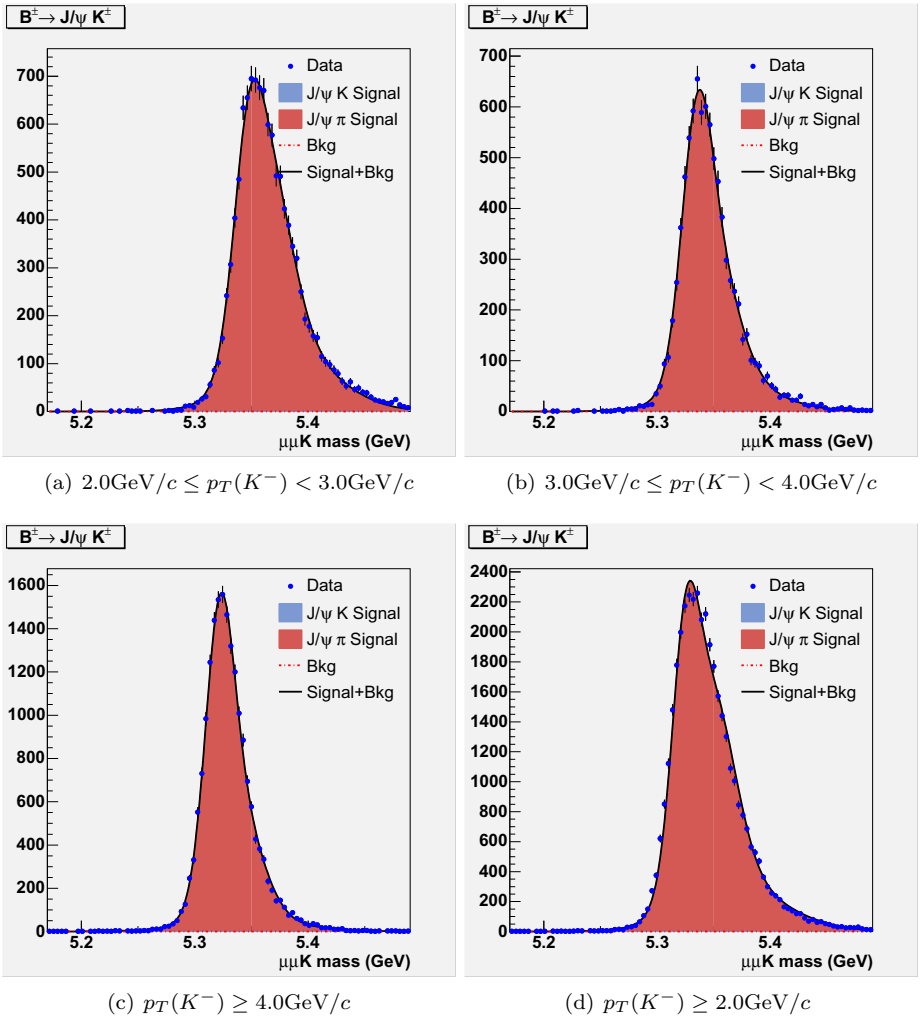

(a) $2.0\text{GeV}/c \leq p_T(K^-) < 3.0\text{GeV}/c$

(b) $3.0\text{GeV}/c \leq p_T(K^-) < 4.0\text{GeV}/c$

(c) $p_T(K^-) \geq 4.0\text{GeV}/c$

(d) $p_T(K^-) \geq 2.0\text{GeV}/c$

Figure 11.1: $B^- \to J/\psi\pi^-$ MC Templates

peaks under the $B^- \to J/\psi K^-$ peak. A large sample of inclusive $B_s \to J\psi X$ MC was generated to test this effect and found that there was no peaking background (Fig. 11.2). An estimate of the yield is found to be negligible compared to the signal.

As a further test for structure in the combinatoric background, a separate set of fits is generated on the data with an extra cut of $L_{xy}(B^-) > 0.015\text{cm}$, which eliminates the dominant prompt background.

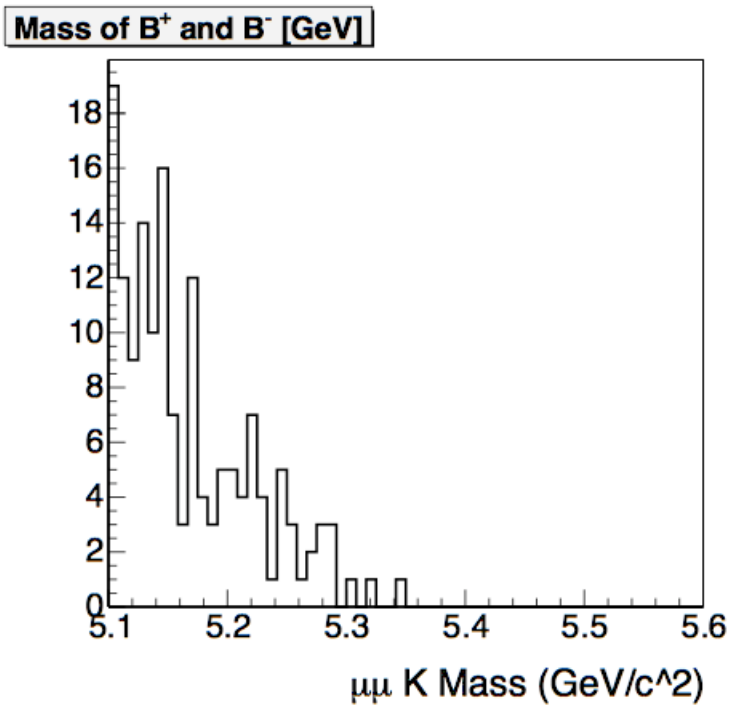

Figure 11.2: $B_s \to J/\psi X$ MC subject to the analysis cuts and reconstructed as a $B^- \to J/\psi K^-$ to test for peaking backgrounds under the signal region

Chapter 12

Likelihood Fit

12.1 Likelihood Function

In order to extract the $B^- \to J/\psi K^-$ yields, a simultaneous unbinned maximum likelihood fit is performed on the reconstructed mass m_{B^-} and proper decay time ct. The uncertainties $\sigma_{m_{B^-}}$ and σ_{ct} are used as an input to the fit on a candidate by candidate basis. The likelihood function is a sum of a signal and background term, with each term being the product of the mass probability density and proper decay time probability density:

$$\begin{aligned}\mathcal{L}\left(m_{B^-}, ct|\sigma_{m_{B^-}}, \sigma_{ct}\right) = f_s \cdot P^s_{m_{B^-}}\left(m|\sigma_{m_{B-}}\right) \cdot P^s_{ct}\left(ct|\sigma_{ct}\right) \\ +(1-f_s) \cdot P^b_{m_{B^-}}\left(m|\sigma_{m_{B-}}\right) \cdot P^b_{ct}\left(ct|\sigma_{ct}\right)\end{aligned} \tag{12.1}$$

where $P^s_{m_{B^-}}$ and $P^b_{m_{B^-}}$ are normalized probability densities for the m_{B^-} signal and background respectively. Similarly, P^s_{ct} and P^b_{ct} describe the probability density function for the proper decay time signal and background, while f_s is the fraction of signal events.

12.2 Mass Probability Density Function

The mass distribution of the signal events is modelled as the sum of two normalized Gaussians centered at the mass of the B^-. The width of the Gaussians are determined on a candidate by candidate basis, based on the mass uncertainty $\sigma_{m_{B^-}}$ and scaled with an overall scale factor. Each Gaussian is allowed an independent scale factor (s_{m1}, s_{m2}).

There is also a contribution from the Cabibbo-suppressed decay $B^- \to J/\psi\pi^-$, where is the π^+ is misidentified as a K^-. This is modeled with three Gaussians, but each with different means. Collecting these terms, the total m_{B^-} signal probability density function is written as:

$$
\begin{aligned}
P^s_{m_{B^-}}\left(m|\sigma_{m_{B-}}\right) = (1 - f_{B^-\to J/\psi\pi^-}) \cdot \Bigg[& \frac{f_{m1}}{\sqrt{2\pi}s_{m1}\sigma_{m_{B^-}}} e^{-(m-m_0)^2/2(s_{m1})^2} \\
& + \frac{1 - f_{m1}}{\sqrt{2\pi}s_{m2}\sigma_{m_{B^-}}} e^{-(m-m_0)^2/2(s_{m2})^2} \Bigg] \\
+ f_{B^-\to J/\psi\pi^-} \Bigg[& \cdot \frac{f_{m\pi1} \cdot (1 - f_{m\pi3})}{\sqrt{2\pi}s_{m\pi1}\sigma_{m_{B^-}}} e^{-(m-m_{\pi1})^2/2(s_{m\pi1})^2} \\
& + \frac{(1 - f_{m\pi1}) \cdot (1 - f_{m\pi3})}{\sqrt{2\pi}s_{m\pi2}\sigma_{m_{B^-}}} e^{-(m-m_{\pi2})^2/2(s_{m\pi2})^2} \\
& + \frac{f_{m\pi3}}{\sqrt{2\pi}s_{m\pi3}\sigma_{m_{B^-}}} e^{-(m-m_{\pi3})^2/2(s_{m\pi3})^2} \Bigg]
\end{aligned}
\tag{12.2}
$$

where m_0 is the center of the $B^- \to J/\psi K^-$ mass distribution, $f_{B^-\to J/\psi\pi^-}$ is the fraction of the Cabibbo-suppressed decay, f_{m1} is the fraction of the $B^- \to J/\psi K^-$ signal covered by the first Gaussian, $f_{m\pi1}$ is the fraction of the $B^- \to J/\psi\pi^-$ signal that is covered by the first $B^- \to J/\psi\pi^-$ Gaussian and $f_{m\pi1}$ is the fraction of the $B^- \to J/\psi\pi^-$ signal that is covered by the third $B^- \to J/\psi\pi^-$ Gaussian. The $B^- \to J/\psi K^-$ signal is covered by the first two terms, while the $B^- \to J/\psi\pi^-$ contribution is covered by the last three.

The background is well modeled by a linear function. The function is normalized, leaving one degree of freedom:

$$
P^b_{m_{B^-}} = C_0 + C_1 \cdot (m - m_c) \tag{12.3}
$$

where $m_c(5.34\text{GeV}/c^2)$ is the center of the mass range used in the fit. C_0 is related to the intercept at $m = 0$, while C_1 is related to the slope and determined by the normalization.

12.3 Proper Decay Time Probability Density Function

12.3.1 Signal Events

Ideal signal events would demonstrate an exponential decay with characteristic decay constant $c\tau$ equal to the lifetime of the $B^- \to J/\psi K^-$. However, this ideal distribution is smeared by uncertainty in the reconstruction of the primary and secondary vertices. In observed measurement, the exponential decay is convoluted with a resolution function $\mathcal{R}$ which accounts for these effects. The resolution function is determined from prompt background as described in the next section.

Table 12.1: Summary of $B^- \to J/\psi K^-$ mass fit parameters

Name	Description	Related Fit
m_0	$B^- \to J/\psi K^-$ mass	Mass, signal
s_{m1}	$\sigma_{M_{B^-}}$ Scale Factor (1st Gauss.)	Mass, signal
s_{m2}	$\sigma_{M_{B^-}}$ Scale Factor (2nd Gauss.)	Mass, signal
f_{m1}	Relative fraction of 1st Gauss.	Mass, signal
$m_{\pi 1}$	Mass center of 1st π^- Gauss.	Mass, signal
$m_{\pi 2}$	Mass center of 2nd π^- Gauss.	Mass, signal
$m_{\pi 3}$	Mass center of 3rd π^- Gauss.	Mass, signal
$s_{m\pi 1}$	$\sigma_{M_{B^-}}$ Scale Factor (1st π^- Gauss.)	Mass, signal
$s_{m\pi 2}$	$\sigma_{M_{B^-}}$ Scale Factor (2nd π^- Gauss.)	Mass, signal
$s_{m\pi 3}$	$\sigma_{M_{B^-}}$ Scale Factor (3rd π^- Gauss.)	Mass, signal
$f_{m\pi 1}$	Relative fraction of 1st π^- Gauss.	Mass, signal
$f_{m\pi 3}$	Relative fraction of 3rd π^- Gauss.	Mass, signal
$f_{B^- \to J/\psi \pi^-}$	Fraction of π^- signal	Mass, signal
C_0	Intercept from norm. linear BG	Mass, background
f_s	Fraction of signal candidates	Mass, Proper Decay Time

12.3.2 Background Events

Background candidates arise from prompt J/ψ events as well as real and fake J/ψ events from other heavy flavor decays. The prompt J/ψ events, assumed to have similar resolution to the signal events, are the handle used to determine $\mathcal{R}$. This is a good assumption since the J/ψ vertex drives the resolution for both cases. The non-prompt background events are modeled using a sum of functions of the form:

$$P_i^b(ct; \lambda_i, s_{bg}|\sigma_{ct}) = \int \frac{1}{\lambda_i} \cdot \frac{1}{\sqrt{2\pi} s_{bg}\sigma_{ct}} e^{-c(t-t')^2/2(s_{bg}\sigma_{ct})^2} e^{-(ct/\lambda_i)} d(ct') \tag{12.4}$$

This function contains a Gaussian resolution convoluted with an exponential decay. The ad hoc parameterization of the non-prompt background is covered with two of these functions with a positive effective lifetime, along with one function with a negative effective lifetime.

The prompt background is fit with the resolution function that is intended to be input into the model for the signal. The model is based on the superposition of two Gaussians, symmetric about $t = 0$:

$$\mathcal{R} = f_1 \cdot \frac{1}{\sqrt{2\pi} s_1 \sigma_{ct}} e^{-ct^2/2(s_1\sigma_{ct})^2} + (1 - f_1) \cdot \frac{1}{\sqrt{2\pi} s_2 \sigma_{ct}} e^{-ct^2/2(s_2\sigma_{ct})^2}. \tag{12.5}$$

The fraction and two scale factors make up the three free parameters in this resolution model. These parameters are extracted from a fit on the background sample. The fit is performed in the sideband region with the total background function:

$$
\begin{aligned}
P^b_{ct}(ct; s_{bg}, f_p, f_-, f_{++}, \lambda_-, \lambda_+, \lambda_{++}, f_1, s_1, s_2|\sigma_{ct}) = f_p \cdot \mathcal{R} + (1 - f_p) \cdot \\
\big[(1 - f_-) \cdot \big((1 - f_{++}) \cdot P^b_+(ct; \lambda_i, s_{bg}|\sigma_{ct}) \\
+ f_{++} \cdot P^b_{++}(ct; \lambda_i, s_{bg}|\sigma_{ct})\big) \\
+ f_- \cdot P^b_-(ct; \lambda_i, s_{bg}|\sigma_{ct})\big] .
\end{aligned}
\tag{12.6}
$$

The factors that determine the shape of the resolution are fixed from this fit and input into the signal function as convolutions with the exponential decay:

$$
P^s_{ct}(ct; c\tau, s_1, s_2, f_1|\sigma_{ct}) = \mathcal{R} \otimes e^{-(ct/c\tau)} \tag{12.7}
$$

where $\otimes$ indicates the convolution.

Table 12.2: Summary of $B^- \to J/\psi K^-$ lifetime fit parameters

Name	Description	Related Fit
$c\tau$	$B^- \to J/\psi K^-$ Proper Decay Time	Lifetime, signal
s_1	σ_{ct} Scale Factor (1st Gauss.)	Lifetime, signal, prompt
s_2	σ_{ct} Scale Factor (2nd Gauss.)	Lifetime, signal, prompt
f_1	Relative fraction of 1st Gauss.	Lifetime, signal, prompt
f_p	Fraction of prompt background	Lifetime, background
f_-	Fraction of negative lifetime BG	Lifetime, background
f_{++}	Rel. fraction of 2nd positive lifetime BG	Lifetime, background
λ_-	Effective lifetime of negative BG	Lifetime, background
λ_+	Effective lifetime of positive BG	Lifetime, background
λ_{++}	Effective lifetime of 2nd positive BG	Lifetime, background

Chapter 13

Results from $B^- \to J/\psi K^-$

This chapter will discuss the results with no detector effects taken into account. The raw $B^- \to J/\psi K^-$ yields are determined and a raw A_{CP} is presented with statistical errors only.

13.1 $B^- \to J/\psi K^-$ Fits

The raw $B^- \to J/\psi K^-$ yields are extracted from the simultaneous $M(B^- \to J/\psi K^-)$ and $ct(B^- \to J/\psi K^-)$ unbinned likelihood fit. Separate fits are performed in three bins of $p_T(K^-)$, six bins of ϕK^- as well as two charge bins for a total of thirty six fits. The measured lifetimes are also extracted as a check of the method. The world average of $c\tau(B^- \to J/\psi K^-)$ is $491.4 \pm 3.3\mu$m [14]. It is important to remember that the focus of this analysis is the measure the yields for $B^- \to J/\psi K^-$, $B^- \to J/\psi \pi^-$, the lifetime fit is performed to increase the statistical power of the signal, not to extract a precise lifetime. For this reason, a full error analysis is not performed on the fitted lifetime and all errors are statistical only. These fits and yields are found in the appendix. A mass only fit was performed on the unbinned $B^- \to J/\psi K^-$ and $B^+ \to J/\psi K^+$ distributions to demonstrate the total yields in this sample. The results are shown in figure 13.1 and the yields with statistical error only are listed in table 13.1.

Table 13.1: $B^- \to J/\psi K^-$ Yields from the Mass Only Fit

	N($B^- \to J/\psi K^-$)	N($B^- \to J/\psi \pi^-$)
$B^- \to J/\psi K^-$	40350 ± 610	1471 ± 335
$B^+ \to J/\psi K^+$	39760 ± 600	1348 ± 335
$B^- \to J/\psi K^-$ and $B^+ \to J/\psi K^+$	80120 ± 860	2810 ± 473

Taking the average of the set of lifetime fits, a total lifetime of $494.9 \pm 2.0(stat.)\mu$m is measured which is consistent with the world average from the PDG. In fact, the statistical uncertainty is competitive with any previous measurement, which demonstrates the size of this dataset.

The main background is prompt decays which can easily be eliminated with a cut on L_{xy} which the distance traveled from the primary vertex in the $x-y$ plane. This cut eliminates a large number of signal

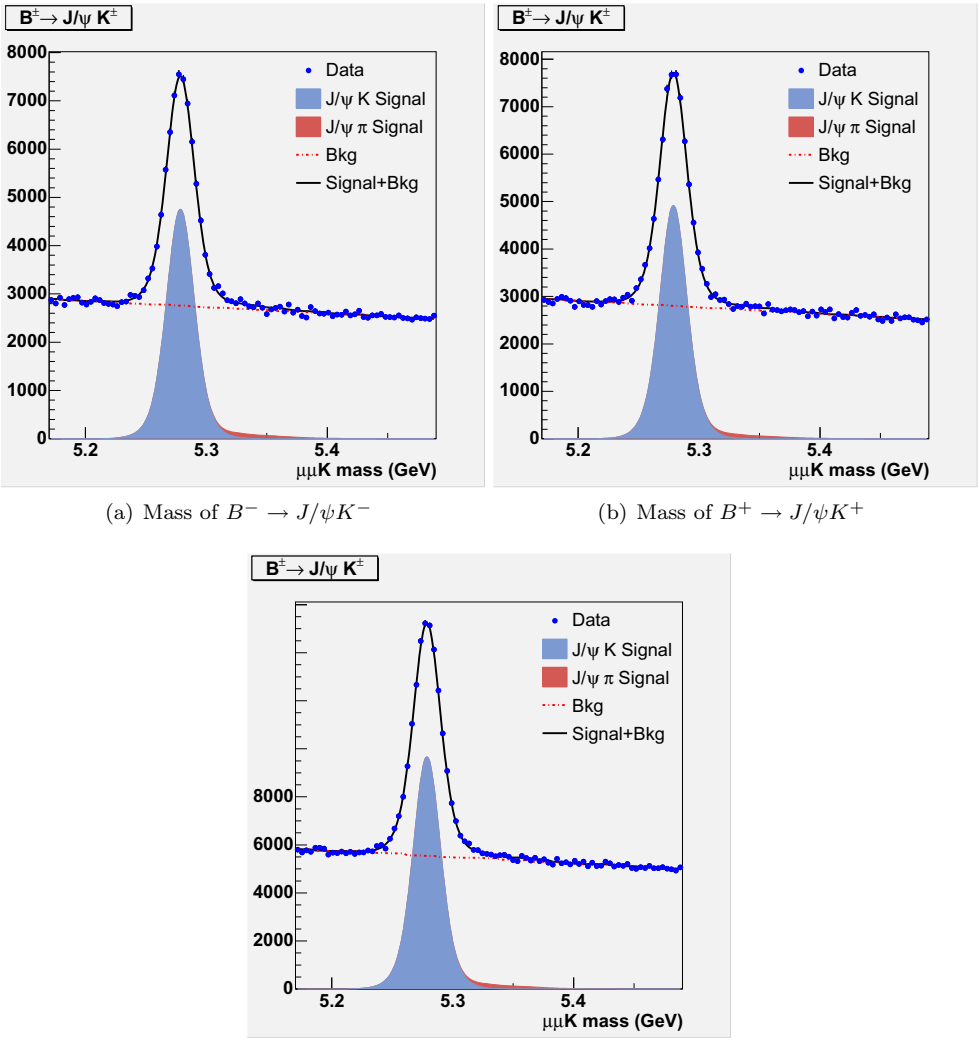

(a) Mass of $B^- \to J/\psi K^-$

(b) Mass of $B^+ \to J/\psi K^+$

(c) Mass of $B^- \to J/\psi K^-$ and $B^+ \to J/\psi K^+$

Figure 13.1: $B^- \to J/\psi K^-$ Mass Fits for the entire data set

events, and the resulting sample cannot be fit for the lifetime, which further reduces the statistical power of the signal. The L_{xy} cut has a tendency to smear the lifetime distribution, which hampers the signal to background discrimination in the simultaneous fit. However, a cross-check of the yields and distributions with a cut of $L_{xy} > 0.015$cm applied can provide some valuable insight into the analysis. The main advantage is the ability to to investigate the potential for any structure in the long-lived backgrounds that may have been obscured by the dominant prompt decays. The full set of fits are performed for the data with this L_{xy} cut applied, which are found in the appendix. Fits of the full dataset are found in Figure 13.2 with the yields in Table 13.2. No structure is observed in the background, aside from $B^- \to J/\psi\pi^-$, which is accounted for.

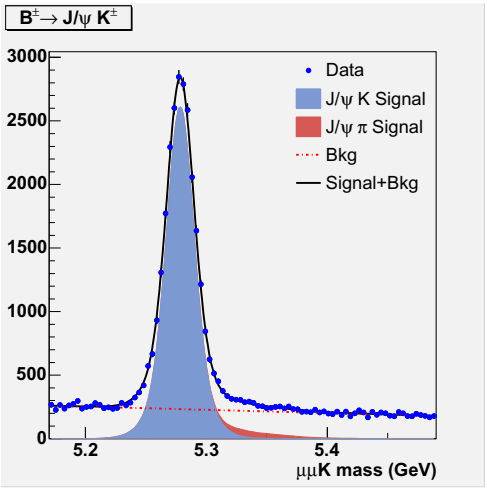

(a) Mass of $B^- \to J/\psi K^-$ with $L_{xy} > 0.015$cm

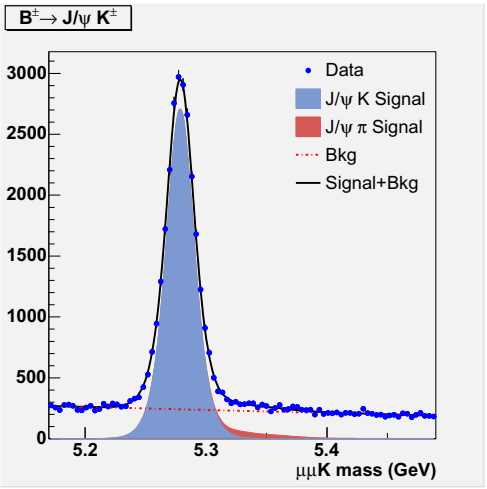

(b) Mass of $B^+ \to J/\psi K^+$ with $L_{xy} > 0.015$cm

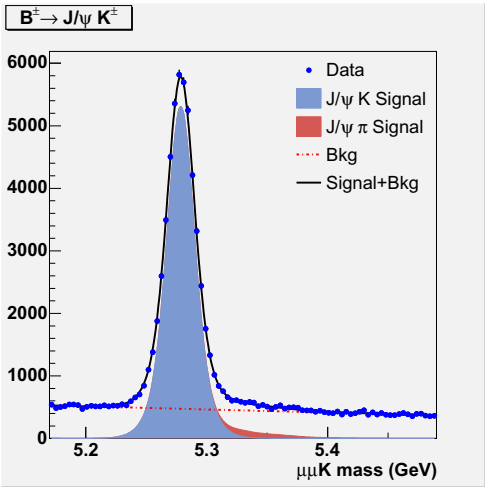

(c) Mass of $B^- \to J/\psi K^-$ and $B^+ \to J/\psi K^+$ with $L_{xy} > 0.015$cm

Figure 13.2: $B^- \to J/\psi K^-$ Mass Fits for the entire data set with $L_{xy} > 0.015$cm

Table 13.2: $B^- \to J/\psi K^-$ Yields from the Mass Only Fit with $L_{xy} > 0.015$cm

	N($B^- \to J/\psi K^-$)
$B^- \to J/\psi K^-$	22570 ± 200
$B^+ \to J/\psi K^+$	22800 ± 200
$B^- \to J/\psi K^-$ and $B^+ \to J/\psi K^+$	45400 ± 290

13.2 Raw $A_{CP}(B^- \to J/\psi K^-)$

A first pass at $A_{CP}(B^- \to J/\psi K^-)$ can be made without any K^- correction. This is referred to as the raw CP asymmetry:

$$A_{CP}^{raw} = \frac{N(B^- \to J/\psi K^-) - N(B^+ \to J/\psi K^+)}{N(B^- \to J/\psi K^-) + N(B^+ \to J/\psi K^+)} \tag{13.1}$$

A_{CP}^{raw} does not correct for any detector biases, but gives a picture of the combined physics and detector effects. Table 13.3 shows A_{CP}^{raw} as a function of $p_T(K^-)$ as well as the integrated result, which is the average of the three independent measurements. The errors shown are statistical only.

Table 13.3: $A_{CP}^{raw}(B^- \to J/\psi K^-)$

$p_T(K^-)$[GeV/c]	A_{CP}^{raw}
$[2.0, 3.0]$	-0.0175 ± 0.008
$[3.0, 4.0]$	-0.004 ± 0.01
$[4.0, 100.0]$	-0.003 ± 0.006
$[2.0, 100.0]$	-0.007 ± 0.003

A_{CP}^{raw} shows a p_T dependence that is qualitatively consistent with the charge bias measured for a K^-−. The measurement of this charge bias is discussed in the next section.

Chapter 14

Semileptonic D^{*+} Decays

14.1 K^- Efficiency Ratio

In order to extract $A_{CP}(B^- \to J/\psi K^-)$, it is necessary to measure the detector charge bias that arise from differences in tracking efficiencies and acceptances between K^+ and K^-. This section will discuss the potential sources of this charge bias as well as the method used to quantify the charge bias. In the following sections, efficiency will generally refer to the combined acceptance and tracking efficiency effects.

Charged Kaons are stable on the lifetime scale of the detector. That is, a K^- will generally traverse the entire tracking volume without decaying. A K^- produced in a decay will be registered as a track if enough hits are found in the COT for the pattern recognition software to generate the track. The charge bias that affects this analysis comes as a result of differences in the efficiency of track reconstruction for a K^- that is generated in the decay $B^- \to J/\psi K^-$. This charge bias can be written as:

$$\epsilon_{K^-} = \frac{N_{reco}(K^-)}{N_{prod}(K^-)} \tag{14.1}$$

where $N_{reco}(K^-)$ is the number of K^- that are reconstructed as tracks, N_{prod} is the number of K^- that are produced and ϵ_{K^-} is the tracking efficiency, which we are interested in measuring. Though it would be ideal to measure ϵ_{K^-} and ϵ_{K^+} independently, there is no data driven method to do so. Further, it is unnecessary for this analysis. The quantity that is required is the ratio:

$$\mathcal{R}_K = \frac{\epsilon_{K^+}}{\epsilon_{K^-}} \tag{14.2}$$

The reason we are limited to the ratio is that there is no source of K^- for which the yield is absolutely certain. However, there are sources which provide K^- and K^+ at equal rates, which allows for the extraction of the ratio.

14.1.1 Sources of charge bias

Absent of any charge bias, $\frac{\epsilon_{K+}}{\epsilon_{K-}}$ would be unity. However, there are several sources of potential bias that are introduced in the detector. Examples include interaction with detector material, geometry of the COT, offset in the interaction point, and trigger biases.

There is a significant amount of material in the tracking volume of the CDF detector, so there is a finite probability that a particle traversing the detector will interact with a nuclei in said material. K^- and K^+ do not have identical nuclear cross-sections. Due to the availability of final states and other factors, K^- is more likely to interact with a nucleus in the material of the detector. This effect will tend to push $\frac{\epsilon_{K+}}{\epsilon_{K-}}$ above 1. The nuclear cross-sections will vary with the momentum of the K^- , with the magnitude of the effect diminishing with increasing p_T.

Another factor is the geometry of the COT. As mentioned in the apparatus section, the COT cells each have a several degree tilt. The result of this is that positively charged particles will tend to travel the length of the cell, while negatively charged particles will tend to cross more perpendicularly through the cells. This effect is due to the curvature of the tracks in the solenoidal magnetic field and, again, will depend of the p_T of the track. As the p_T of the track increases, the radius of curvature also increases, and minimizes this effect. The direction through the cell is important for two reasons. First, the pattern recognition software requires 3 contiguous hits in a single cell in each SL to generate a track, which is more likely for a track that is following the length of the cell. Second, hits are not generated at cell boundaries so a track that is crossing many cell boundaries is missing many potential hits.

There are almost certainly other sources of charge bias for tracking K^- , but the source is immaterial to this analysis. It is only necessary to know the magnitude of the efficiency ratio. This ratio is obtained using the method described in the following sections.

14.2 Determination of $\frac{\epsilon_{K+}}{\epsilon_{K-}}$

A source of equal rate of K^- and K^+ production is identified in the semileptonic charm decay $D^{*+} \to D^0\pi^+, D^0 \to \mu^+K^-\nu_\mu$. The events are isolated from and corrected for any sources of charge bias outside of that which should be attributed to the K^-. From this it is possible to extract the K^- efficiency ratio $\frac{\epsilon_{K+}}{\epsilon_{K-}}$.

For a given number N_{prod} of decay $D^{*+} \to D^0\pi^+, D^0 \to \mu^+K^-\nu_\mu$ produced, the number of signal candidates reconstructed N_{reco} is expected to be:

$$N_{reco}(D^{*+}) = N_{prod}(D^{*+})\epsilon_{K^-\mu\pi^+} \tag{14.3}$$

where $\epsilon_{K^-\mu^+\pi^+}$ is the efficiency of tracking the three daughter particles. Assuming the efficiencies factorize:

$$N_{reco}(D^{*+}) = N_{prod}(D^{*+})\epsilon_{K^-}\epsilon_{\mu^+}\epsilon_{\pi^+} \tag{14.4}$$

where ϵ_{K^-}, ϵ_{μ^+}, and ϵ_{π^+} are the efficiencies for tracking K^-,μ^+, and π^+ respectively. The assumption that the efficiencies factorize is motivated by the fact that no kinematic fitting was performed, which should leave the tracks uncorrelated.

$c\bar{c}$ production, which is the first ingredient in D^{*+} production, is almost exclusively a strong interaction, which preserves CP. Further, CP violation has never been observed in the charm sector, so it is expected that the $D^{*+} \to D^0\pi^+, D^0 \to \mu^+K^-\nu_\mu$ production rate is independent of charge:

$$N_{prod}(D^{*+}) = N_{prod}(D^{*-}) \tag{14.5}$$

Using this information, the following expression can be extracted:

$$\frac{\epsilon_{K^+}}{\epsilon_{K^-}} = \frac{N_{reco}(D^{*-})}{N_{reco}(D^{*+})}\frac{\epsilon_{\mu^+}}{\epsilon_{\mu^-}}\frac{\epsilon_{\pi^+}}{\epsilon_{\pi^-}} \tag{14.6}$$

which shows that in order to determine the K^- efficiency ratio from $D^{*+} \to D^0\pi^+, D^0 \to \mu^+K^-\nu_\mu$ decays, it is necessary to determine the yields (N_{prod}), the μ^+ efficiency ratio and the π^+ efficiency ratio.

14.3 π^+ Efficiency Ratio

The π^+ efficiency ratio has been measured previously in an another analysis at CDF. A measurement of the CP Asymmetry in the Decay $D^0 \to \pi^+\pi^-$ [27] was performed. This measurement was performed by reconstructing $D^{*+} \to D^0\pi^+, D^0 \to \pi^+\pi^-$. The soft pion charge asymmetry was extracted and is shown in Fig. 14.1. The use of this efficiency ratio dictates that the cuts on the soft π should be identical to those used for the π used to generate this efficiency histogram.

14.4 μ^+ Efficiency Ratio

Since the events used in this section of the analysis were collected on the 8 GeV/c CMUP trigger, all the μ^+ have $p_T > 8.0$ GeV/c by construction. At $p_T > 8.0$ GeV/c the track curvature is so small that any geometric effects must be negligible even while the COT is capable of providing accurate p_T measurements. Also, the μ^+ nuclear cross section is expected to be charge independent at high p_T. For these reasons,

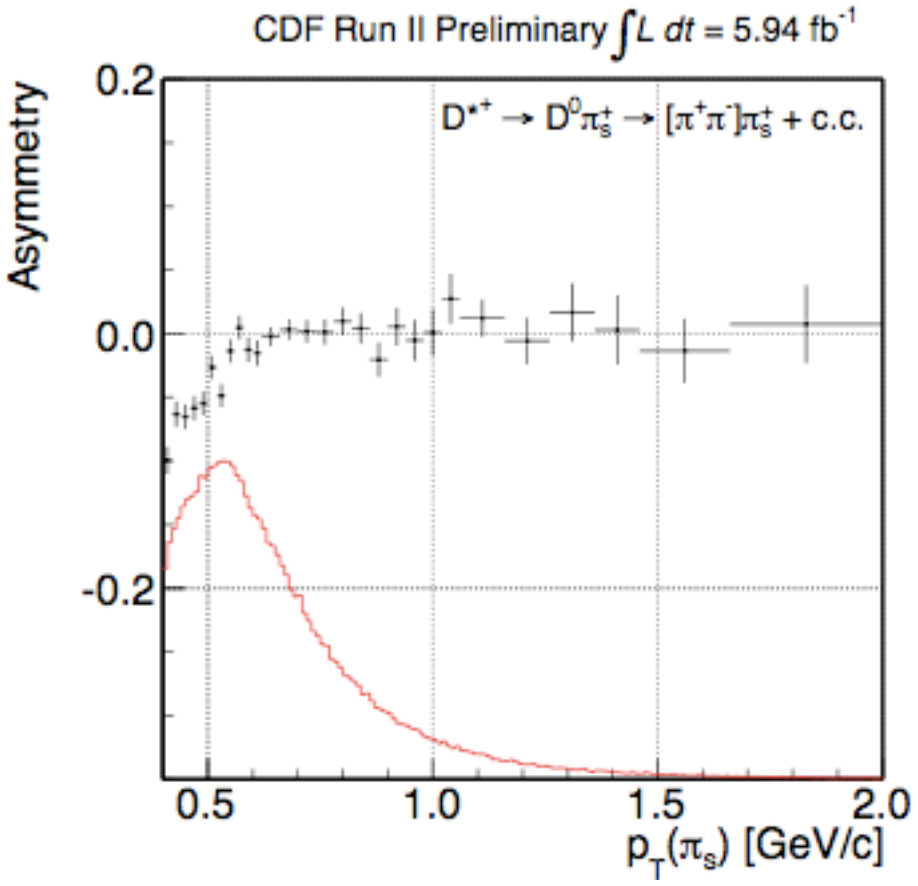

Figure 14.1: Soft pion efficiency as a function of $p_T(\pi^+)$. The red line shows the $p_T(\pi^+)$ distribution from the $D^{*+} \to D^0\pi^+, D^0 \to \pi^+\pi^-$ decays. A bin by bin p_T correction is applied to account for any differences in p_T spectra.

the μ^+ efficiency ratio is expected to be 1, to good approximation. This assumption is later assessed as a systematic.

14.5 Method

The ingredients required to extract the K^- efficiency ratio are the D^{*+} and D^{*-} yields, as well as the π^+ efficiency ratio. The candidates are reconstructed without any kinematic fit, which is possible due to the discrimination provided by the mass difference variable.

A trigger muon is selected in each event, then the stable tracks are looped through with the K^- mass assumption applied to generate a partially reconstructed D^0 candidate (μ^+K^-). The stable tracks are then looped through again, applying a π^+ mass assumption to generate a partially reconstructed D^{*+} candidate ($\mu^+K^-\pi^+$). In order to avoid any CP violation introduced from B decays, prompt D^{*+} are desired. A

series of quality cuts are applied to maximize the statistical power of the signal events.

Table 14.1: Cuts on μ^+

	Units	Requirement
p_T	GeV/c	≥ 8.0
is CMU	–	true
is CMP	–	true

Table 14.2: Cuts on K^-

	Units	Requirement
p_T	GeV/c	≥ 2.0
$M(\mu^+K^-)$	GeV/c^2	≤ 1.8
$\Delta R(\mu^+, K^-)$	–	≤ 0.7
$\Delta Z(\mu^+, K^-)$	cm	≤ 1.5
$L_{xy}(\mu^+, K)$	cm	≤ 0.4
$L_{xy}(\mu^+, K)$	cm	≥ -0.2
η	–	≤ 1.0
Radial Si Hits	–	≥ 3.0
COT Hits	–	≥ 40
$q(\mu) * q(K)$	–	$= -1$

Table 14.3: Cuts on π^+

	Units	Requirement
p_T	GeV/c	≥ 0.4
p_T	GeV/c	$\leq p_T(K^-)$
$M(\mu^+K^-\pi^+)$	GeV/c^2	≤ 2.01
$\Delta Z(\mu^+, K^-)$	cm	≤ 1.5
$L_{xy}(\mu^+, \pi^+)$	cm	≤ 0.4
$L_{xy}(\mu^+, \pi^+)$	cm	≥ -0.2
$L_{xy}(K^-, \pi^+)$	cm	≤ 0.4
$L_{xy}(K^-, \pi^+)$	cm	≥ -0.2
η	–	≤ 1.0
Si Hits	–	≥ 1.0
COT Hits	–	≥ 30
$q(\mu) * q(\pi)$	–	$= +1$

The cuts on the π^+ match those applied in the $A_{CP}(D^0 \to \pi^+\pi^-)$ analysis to ensure the π^+ asymmetry can be applied appropriately. This asymmetry is applied as a weight on an event by event basis according to $p_T(\pi^+)$. The analysis is performed in 3 bins of $p_T(K^-)$, 6 bins of $M(\mu^+K^-)$ and 2 bins of charge for a total of 36 separate bins.

Histograms of $\delta(M(\mu^+K^-\pi^+), M(\mu^+, K^-))$ are generated in each bin. The histograms consist of several components:

- **Signal events** K^- : The actual physics events which are targeted in this section of the analysis
- **Peaking background:** π^+ **as** K^- : A background of actual $D^{*+} \to D^0\pi^+$ decays, where the D^0 decay includes a π^- which is assumed to be a K^-
- **Peaking background: Generic** D^{*+} **decays**: A background of generic D^{*+} decays where D^0 decays and generates a fake μ^+
- **Combinatoric background** : Three random tracks that happen to pass the quality cuts

The shape of the signal events and peaking background are determined by MC simulations. The combinatoric background is modeled from the data. Exclusive $D^{*+} \to D^0\pi^+, D^0 \to \mu^+K^-\nu_\mu$ events are generated and run through the analysis module to determine the shape in each of the 6 $M(\mu^+K^-)$ bins. Since the resolution is dominated by decay kinematics, specifically from the missing neutrino, it is expected to be well modeled by the simulation. The π^+ as K^- shape is determined from the same MC, where the π^+ track passes the analysis cuts as a K^-. The relative rate of signal events to π^+ peaking background is also determined from the MC. Inclusive $D^{*+} \to D^0\pi^+, D^0 \to X$ MC is generated to determine the shape from the generic D^{*+} decay peaking background.

The relative charges of the three tracks in a candidate provide an important handle on the background yields. The events are divided into three categories as described in table 14.4.

Table 14.4: Sign Combinations

Combination	$q(\mu) \times q(K)$	$q(\mu) \times q(\pi)$	Example
RS	-1	$+1$	$\mu^+K^-\pi^+$
WS	-1	-1	$\mu^+K^-\pi^-$
SS	$+1$	$+1$	$\mu^+K^+\pi^+$

The $D^{*+} \to D^0\pi^+, D^0 \to \mu^+K^-\nu_\mu$ events are right sign (RS) along with the background contributions. The same sign (SS) events are expected to be dominated by combinatorics (three random tracks) and are expected to contain a negligible physics contribution. Some of the events are coming with fake muons. For example, the wrong sign (WS) events are expected to contain a contribution from generic D^{*+} decays where a hadron fakes a muon.

MC and SS distributions are used as templates in the fit to extract the yields. Figure 14.3 shows example plots to provide some understanding of the method. The RS, WS and SS show a similar shape in the sideband above the signal region (Fig. 14.5). The SS can be scaled to match the number of events above the signal region. Then an estimate of the WS physics contribution can be made as the excess above the scaled SS

distribution in the signal region (Fig. 14.3(a)). Finally, the RS signal yield can be estimated by now scaling the SS distribution to match the number of events in the RS sideband (Fig. 14.3(b)).

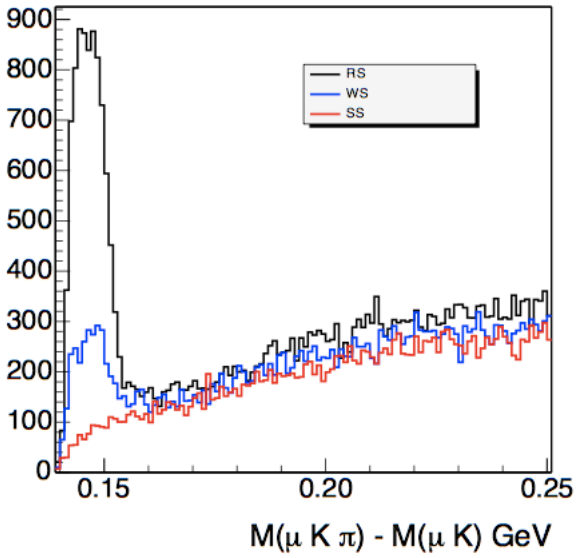

Figure 14.2: Example plots showing the RS, SS and WS distributions from the semileptonic D^{*+} decays.

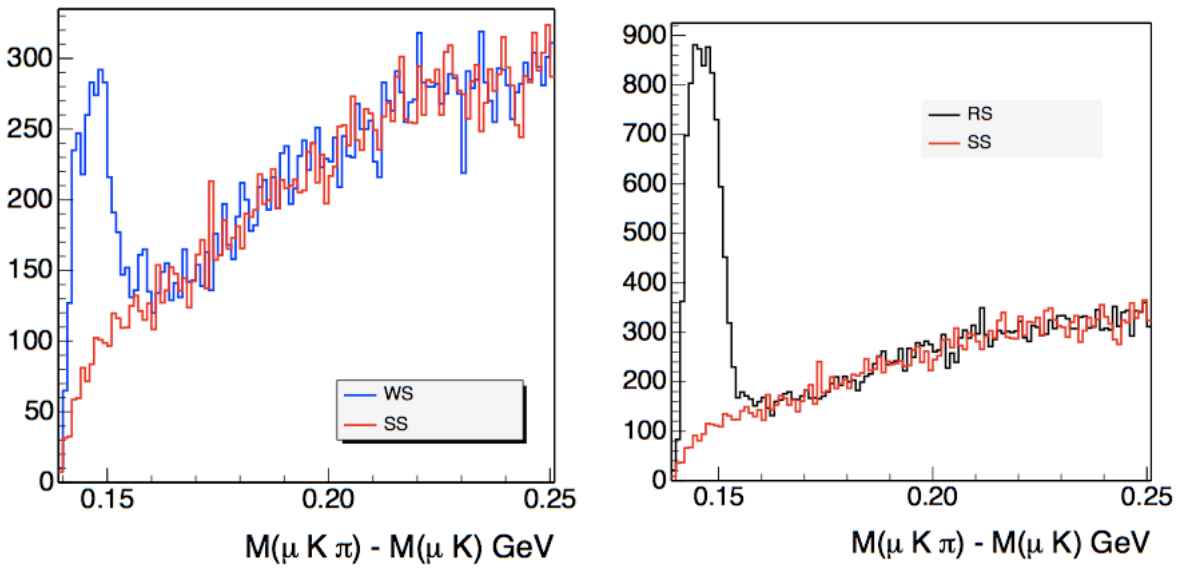

(a) WS and SS, with SS scaled to match number of events above 0.17GeV/c^2

(b) RS and SS, with SS scaled to match number of events above 0.17GeV/c^2

Figure 14.3: Example plots showing the RS, SS and WS with scaling to demonstrate SS as combinatoric background template

Although it is expected that the RS signal events are dominated by the physics process $D^{*+} \to D^0\pi^+, D^0 \to \mu^+K^-\nu_\mu$, there are contributions from hadronic D^0 decays as well as other semileptonic D^{*+} decays with

a π^- reconstructed as a K^-. Without a data driven method to quantify these effects, MC templates are generated.

14.6 $D^{*+} \to D^0\pi^+$ Monte Carlo

In order to estimate the composition of the RS yields, two MC samples were produced. First, an inclusive $D^{*+} \to D^0\pi^+, D^0 \to X$ sample was produced. This was used to determine the contribution from any hadronic D^0 decays, where a hadron (π^+ ,K^-) may have faked a μ^+. The other sample required a μ^+ in the final decay. It was necessary to generate a separate sample because of the domination of hadronic decays. The inclusive μ^+ branching ratio is only $\sim 6\%$ [14].

The hadronic D^0 decays contribute to the RS yield when a hadron (π^+ or K^+) is reconstructed as a μ^+. This occurs when either punch-through or decay-in-flight takes place. Punch-through occurs when a hadron traverses through all the detector material and reaches the muon chambers. Even though there is shielding to minimize this effect, the probability is finite and the large source of hadrons makes it non-neglibile. Decay-in-flight refers to a hadron decaying to a μ^+ at a secondary vertex before the muon chamber. This potentially leaves a track pointing at a real μ^+ stub, which may be reconstructed as a μ^+. These factors can be quantified with a μ^+ fake rate which describes the probability that a hadron will be reconstructed or "fake" a μ^+. A previous analysis[28] determined this μ^+ fake rate as a function of charge, hadron flavor and hadron p_T as given in equations 14.7 - 14.10.

$$P(K^+) = 1.157 \cdot (0.00066 + 0.000796 \cdot p_T(K^+)) \quad (14.7)$$

$$P(K^-) = 0.0845 \cdot (0.00066 + 0.000796 \cdot p_T(K^-)) \quad (14.8)$$

$$P(\pi^+) = 1.05 \cdot (0.00158 + 0.000228 \cdot p_T(\pi^+)) \quad (14.9)$$

$$P(\pi^-) = 0.95 \cdot (0.00158 + 0.000228 \cdot p_T(\pi^-)) \quad (14.10)$$

Applying these fake rates to the hadronic D^0 MC decays provides a template for these contributions in data. However, these processes are a product of complex interactions, and so it is preferable to not wholly trust the MC. Instead, it is possible to take advantage of the fact that the WS yield is expected to be dominated by these decays. Then, the MC can be used to determine both a shape template and a relative rate of the RS and WS fake muon events. The templates are generated in 6 bins of $M(\mu^+K^-)$. It was determined that the templates were largely independent of charge and $p_T(K^-)$. The templates

are shown in figures 14.4. The templates demonstrate a variation in resolution in the different $M(\mu K)$ bins. This arises because these are partially reconstructed D^0 decays. The difference between $M(\mu K)$ and $M(D^0) = 1.8626\text{GeV}/c^2$ is related to the amount of energy carried by the decay daughter that was not reconstructed. This is the main factor in determining the resolution for the partially reconstructed decays. The ratio between RS and WS can also be extracted from the MC events as summarized in Table 14.5.

These ratios only take the kinematic effects into account. The assumption is made that the any other factors will effect the RS and WS events equally. This implies that these ratios should remain as a good approximation in data.

Table 14.5: Ratio of RS : WS events from fake μ^+ from MC

$M(\mu K)$	μ^+K^-	μ^-K^+
$[1.2, 1.3]$	0.56 ± 0.01	0.65 ± 0.01
$[1.3, 1.4]$	0.59 ± 0.01	0.67 ± 0.01
$[1.4, 1.5]$	0.56 ± 0.01	0.65 ± 0.01
$[1.5, 1.6]$	0.40 ± 0.01	0.51 ± 0.01
$[1.6, 1.7]$	0.29 ± 0.01	0.38 ± 0.01
$[1.7, 1.8]$	0.43 ± 0.01	0.45 ± 0.01

The other contribution to the RS yield is from D^{*+} decays which include an actual μ^+ but have a π^- instead of a K^-. In order to estimate this, MC with muonic D^{*+} decays were generated and templates are created for the mistagged π^- and properly tagged K^- signal events (Fig. 14.5). The resolution of these peaks is dominated by kinematics, specifically the missing neutrino. The ratio of π^- to K^- events is also estimated as summarized in table 14.6.

Table 14.6: Ratio of π^- : K^- events from MC

$M(\mu K)$	$R_{K:\pi}$
$[1.2, 1.3]$	0.166 ± 0.006
$[1.3, 1.4]$	0.135 ± 0.005
$[1.4, 1.5]$	0.107 ± 0.004
$[1.5, 1.6]$	0.101 ± 0.004
$[1.6, 1.7]$	0.115 ± 0.005
$[1.7, 1.8]$	0.210 ± 0.009

14.7 $D^{*+} \to D^0\pi^+, D^0 \to \mu^+K^-\nu_\mu$ Results

A series of binned likelihood fits are performed to extract the K^- efficiency ratio. The fits are performed in six bins of $\phi(K^-)$, three bins of $p_T(K^-)$, six bins of $M(\mu^+K^-)$ and two charge bins for a total of 216 fits.

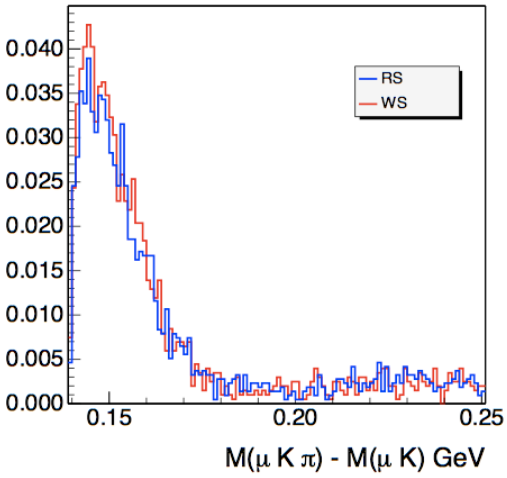

(a) $1.2\text{GeV}/c^2 < M(\mu^+K^-) \leq 1.3\text{GeV}/c^2$

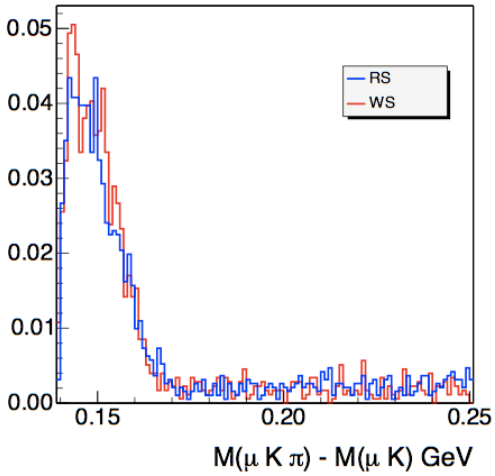

(b) $1.3\text{GeV}/c^2 < M(\mu^+K^-) \leq 1.4\text{GeV}/c^2$

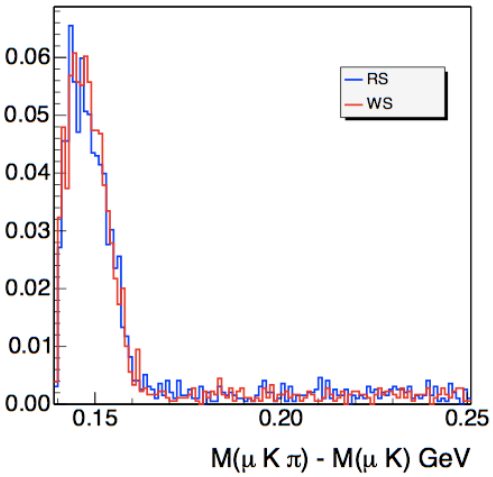

(c) $1.4\text{GeV}/c^2 < M(\mu^+K^-) \leq 1.5\text{GeV}/c^2$

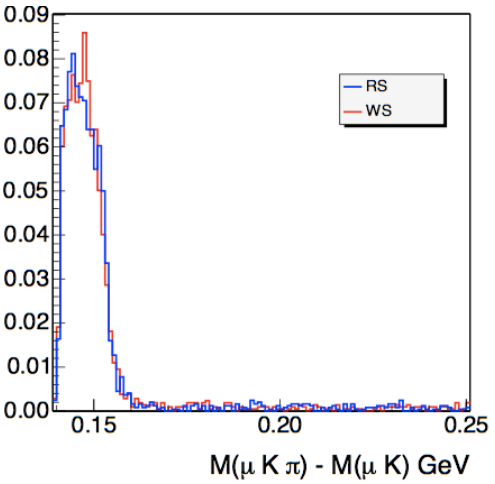

(d) $1.5\text{GeV}/c^2 < M(\mu^+K^-) \leq 1.6\text{GeV}/c^2$

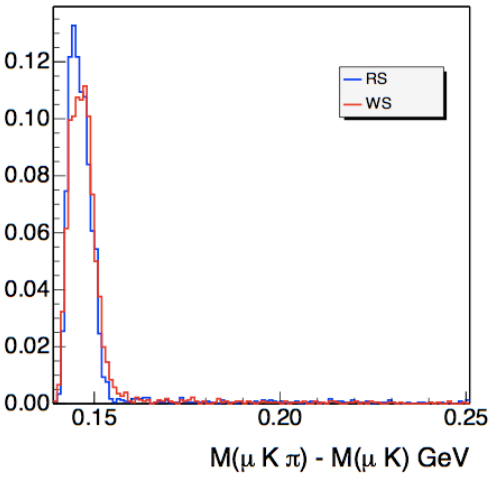

(e) $1.6\text{GeV}/c^2 < M(\mu^+K^-) \leq 1.7\text{GeV}/c^2$

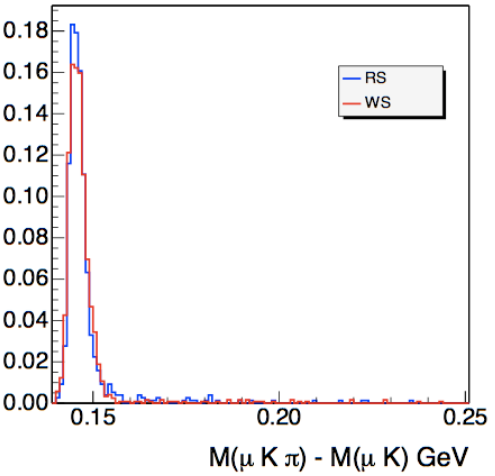

(f) $1.7\text{GeV}/c^2 < M(\mu^+K^-) \leq 1.8\text{GeV}/c^2$

Figure 14.4: Fake μ^+ MC templates

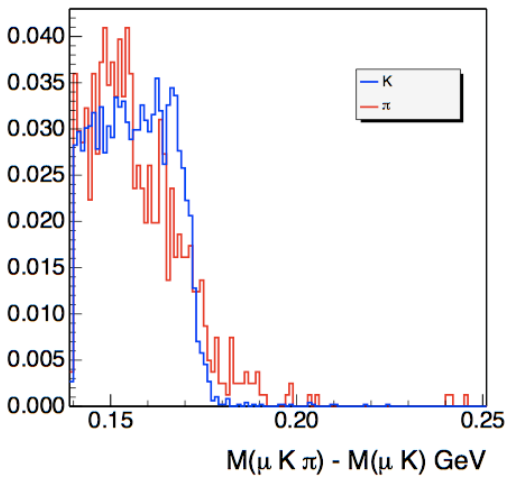

(a) $1.2\text{GeV}/c^2 < M(\mu^+K^-) \leq 1.3\text{GeV}/c^2$

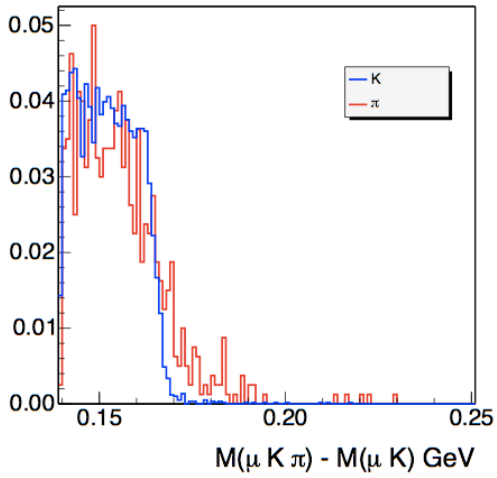

(b) $1.3\text{GeV}/c^2 < M(\mu^+K^-) \leq 1.4\text{GeV}/c^2$

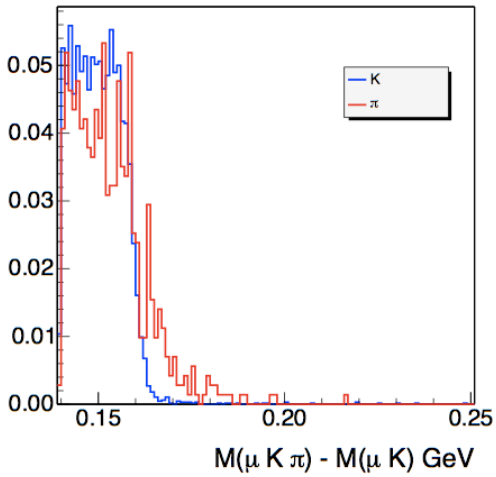

(c) $1.4\text{GeV}/c^2 < M(\mu^+K^-) \leq 1.5\text{GeV}/c^2$

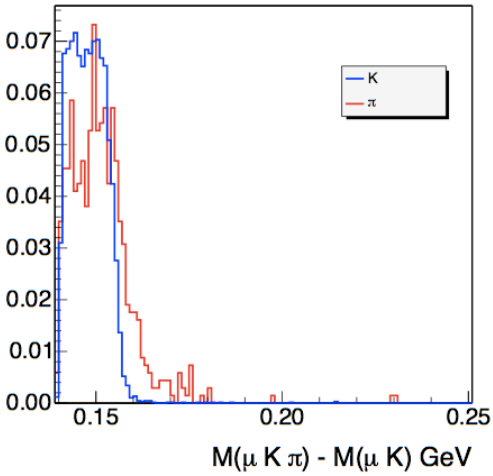

(d) $1.5\text{GeV}/c^2 < M(\mu^+K^-) \leq 1.6\text{GeV}/c^2$

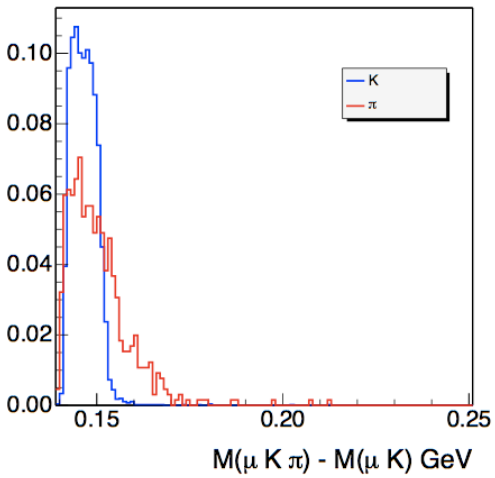

(e) $1.6\text{GeV}/c^2 < M(\mu^+K^-) \leq 1.7\text{GeV}/c^2$

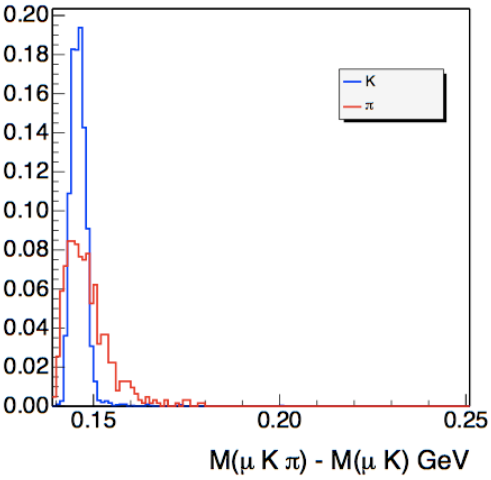

(f) $1.7\text{GeV}/c^2 < M(\mu^+K^-) \leq 1.8\text{GeV}/c^2$

Figure 14.5: Signal (K^-) and π^- MC templates

The p_T binning accounts for the expectation that the efficiency ratio will vary with p_T, and accounts for any difference in the $p_T(K^-)$ spectra of $B^- \to J/\psi K^-$ and $D^{*+} \to D^0\pi^+, D^0 \to \mu^+K^-\nu_\mu$. The ϕ binning is to account for any difference in the $\phi(K^-)$ distributions between $D^{*+} \to D^0\pi^+, D^0 \to \mu^+K^-\nu_\mu$ and $B^- \to J/\psi K^-$. This is expected to be necessary because the detector material and COT tracking efficiency at CDF is not azimuthally symmetric, which could conceivably impact the K^- efficiency ratio. Finally the $M(\mu^+K^-)$ mass binning is used since the various fit templates vary so strongly across $M(\mu^+K^-)$.

The first step is to extract the WS fake muon yield. The appropriate MC template plus a normalized SS distribution is used to make the following fit function for the number of events n_{WS} in the bin at a given $\delta(M(\mu K\pi), M(\mu K))$:

$$n(\delta(M(\mu K\pi), M(\mu K))_{WS} = N_{data} \cdot \left(f_{bg} \cdot SS_t + (1 - f_{bg}) \cdot WS_{MC}^{fake}\right) \tag{14.11}$$

where N_{data} is the total number of events in the slice of data being fitted, f_{bg} is the fraction of events in the combinatoric background, SS_t refers to a normalized template for the combinatoric background from SS data and WS_{MC}^{fake} is the WS fake muon template from MC. From the converged fit, the WS fake muon yield is extracted as:

$$N_{WS}^{fake} = N_{data} \cdot (1 - f_{bg}). \tag{14.12}$$

With this WS yield determined, the signal histogram can be fit. The function employed is again a collection of templates:

$$\begin{aligned} n(\delta(M(\mu K\pi), M(\mu K))_{RS} = N_{data} \cdot \; & (f_{bg} \cdot SS_t \\ & +(1 - f_{bg}) \cdot (1 - f_\pi) \cdot K_{MC} \\ & +(1 - f_{bg}) \cdot f_{pi} \cdot \pi_{MC} \\ & +f_{RS/WS}^{fake} \cdot N_{WS}^{fake} \cdot RS_{MC}^{fake}\Big) \end{aligned} \tag{14.13}$$

where $n(\delta(M(\mu K\pi), M(\mu K))_{RS}$ is the number of events in the bin at $\delta(M(\mu K\pi), M(\mu K))$. N_{data} is again the number of events in the slice of data being fitted. SS_t is the combinatoric background template from data, K_{MC} is the signal function template form MC. f_pi is the fraction of non-fake, non-combinatoric events which are π^- reconstructed as K^-, while π_{MC} is the MC template for those events. $f_{RS/WS}^{fake}$ is the ratio between the RS and WS fake muon contribution, while N_{WS}^{fake} is the WS fake yield extracted from the WS fit. Finally, RS_{MC}^{fake} is the MC template for RS fake muon events. The two ratios (f_{pi} and $f_{RS/WS}^{fake}$) from

MC are fixed in the fit and their uncertainty will be assessed as a systematic. Each of these templates are normalized to 1 over the fit range of $0.139\text{GeV}/c^2 < \delta(M(\mu K\pi), M(\mu K)) < 0.25\text{GeV}/c^2$.

Once the fit has converged, the $D^{*+} \to D^0\pi^+, D^0 \to \mu^+K^-\nu_\mu$ yield can be extracted as:

$$N(D^{*+} \to D^0\pi^+, D^0 \to \mu^+K^-\nu_\mu) = (N_{data} - f^{fake}_{RS/WS} \cdot N^{fake}_{WS}) \cdot (1 - f_{bg}) \cdot (1 - f_\pi). \tag{14.14}$$

The distributions for RS and WS are shown in the Figure 14.7. The yields for the WS fake muon contribution and the signal events is shown in Table B.1 in the appendix in each of the 216 bins. The total yields for $N(D^{*+} \to D^0\pi^+, D^0 \to \mu^+K^-\nu_\mu)$ and N^{fake}_{WS} as integrated across the independent measurements are shown in table 14.7. The errors shown are statistical only.

Table 14.7: Signal and WS Yields for the entire D^{*+} dataset

	D^{*+}	D^{*-}
$N(D^{*+})$	50740 ± 220	52070 ± 230
N^{fake}_{WS}	12901 ± 189	9986 ± 180

Now, the D^{*+} signal yields, which have been weighted to correct for the π efficiency ratio, can simply be divided to determine the K^- efficiency ratio $\frac{\epsilon_{K^+}}{\epsilon_{K^-}}$. The results with statistical errors are shown in Table 14.8.

Table 14.8: K^+ efficiency ratio $\frac{\epsilon_{K^+}}{\epsilon_{K^-}}$

$p_T(K^+)[\text{GeV}/c]$	$\phi(K^+)$	$\frac{\epsilon_{K^+}}{\epsilon_{K^-}}$
$[2.0, 3.0]$	$[-\frac{\pi}{12}, \frac{3\pi}{12}]$	1.14 ± 0.03
	$[\frac{3\pi}{12}, \frac{7\pi}{12}]$	1.02 ± 0.03
	$[\frac{7\pi}{12}, \frac{11\pi}{12}]$	1.01 ± 0.03
	$[\frac{11\pi}{12}, \frac{15\pi}{12}]$	1.04 ± 0.03
	$[\frac{15\pi}{12}, \frac{19\pi}{12}]$	0.94 ± 0.03
	$[\frac{19\pi}{12}, \frac{23\pi}{12}]$	1.14 ± 0.03
$[3.0, 4.0]$	$[-\frac{\pi}{12}, \frac{3\pi}{12}]$	1.03 ± 0.03
	$[\frac{3\pi}{12}, \frac{7\pi}{12}]$	0.99 ± 0.04
	$[\frac{7\pi}{12}, \frac{11\pi}{12}]$	0.90 ± 0.03
	$[\frac{11\pi}{12}, \frac{15\pi}{12}]$	1.06 ± 0.03
	$[\frac{15\pi}{12}, \frac{19\pi}{12}]$	0.99 ± 0.03
	$[\frac{19\pi}{12}, \frac{23\pi}{12}]$	1.05 ± 0.03
$[4.0, 100.0]$	$[-\frac{\pi}{12}, \frac{3\pi}{12}]$	1.06 ± 0.02
	$[\frac{3\pi}{12}, \frac{7\pi}{12}]$	1.00 ± 0.02
	$[\frac{7\pi}{12}, \frac{11\pi}{12}]$	0.98 ± 0.02
	$[\frac{11\pi}{12}, \frac{15\pi}{12}]$	1.03 ± 0.02
	$[\frac{15\pi}{12}, \frac{19\pi}{12}]$	1.00 ± 0.02
	$[\frac{19\pi}{12}, \frac{23\pi}{12}]$	1.06 ± 0.03

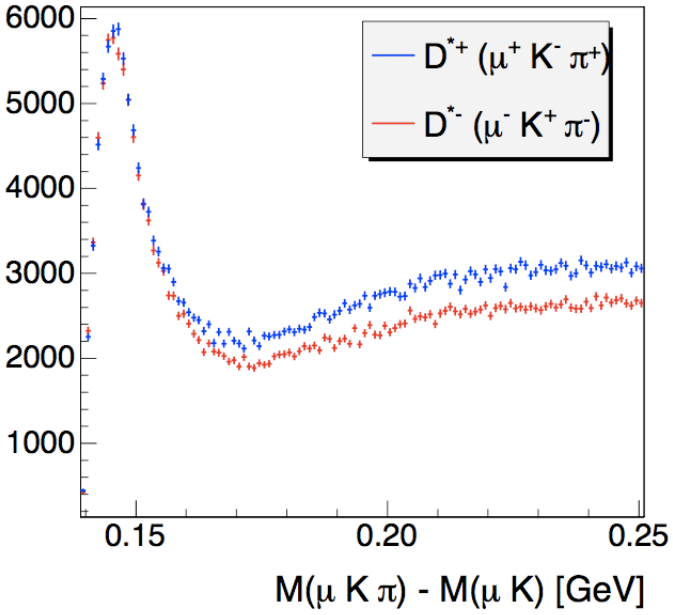

(a) RS Distribution for $D^{*+} \to D^0\pi^+, D^0 \to \mu^+K^-\nu_\mu$

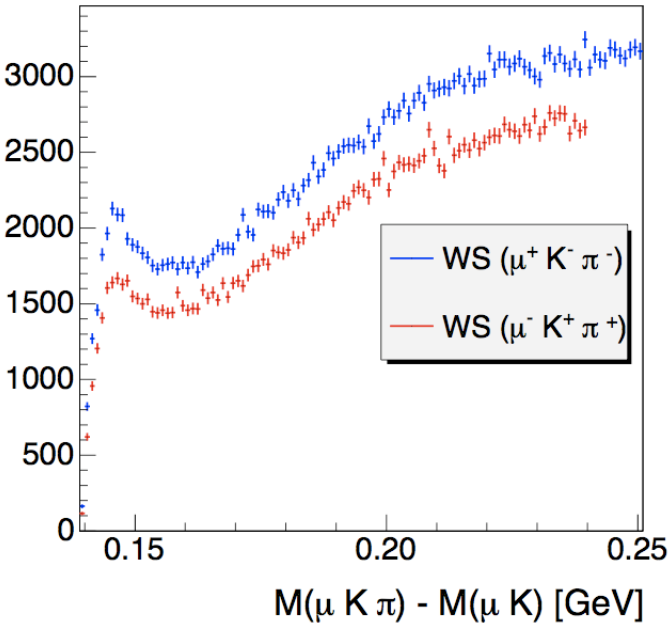

(b) WS Distribution for $D^{*+} \to D^0\pi^+, D^0 \to \mu^+K^-\nu_\mu$

Figure 14.6: D^{*+} $\delta(M(\mu^+K^-\pi^+), M(\mu^+K^-))$ distributions for RS and WS to demonstrate the size of the sample.

Chapter 15

Results

15.1 Measurement of $A_{CP}(B^- \to J/\psi K^-)$

In the final calculation of $A_{CP}(B^- \to J/\psi K^-)$, the K^+ efficiency ratio from Table 14.8 is applied bin by bin in $p_T(K^-)$ and $\phi(K^-)$ to the yields from Appendix A according to the following formula:

$$A_{CP}(B^- \to J/\psi K^-) = \frac{\Sigma_{ij}\left(N(B^- \to J/\psi K^-)_{ij}\left(\frac{\epsilon_{K^+}}{\epsilon_{K^-}}\right)_{ij} - N(B^+ \to J/\psi K^+)_{ij}\right)}{\Sigma_{km}\left(N(B^- \to J/\psi K^-)_{km}\left(\frac{\epsilon_{K^+}}{\epsilon_{K^-}}\right)_{km} + N(B^+ \to J/\psi K^+)_{km}\right)}, \tag{15.1}$$

where ij and km are indices representing the $p_T(K^-$ and $\phi(K^-)$ bins. Table 15.1 shows $A_{CP}(B^- \to J/\psi K^-)$ as a function of $p_T(K^-)$ with statistical uncertainties only. The integrated measurement was calculated as a weighted mean of the independent measurements in the separate p_T bins. The systematic uncertainties will be discussed in the next chapter.

As a cross check, the yields were found in 4 bins of proper decay time (ct) using an unbinned likiehood of the mass. A_{CP} should not vary with ct, so this provides a test of the robustness of the measurement. Figure 15.1 shows that there is agreement across the ct range. The average of the 4 binned measurements will not necessarily agree exactly with the full fit, since the strategies are slightly different (mass and lifetime fit vs. mass only fit), and some of the data (ct ¡ 0) is not included in this figure.

Table 15.1: $A_{CP}(B^- \to J/\psi K^-)$

$pT(K^-)$[GeV/c]	A_{CP}
$[2.0, 3.0]$	$0.0054 \pm 0.0081(stat.)$
$[3.0, 4.0]$	$-0.0055 \pm 0.0099(stat.)$
$[4.0, 100.0]$	$0.0063 \pm 0.0061(stat.)$
$[2.0, 100.0]$	$0.0034 \pm 0.0043(stat.)$

The integrated result is consistent with both the SM (~ 0.003) and the unofficial current world average

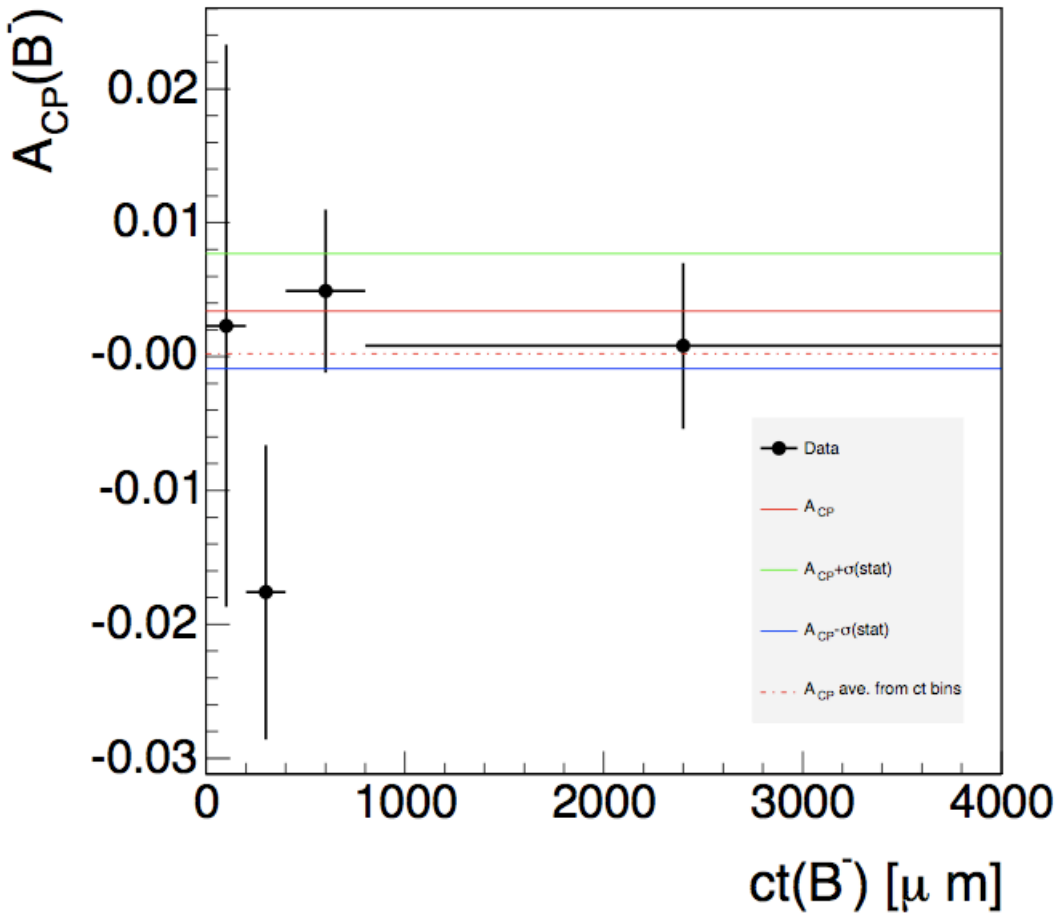

Figure 15.1: A_{CP} is displayed as a function of proper decay length (ct).

(0.0003 ± 0.0041). The next step is to assess any systematic uncertainties that may have arisen in the data collection and analysis.

Chapter 16

Systematic Uncertainties

Systematic uncertainties on A_{CP} must be evaluated. Only those effects which introduce a charge bias are relevant. There are several potential sources, some arising from the $B^- \to J/\psi K^-$ decay, but most arising from the measurement of the K^- efficiency ratio. This section will evaluate each of these factors in the context of the full $A_{CP}(B^- \to J/\psi K^-)$ measurement.

16.1 Systematics from $B^- \to J/\psi K^-$

The potential systematic uncertainties on A_{CP} arising from the $B^- \to J/\psi K^-$ candidates come from the candidate reconstruction and background modeling.

16.1.1 $B^- \to J/\psi K^-$ Candidate Reconstruction

It has already been argued earlier in the thesis that since both the B^+ and B^- decay to the neutral J/ψ in this mode, any charge bias must come from the K^- tracking efficiency and acceptance. However, there is also a potential for bias to be introduced through the kinematic fit of the candidates. Conceivably, based on the geometry of the track, there could be a difference the the fitting efficiency for $B^- \to J/\psi K^-$ and $B^- \to J/\psi \pi^-$. If this were the case, a charge asymmetric tail would be evident in the χ^2 fit quality distribution. In order to investigate this, a exponential decay is fit to the tail and integrated in the extrapolated range $[100, \infty]$. 787 events were found for B^+ compared to 775 events for B^-. With the conservative assumption that all of these events are signal, and applying the average K^- efficiency ratio of $\frac{\epsilon_{K+}}{\epsilon_{K^-}} = 1.03$ the A_{CP} shifts by 0.0001, which is taken as a systematic.

16.1.2 Background Modeling in $B^- \to J/\psi K^-$

The background in the $B^- \to J/\psi K^-$ mass plots is a simple linear function which agrees quite well with the data. Further, the background fraction is floating in the fit, so any uncertainty is taken up in the statistics.

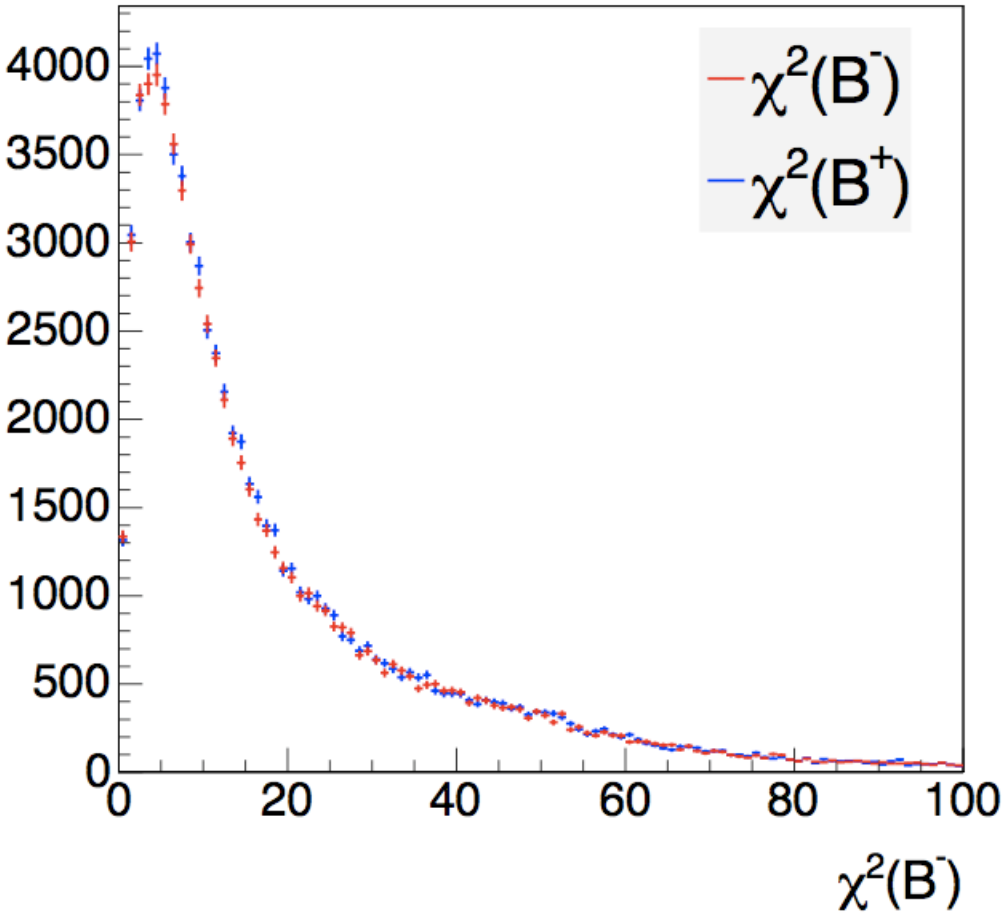

Figure 16.1: Kinematic fit quality distribution for $B^- \to J/\psi K^-$ and $B^+ \to J/\psi K^+$

16.1.3 $B^- \to J/\psi\pi^-$ Contribution

Misreconstructed $B^- \to J/\psi\pi^-$ shows up on the upper shoulder of the $B^- \to J/\psi K^-$ mass distribution. This is accounted for with MC templates in each of the p_T bins. With the shape of the $B^- \to J/\psi\pi^-$ contribution fixed, the relative fraction (compared to $B^- \to J/\psi K^-$) is allowed to float in the fit. The fraction of $B^- \to J/\psi\pi^-$ to $B^- \to J/\psi K^-$ integrated over the entire dataset is found to be:

$$f_{B^- \to J/\psi\pi^-} = 0.0204 \pm 0.0068 \tag{16.1}$$

Which is about a 3σ variation from the PDG value[14] for the relative branching fraction:

$$\frac{BR(B^- \to J/\psi\pi^-)}{BR(B^- \to J/\psi K^-)} = 0.0483 \pm 0.0043. \tag{16.2}$$

Even though a precise measurement of $\frac{BR(B^- \to J/\psi\pi^-)}{BR(B^- \to J/\psi K^-)}$ is not attempted. The relative fraction of

$f_{B^- \to J/\psi\pi^-}$ is expected to be similar. A mismeasurement of $f_{bjpsipi}$ could affect the extracted A_{CP} in several ways.

For example, if f_{pi} is not correct, then the signal model for $B^- \to J/\psi K^-$ could be incorrect since it will affect the resolution. Any events that should be accounted for by $B^- \to J/\psi\pi^-$ could falsely pull the $B^- \to J/\psi K^-$ resoltution wider.

In order to account for this as a possible systematic uncertainty, the $f_{B^- \to J/\psi\pi^-}$ is fixed to the PDG central value for $\frac{BR(B^- \to J/\psi\pi^-)}{BR(B^- \to J/\psi K^-)}$ and the analysis is performed again. This results in a shift of 0.0018 on A_{CP}. This is taken as a conservative estimate of the systematic.

16.2 Systematics from $D^{*+} \to D^0\pi^+, D^0 \to \mu^+K^-\nu_\mu$

The K^- efficiency ratio is the dominant source of systematic uncertainty in A_{CP}. The potential sources are summarized and evaluated in the next sections.

16.2.1 μ^+ vs. μ^- Efficiency

The $D^{*+} \to D^0\pi^+, D^0 \to \mu^+K^-\nu_\mu$ decays are collected on a single μ^+ trigger which could potentially be a source of a systematic uncertainty if there is an unmeasured charge bias for tracking or trigger efficiency. This potential effect was discussed in the thesis of Christopher Marino[29]. A μ must leave three hits in a muon chamber to be registered as a stub. So, a track with only two hits in the chamber would not be recognized as a μ and could not fire the trigger. Especially for $p_T > 8\text{GeV}/c$ tracks, this must be the only effect since the geometry would have a negligible effect on these tracks with extremely small (but measurable) curvature. The relative efficiency for a μ^+ recording the necessary three hits was probed in the following way.

It is assumed that the relative rates for N hits vs. N-1 hits shows some correlation across N. Taking advantage of this assumption, the number of μ^+ candidates with 4 CMU hits is compared to the number with 3 CMU hits. This ratio is then assumed to be related to the rate of candidates which have 2 CMU hits compared to 3 hits, which is the threshold for a registering a muon stub. The same measurement is performed for μ^- and the ratio of these two measurements is used as a indicator of the relative efficiency ratios. It is found that for μ with $p_T > 3\text{GeV}/c$ this ratio is consistent with unity. This implies there is no single muon trigger charge bias. Since any effect would be expected to be inversely proportional to p_T, the $8\text{GeV}/c$ sample used in this analysis is even less likely to show any bias. For this reason, the systematic from μ efficiency is assumed to be negligible.

16.2.2 Background Modeling in $D^{*+} \to D^0\pi^+, D^0 \to \mu^+K^-\nu_\mu$

The background in the $D^{*+} \to D^0\pi^+, D^0 \to \mu^+K^-\nu_\mu$ distribution is a different issue since the model under the peak is not as obvious. This background is assumed to be dominated by three random tracks. The SS distribution is expected to be dominated by these combinatoric events. This motivates the use of the SS events as a template for the background under the peak. This is likely a good assumption, but it is prudent to assess any potential variation due to mismodeling. The SS distribution with charge of the μ matching the RS is used to model the background. In order to test the effect of mismodeling, the templates are swapped for μ^+ and μ^-. A_{CP} varies by 0.001 with this swap applied, which is applied as a systematic uncertainty.

16.2.3 Signal Modeling

MC templates are generated to model the signal component of the data. The resolution is expected to be dominated by kinematics, which the MC models well. This agreement is apparent in the fits, but there is potential for the shape to be mismodeled even with a correct width. This is quantified by taking another approach to determining the signal yields. Instead of performing a fit, the backgrounds are subtracted by scaling the SS distribution to match the RS sideband while the yields are determined by straight event counting. Fakes in the RS are accounted for by subtracting the RS fake yield as determined by the WS fake yield and the MC RS/WS relative rate from MC from Table 14.5.

The variation on A_{CP} is 0.003, which is assessed as a systematic uncertainty.

16.2.4 Fake Muon Rate

One of the major background components for $D^{*+} \to D^0\pi^+, D^0 \to \mu^+K^-\nu_\mu$ is fake muons from hadronic D^{*+} decay daughters. The WS fake muon contribution is isolated, and can be determined through a fit. MC templates are generated and used to estimate the relative rate of RS fake muons to WS fake muons. The uncertainty from the MC relative should be small, since they are driven largely by kinematics and the muon fake rate, which is well measured in data[28]. The uncertainty on the WS yield is likely the major source of systematic uncertainty from the fake muon rate.

The statistical uncertainty on the integrated WS yield is $\sim 2\%$. The WS yield is at most $\sim 25\%$ of the signal yield in some bins. Then, a conservative estimate of a potential shift of the D^{*+} signal yield due to a mismeasurement of the background would be 0.25×0.02. Rounding this up to $\sim 1\%$ and making shift in signal yield for either D^{*+} or D^{*-} results in a shift on A_{CP} of 0.005 which is applied as a systematic. This is likely to be over conservative, but a more concrete handle is not apparent.

16.2.5 π^+ as K^- Rate

There are real μ^+ decays from D^{*+} which have a π with the opposite charge to the μ, which is the only K^- specific requirement of the analysis. This means that the K^- sample is diluted with a certain fraction of π. This fraction is determined from MC, and could be sensitive to detector effects. Any charge bias in this rate will be determined by the fraction of π^+ from D^0 decays that are reconstructed, namely the efficiency ratio. In fact, a correction to the ratio could be estimated by the ratio of the K^+ tracking efficiency to the π^+ tracking efficiency.

$$R^+_{K:\pi\,corr} \sim R_{K:\pi}\frac{\epsilon_{K^+}}{\epsilon_{\pi^+}} \tag{16.3}$$

where $R^+_{K:\pi\,corr}$ is the corrected ratio, $R^+_{K:\pi}$ is the ratio from MC used in the analysis and ϵ_{K^+} and ϵ_{π} are the efficiency ratios as defined in the analysis. Variations in this quantity will contribute to A_{CP} through the K^+ efficiency ratio. So, the interesting quantity is the ratio of this correction and the same for negatively charged tracks:

$$\frac{R^+_{K:\pi\,corr}}{R^-_{K:\pi\,corr}} = \frac{R_{K:\pi}\frac{\epsilon_{K^+}}{\epsilon_{\pi^+}}}{R_{K:\pi}\frac{\epsilon_{K^-}}{\epsilon_{\pi^-}}}. \tag{16.4}$$

$R_{K:\pi}$ is assumed to be charge independent in the analysis, so those terms will cancel. Further the minimum $p_T(K^-)$ in this analysis is 2.0GeV/c, and as shown in Table 14.1, the π asymmetry is quite small above that range, so the assumption is made that $\epsilon_{\pi^+} \sim \epsilon_{\pi^+}$, leaving the following expression:

$$\frac{R^+_{K:\pi\,corr}}{R^-_{K:\pi\,corr}} \sim \frac{\epsilon_{K^+}}{\epsilon_{K^-}} \tag{16.5}$$

Considering the complications that arise from measuring the efficiency ratio with a self dependent correction, the analysis is performed with the charge independent correction. A systematic for this effect is evaluated by applying the measured K^- efficiency ratio to the $K:\pi$ ratio, and observing the effect on A_{CP}. The magnitude of this systematic is $\delta A_{CP} = 0.0008$.

16.2.6 η Dependence

It is possible that there is some η dependence on the K^- efficiency ratio as a result of forward-backward asymmetry in the charm decays. In order to investigate this, distributions of $\eta(K^-)$ and $\eta(K^+)$ are generated which showed no charge asymmetry (Fig. 16.2) as a function of η. No systematic uncertainty is introduced.

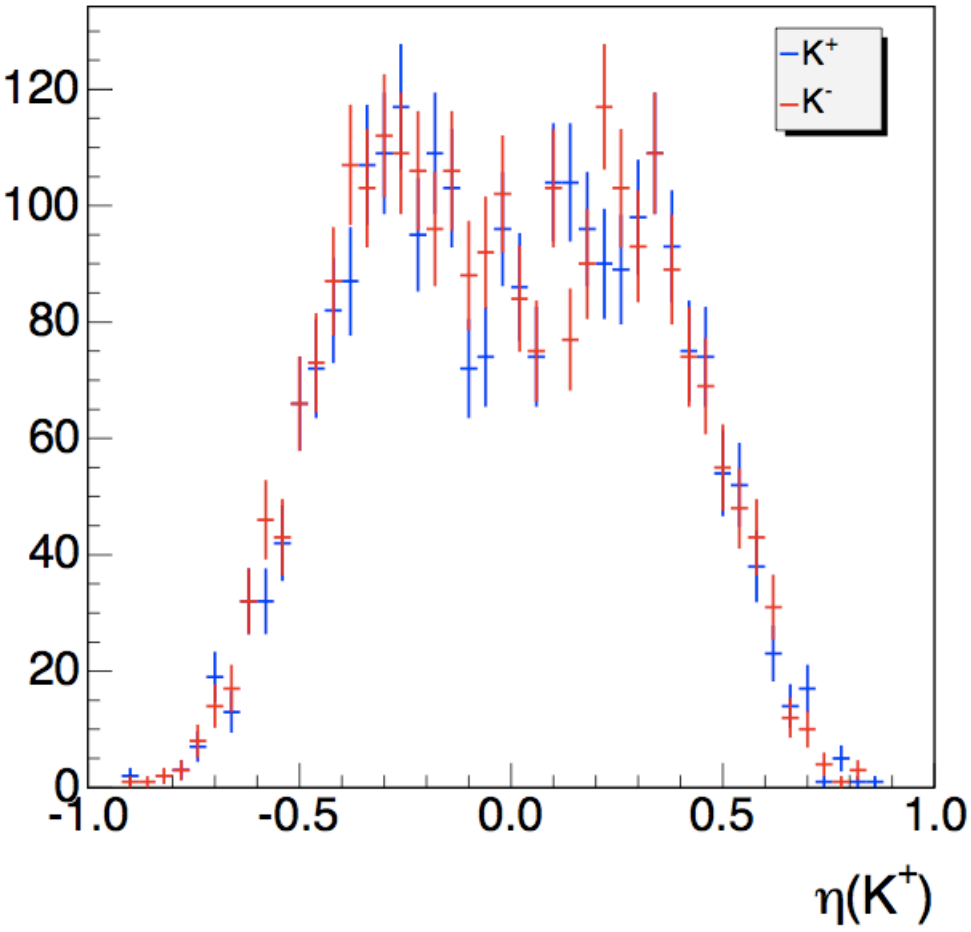

Figure 16.2: η distribution for K^+ and K^-

16.2.7 Mismeasured π Efficiency Ratio

The π efficiency ratio was extracted from another analysis with a similar, but not identical analysis strategy. For this reason, there is minor speculation that the uncertainty could have been misapplied in this analysis. The maximum uncertainty on any bin in the π efficiency ratio is 0.001. Apply a global shift of that ratio $\pm 1\sigma$ varies A_{CP} by 0.0005, which is taken as a systematic.

16.2.8 Summary of Systematics

Each of the non-negligible systematic uncertainties can be added in quadrature to determine the total systematic uncertainty. Table 16.1 summarizes the effects which contribute and provides the final estimate of the systematic uncertainty.

Table 16.1: Systematic Uncertainties on $A_{CP}(B^- \to J/\psi K^-)$

Source	δA_{CP}
$B^- \to J/\psi K^-$ Reconstruction	0.0001
$B^- \to J/\psi \pi^-$ Contribution	0.0018
Background Modeling in D^{*+}	0.001
Signal Modeling in D^{*+}	0.003
Fake Muon Rate in D^{*+}	0.005
$K : \pi$ Signal Ratio in D^{*+}	0.0008
π Efficiency Ratio	0.0005
Total	0.0062

Chapter 17

Summary

A measurement of $A_{CP}(B^- \to J/\psi K^-)$ is performed using $6fb^{-1}$ of $p\bar{p}$ collisions at $\sqrt{s} = 1.96$TeV from the CDF detector at the Fermi National Accelerator Laboratory. $B^- \to J/\psi K^-$ events were selected on the dimuon trigger and the yields were determined using a simultaneous mass and lifetime fit. The charge bias introduced by the K^- candidate was measured by analyzing the semileptonic charm decay $D^{*+} \to D^0\pi^+, D^0 \to \mu^+ K^- \nu_\mu$. The charge bias was measured independently in bins across $\phi(K^-)$ and $p_T(K^-)$ to account for any differences in the ϕ and p_T spectra of $B^- \to J/\psi K^-$ and $D^{*+} \to D^0\pi^+, D^0 \to \mu^+ K^- \nu_\mu$. Sources of systematic uncertainties were evaluated and any non-negligible effects were quantified. The final result is:

$$A_{CP} = 0.0034 \pm 0.0043(stat.) \pm 0.0062(syst.) \tag{17.1}$$

Which is in agreement with both the SM prediction of a small $A_{CP}(B^- \to J/\psi K^-)$ and the unofficial average of the existing current measurements. A sensitivity of 0.01 is observed in the measurement which is on the threshold of what would be required to observe anomalous CP violation that would indicate new physics. No evidence is found for physics beyond the SM in this result; however, this result does not rule out any potential new physics models. An updated summary of the current world measurements is presented in Table 17.1.

Table 17.1: Updated $A_{CP}\,(B^- \to J/\psi K^-)$ Measurements

Experiment	Result		(stat.)		(syst.)	Year	Sample
CLEO	0.018	±	0.043	±	0.004	2000	$e^+e^- \to \Upsilon(4S)$
Babar	0.030	±	0.014	±	0.010	2005	$e^+e^- \to \Upsilon(4S)$
DØ	0.0075	±	0.0061	±	0.0030	2008	$p\bar{p}$ at 1.96TeV
Belle	−0.0076	±	0.0050	±	0.0022	2010	$e^+e^- \to \Upsilon(4S)$
CDF	0.0034	±	0.0043	±	0.0062	2011	$p\bar{p}$ at 1.96TeV
Average	0.0010	±	0.0036				

Chapter 18

Conclusion

The measurement of $A_{CP}(B^- \to J/\psi K^-)$ is consistent with the Standard Model of Particle Physics and current measurements. The huge sample of events collected over the immensely successful running of the Tevatron and CDF provided great power to make a precision measurement of this quantity. Also, the K^- efficiency ratio that was measured to perform this analysis has never been measured at CDF and will provide a important tool for future analyses.

The measurement of the K^- efficiency ratio was the most challenging aspect of this analysis and was the source of the largest contributions to the systematic uncertainty on the asymmetry. A future analysis could likely benefit from greater statistics from the $D^{*+} \to D^0\pi^+, D^0 \to \mu^+K^-\nu_\mu$ decays. However, this method is dominated by systematics which are unlikely to improve. Unfortunately, another technique is not apparent.

This analysis also shows that it is likely within the reach of CDF to make a measurement of $A_{CP}(B^- \to J/\psi\pi^-)$, which could be interesting to pursue.

Appendix A

$B^- \to J/\psi K^-$ Fits

The fits and extracted yields are presented here for each $p_T(K^-)$ and $\phi(K^-)$ bin for both B^+ and B^-. The yields for the individual bins are shown with statistical errors.

A.1 Mass Lifetime Fits

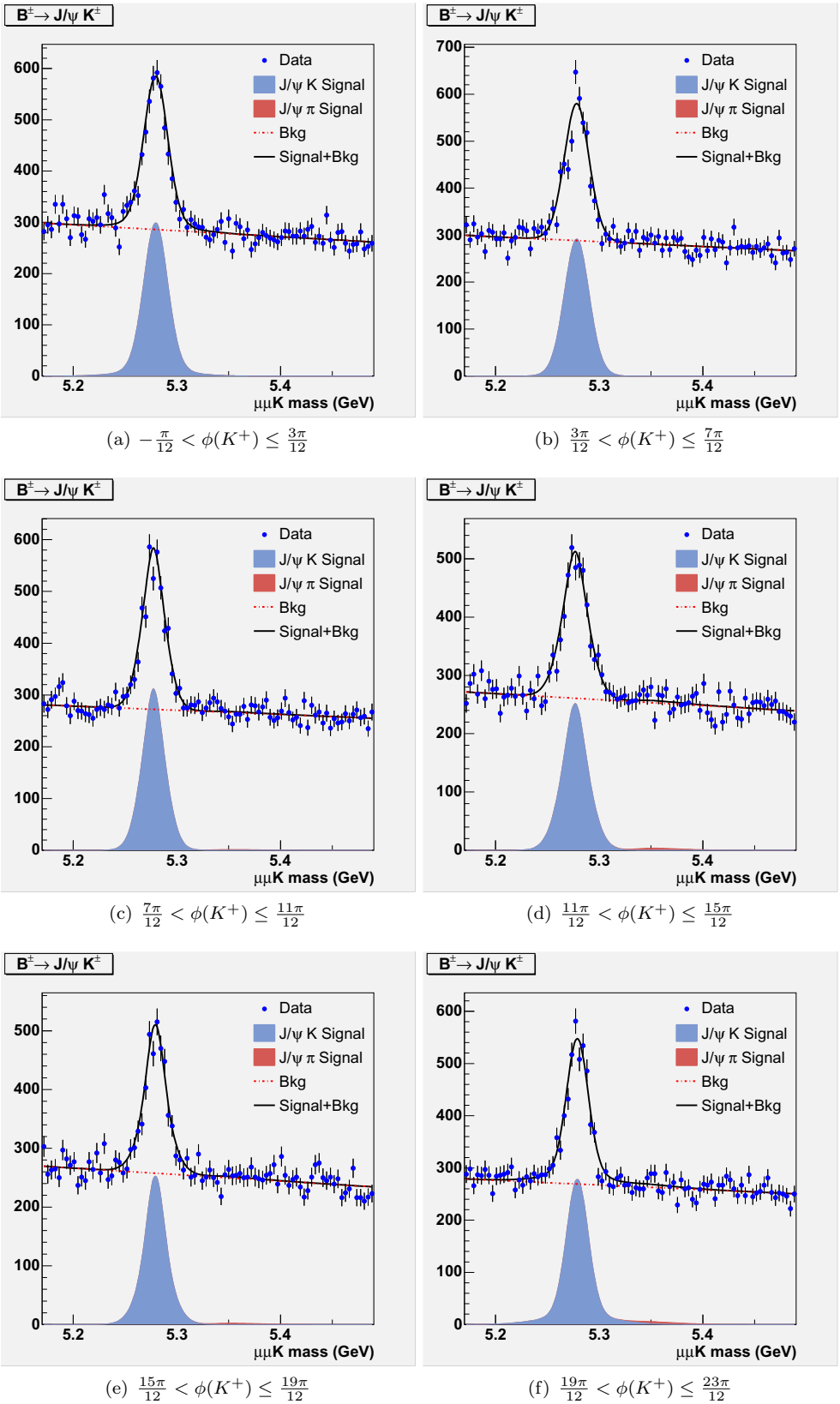

(a) $-\frac{\pi}{12} < \phi(K^+) \leq \frac{3\pi}{12}$

(b) $\frac{3\pi}{12} < \phi(K^+) \leq \frac{7\pi}{12}$

(c) $\frac{7\pi}{12} < \phi(K^+) \leq \frac{11\pi}{12}$

(d) $\frac{11\pi}{12} < \phi(K^+) \leq \frac{15\pi}{12}$

(e) $\frac{15\pi}{12} < \phi(K^+) \leq \frac{19\pi}{12}$

(f) $\frac{19\pi}{12} < \phi(K^+) \leq \frac{23\pi}{12}$

Figure A.1: $M(B^+ \to J/\psi K^+), 2.0\text{GeV}/c < p_T(K^+) \leq 3.0\text{GeV}/c$

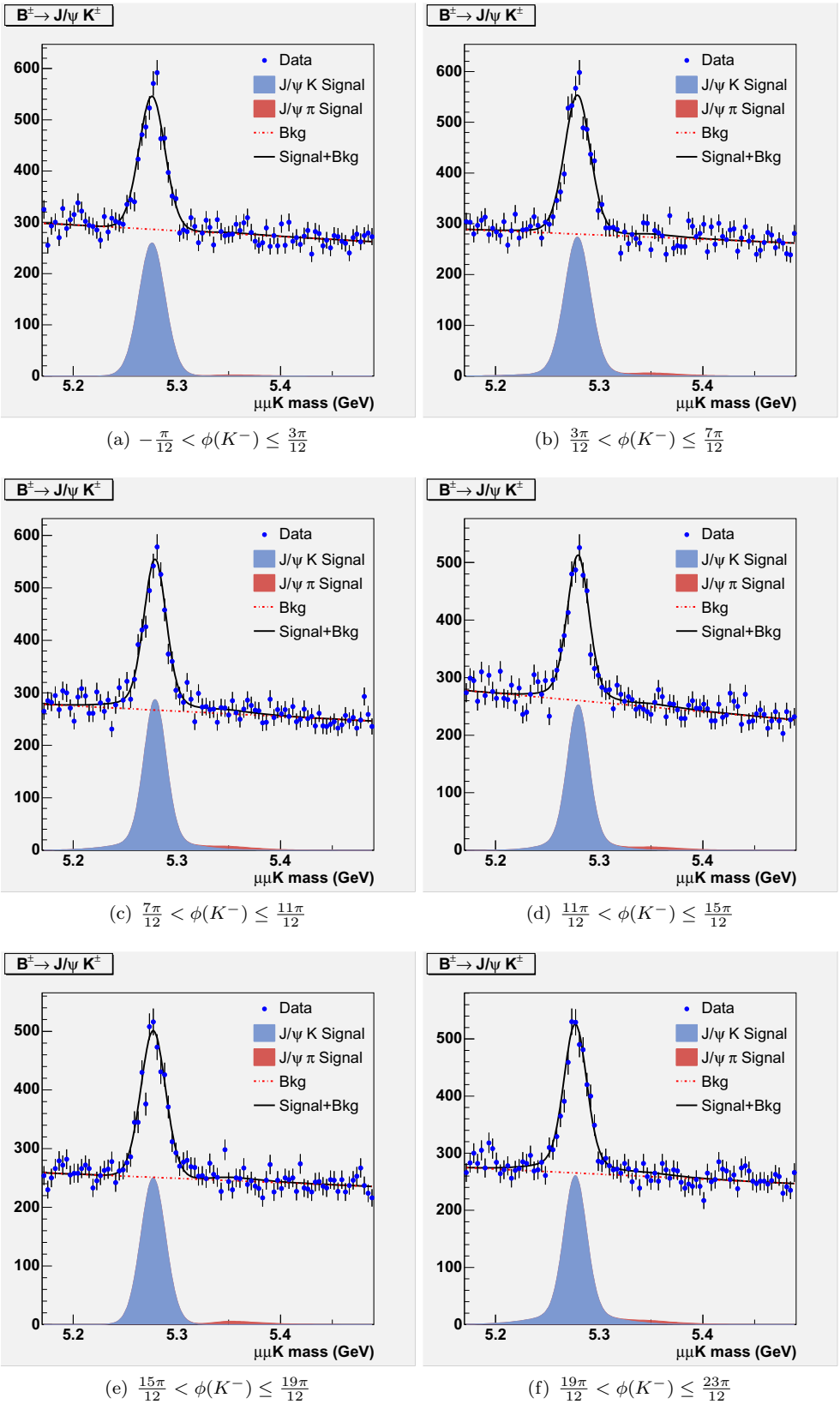

(a) $-\frac{\pi}{12} < \phi(K^-) \leq \frac{3\pi}{12}$

(b) $\frac{3\pi}{12} < \phi(K^-) \leq \frac{7\pi}{12}$

(c) $\frac{7\pi}{12} < \phi(K^-) \leq \frac{11\pi}{12}$

(d) $\frac{11\pi}{12} < \phi(K^-) \leq \frac{15\pi}{12}$

(e) $\frac{15\pi}{12} < \phi(K^-) \leq \frac{19\pi}{12}$

(f) $\frac{19\pi}{12} < \phi(K^-) \leq \frac{23\pi}{12}$

Figure A.2: $M(B^- \to J/\psi K^-), 2.0\text{GeV}/c < p_T(K^-) \leq 3.0\text{GeV}/c$

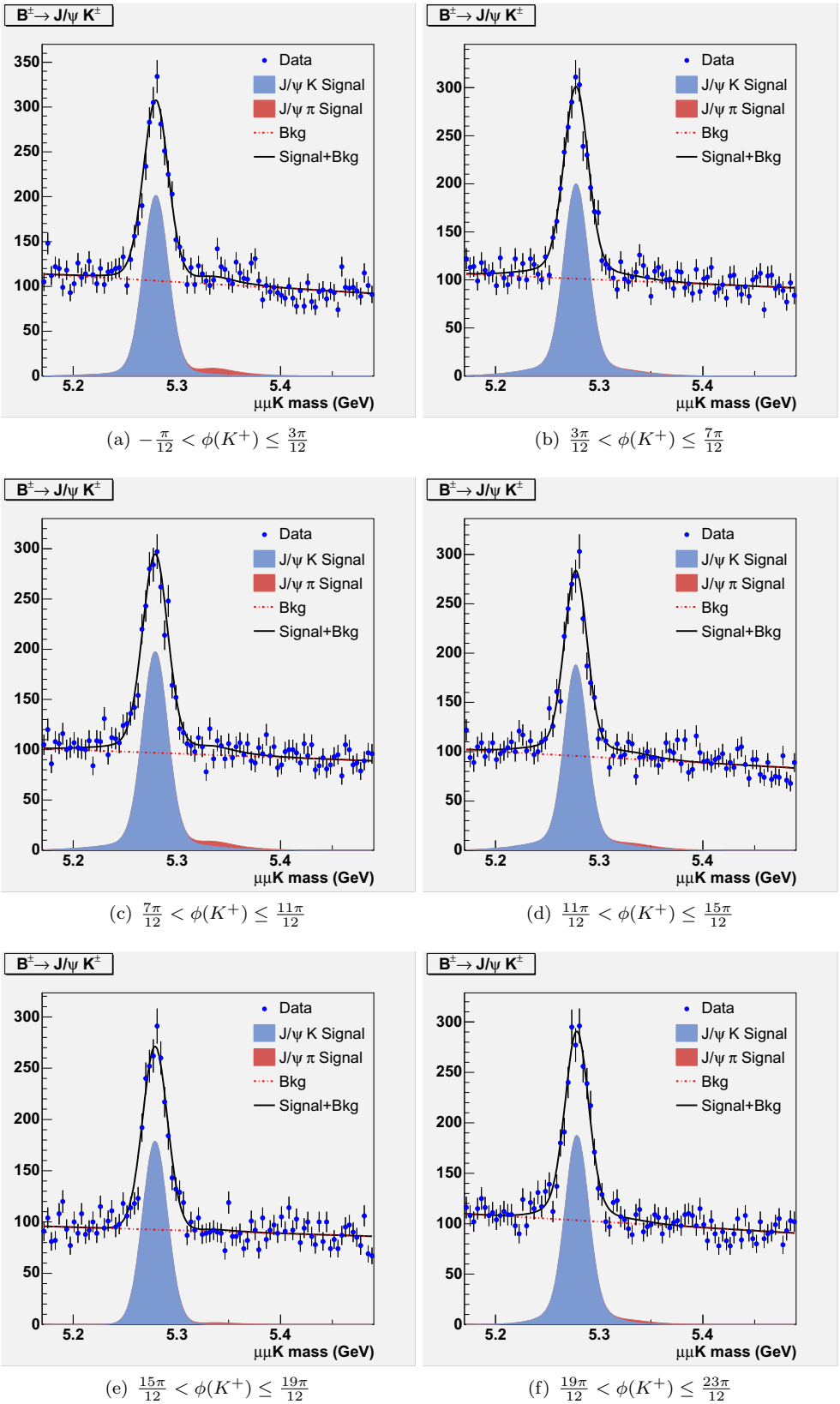

(a) $-\frac{\pi}{12} < \phi(K^+) \leq \frac{3\pi}{12}$

(b) $\frac{3\pi}{12} < \phi(K^+) \leq \frac{7\pi}{12}$

(c) $\frac{7\pi}{12} < \phi(K^+) \leq \frac{11\pi}{12}$

(d) $\frac{11\pi}{12} < \phi(K^+) \leq \frac{15\pi}{12}$

(e) $\frac{15\pi}{12} < \phi(K^+) \leq \frac{19\pi}{12}$

(f) $\frac{19\pi}{12} < \phi(K^+) \leq \frac{23\pi}{12}$

Figure A.3: $M(B^+ \to J/\psi K^+), 3.0\text{GeV}/c < p_T(K^+) \leq 4.0\text{GeV}/c$

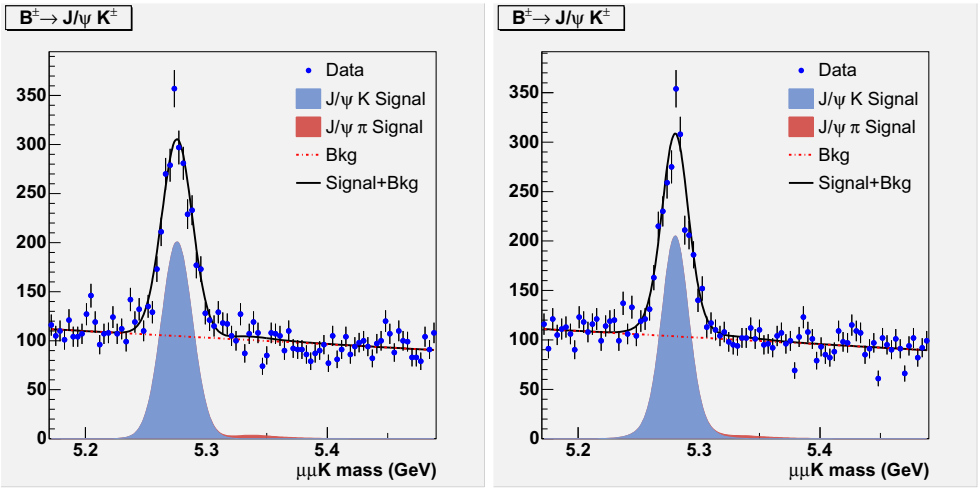

(a) $-\frac{\pi}{12} < \phi(K^-) \leq \frac{3\pi}{12}$ (b) $\frac{3\pi}{12} < \phi(K^-) \leq \frac{7\pi}{12}$

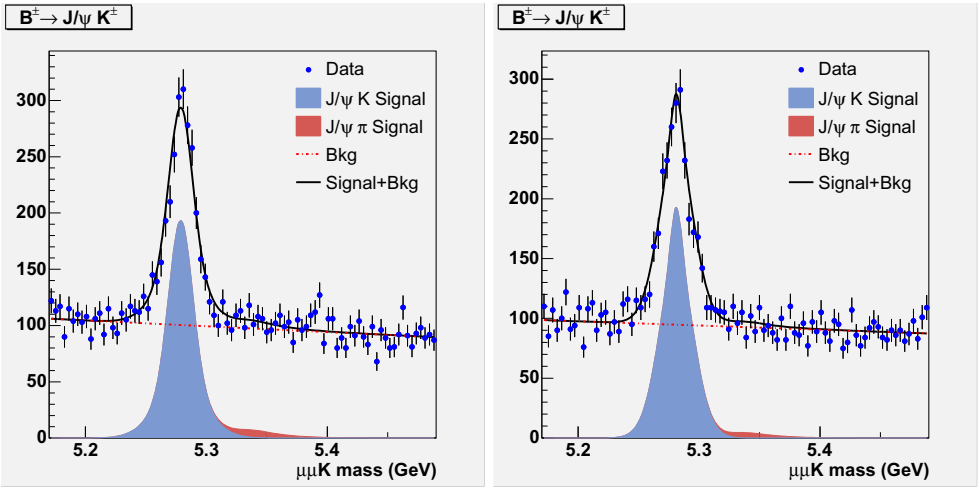

(c) $\frac{7\pi}{12} < \phi(K^-) \leq \frac{11\pi}{12}$ (d) $\frac{11\pi}{12} < \phi(K^-) \leq \frac{15\pi}{12}$

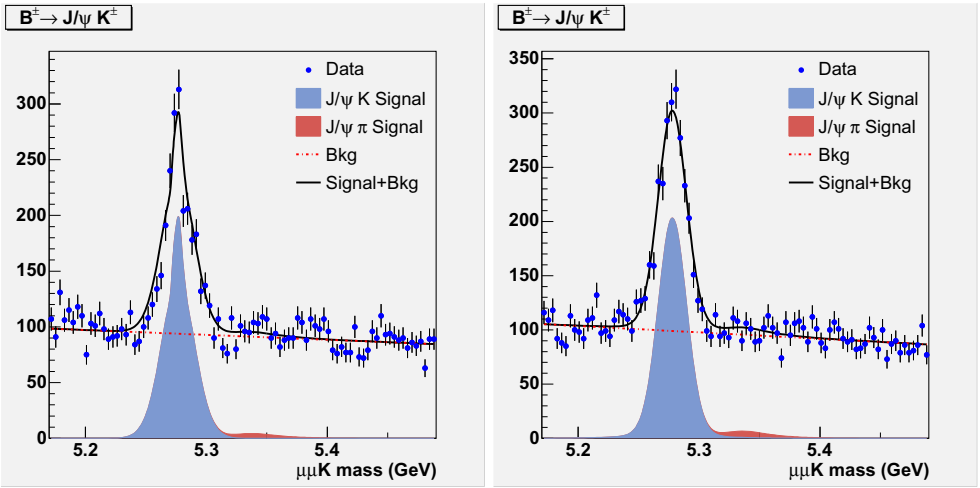

(e) $\frac{15\pi}{12} < \phi(K^-) \leq \frac{19\pi}{12}$ (f) $\frac{19\pi}{12} < \phi(K^-) \leq \frac{23\pi}{12}$

Figure A.4: $M(B^- \to J/\psi K^-), 3.0\text{GeV}/c < p_T(K^-) \leq 4.0\text{GeV}/c$

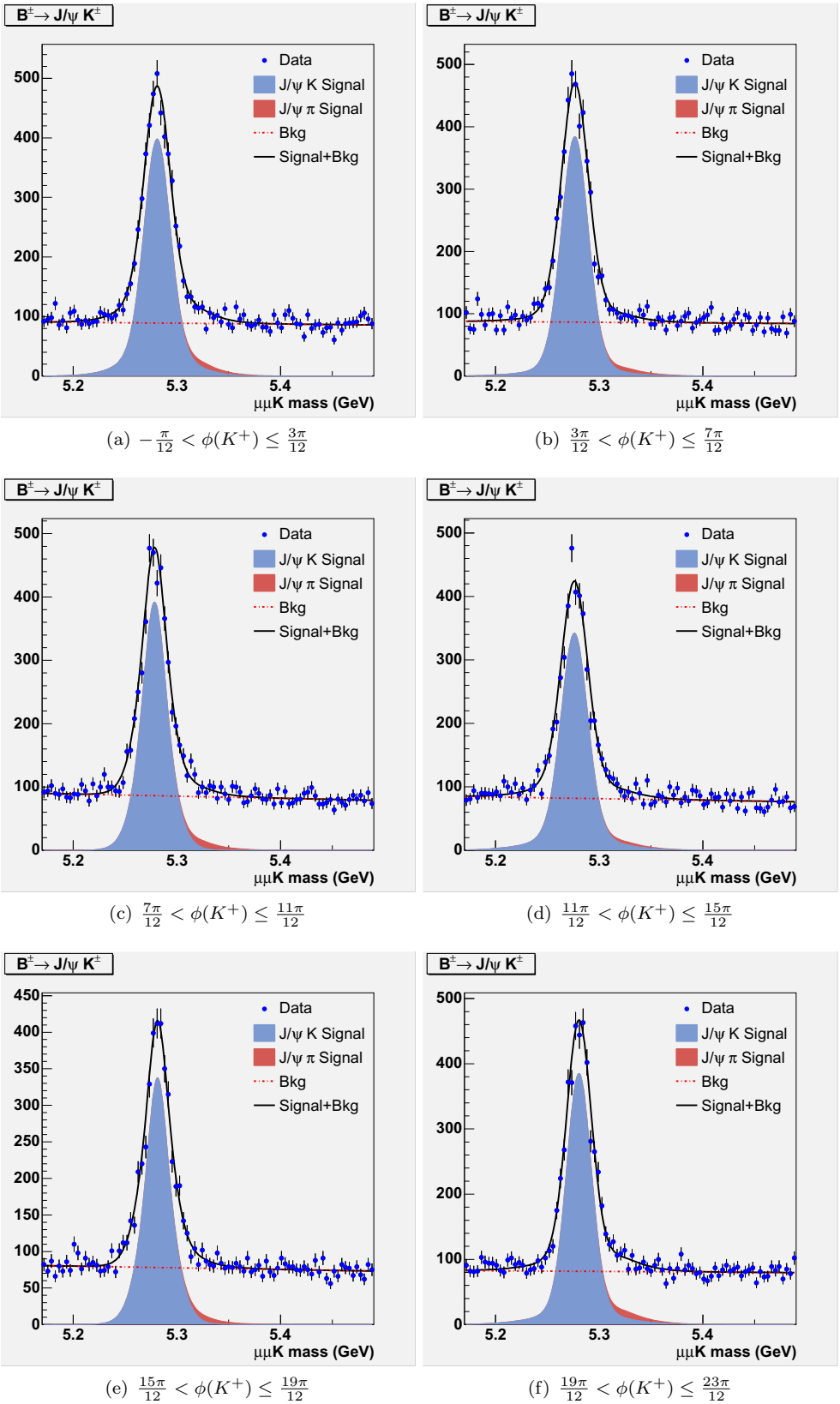

(a) $-\frac{\pi}{12} < \phi(K^+) \leq \frac{3\pi}{12}$

(b) $\frac{3\pi}{12} < \phi(K^+) \leq \frac{7\pi}{12}$

(c) $\frac{7\pi}{12} < \phi(K^+) \leq \frac{11\pi}{12}$

(d) $\frac{11\pi}{12} < \phi(K^+) \leq \frac{15\pi}{12}$

(e) $\frac{15\pi}{12} < \phi(K^+) \leq \frac{19\pi}{12}$

(f) $\frac{19\pi}{12} < \phi(K^+) \leq \frac{23\pi}{12}$

Figure A.5: $M(B^+ \to J/\psi K^+), p_T(K^+) \geq 4.0\text{GeV}/c$

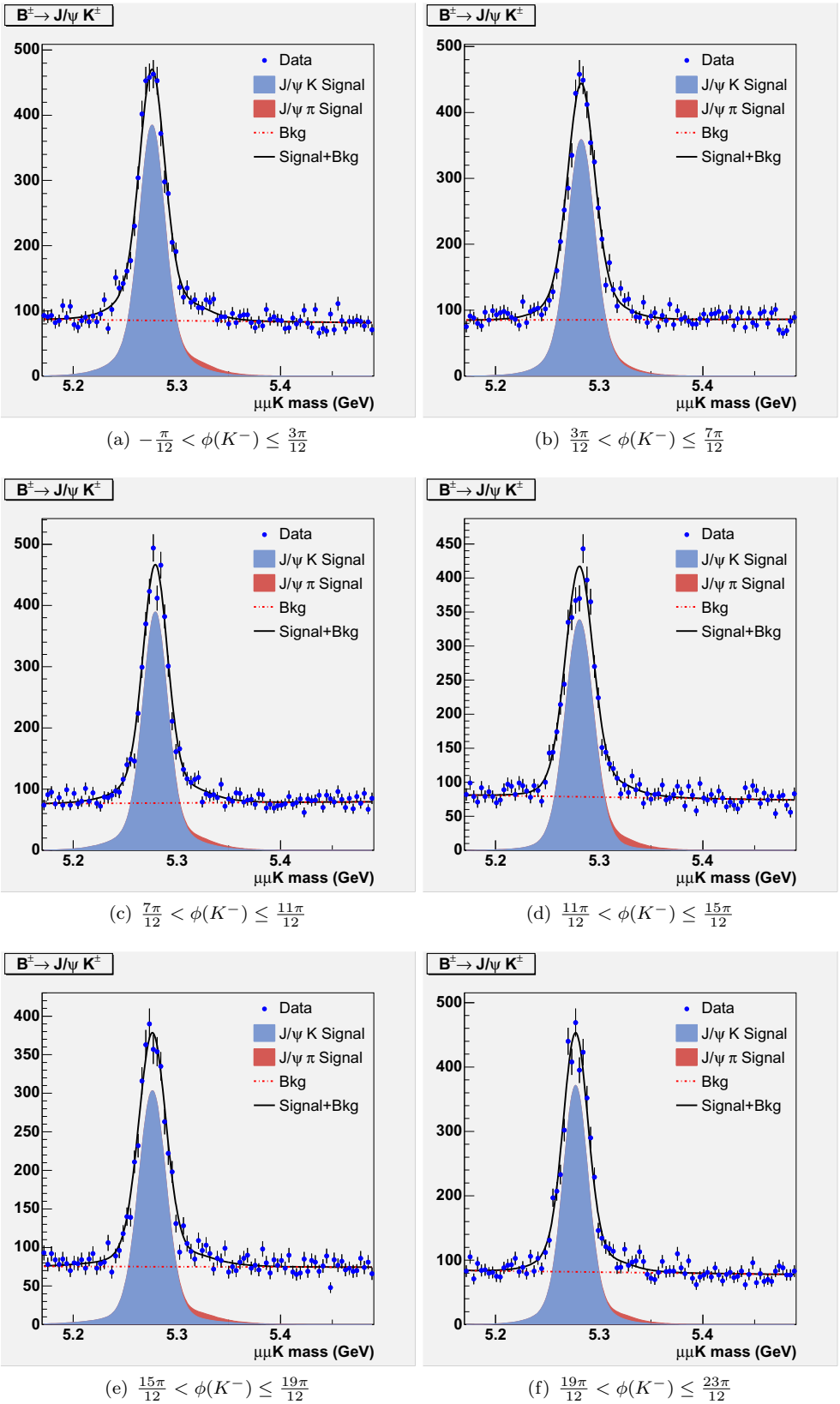

(a) $-\frac{\pi}{12} < \phi(K^-) \leq \frac{3\pi}{12}$

(b) $\frac{3\pi}{12} < \phi(K^-) \leq \frac{7\pi}{12}$

(c) $\frac{7\pi}{12} < \phi(K^-) \leq \frac{11\pi}{12}$

(d) $\frac{11\pi}{12} < \phi(K^-) \leq \frac{15\pi}{12}$

(e) $\frac{15\pi}{12} < \phi(K^-) \leq \frac{19\pi}{12}$

(f) $\frac{19\pi}{12} < \phi(K^-) \leq \frac{23\pi}{12}$

Figure A.6: $M(B^- \to J/\psi K^-), p_T(K^-) \geq 4.0\text{GeV}/c$

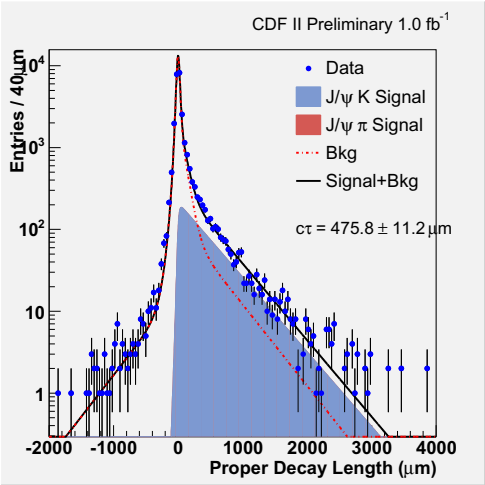

(a) $-\frac{\pi}{12} < \phi(K^+) \leq \frac{3\pi}{12}$

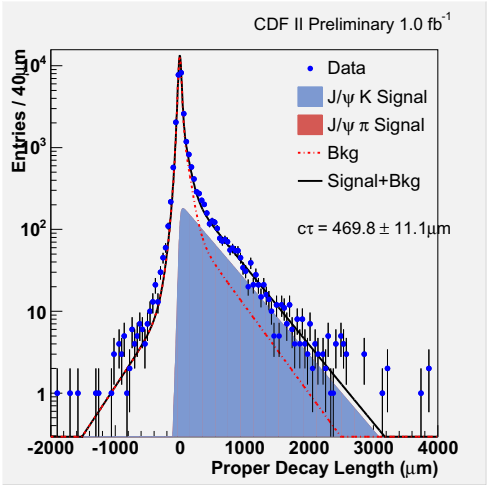

(b) $\frac{3\pi}{12} < \phi(K^+) \leq \frac{7\pi}{12}$

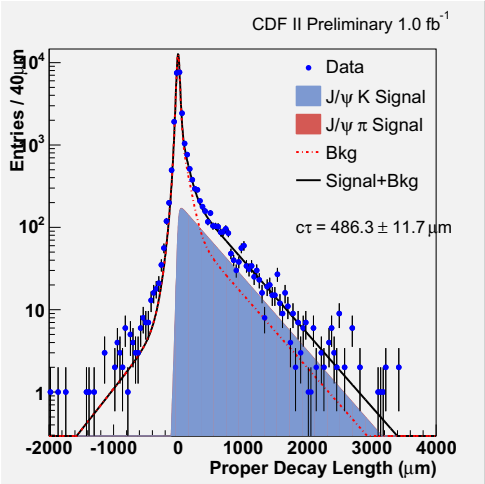

(c) $\frac{7\pi}{12} < \phi(K^+) \leq \frac{11\pi}{12}$

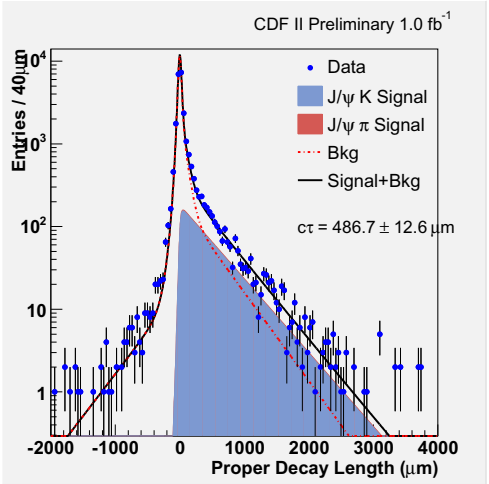

(d) $\frac{11\pi}{12} < \phi(K^+) \leq \frac{15\pi}{12}$

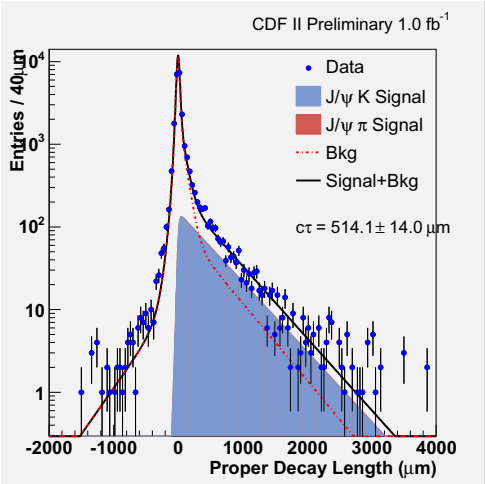

(e) $\frac{15\pi}{12} < \phi(K^+) \leq \frac{19\pi}{12}$

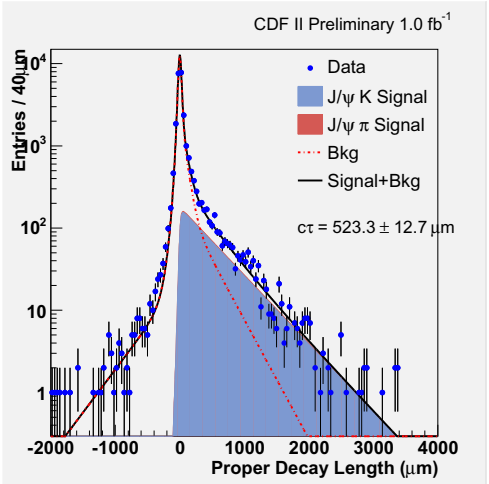

(f) $\frac{19\pi}{12} < \phi(K^+) \leq \frac{23\pi}{12}$

Figure A.7: $ct(B^+ \to J/\psi K^+), 2.0\text{GeV}/c < p_T(K^+) \leq 3.0\text{GeV}/c$

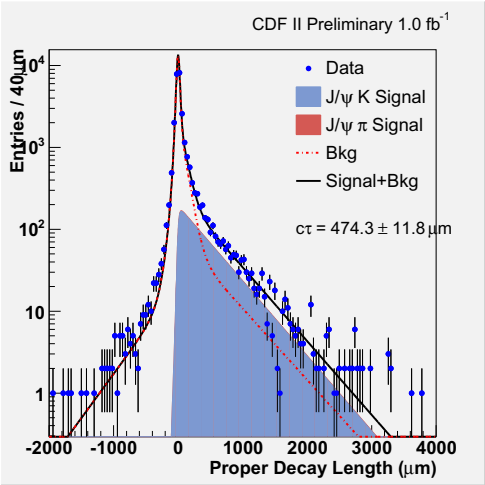

(a) $-\frac{\pi}{12} < \phi(K^-) \leq \frac{3\pi}{12}$

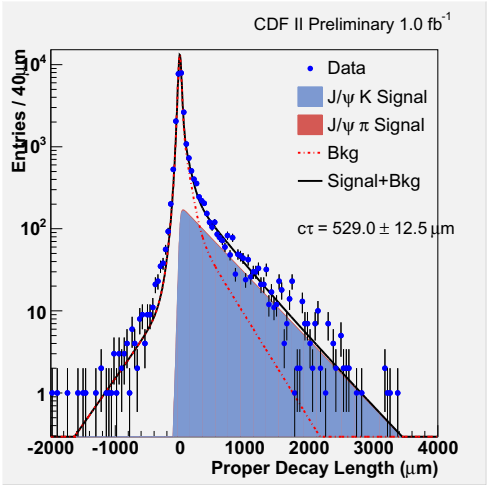

(b) $\frac{3\pi}{12} < \phi(K^-) \leq \frac{7\pi}{12}$

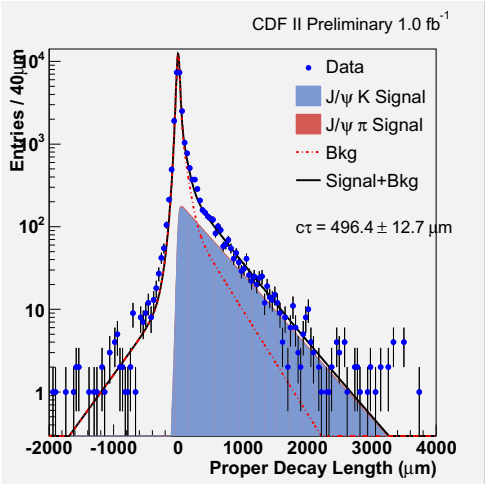

(c) $\frac{7\pi}{12} < \phi(K^-) \leq \frac{11\pi}{12}$

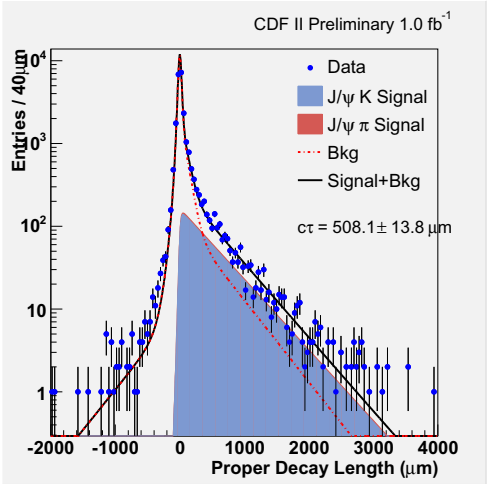

(d) $\frac{11\pi}{12} < \phi(K^-) \leq \frac{15\pi}{12}$

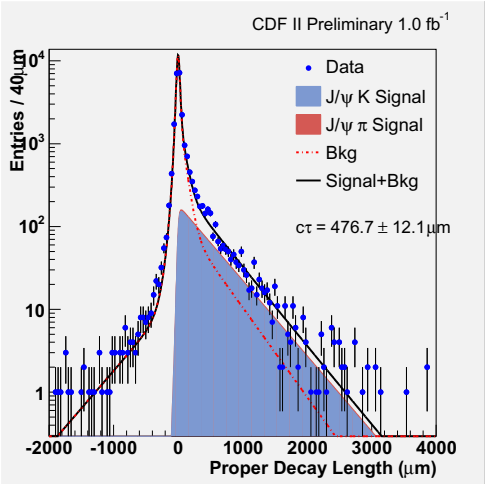

(e) $\frac{15\pi}{12} < \phi(K^-) \leq \frac{19\pi}{12}$

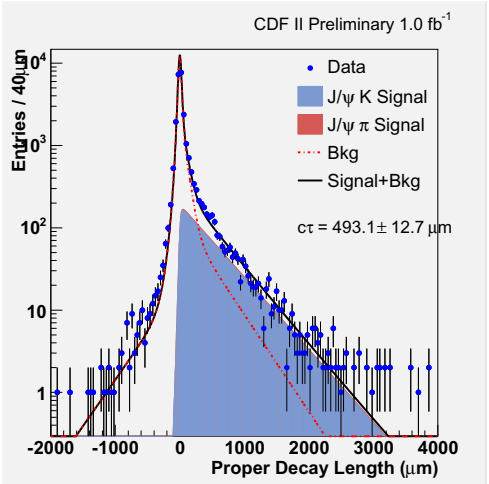

(f) $\frac{19\pi}{12} < \phi(K^-) \leq \frac{23\pi}{12}$

Figure A.8: $ct(B^- \to J/\psi K^-), 2.0\text{GeV}/c < p_T(K^-) \leq 3.0\text{GeV}/c$

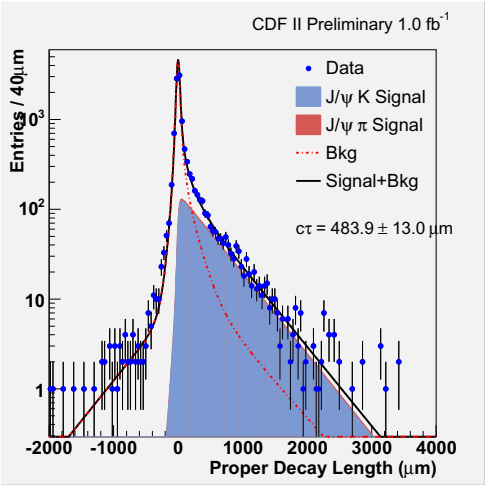

(a) $-\frac{\pi}{12} < \phi(K^+) \leq \frac{3\pi}{12}$

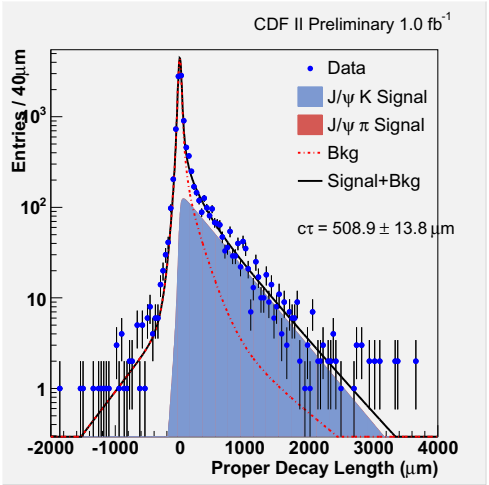

(b) $\frac{3\pi}{12} < \phi(K^+) \leq \frac{7\pi}{12}$

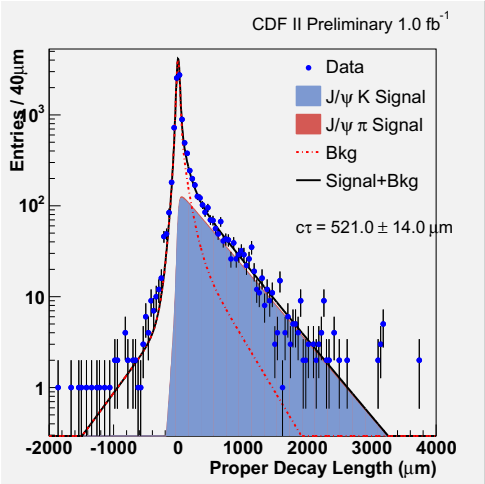

(c) $\frac{7\pi}{12} < \phi(K^+) \leq \frac{11\pi}{12}$

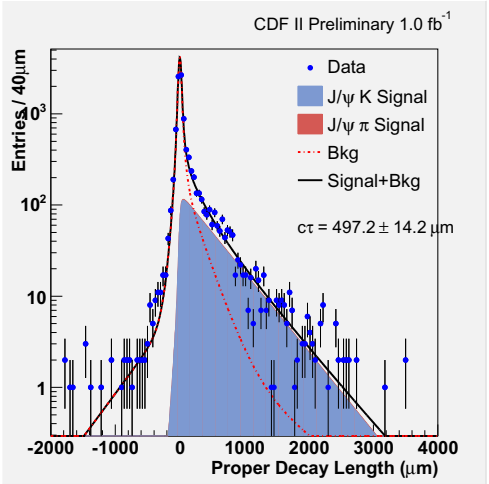

(d) $\frac{11\pi}{12} < \phi(K^+) \leq \frac{15\pi}{12}$

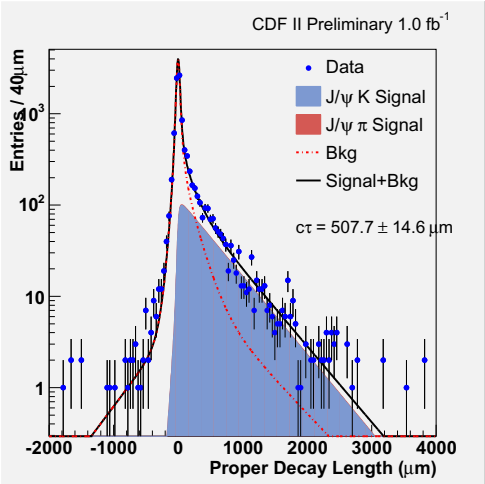

(e) $\frac{15\pi}{12} < \phi(K^+) \leq \frac{19\pi}{12}$

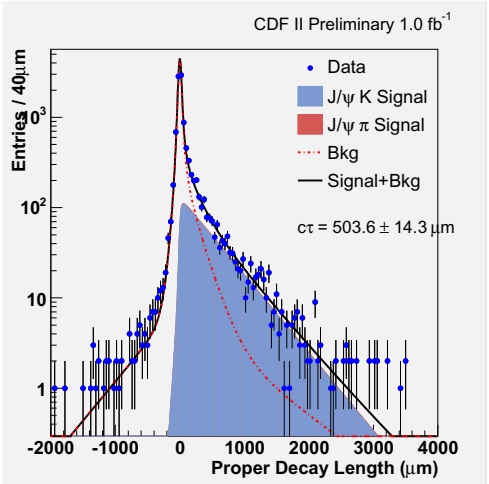

(f) $\frac{19\pi}{12} < \phi(K^+) \leq \frac{23\pi}{12}$

Figure A.9: $ct(B^+ \to J/\psi K^+), 3.0\text{GeV}/c < p_T(K^+) \leq 4.0\text{GeV}/c$

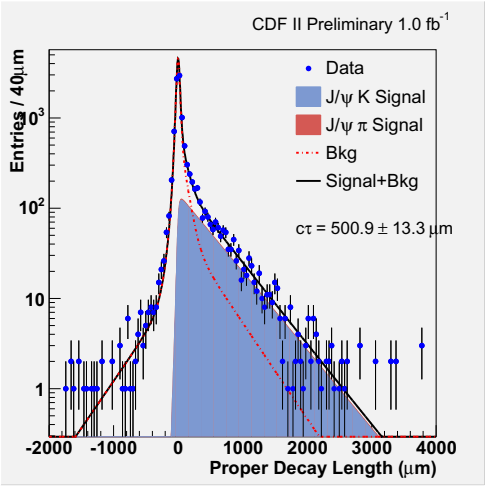

(a) $-\frac{\pi}{12} < \phi(K^-) \leq \frac{3\pi}{12}$

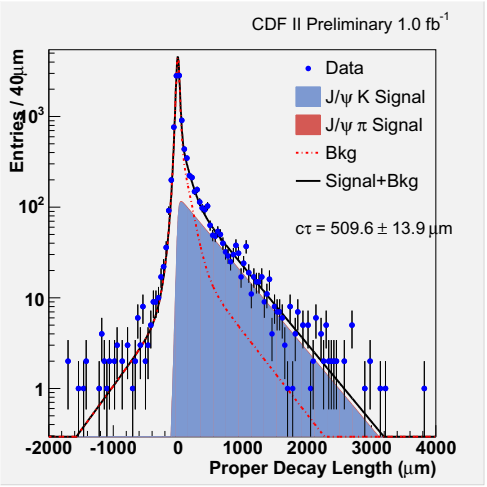

(b) $\frac{3\pi}{12} < \phi(K^-) \leq \frac{7\pi}{12}$

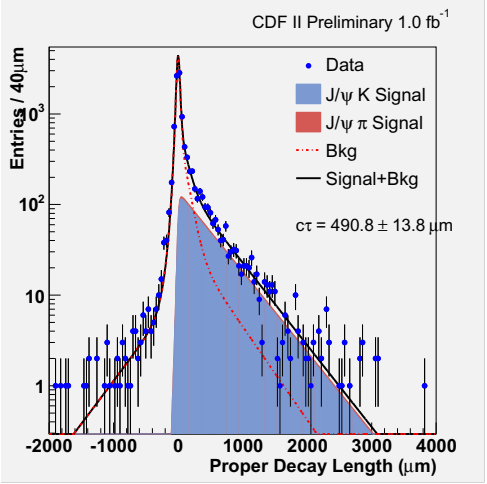

(c) $\frac{7\pi}{12} < \phi(K^-) \leq \frac{11\pi}{12}$

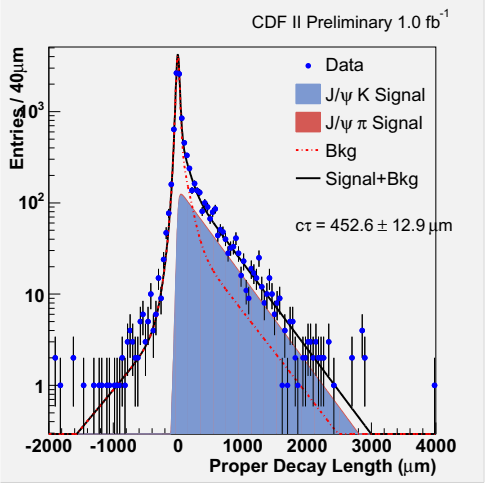

(d) $\frac{11\pi}{12} < \phi(K^-) \leq \frac{15\pi}{12}$

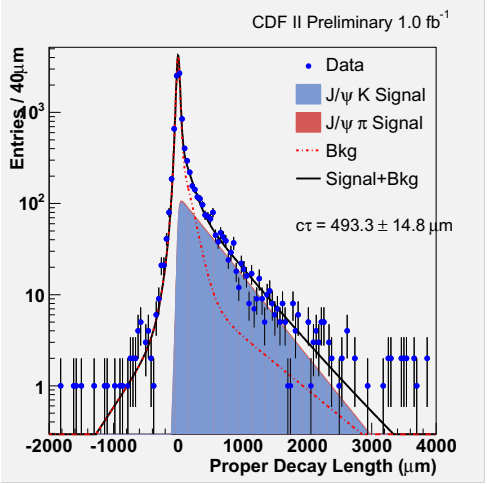

(e) $\frac{15\pi}{12} < \phi(K^-) \leq \frac{19\pi}{12}$

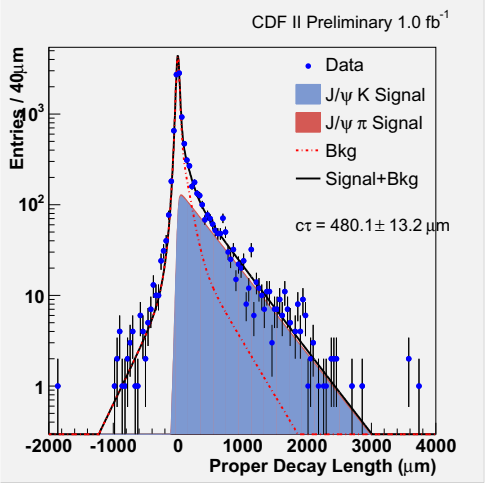

(f) $\frac{19\pi}{12} < \phi(K^-) \leq \frac{23\pi}{12}$

Figure A.10: $ct(B^- \to J/\psi K^-), 3.0\text{GeV}/c < p_T(K^-) \leq 4.0\text{GeV}/c$

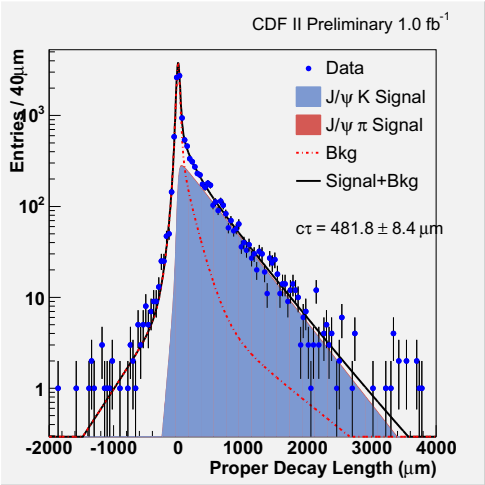

(a) $-\frac{\pi}{12} < \phi(K^+) \leq \frac{3\pi}{12}$

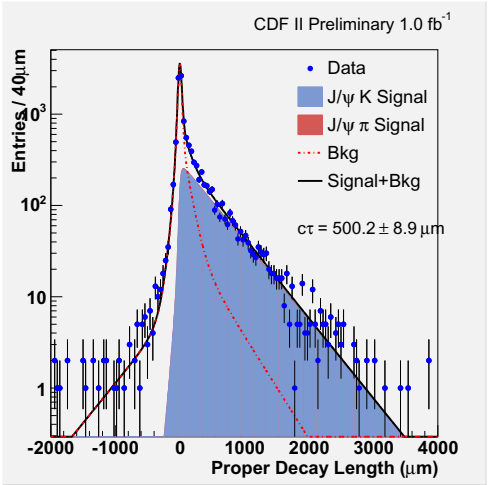

(b) $\frac{3\pi}{12} < \phi(K^+) \leq \frac{7\pi}{12}$

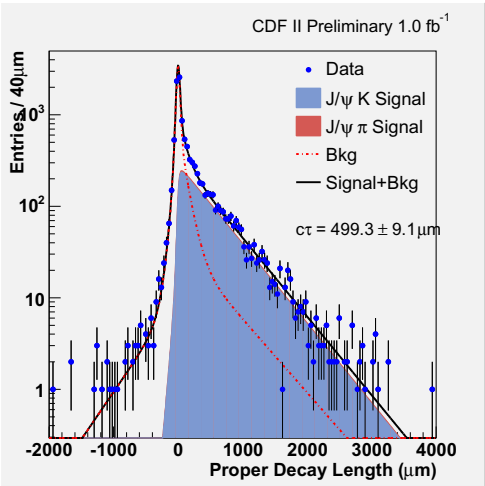

(c) $\frac{7\pi}{12} < \phi(K^+) \leq \frac{11\pi}{12}$

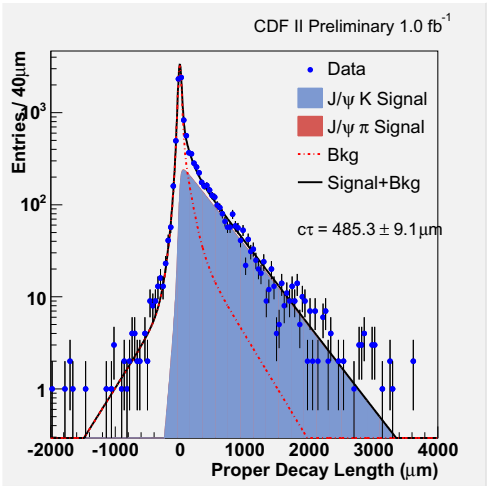

(d) $\frac{11\pi}{12} < \phi(K^+) \leq \frac{15\pi}{12}$

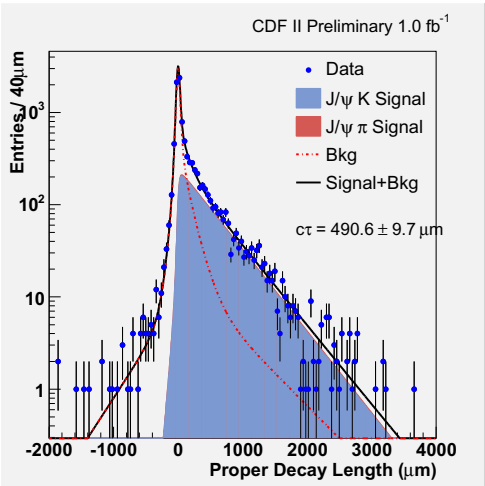

(e) $\frac{15\pi}{12} < \phi(K^+) \leq \frac{19\pi}{12}$

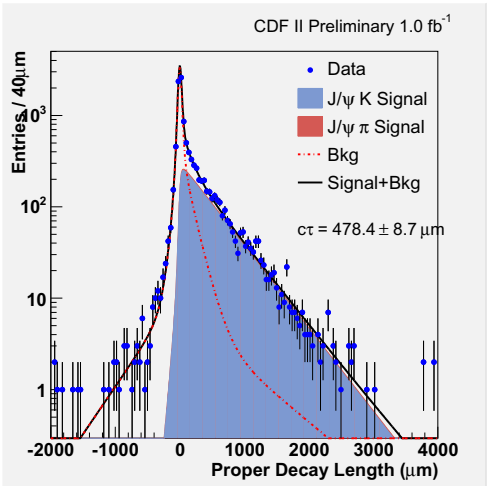

(f) $\frac{19\pi}{12} < \phi(K^+) \leq \frac{23\pi}{12}$

Figure A.11: $ct(B^+ \to J/\psi K^+), p_T(K^+) \geq 4.0\text{GeV}/c$

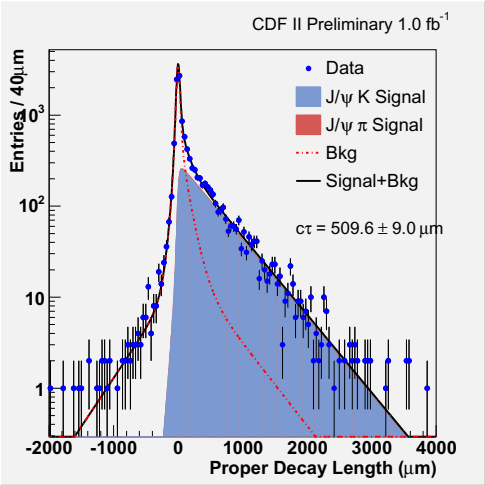

(a) $-\frac{\pi}{12} < \phi(K^-) \leq \frac{3\pi}{12}$

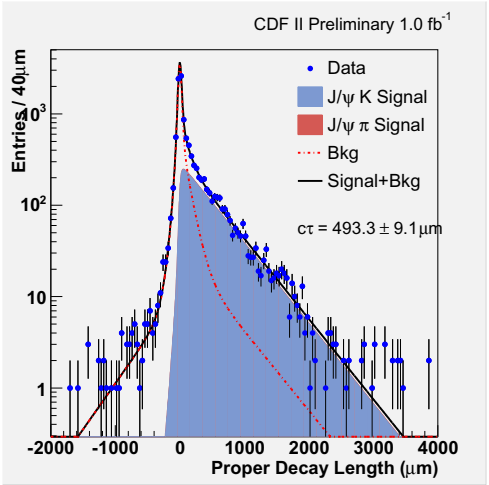

(b) $-\frac{\pi}{12} < \phi(K^-) \leq \frac{3\pi}{12}$

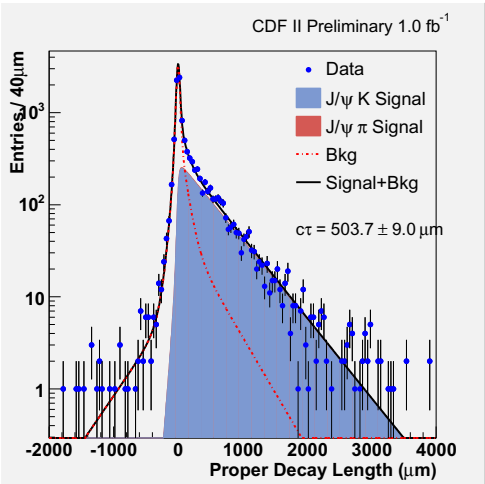

(c) $-\frac{\pi}{12} < \phi(K^-) \leq \frac{3\pi}{12}$

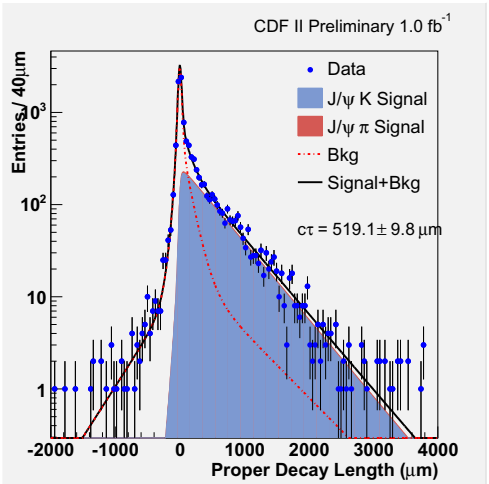

(d) $-\frac{\pi}{12} < \phi(K^-) \leq \frac{3\pi}{12}$

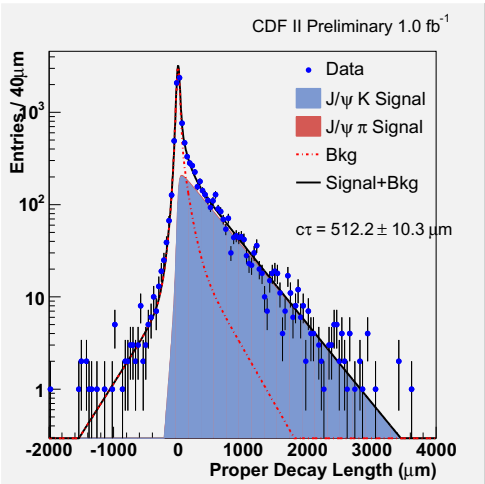

(e) $-\frac{\pi}{12} < \phi(K^-) \leq \frac{3\pi}{12}$

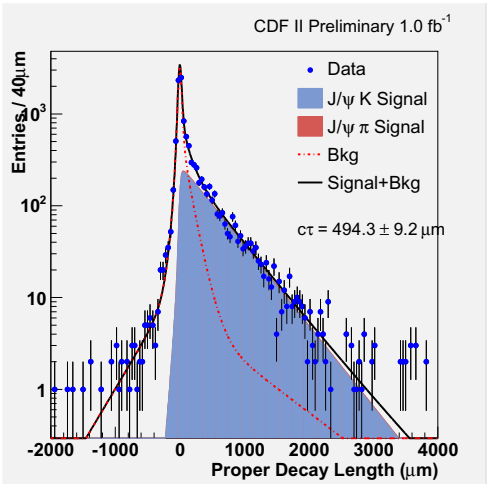

(f) $-\frac{\pi}{12} < \phi(K^-) \leq \frac{3\pi}{12}$

Figure A.12: $ct(B^- \to J/\psi K^-), p_T(K^-) \geq 4.0\text{GeV}/c$

	N($B^- \to J/\psi K^-$)	
$-\frac{\pi}{12} < \phi(K^-) \leq \frac{3\pi}{12}$	2260	± 80
$\frac{3\pi}{12} < \phi(K^-) \leq \frac{7\pi}{12}$	2480	± 80
$\frac{7\pi}{12} < \phi(K^-) \leq \frac{11\pi}{12}$	2420	± 90
$\frac{11\pi}{12} < \phi(K^-) \leq \frac{15\pi}{12}$	2010	± 80
$\frac{15\pi}{12} < \phi(K^-) \leq \frac{19\pi}{12}$	2215	± 80
$\frac{19\pi}{12} < \phi(K^-) \leq \frac{23\pi}{12}$	2300	± 80

Table A.1: $B^- \to J/\psi K^-$ Yields for 2.0GeV/$c < p_T(K^-) \leq$ 3.0GeV/c

	N($B^+ \to J/\psi K^+$)	
$-\frac{\pi}{12} < \phi(K^+) \leq \frac{3\pi}{12}$	2540	± 90
$\frac{3\pi}{12} < \phi(K^+) \leq \frac{7\pi}{12}$	2526	± 70
$\frac{7\pi}{12} < \phi(K^+) \leq \frac{11\pi}{12}$	2350	± 80
$\frac{11\pi}{12} < \phi(K^+) \leq \frac{15\pi}{12}$	2150	± 80
$\frac{15\pi}{12} < \phi(K^+) \leq \frac{19\pi}{12}$	1920	± 70
$\frac{19\pi}{12} < \phi(K^+) \leq \frac{23\pi}{12}$	2300	± 80

Table A.2: $B^+ \to J/\psi K^+$ Yields for 2.0GeV/$c < p_T(K^-) \leq$ 3.0GeV/c

	N($B^- \to J/\psi K^-$)	
$-\frac{\pi}{12} < \phi(K^-) \leq \frac{3\pi}{12}$	1870	± 60
$\frac{3\pi}{12} < \phi(K^-) \leq \frac{7\pi}{12}$	1650	± 50
$\frac{7\pi}{12} < \phi(K^-) \leq \frac{11\pi}{12}$	1630	± 60
$\frac{11\pi}{12} < \phi(K^-) \leq \frac{15\pi}{12}$	1580	± 50
$\frac{15\pi}{12} < \phi(K^-) \leq \frac{19\pi}{12}$	1450	± 40
$\frac{19\pi}{12} < \phi(K^-) \leq \frac{23\pi}{12}$	1700	± 60

Table A.3: $B^- \to J/\psi K^-$ Yields for 3.0GeV/$c < p_T(K^-) \leq$ 4.0GeV/c

	N($B^+ \to J/\psi K^+$)	
$-\frac{\pi}{12} < \phi(K^+) \leq \frac{3\pi}{12}$	1770	± 60
$\frac{3\pi}{12} < \phi(K^+) \leq \frac{7\pi}{12}$	1860	± 60
$\frac{7\pi}{12} < \phi(K^+) \leq \frac{11\pi}{12}$	1850	± 60
$\frac{11\pi}{12} < \phi(K^+) \leq \frac{15\pi}{12}$	1670	± 70
$\frac{15\pi}{12} < \phi(K^+) \leq \frac{19\pi}{12}$	1531	± 50
$\frac{19\pi}{12} < \phi(K^+) \leq \frac{23\pi}{12}$	1630	± 60

Table A.4: $B^+ \to J/\psi K^+$ Yields for 3.0GeV/$c < p_T(K^-) \leq$ 4.0GeV/c

A.2 Mass Fits with $L_{xy} > 0.015$cm

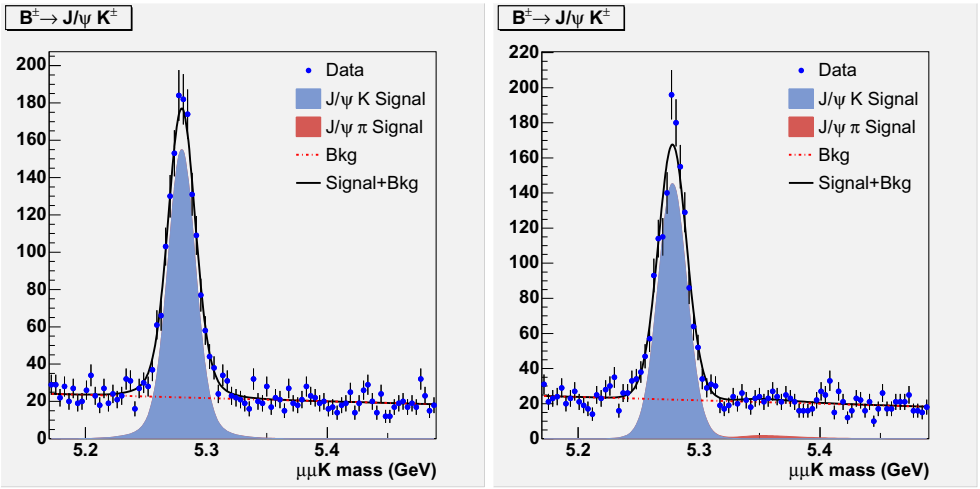

(a) $-\frac{\pi}{12} < \phi(K^+) \leq \frac{3\pi}{12}$ (b) $\frac{3\pi}{12} < \phi(K^+) \leq \frac{7\pi}{12}$

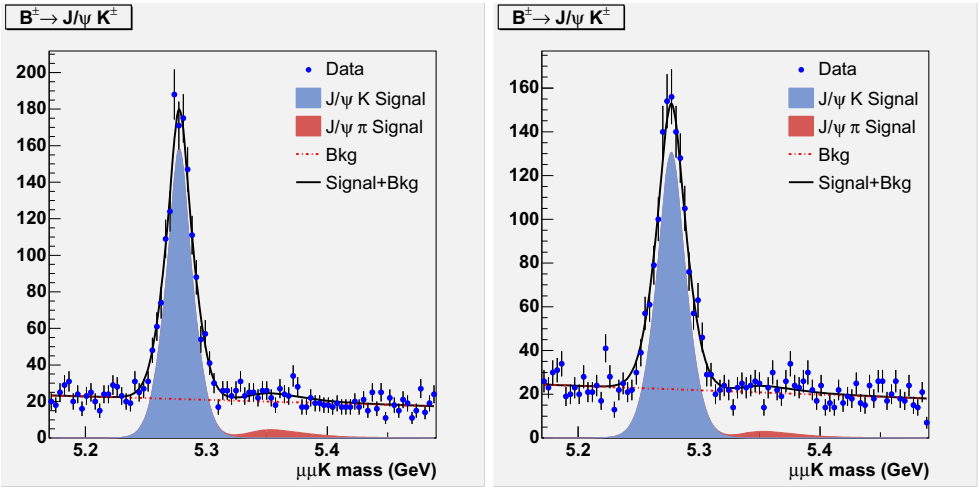

(c) $\frac{7\pi}{12} < \phi(K^+) \leq \frac{11\pi}{12}$ (d) $\frac{11\pi}{12} < \phi(K^+) \leq \frac{15\pi}{12}$

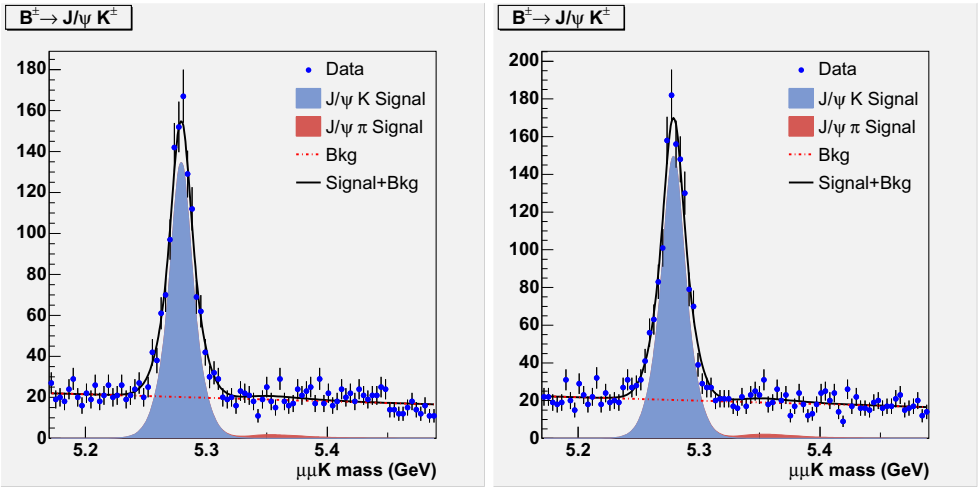

(e) $\frac{15\pi}{12} < \phi(K^+) \leq \frac{19\pi}{12}$ (f) $\frac{19\pi}{12} < \phi(K^+) \leq \frac{23\pi}{12}$

Figure A.13: $M(B^+ \to J/\psi K^+), 2.0\text{GeV}/c < p_T(K^+) \leq 3.0\text{GeV}/c$

	N($B^- \to J/\psi K^-$)	
$-\frac{\pi}{12} < \phi(K^-) \leq \frac{3\pi}{12}$	3790	± 70
$\frac{3\pi}{12} < \phi(K^-) \leq \frac{7\pi}{12}$	3590	± 80
$\frac{7\pi}{12} < \phi(K^-) \leq \frac{11\pi}{12}$	3690	± 70
$\frac{11\pi}{12} < \phi(K^-) \leq \frac{15\pi}{12}$	3340	± 70
$\frac{15\pi}{12} < \phi(K^-) \leq \frac{19\pi}{12}$	3050	± 70
$\frac{19\pi}{12} < \phi(K^-) \leq \frac{23\pi}{12}$	3420	± 70

Table A.5: $B^- \to J/\psi K^-$ Yields for $p_T(K^-) > 4.0\text{GeV}/c$

	N($B^+ \to J/\psi K^+$)	
$-\frac{\pi}{12} < \phi(K^+) \leq \frac{3\pi}{12}$	3930	± 80
$\frac{3\pi}{12} < \phi(K^+) \leq \frac{7\pi}{12}$	3690	± 70
$\frac{7\pi}{12} < \phi(K^+) \leq \frac{11\pi}{12}$	3500	± 70
$\frac{11\pi}{12} < \phi(K^+) \leq \frac{15\pi}{12}$	3420	± 60
$\frac{15\pi}{12} < \phi(K^+) \leq \frac{19\pi}{12}$	2990	± 60
$\frac{19\pi}{12} < \phi(K^+) \leq \frac{23\pi}{12}$	3560	± 70

Table A.6: $B^+ \to J/\psi K^+$ Yields for $p_T(K^-) > 4.0\text{GeV}/c$

	$c\tau(B^- \to J/\psi K^-)$[µm]	
$-\frac{\pi}{12} < \phi(K^-) \leq \frac{3\pi}{12}$	474	± 12
$\frac{3\pi}{12} < \phi(K^-) \leq \frac{7\pi}{12}$	529	± 12
$\frac{7\pi}{12} < \phi(K^-) \leq \frac{11\pi}{12}$	496	± 12
$\frac{11\pi}{12} < \phi(K^-) \leq \frac{15\pi}{12}$	508	± 14
$\frac{15\pi}{12} < \phi(K^-) \leq \frac{19\pi}{12}$	482	± 12
$\frac{19\pi}{12} < \phi(K^-) \leq \frac{23\pi}{12}$	493	± 13

Table A.7: $B^- \to J/\psi K^-$ Fitted Lifetime for $2.0\text{GeV}/c < p_T(K^-) \leq 3.0\text{GeV}/c$

	$c\tau(B^+ \to J/\psi K^+)$[µm]	
$-\frac{\pi}{12} < \phi(K^+) \leq \frac{3\pi}{12}$	475	± 11
$\frac{3\pi}{12} < \phi(K^+) \leq \frac{7\pi}{12}$	469	± 11
$\frac{7\pi}{12} < \phi(K^+) \leq \frac{11\pi}{12}$	486	± 12
$\frac{11\pi}{12} < \phi(K^+) \leq \frac{15\pi}{12}$	487	± 13
$\frac{15\pi}{12} < \phi(K^+) \leq \frac{19\pi}{12}$	514	± 14
$\frac{19\pi}{12} < \phi(K^+) \leq \frac{23\pi}{12}$	523	± 13

Table A.8: $B^+ \to J/\psi K^+$ Fitted Lifetime for $2.0\text{GeV}/c < p_T(K^+) \leq 3.0\text{GeV}/c$

	$c\tau(B^- \to J/\psi K^-)$[µm]	
$-\frac{\pi}{12} < \phi(K^-) \leq \frac{3\pi}{12}$	498	± 13
$\frac{3\pi}{12} < \phi(K^-) \leq \frac{7\pi}{12}$	510	± 14
$\frac{7\pi}{12} < \phi(K^-) \leq \frac{11\pi}{12}$	491	± 14
$\frac{11\pi}{12} < \phi(K^-) \leq \frac{15\pi}{12}$	453	± 13
$\frac{15\pi}{12} < \phi(K^-) \leq \frac{19\pi}{12}$	493	± 15
$\frac{19\pi}{12} < \phi(K^-) \leq \frac{23\pi}{12}$	480	± 13

Table A.9: $B^- \to J/\psi K^-$ Fitted Lifetime for $3.0\text{GeV}/c < p_T(K^-) \leq 4.0\text{GeV}/c$

	$c\tau(B^+ \to J/\psi K^+)$[μm]
$-\frac{\pi}{12} < \phi(K^+) \leq \frac{3\pi}{12}$	484 ± 13
$\frac{3\pi}{12} < \phi(K^+) \leq \frac{7\pi}{12}$	509 ± 14
$\frac{7\pi}{12} < \phi(K^+) \leq \frac{11\pi}{12}$	521 ± 14
$\frac{11\pi}{12} < \phi(K^+) \leq \frac{15\pi}{12}$	497 ± 14
$\frac{15\pi}{12} < \phi(K^+) \leq \frac{19\pi}{12}$	507 ± 15
$\frac{19\pi}{12} < \phi(K^+) \leq \frac{23\pi}{12}$	503 ± 14

Table A.10: $B^+ \to J/\psi K^+$ Fitted Lifetime for 3.0GeV/$c < p_T(K^+) \leq$ 4.0GeV/c

	$c\tau(B^- \to J/\psi K^-)$[μm]
$-\frac{\pi}{12} < \phi(K^-) \leq \frac{3\pi}{12}$	509 ± 9
$\frac{3\pi}{12} < \phi(K^-) \leq \frac{7\pi}{12}$	493 ± 9
$\frac{7\pi}{12} < \phi(K^-) \leq \frac{11\pi}{12}$	503 ± 9
$\frac{11\pi}{12} < \phi(K^-) \leq \frac{15\pi}{12}$	519 ± 10
$\frac{15\pi}{12} < \phi(K^-) \leq \frac{19\pi}{12}$	512 ± 10
$\frac{19\pi}{12} < \phi(K^-) \leq \frac{23\pi}{12}$	494 ± 9

Table A.11: $B^- \to J/\psi K^-$ Fitted Lifetime for $p_T(K^-) >$ 4.0GeV/c

	$c\tau(B^+ \to J/\psi K^+)$[μm]
$-\frac{\pi}{12} < \phi(K^+) \leq \frac{3\pi}{12}$	482 ± 8
$\frac{3\pi}{12} < \phi(K^+) \leq \frac{7\pi}{12}$	500 ± 9
$\frac{7\pi}{12} < \phi(K^+) \leq \frac{11\pi}{12}$	499 ± 9
$\frac{11\pi}{12} < \phi(K^+) \leq \frac{15\pi}{12}$	485 ± 9
$\frac{15\pi}{12} < \phi(K^+) \leq \frac{19\pi}{12}$	490 ± 10
$\frac{19\pi}{12} < \phi(K^+) \leq \frac{23\pi}{12}$	478 ± 8

Table A.12: $B^+ \to J/\psi K^+$ Fitted Lifetime for $p_T(K^+) >$ 4.0GeV/c

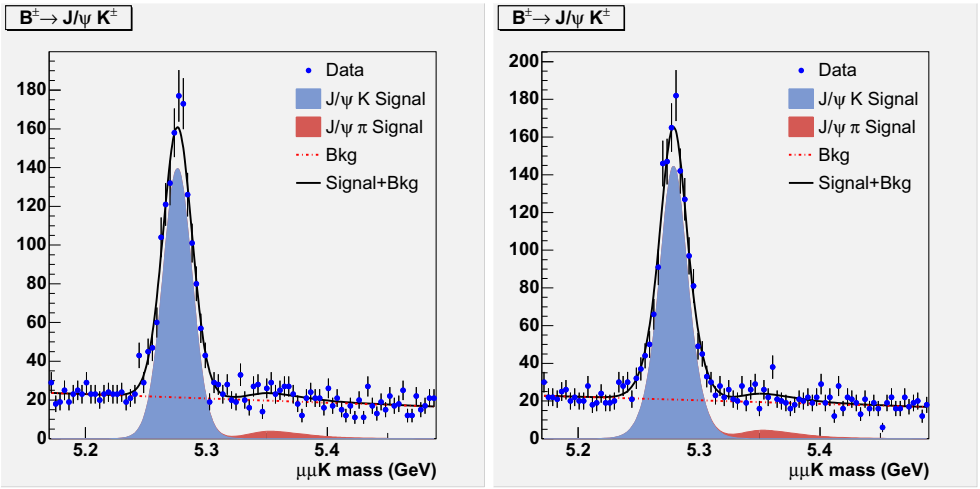

(a) $-\frac{\pi}{12} < \phi(K^-) \leq \frac{3\pi}{12}$ (b) $\frac{3\pi}{12} < \phi(K^-) \leq \frac{7\pi}{12}$

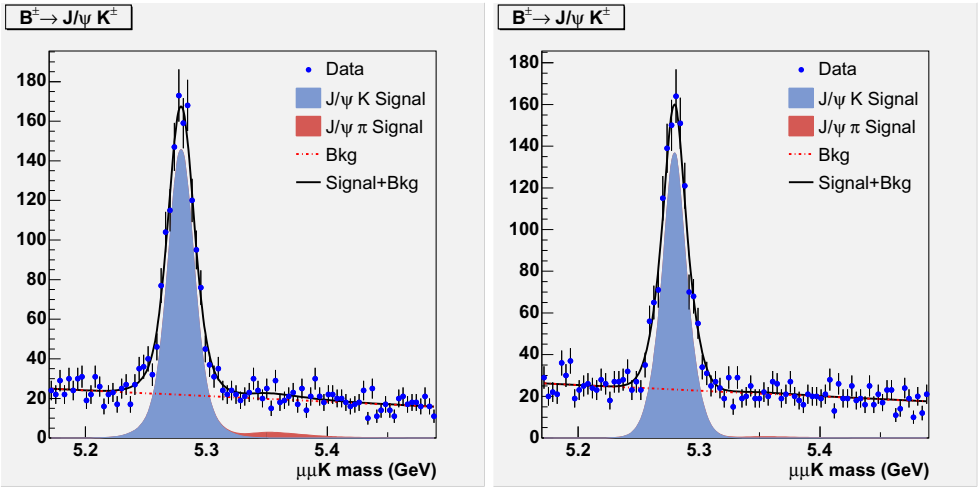

(c) $\frac{7\pi}{12} < \phi(K^-) \leq \frac{11\pi}{12}$ (d) $\frac{11\pi}{12} < \phi(K^-) \leq \frac{15\pi}{12}$

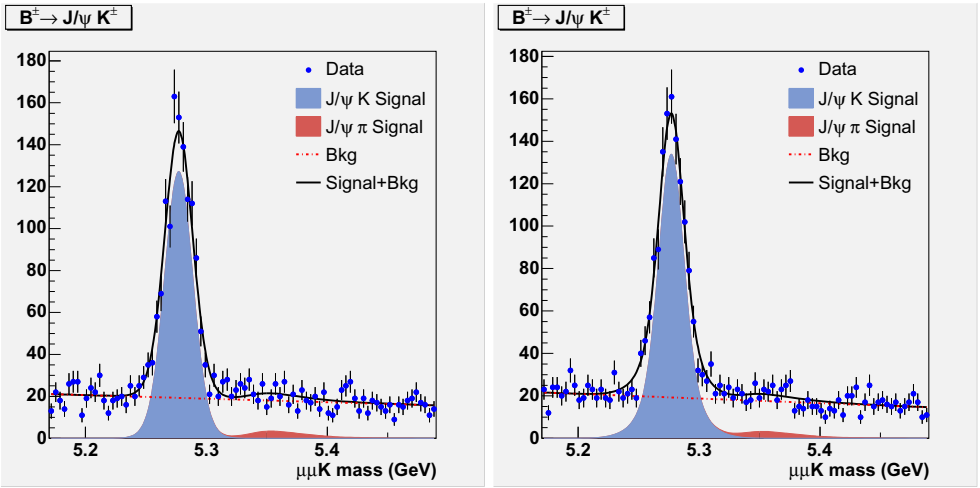

(e) $\frac{15\pi}{12} < \phi(K^-) \leq \frac{19\pi}{12}$ (f) $\frac{19\pi}{12} < \phi(K^-) \leq \frac{23\pi}{12}$

Figure A.14: $M(B^- \to J/\psi K^-), 2.0\text{GeV}/c < p_T(K^-) \leq 3.0\text{GeV}/c$

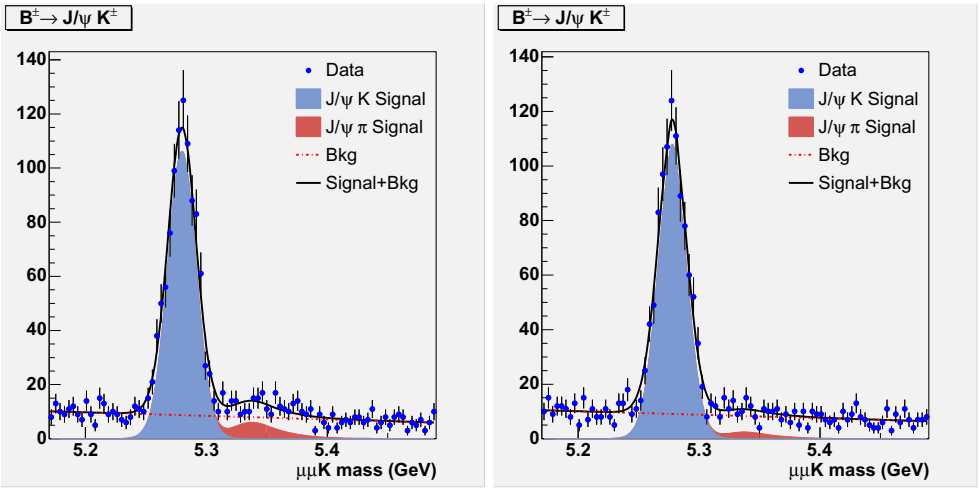

(a) $-\frac{\pi}{12} < \phi(K^+) \leq \frac{3\pi}{12}$ (b) $\frac{3\pi}{12} < \phi(K^+) \leq \frac{7\pi}{12}$

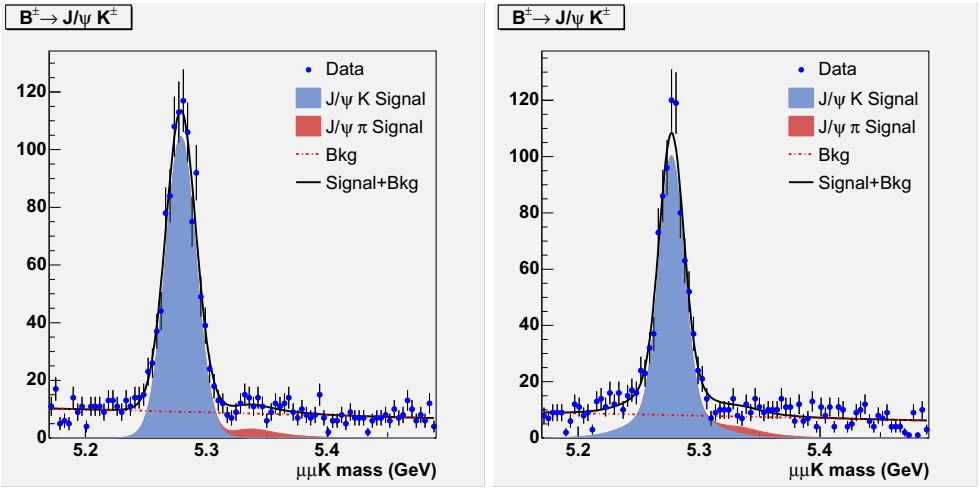

(c) $\frac{7\pi}{12} < \phi(K^+) \leq \frac{11\pi}{12}$ (d) $\frac{11\pi}{12} < \phi(K^+) \leq \frac{15\pi}{12}$

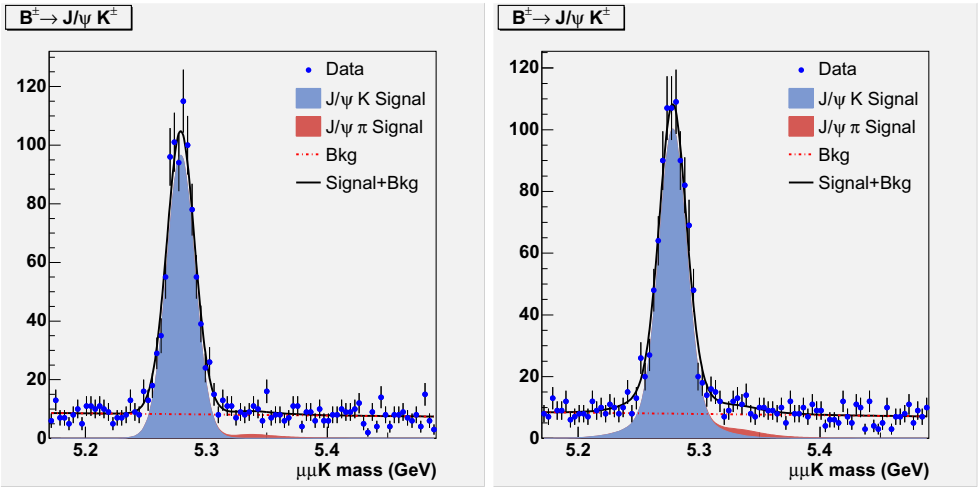

(e) $\frac{15\pi}{12} < \phi(K^+) \leq \frac{19\pi}{12}$ (f) $\frac{19\pi}{12} < \phi(K^+) \leq \frac{23\pi}{12}$

Figure A.15: $M(B^+ \to J/\psi K^+), 3.0\text{GeV}/c < p_T(K^+) \leq 4.0\text{GeV}/c$

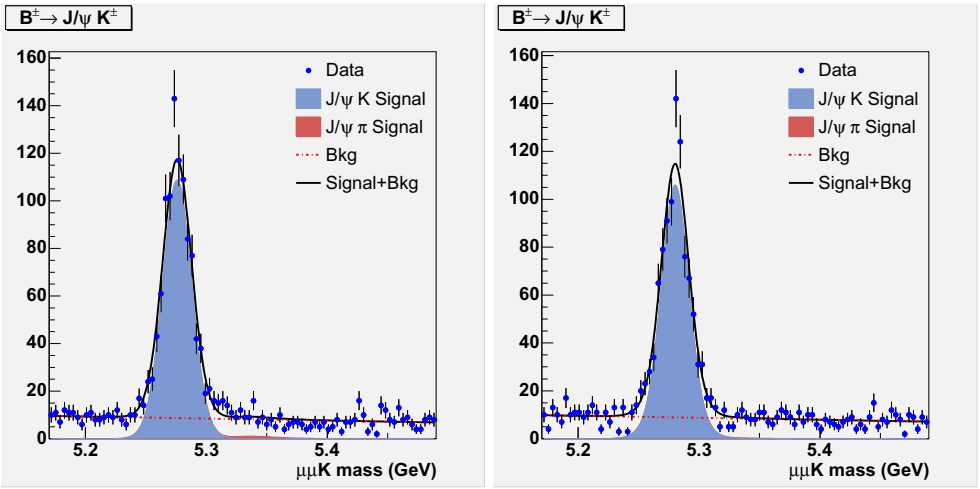

(a) $-\frac{\pi}{12} < \phi(K^-) \leq \frac{3\pi}{12}$ (b) $\frac{3\pi}{12} < \phi(K^-) \leq \frac{7\pi}{12}$

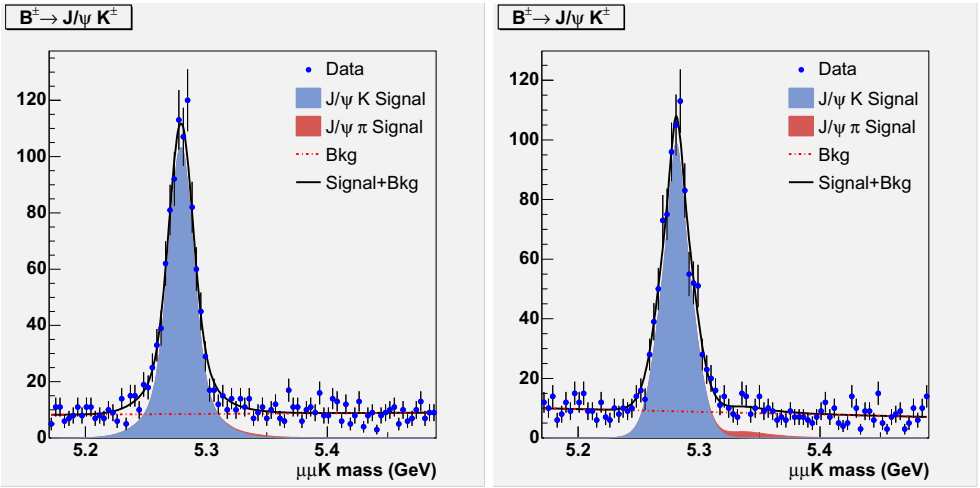

(c) $\frac{7\pi}{12} < \phi(K^-) \leq \frac{11\pi}{12}$ (d) $\frac{11\pi}{12} < \phi(K^-) \leq \frac{15\pi}{12}$

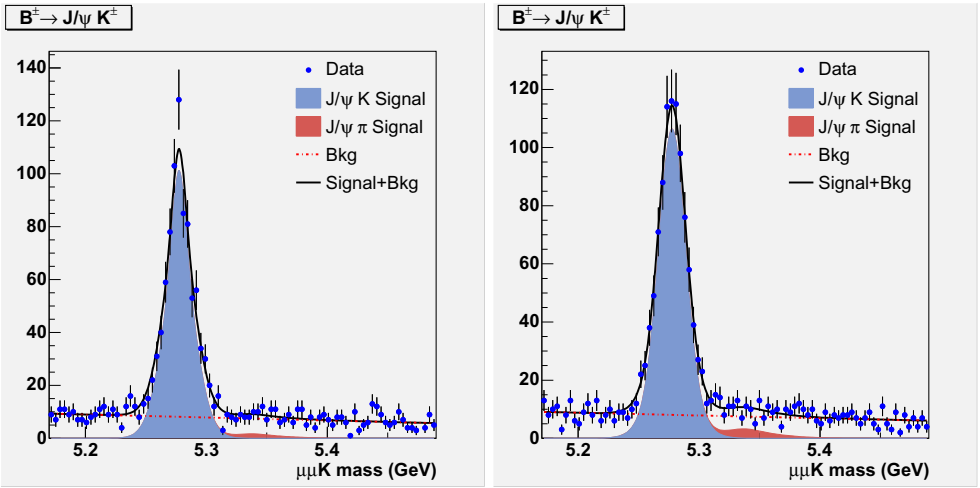

(e) $\frac{15\pi}{12} < \phi(K^-) \leq \frac{19\pi}{12}$ (f) $\frac{19\pi}{12} < \phi(K^-) \leq \frac{23\pi}{12}$

Figure A.16: $M(B^- \to J/\psi K^-), 3.0\text{GeV}/c < p_T(K^-) \leq 4.0\text{GeV}/c$

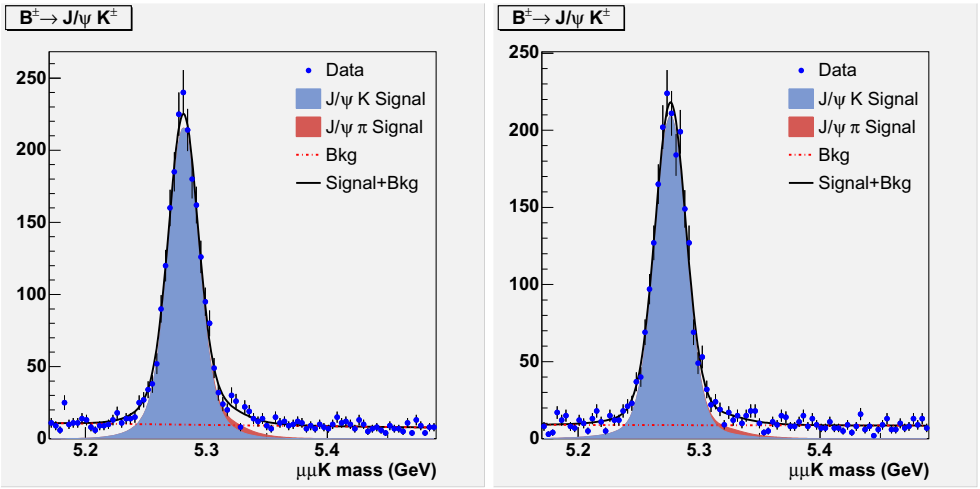

(a) $-\frac{\pi}{12} < \phi(K^+) \leq \frac{3\pi}{12}$ (b) $\frac{3\pi}{12} < \phi(K^+) \leq \frac{7\pi}{12}$

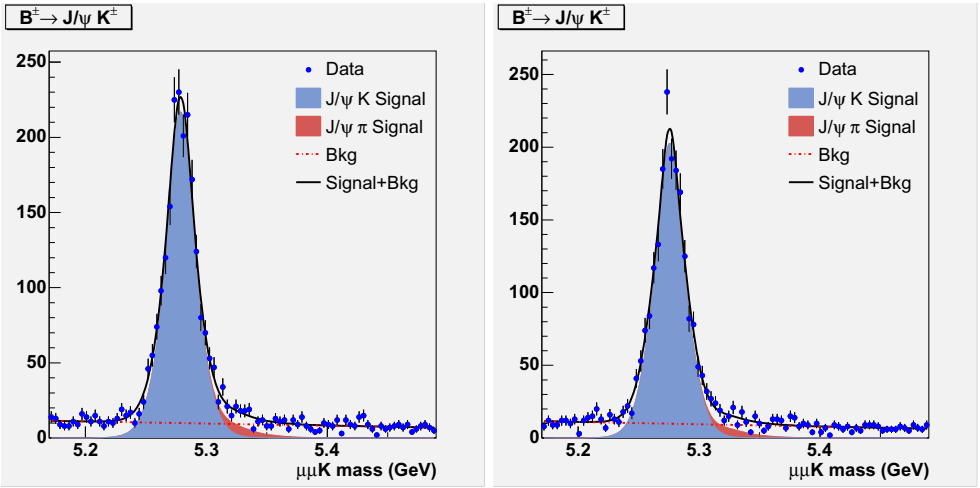

(c) $\frac{7\pi}{12} < \phi(K^+) \leq \frac{11\pi}{12}$ (d) $\frac{11\pi}{12} < \phi(K^+) \leq \frac{15\pi}{12}$

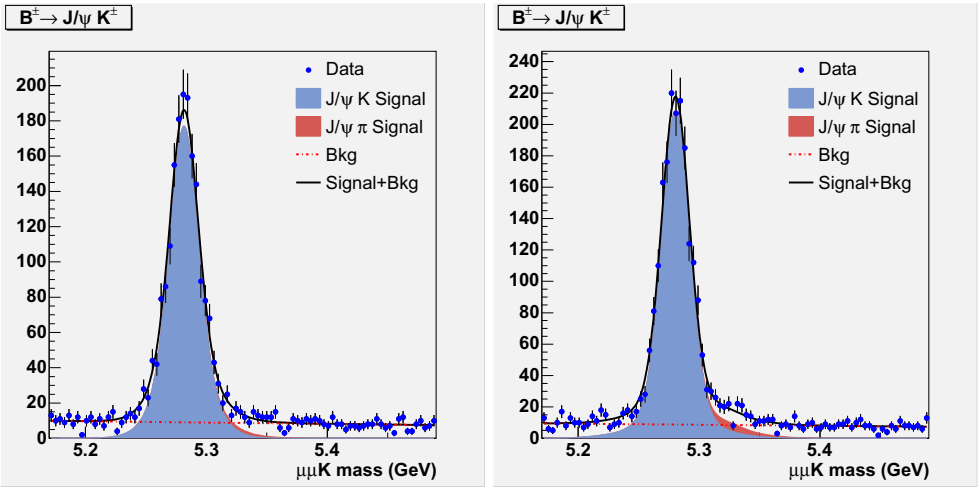

(e) $\frac{15\pi}{12} < \phi(K^+) \leq \frac{19\pi}{12}$ (f) $\frac{19\pi}{12} < \phi(K^+) \leq \frac{23\pi}{12}$

Figure A.17: $M(B^+ \to J/\psi K^+), p_T(K^+) \geq 4.0\text{GeV}/c$

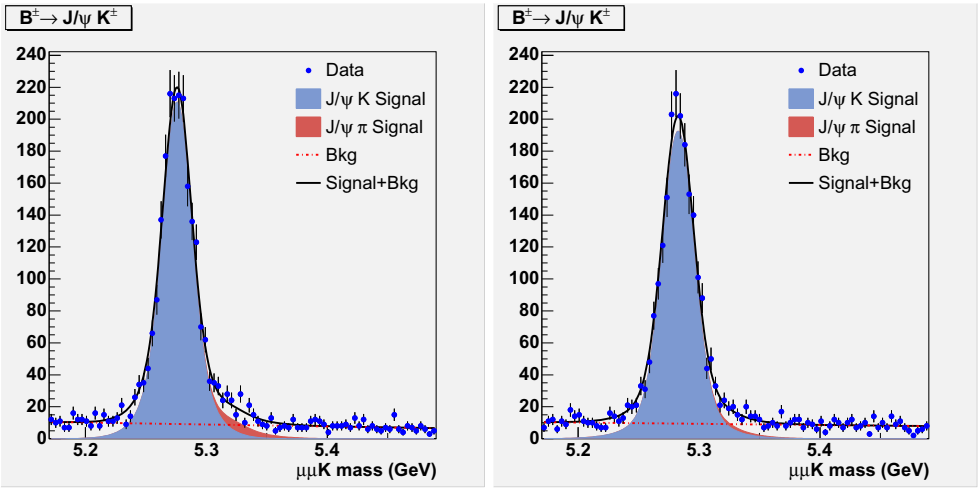

(a) $-\frac{\pi}{12} < \phi(K^-) \leq \frac{3\pi}{12}$ (b) $\frac{3\pi}{12} < \phi(K^-) \leq \frac{7\pi}{12}$

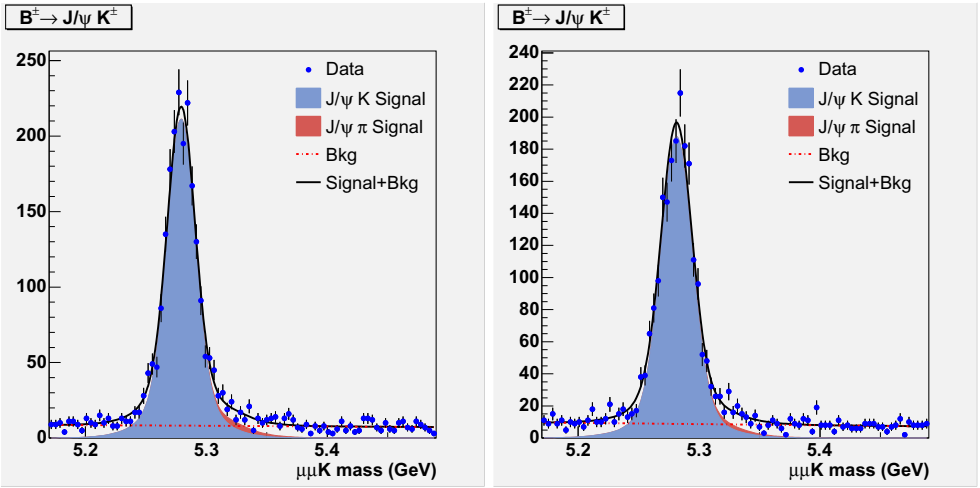

(c) $\frac{7\pi}{12} < \phi(K^-) \leq \frac{11\pi}{12}$ (d) $\frac{11\pi}{12} < \phi(K^-) \leq \frac{15\pi}{12}$

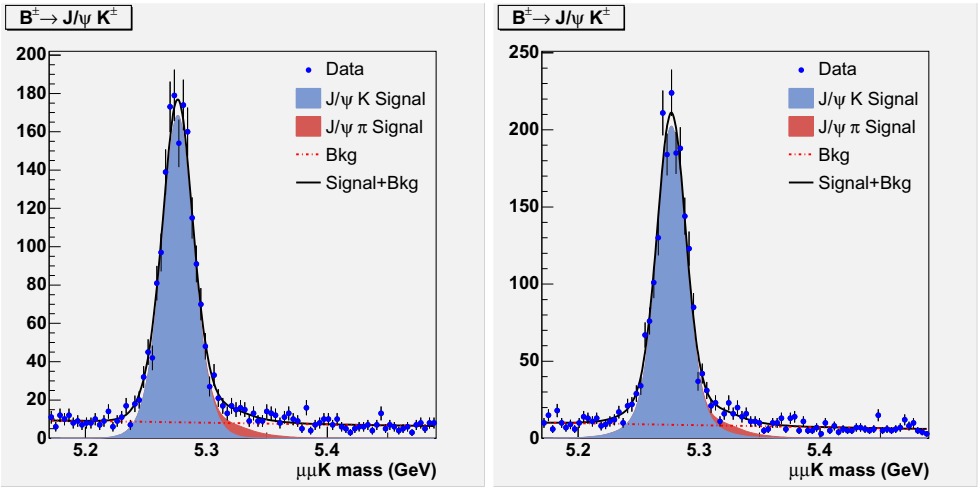

(e) $\frac{15\pi}{12} < \phi(K^-) \leq \frac{19\pi}{12}$ (f) $\frac{19\pi}{12} < \phi(K^-) \leq \frac{23\pi}{12}$

Figure A.18: $M(B^- \to J/\psi K^-), p_T(K^-) \geq 4.0\text{GeV}/c$

Appendix B

$D^{*+} \to D^0\pi^+, D^0 \to \mu^+K^-\nu_\mu$ Fits

B.1 Yields

Table B.1: $D^{*+} \to D^0\pi^+, D^0 \to \mu^+K^-\nu_\mu$ Yields

			D^{*+}		D^{*-}	
$p_T(K^-)\text{GeV}/c$	$\phi(K^-)$	$M(\mu^+K^-)\text{GeV}/c^2$	$N(D^{*+})$	N_{WS}^{fake}	$N(D^{*-})$	N_{WS}^{fake}
$[2.0, 3.0]$	$[-\frac{\pi}{12}, \frac{3\pi}{12}]$	$[1.2, 1.3]$	265 ± 16	36 ± 18	380 ± 26	38 ± 16
		$[1.3, 1.4]$	318 ± 26	11 ± 19	299 ± 25	23 ± 15
		$[1.4, 1.5]$	270 ± 17	43 ± 19	271 ± 25	24 ± 17
		$[1.5, 1.6]$	267 ± 25	51 ± 19	313 ± 24	40 ± 17
		$[1.6, 1.7]$	324 ± 28	45 ± 22	310 ± 27	60 ± 19
		$[1.7, 1.8]$	249 ± 11	44 ± 16	291 ± 16	7 ± 15
	$[\frac{3\pi}{12}, \frac{7\pi}{12}]$	$[1.2, 1.3]$	238 ± 9	54 ± 15	244 ± 9	62 ± 15
		$[1.3, 1.4]$	227 ± 27	75 ± 17	248 ± 20	24 ± 11
		$[1.4, 1.5]$	260 ± 15	10 ± 13	195 ± 12	59 ± 13
		$[1.5, 1.6]$	242 ± 19	38 ± 11	194 ± 18	41 ± 14
		$[1.6, 1.7]$	314 ± 17	79 ± 16	260 ± 21	82 ± 17
		$[1.7, 1.8]$	260 ± 14	33 ± 13	240 ± 20	48 ± 13
	$[\frac{7\pi}{12}, \frac{11\pi}{12}]$	$[1.2, 1.3]$	471 ± 19	75 ± 18	534 ± 26	34 ± 13
		$[1.3, 1.4]$	457 ± 21	130 ± 19	545 ± 19	62 ± 14
		$[1.4, 1.5]$	450 ± 25	94 ± 16	430 ± 23	62 ± 15
		$[1.5, 1.6]$	417 ± 22	72 ± 17	419 ± 24	83 ± 15
		$[1.6, 1.7]$	489 ± 15	107 ± 19	562 ± 27	92 ± 20
		$[1.7, 1.8]$	478 ± 24	62 ± 16	488 ± 25	94 ± 16
	$[\frac{11\pi}{12}, \frac{15\pi}{12}]$	$[1.2, 1.3]$	457 ± 29	47 ± 17	501 ± 19	57 ± 18
		$[1.3, 1.4]$	398 ± 18	45 ± 22	446 ± 27	7 ± 17

Continued on next page...

Table B.1 continued from previous page

			D^{*+}		D^{*-}	
$p_T(K^-)$GeV/c	$\phi(K^-)$	$M(\mu^+K^-)$GeV/c^2	$N(D^{*+})$	N_{WS}^{fake}	$N(D^{*-})$	N_{WS}^{fake}
		[1.4, 1.5]	411 ± 3	38 ± 18	406 ± 16	25 ± 13
		[1.5, 1.6]	386 ± 27	60 ± 22	395 ± 19	5 ± 17
		[1.6, 1.7]	438 ± 31	16 ± 22	458 ± 29	38 ± 19
		[1.7, 1.8]	380 ± 26	0 ± 9	522 ± 19	28 ± 19
	$[\frac{15\pi}{12}, \frac{19\pi}{12}]$	[1.2, 1.3]	366 ± 15	28 ± 15	335 ± 22	39 ± 16
		[1.3, 1.4]	287 ± 22	71 ± 17	344 ± 15	39 ± 12
		[1.4, 1.5]	267 ± 7	33 ± 12	309 ± 29	67 ± 15
		[1.5, 1.6]	341 ± 21	23 ± 14	259 ± 14	62 ± 14
		[1.6, 1.7]	344 ± 24	63 ± 16	369 ± 22	45 ± 16
		[1.7, 1.8]	275 ± 21	95 ± 15	318 ± 20	74 ± 14
	$[\frac{19\pi}{12}, \frac{23\pi}{12}]$	[1.2, 1.3]	518 ± 26	153 ± 19	595 ± 17	129 ± 19
		[1.3, 1.4]	617 ± 27	154 ± 20	626 ± 26	118 ± 17
		[1.4, 1.5]	585 ± 26	137 ± 19	541 ± 25	91 ± 15
		[1.5, 1.6]	623 ± 26	129 ± 19	538 ± 17	112 ± 19
		[1.6, 1.7]	612 ± 29	143 ± 21	634 ± 28	107 ± 18
		[1.7, 1.8]	609 ± 26	141 ± 19	603 ± 26	114 ± 18
[3.0, 4.0]	$[-\frac{\pi}{12}, \frac{3\pi}{12}]$	[1.2, 1.3]	457 ± 29	47 ± 17	501 ± 19	57 ± 18
		[1.3, 1.4]	398 ± 18	45 ± 22	446 ± 27	7 ± 17
		[1.4, 1.5]	411 ± 3	38 ± 18	406 ± 16	25 ± 13
		[1.5, 1.6]	386 ± 27	60 ± 22	395 ± 19	5 ± 17
		[1.6, 1.7]	438 ± 31	16 ± 22	458 ± 29	38 ± 19
		[1.7, 1.8]	380 ± 26	0 ± 9	522 ± 19	28 ± 19
	$[\frac{3\pi}{12}, \frac{7\pi}{12}]$	[1.2, 1.3]	366 ± 15	28 ± 15	335 ± 22	39 ± 16
		[1.3, 1.4]	287 ± 22	71 ± 17	344 ± 15	39 ± 12
		[1.4, 1.5]	267 ± 7	33 ± 12	309 ± 29	67 ± 15
		[1.5, 1.6]	341 ± 21	23 ± 14	259 ± 14	62 ± 14
		[1.6, 1.7]	344 ± 24	63 ± 16	369 ± 22	45 ± 16
		[1.7, 1.8]	275 ± 21	95 ± 15	318 ± 20	74 ± 14
	$[\frac{7\pi}{12}, \frac{11\pi}{12}]$	[1.2, 1.3]	518 ± 26	153 ± 19	595 ± 17	129 ± 19
		[1.3, 1.4]	617 ± 27	154 ± 20	626 ± 26	118 ± 17
		[1.4, 1.5]	585 ± 26	137 ± 19	541 ± 25	91 ± 15

Continued on next page...

Table B.1 continued from previous page

			D^{*+}		D^{*-}	
$p_T(K^-)$GeV/c	$\phi(K^-)$	$M(\mu^+K^-)$GeV/c^2	$N(D^{*+})$	N_{WS}^{fake}	$N(D^{*-})$	N_{WS}^{fake}
		[1.5, 1.6]	623 ± 26	129 ± 19	538 ± 17	112 ± 19
		[1.6, 1.7]	612 ± 29	143 ± 21	634 ± 28	107 ± 18
		[1.7, 1.8]	609 ± 26	141 ± 19	603 ± 26	114 ± 18
	$[\frac{11\pi}{12}, \frac{15\pi}{12}]$	[1.2, 1.3]	506 ± 30	94 ± 22	617 ± 21	47 ± 21
		[1.3, 1.4]	588 ± 30	78 ± 22	585 ± 21	65 ± 19
		[1.4, 1.5]	489 ± 26	84 ± 20	541 ± 28	0 ± 52
		[1.5, 1.6]	544 ± 20	55 ± 18	577 ± 20	17 ± 18
		[1.6, 1.7]	662 ± 8	21 ± 24	588 ± 42	11 ± 21
		[1.7, 1.8]	529 ± 29	48 ± 17	650 ± 31	10 ± 18
	$[\frac{15\pi}{12}, \frac{19\pi}{12}]$	[1.2, 1.3]	409 ± 13	101 ± 17	449 ± 16	73 ± 15
		[1.3, 1.4]	387 ± 23	80 ± 17	386 ± 22	60 ± 15
		[1.4, 1.5]	382 ± 15	97 ± 16	342 ± 21	86 ± 14
		[1.5, 1.6]	318 ± 21	85 ± 15	398 ± 21	32 ± 13
		[1.6, 1.7]	418 ± 24	97 ± 17	439 ± 16	98 ± 15
		[1.7, 1.8]	374 ± 14	60 ± 13	347 ± 22	112 ± 17
	$[\frac{19\pi}{12}, \frac{23\pi}{12}]$	[1.2, 1.3]	655 ± 28	151 ± 19	755 ± 20	143 ± 18
		[1.3, 1.4]	773 ± 20	149 ± 18	686 ± 27	153 ± 18
		[1.4, 1.5]	684 ± 28	177 ± 20	609 ± 18	116 ± 17
		[1.5, 1.6]	678 ± 27	140 ± 17	651 ± 26	143 ± 18
		[1.6, 1.7]	842 ± 29	191 ± 20	692 ± 28	176 ± 20
		[1.7, 1.8]	685 ± 27	174 ± 20	752 ± 28	118 ± 17
[4.0, 100.0]	$[-\frac{\pi}{12}, \frac{3\pi}{12}]$	[1.2, 1.3]	506 ± 30	94 ± 22	617 ± 21	47 ± 21
		[1.3, 1.4]	588 ± 30	78 ± 22	585 ± 21	65 ± 19
		[1.4, 1.5]	489 ± 26	84 ± 20	541 ± 28	0 ± 52
		[1.5, 1.6]	544 ± 20	55 ± 18	577 ± 20	17 ± 18
		[1.6, 1.7]	662 ± 8	21 ± 24	588 ± 42	11 ± 21
		[1.7, 1.8]	529 ± 29	48 ± 17	650 ± 31	10 ± 18
	$[\frac{3\pi}{12}, \frac{7\pi}{12}]$	[1.2, 1.3]	409 ± 13	101 ± 17	449 ± 16	73 ± 15
		[1.3, 1.4]	387 ± 23	80 ± 17	386 ± 22	60 ± 15
		[1.4, 1.5]	382 ± 15	97 ± 16	342 ± 21	86 ± 14
		[1.5, 1.6]	318 ± 21	85 ± 15	398 ± 21	32 ± 13

Continued on next page...

Table B.1 continued from previous page

			D^{*+}		D^{*-}	
$p_T(K^-)$GeV/c	$\phi(K^-)$	$M(\mu^+K^-)$GeV/c^2	$N(D^{*+})$	N_{WS}^{fake}	$N(D^{*-})$	N_{WS}^{fake}
		[1.6, 1.7]	418 ± 24	97 ± 17	439 ± 16	98 ± 15
		[1.7, 1.8]	374 ± 14	60 ± 13	347 ± 22	112 ± 17
	$[\frac{7\pi}{12}, \frac{11\pi}{12}]$	[1.2, 1.3]	655 ± 28	151 ± 19	755 ± 20	143 ± 18
		[1.3, 1.4]	773 ± 20	149 ± 18	686 ± 27	153 ± 18
		[1.4, 1.5]	684 ± 28	177 ± 20	609 ± 18	116 ± 17
		[1.5, 1.6]	678 ± 27	140 ± 17	651 ± 26	143 ± 18
		[1.6, 1.7]	842 ± 29	191 ± 20	692 ± 28	176 ± 20
		[1.7, 1.8]	685 ± 27	174 ± 20	752 ± 28	118 ± 17
	$[\frac{11\pi}{12}, \frac{15\pi}{12}]$	[1.2, 1.3]	683 ± 31	99 ± 19	733 ± 31	59 ± 18
		[1.3, 1.4]	666 ± 30	109 ± 19	682 ± 21	48 ± 19
		[1.4, 1.5]	627 ± 29	61 ± 19	596 ± 28	12 ± 16
		[1.5, 1.6]	628 ± 20	23 ± 17	644 ± 29	39 ± 17
		[1.6, 1.7]	771 ± 8	76 ± 23	703 ± 31	140 ± 22
		[1.7, 1.8]	673 ± 30	83 ± 19	745 ± 30	23 ± 17
	$[\frac{15\pi}{12}, \frac{19\pi}{12}]$	[1.2, 1.3]	443 ± 23	118 ± 16	485 ± 16	76 ± 15
		[1.3, 1.4]	494 ± 23	74 ± 16	375 ± 31	116 ± 15
		[1.4, 1.5]	370 ± 22	74 ± 15	364 ± 7	56 ± 14
		[1.5, 1.6]	325 ± 14	110 ± 15	414 ± 15	49 ± 12
		[1.6, 1.7]	473 ± 16	113 ± 18	520 ± 25	78 ± 15
		[1.7, 1.8]	408 ± 14	61 ± 13	449 ± 16	92 ± 14
	$[\frac{19\pi}{12}, \frac{23\pi}{12}]$	[1.2, 1.3]	831 ± 20	202 ± 19	792 ± 27	154 ± 17
		[1.3, 1.4]	758 ± 20	198 ± 19	767 ± 28	177 ± 18
		[1.4, 1.5]	725 ± 19	149 ± 16	723 ± 26	112 ± 16
		[1.5, 1.6]	718 ± 26	192 ± 18	809 ± 27	143 ± 17
		[1.6, 1.7]	884 ± 21	242 ± 22	902 ± 31	236 ± 21
		[1.7, 1.8]	740 ± 27	162 ± 18	860 ± 29	126 ± 16

B.2 RS Fits

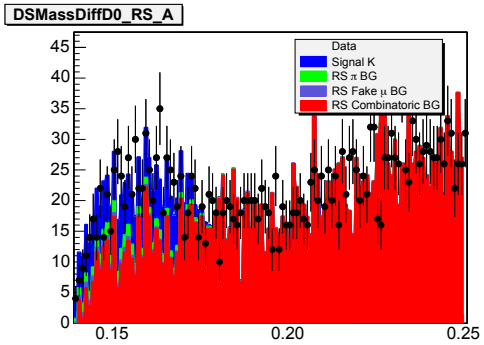

(a) $1.2 < M(\mu^+K^-) \leq 1.3$

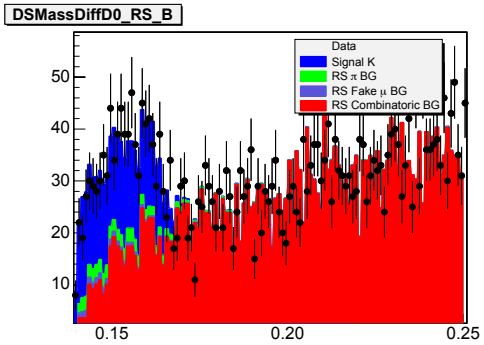

(b) $1.3 < M(\mu^+K^-) \leq 1.4$

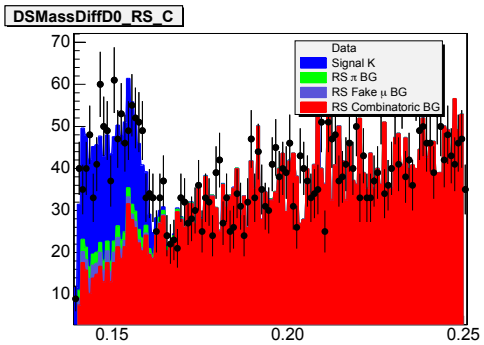

(c) $1.4 < M(\mu^+K^-) \leq 1.5$

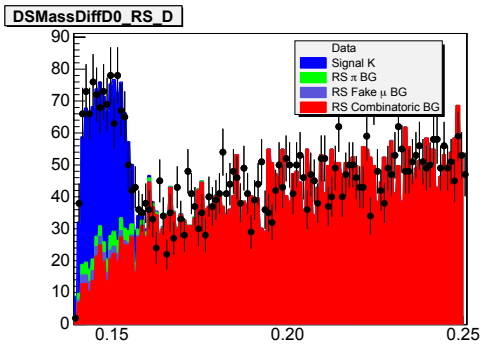

(d) $1.5 < M(\mu^+K^-) \leq 1.6$

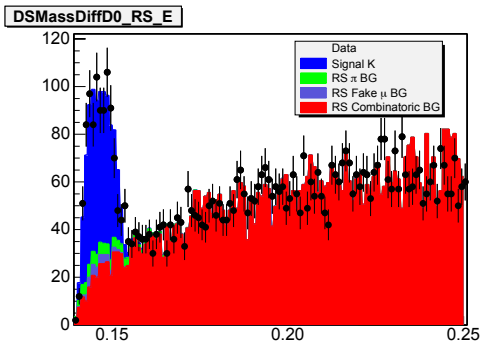

(e) $1.6 < M(\mu^+K^-) \leq 1.7$

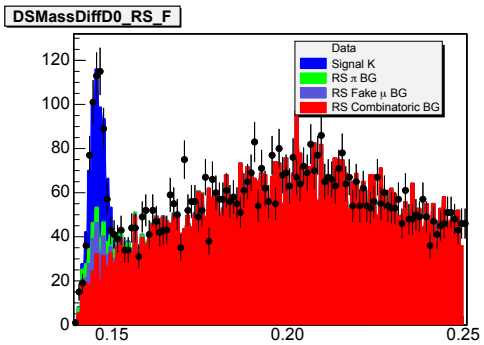

(f) $1.7 < M(\mu^+K^-) \leq 1.8$

Figure B.1: $D^{*+} Fits : \delta(M(\mu K\pi), M(\mu K)), 2.0\text{GeV}/c < p_T(K^-) \leq 3.0\text{GeV}/c$, $-\frac{\pi}{12} < \phi(K^-) \leq \frac{3\pi}{12}$

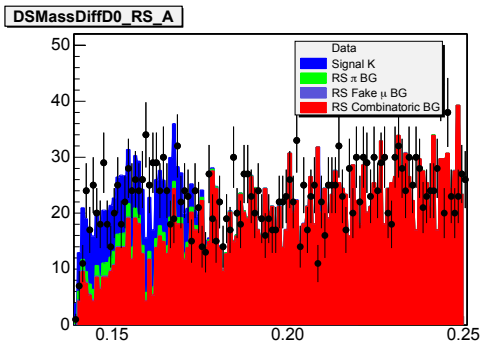

(a) $1.2 < M(\mu^+K^-) \leq 1.3$

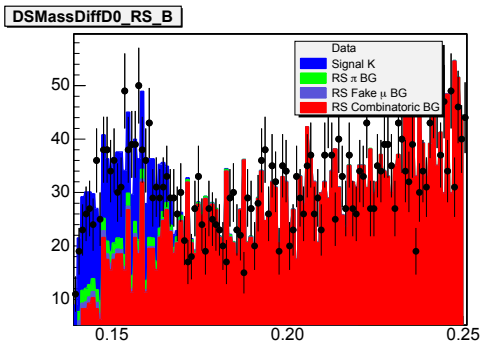

(b) $1.3 < M(\mu^+K^-) \leq 1.4$

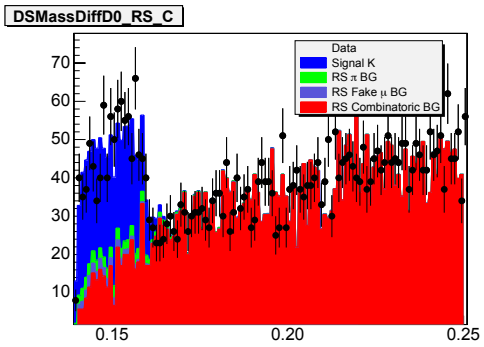

(c) $1.4 < M(\mu^+K^-) \leq 1.5$

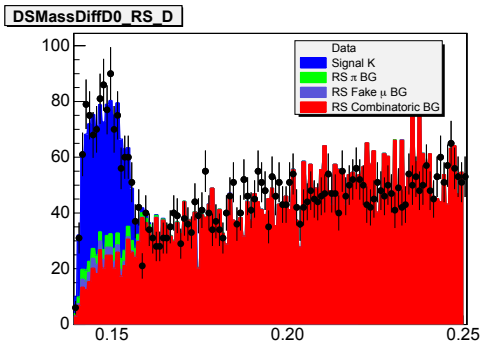

(d) $1.5 < M(\mu^+K^-) \leq 1.6$

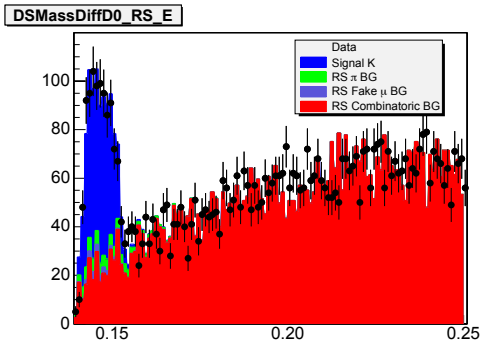

(e) $1.6 < M(\mu^+K^-) \leq 1.7$

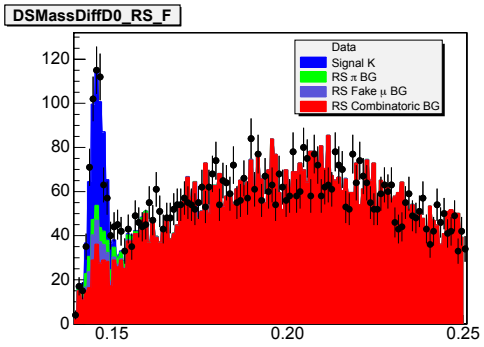

(f) $1.7 < M(\mu^+K^-) \leq 1.8$

Figure B.2: $D^{*+} Fits : \delta(M(\mu K\pi), M(\mu K)), 2.0\text{GeV}/c < p_T(K^-) \leq 3.0\text{GeV}/c$, $\frac{3\pi}{12} < \phi(K^-) \leq \frac{7\pi}{12}$

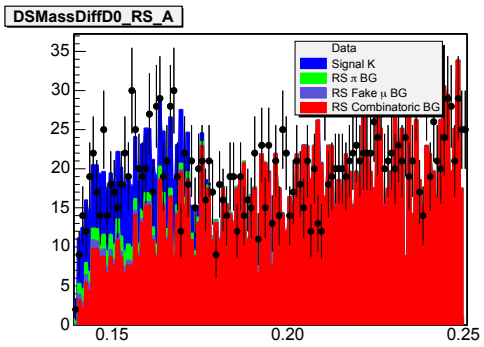

(a) $1.2 < M(\mu^+K^-) \leq 1.3$

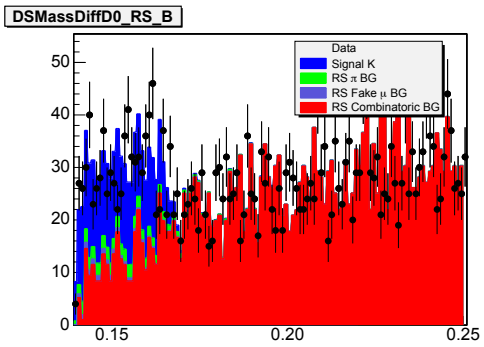

(b) $1.3 < M(\mu^+K^-) \leq 1.4$

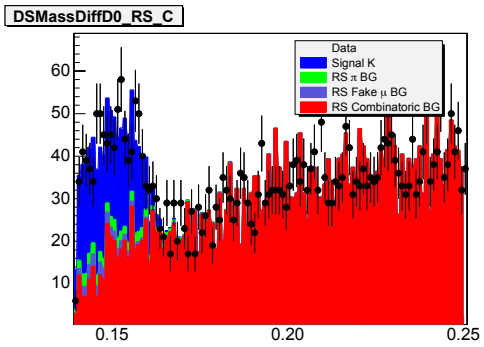

(c) $1.4 < M(\mu^+K^-) \leq 1.5$

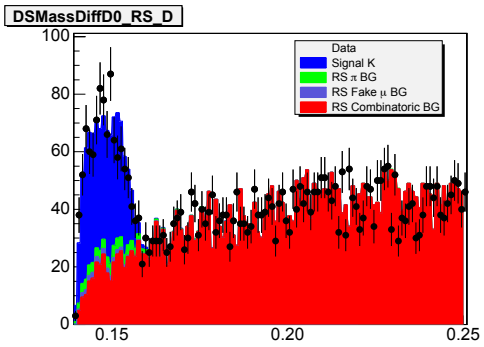

(d) $1.5 < M(\mu^+K^-) \leq 1.6$

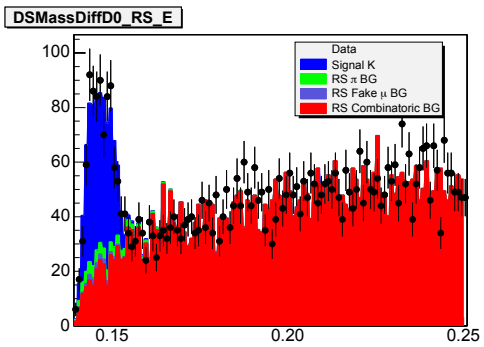

(e) $1.6 < M(\mu^+K^-) \leq 1.7$

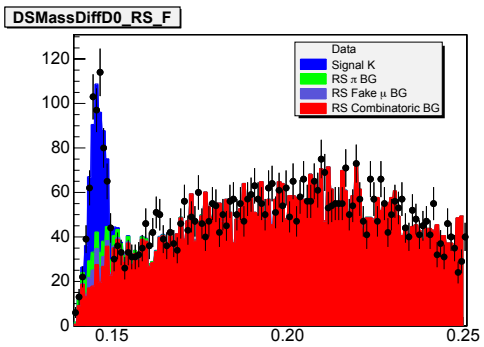

(f) $1.7 < M(\mu^+K^-) \leq 1.8$

Figure B.3: $D^{*+} Fits : \delta(M(\mu K\pi), M(\mu K)), 2.0\text{GeV}/c < p_T(K^-) \leq 3.0\text{GeV}/c$, $\frac{7\pi}{12} < \phi(K^-) \leq \frac{11\pi}{12}$

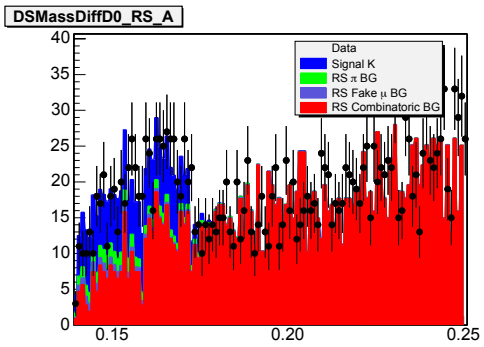

(a) $1.2 < M(\mu^+K^-) \leq 1.3$

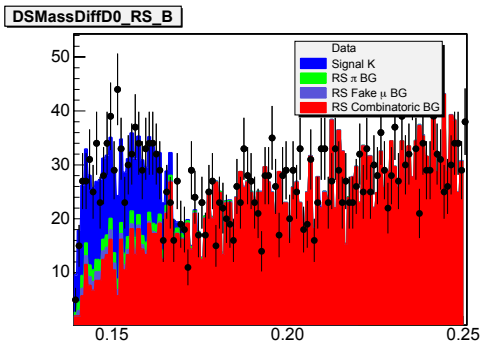

(b) $1.3 < M(\mu^+K^-) \leq 1.4$

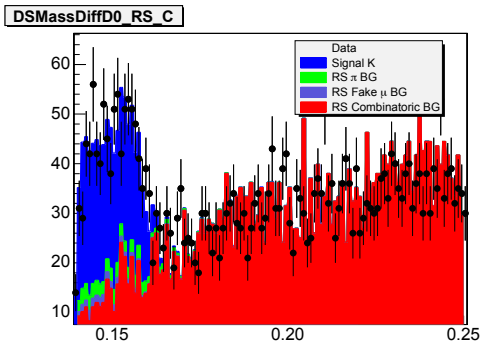

(c) $1.4 < M(\mu^+K^-) \leq 1.5$

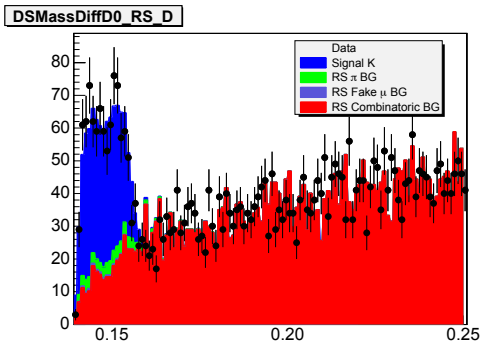

(d) $1.5 < M(\mu^+K^-) \leq 1.6$

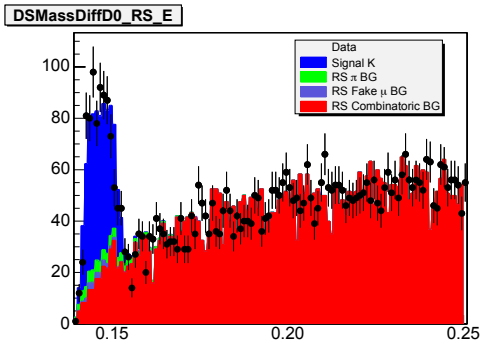

(e) $1.6 < M(\mu^+K^-) \leq 1.7$

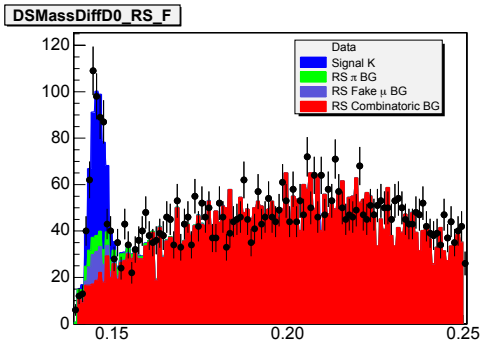

(f) $1.7 < M(\mu^+K^-) \leq 1.8$

Figure B.4: $D^{*+}Fits : \delta(M(\mu K\pi), M(\mu K)), 2.0\text{GeV}/c < p_T(K^-) \leq 3.0\text{GeV}/c$, $\frac{11\pi}{12} < \phi(K^-) \leq \frac{15\pi}{12}$

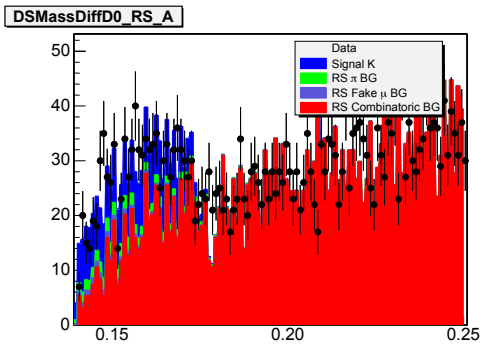

(a) $1.2 < M(\mu^+K^-) \leq 1.3$

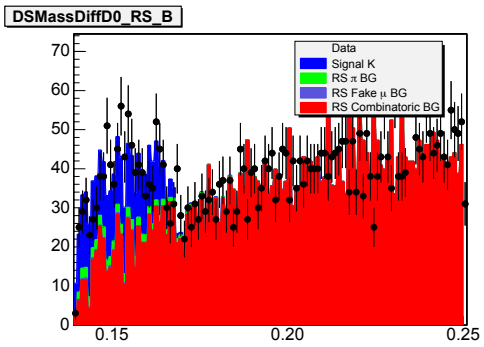

(b) $1.3 < M(\mu^+K^-) \leq 1.4$

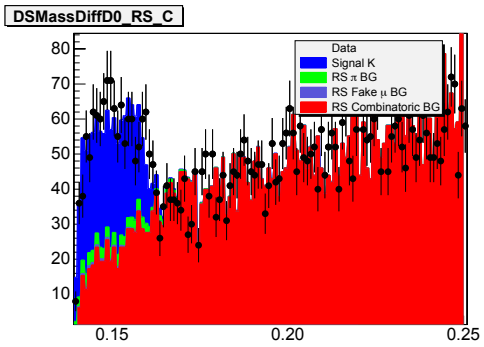

(c) $1.4 < M(\mu^+K^-) \leq 1.5$

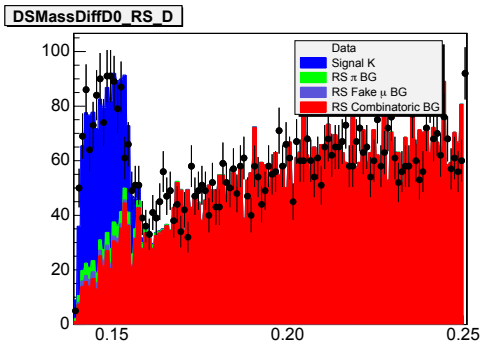

(d) $1.5 < M(\mu^+K^-) \leq 1.6$

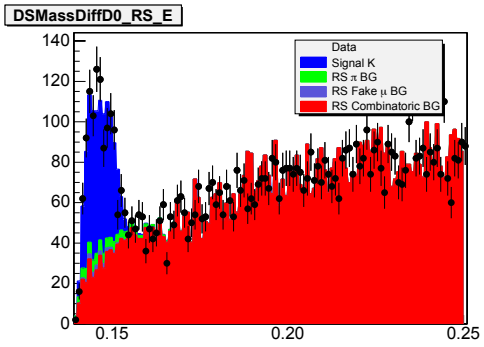

(e) $1.6 < M(\mu^+K^-) \leq 1.7$

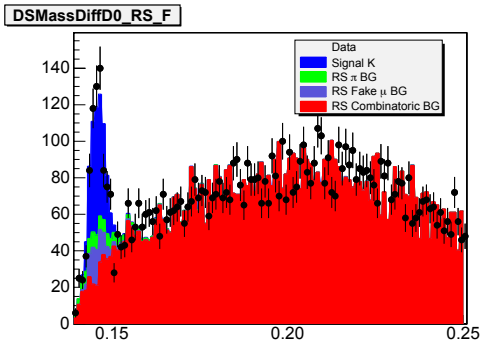

(f) $1.7 < M(\mu^+K^-) \leq 1.8$

Figure B.5: $D^{*+}Fits : \delta(M(\mu K\pi), M(\mu K)), 2.0\text{GeV}/c < p_T(K^-) \leq 3.0\text{GeV}/c$, $\frac{15\pi}{12} < \phi(K^-) \leq \frac{19\pi}{12}$

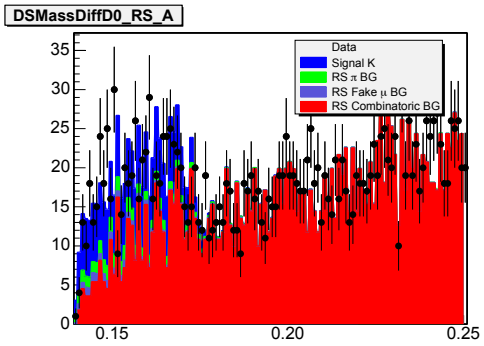

(a) $1.2 < M(\mu^+K^-) \leq 1.3$

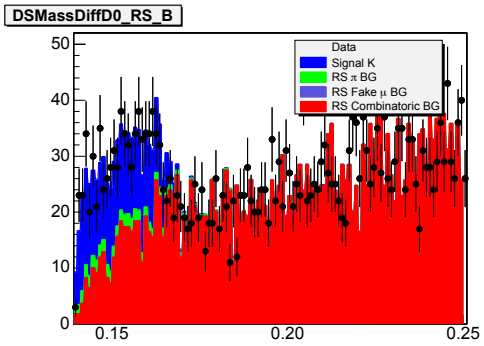

(b) $1.3 < M(\mu^+K^-) \leq 1.4$

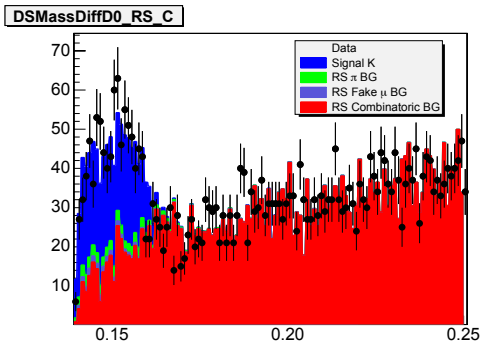

(c) $1.4 < M(\mu^+K^-) \leq 1.5$

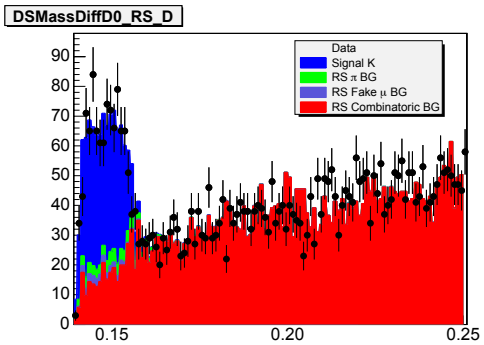

(d) $1.5 < M(\mu^+K^-) \leq 1.6$

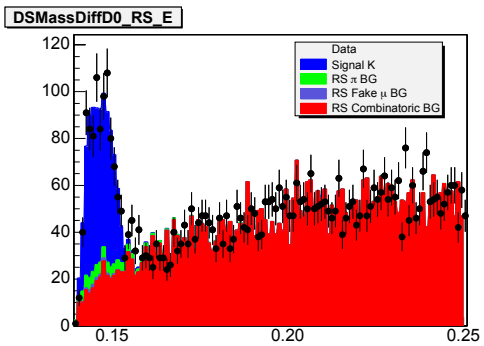

(e) $1.6 < M(\mu^+K^-) \leq 1.7$

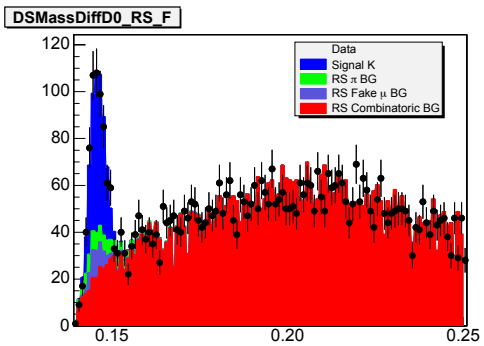

(f) $1.7 < M(\mu^+K^-) \leq 1.8$

Figure B.6: $D^{*+} Fits : \delta(M(\mu K\pi), M(\mu K)), 2.0\text{GeV}/c < p_T(K^-) \leq 3.0\text{GeV}/c$, $\frac{19\pi}{12} < \phi(K^-) \leq \frac{23\pi}{12}$

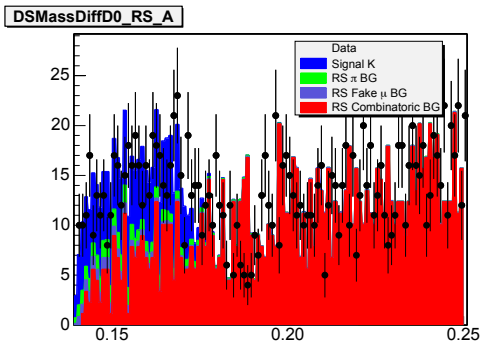

(a) $1.2 < M(\mu^+K^-) \leq 1.3$

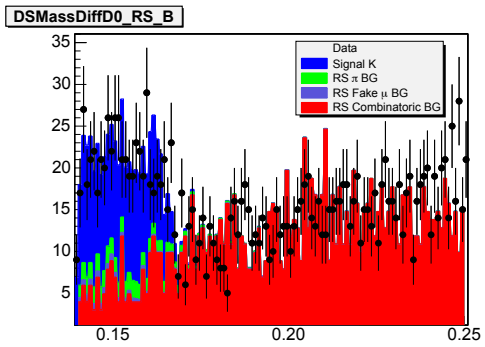

(b) $1.3 < M(\mu^+K^-) \leq 1.4$

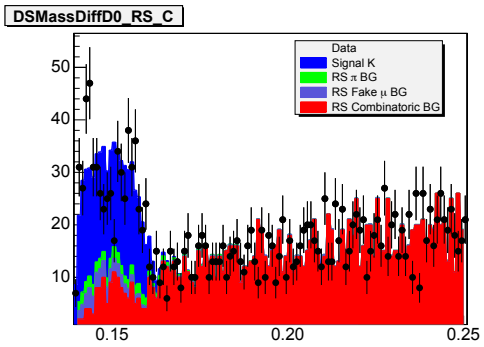

(c) $1.4 < M(\mu^+K^-) \leq 1.5$

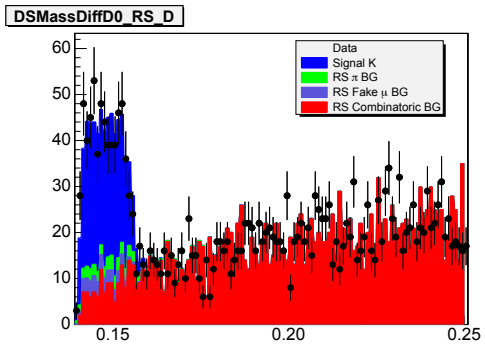

(d) $1.5 < M(\mu^+K^-) \leq 1.6$

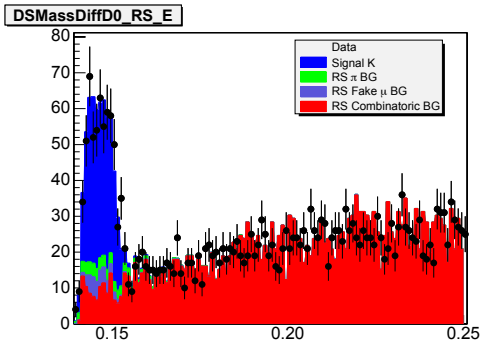

(e) $1.6 < M(\mu^+K^-) \leq 1.7$

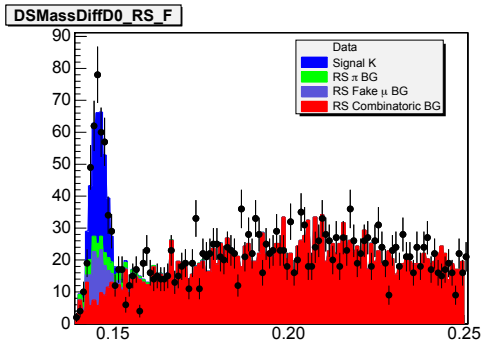

(f) $1.7 < M(\mu^+K^-) \leq 1.8$

Figure B.7: $D^{*+} Fits : \delta(M(\mu K\pi), M(\mu K)), 3.0\text{GeV}/c < p_T(K^-) \leq 4.0\text{GeV}/c, -\frac{\pi}{12} < \phi(K^-) \leq \frac{3\pi}{12}$

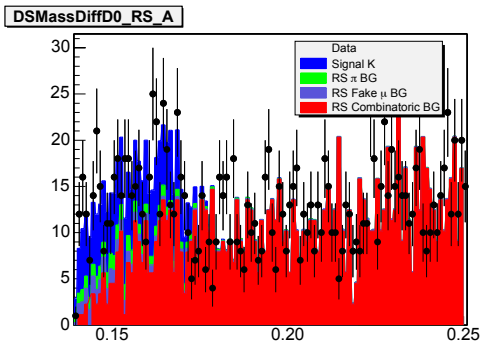

(a) $1.2 < M(\mu^+K^-) \leq 1.3$

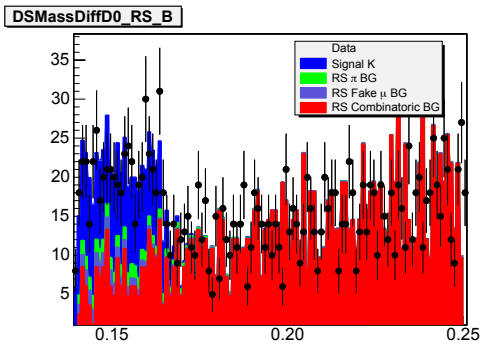

(b) $1.3 < M(\mu^+K^-) \leq 1.4$

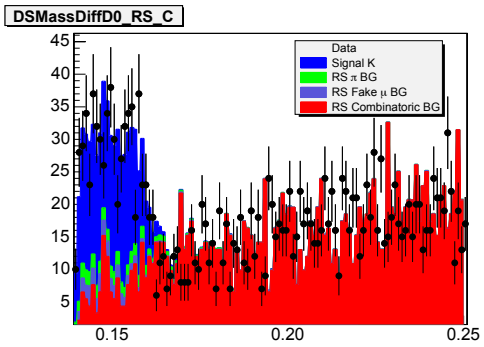

(c) $1.4 < M(\mu^+K^-) \leq 1.5$

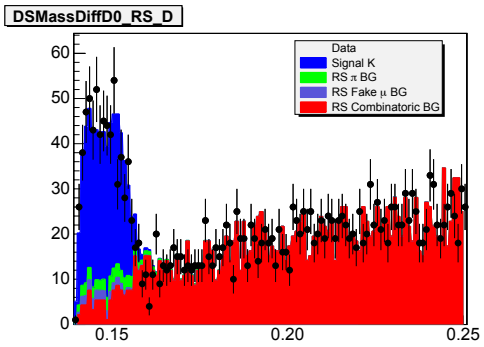

(d) $1.5 < M(\mu^+K^-) \leq 1.6$

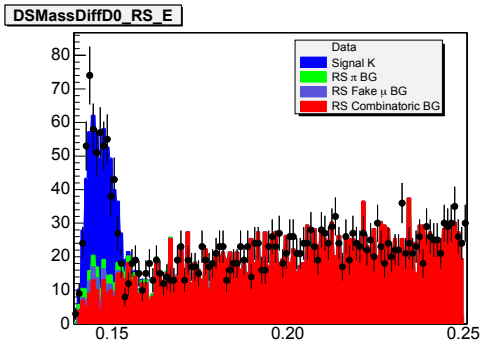

(e) $1.6 < M(\mu^+K^-) \leq 1.7$

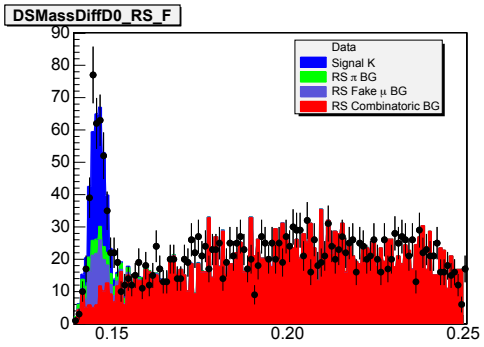

(f) $1.7 < M(\mu^+K^-) \leq 1.8$

Figure B.8: $D^{*+} Fits : \delta(M(\mu K\pi), M(\mu K)), 3.0\text{GeV}/c < p_T(K^-) \leq 4.0\text{GeV}/c$, $\frac{3\pi}{12} < \phi(K^-) \leq \frac{7\pi}{12}$

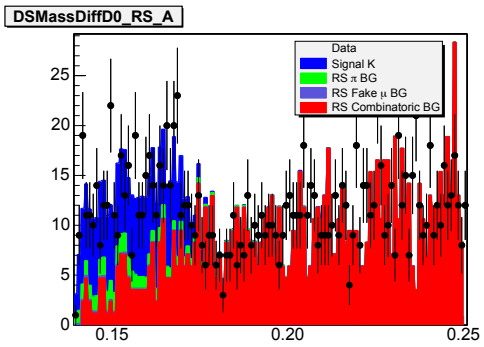

(a) $1.2 < M(\mu^+K^-) \leq 1.3$

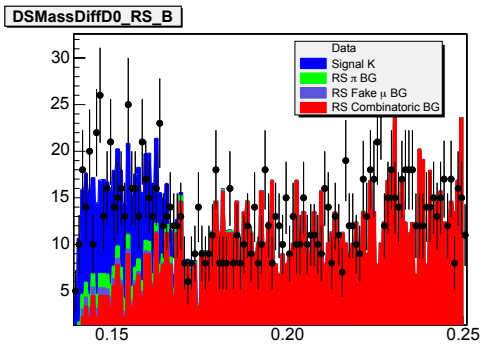

(b) $1.3 < M(\mu^+K^-) \leq 1.4$

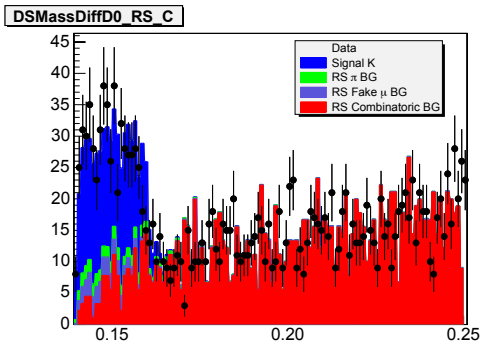

(c) $1.4 < M(\mu^+K^-) \leq 1.5$

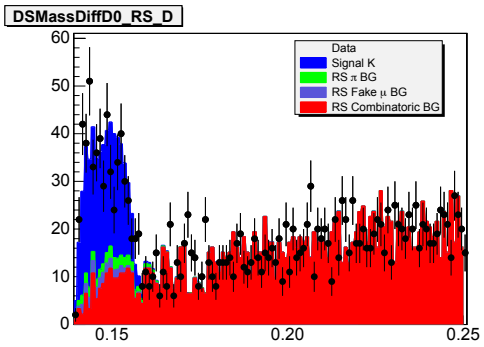

(d) $1.5 < M(\mu^+K^-) \leq 1.6$

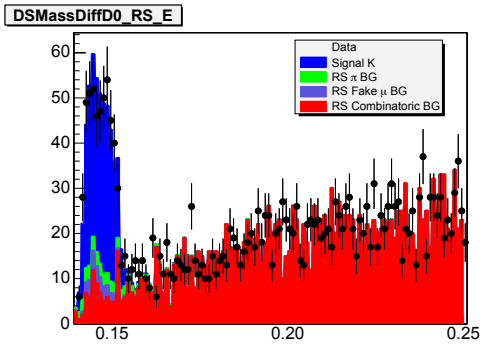

(e) $1.6 < M(\mu^+K^-) \leq 1.7$

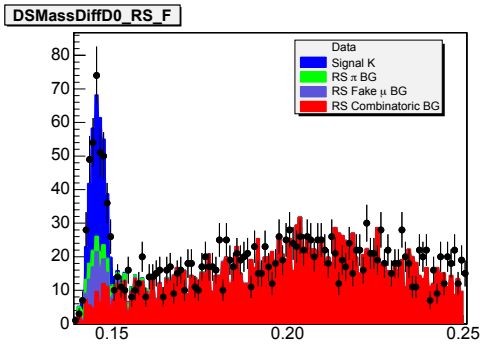

(f) $1.7 < M(\mu^+K^-) \leq 1.8$

Figure B.9: $D^{*+} Fits : \delta(M(\mu K\pi), M(\mu K)), 3.0\text{GeV}/c < p_T(K^-) \leq 4.0\text{GeV}/c$, $\frac{7\pi}{12} < \phi(K^-) \leq \frac{11\pi}{12}$

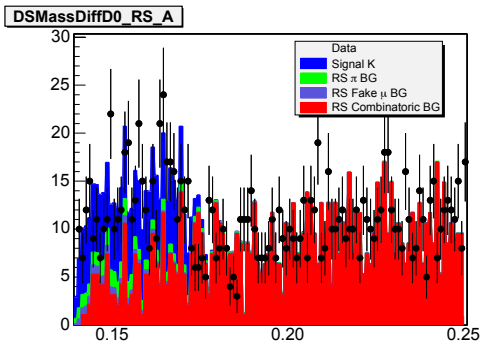

(a) $1.2 < M(\mu^+K^-) \leq 1.3$

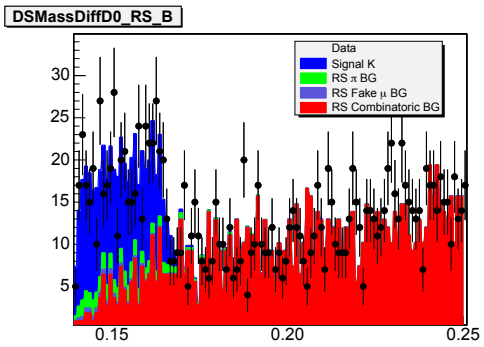

(b) $1.3 < M(\mu^+K^-) \leq 1.4$

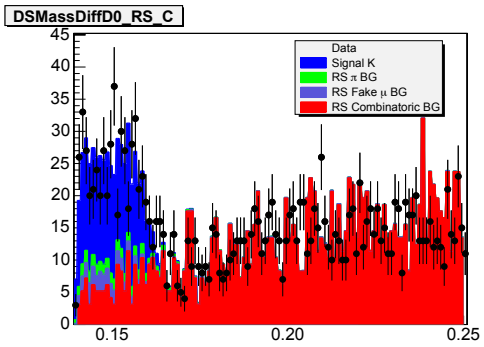

(c) $1.4 < M(\mu^+K^-) \leq 1.5$

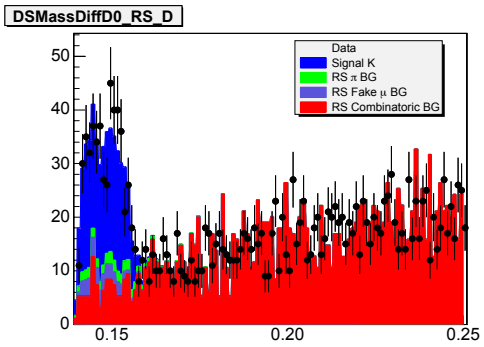

(d) $1.5 < M(\mu^+K^-) \leq 1.6$

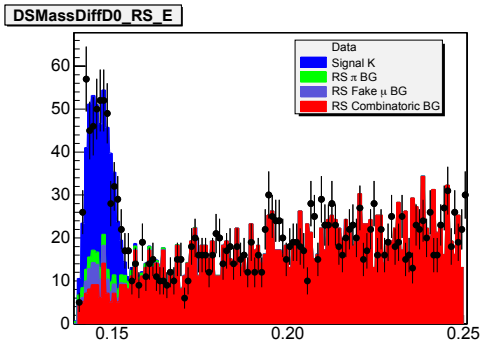

(e) $1.6 < M(\mu^+K^-) \leq 1.7$

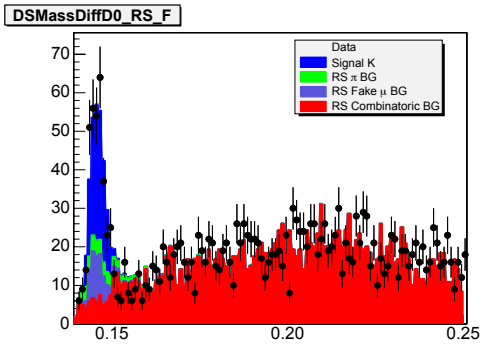

(f) $1.7 < M(\mu^+K^-) \leq 1.8$

Figure B.10: $D^{*+} Fits : \delta(M(\mu K\pi), M(\mu K)), 3.0\text{GeV}/c < p_T(K^-) \leq 4.0\text{GeV}/c$, $\frac{11\pi}{12} < \phi(K^-) \leq \frac{15\pi}{12}$

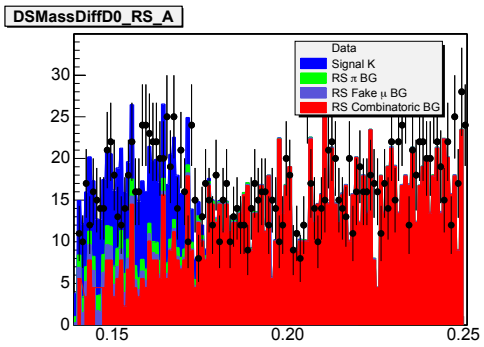

(a) $1.2 < M(\mu^+K^-) \leq 1.3$

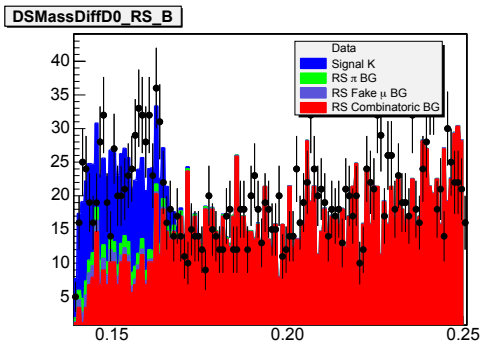

(b) $1.3 < M(\mu^+K^-) \leq 1.4$

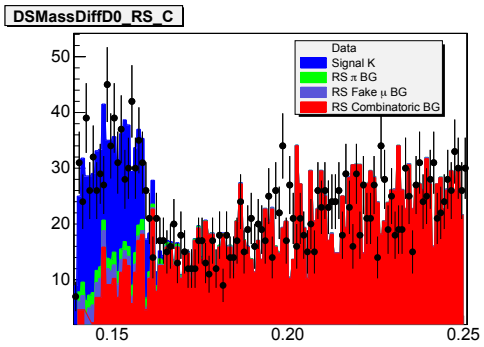

(c) $1.4 < M(\mu^+K^-) \leq 1.5$

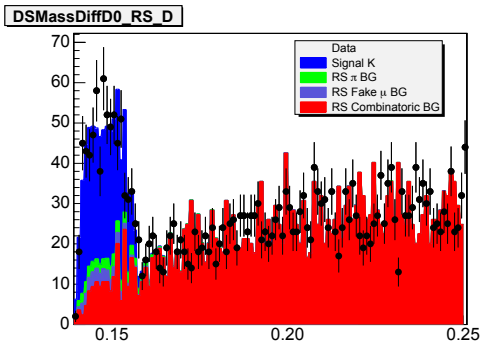

(d) $1.5 < M(\mu^+K^-) \leq 1.6$

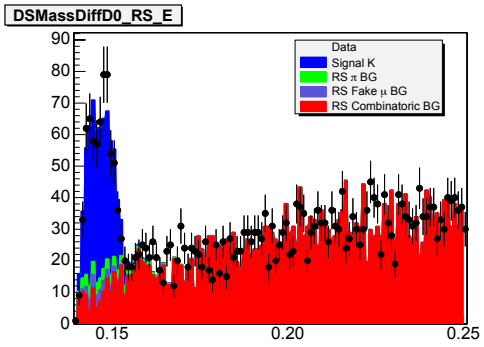

(e) $1.6 < M(\mu^+K^-) \leq 1.7$

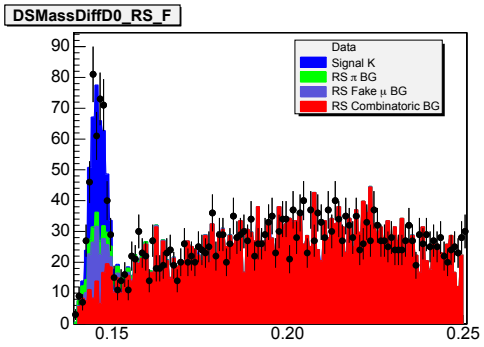

(f) $1.7 < M(\mu^+K^-) \leq 1.8$

Figure B.11: $D^{*+} Fits : \delta(M(\mu K\pi), M(\mu K)), 3.0\text{GeV}/c < p_T(K^-) \leq 4.0\text{GeV}/c$, $\frac{15\pi}{12} < \phi(K^-) \leq \frac{19\pi}{12}$

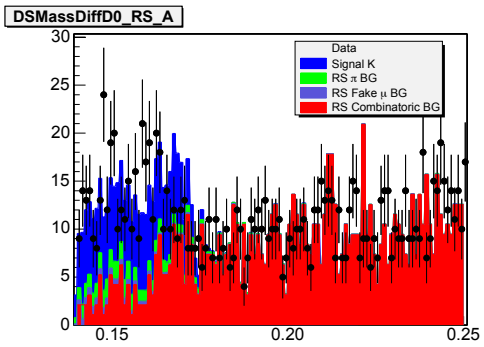

(a) $1.2 < M(\mu^+K^-) \leq 1.3$

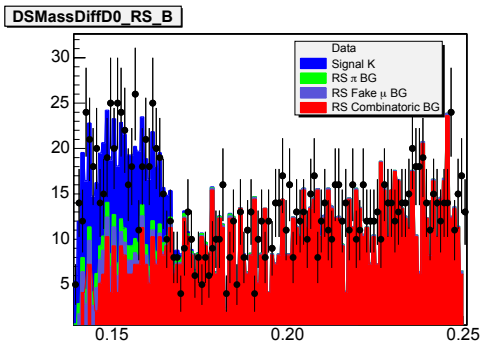

(b) $1.3 < M(\mu^+K^-) \leq 1.4$

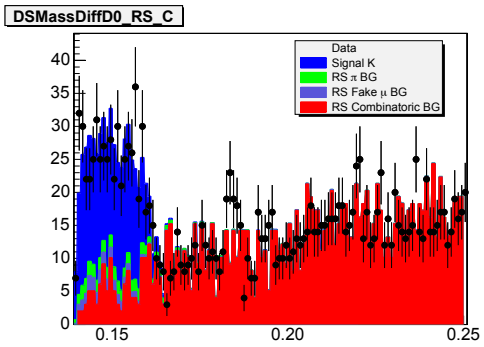

(c) $1.4 < M(\mu^+K^-) \leq 1.5$

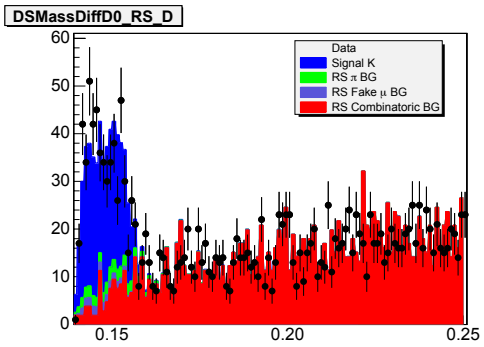

(d) $1.5 < M(\mu^+K^-) \leq 1.6$

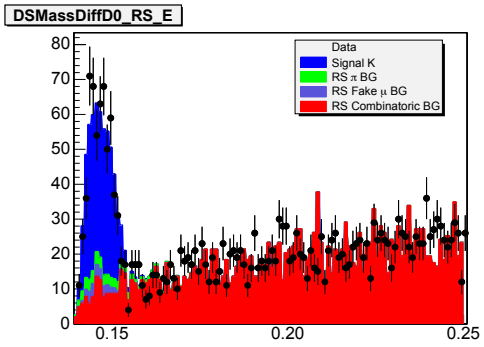

(e) $1.6 < M(\mu^+K^-) \leq 1.7$

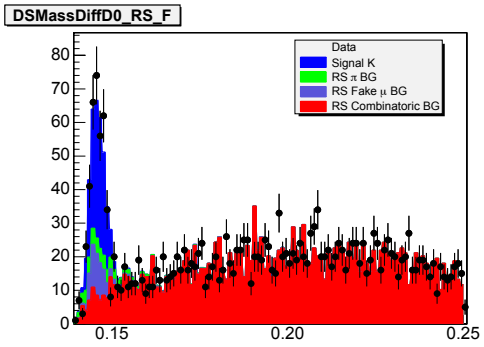

(f) $1.7 < M(\mu^+K^-) \leq 1.8$

Figure B.12: $D^{*+} Fits : \delta(M(\mu K\pi), M(\mu K)), 3.0\text{GeV}/c < p_T(K^-) \leq 4.0\text{GeV}/c$, $\frac{19\pi}{12} < \phi(K^-) \leq \frac{23\pi}{12}$

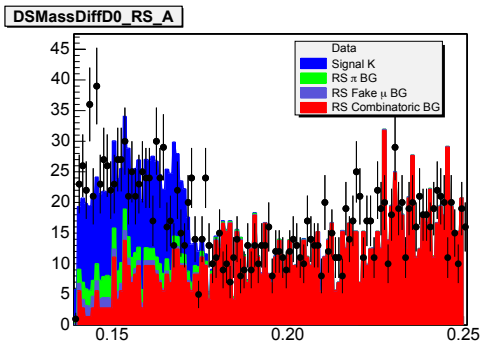

(a) $1.2 < M(\mu^+K^-) \leq 1.3$

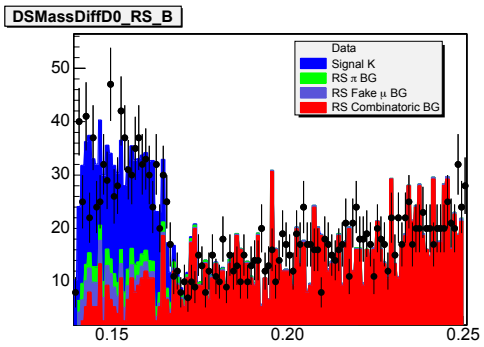

(b) $1.3 < M(\mu^+K^-) \leq 1.4$

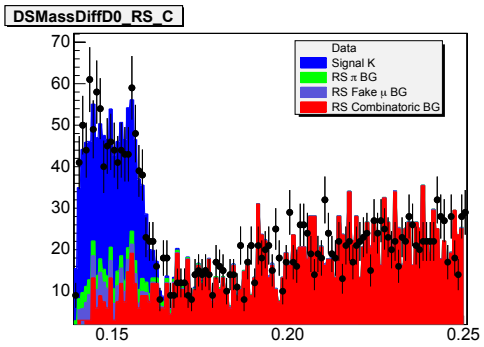

(c) $1.4 < M(\mu^+K^-) \leq 1.5$

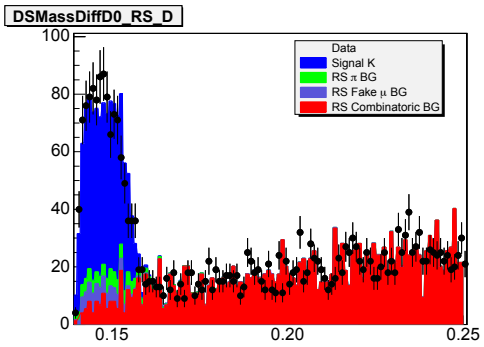

(d) $1.5 < M(\mu^+K^-) \leq 1.6$

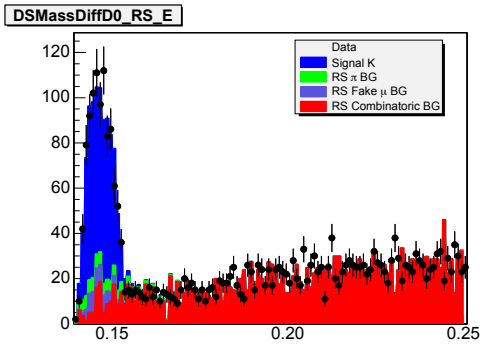

(e) $1.6 < M(\mu^+K^-) \leq 1.7$

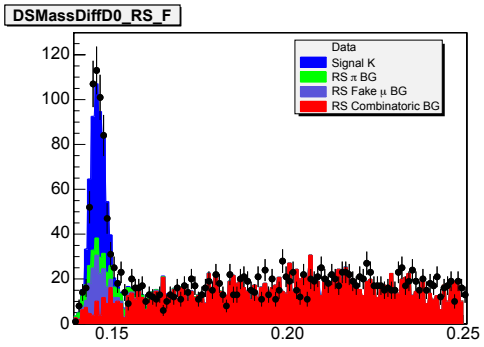

(f) $1.7 < M(\mu^+K^-) \leq 1.8$

Figure B.13: $D^{*+}Fits : \delta(M(\mu K\pi), M(\mu K)), p_T(K^-) > 4.0\text{GeV}/c, -\frac{\pi}{12} < \phi(K^-) \leq \frac{3\pi}{12}$

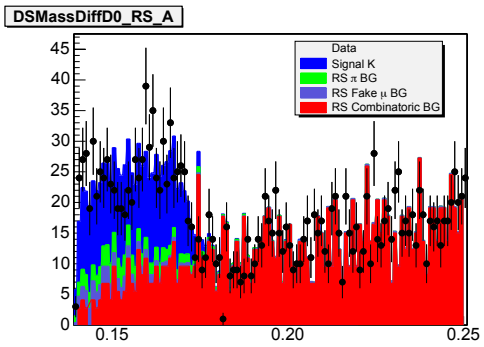

(a) $1.2 < M(\mu^+K^-) \leq 1.3$

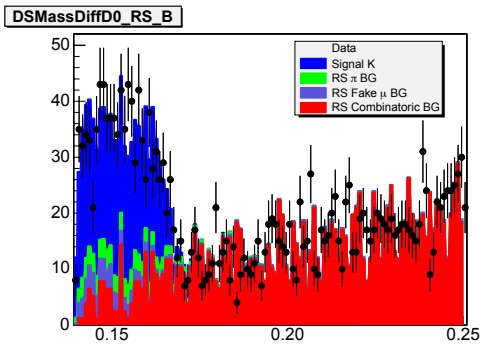

(b) $1.3 < M(\mu^+K^-) \leq 1.4$

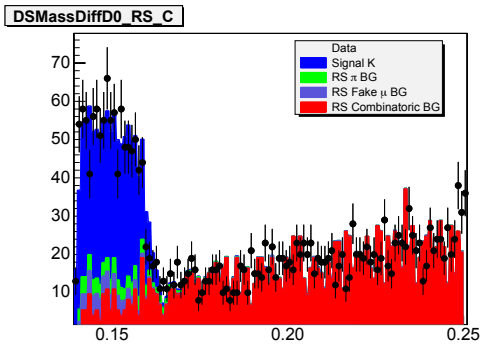

(c) $1.4 < M(\mu^+K^-) \leq 1.5$

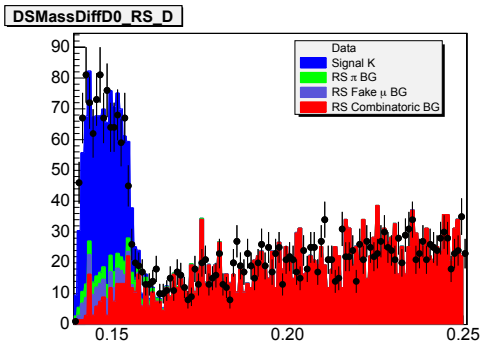

(d) $1.5 < M(\mu^+K^-) \leq 1.6$

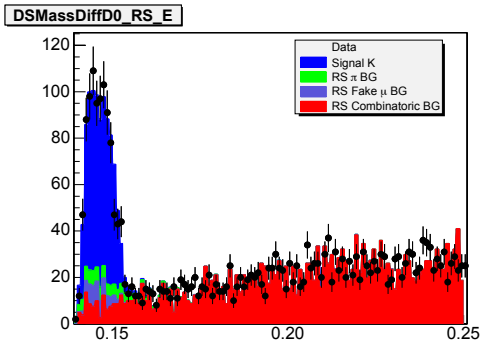

(e) $1.6 < M(\mu^+K^-) \leq 1.7$

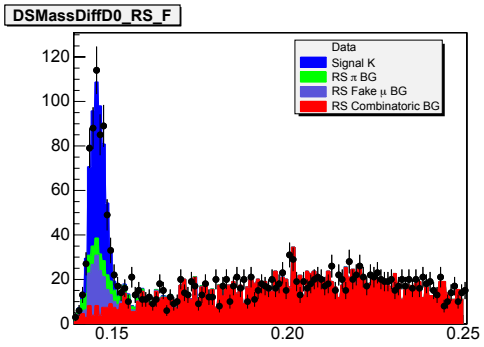

(f) $1.7 < M(\mu^+K^-) \leq 1.8$

Figure B.14: $D^{*+} Fits : \delta(M(\mu K\pi), M(\mu K)), p_T(K^-) > 4.0\text{GeV}/c,\ \frac{3\pi}{12} < \phi(K^-) \leq \frac{7\pi}{12}$

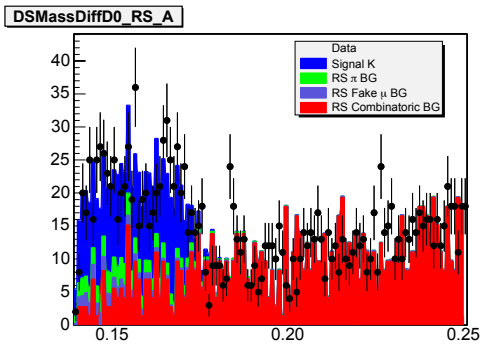

(a) $1.2 < M(\mu^+K^-) \leq 1.3$

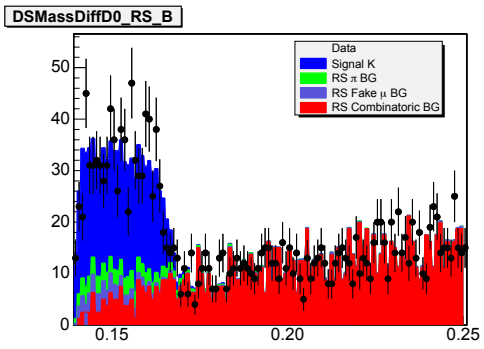

(b) $1.3 < M(\mu^+K^-) \leq 1.4$

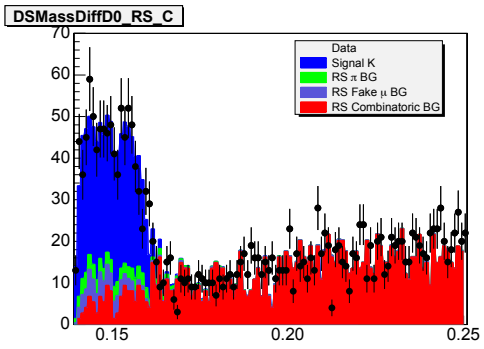

(c) $1.4 < M(\mu^+K^-) \leq 1.5$

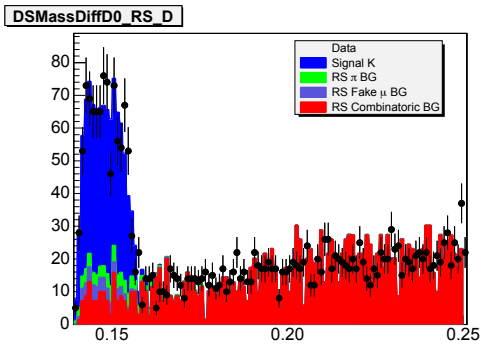

(d) $1.5 < M(\mu^+K^-) \leq 1.6$

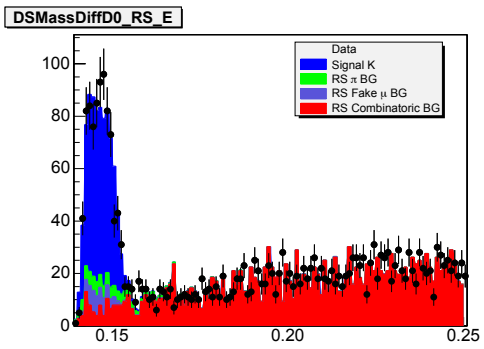

(e) $1.6 < M(\mu^+K^-) \leq 1.7$

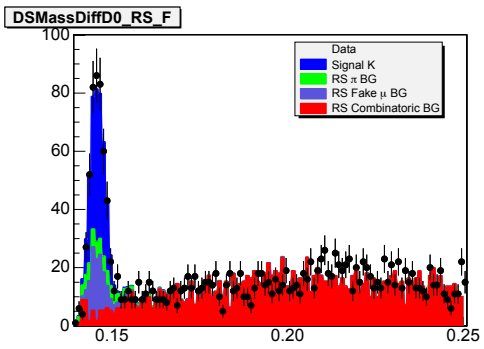

(f) $1.7 < M(\mu^+K^-) \leq 1.8$

Figure B.15: $D^{*+}Fits : \delta(M(\mu K\pi), M(\mu K)), p_T(K^-) > 4.0\text{GeV}/c,\ \frac{7\pi}{12} < \phi(K^-) \leq \frac{11\pi}{12}$

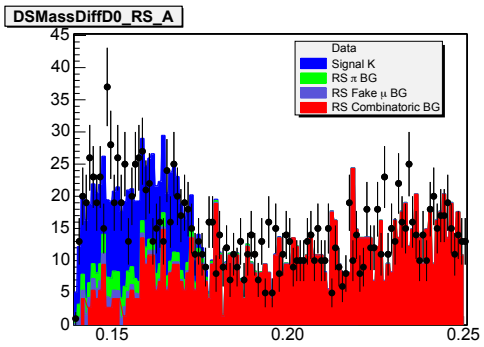

(a) $1.2 < M(\mu^+K^-) \leq 1.3$

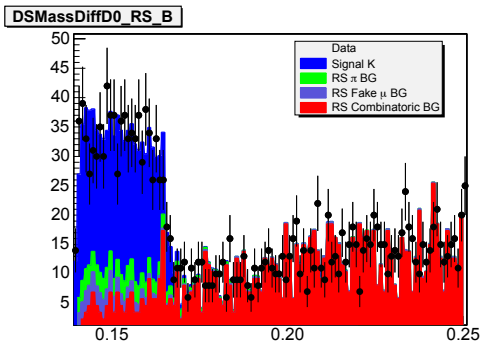

(b) $1.3 < M(\mu^+K^-) \leq 1.4$

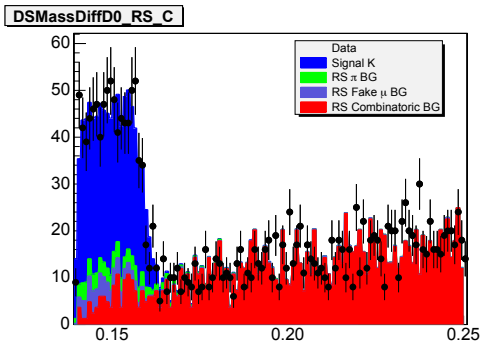

(c) $1.4 < M(\mu^+K^-) \leq 1.5$

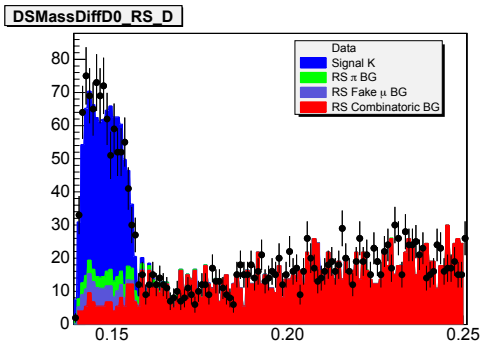

(d) $1.5 < M(\mu^+K^-) \leq 1.6$

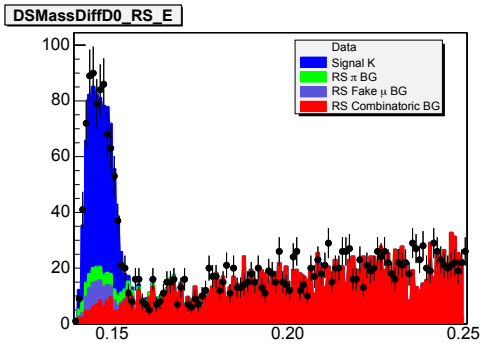

(e) $1.6 < M(\mu^+K^-) \leq 1.7$

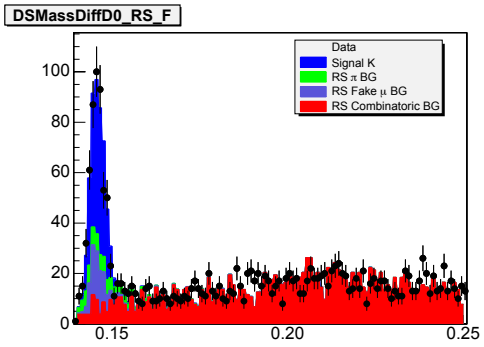

(f) $1.7 < M(\mu^+K^-) \leq 1.8$

Figure B.16: $D^{*+} Fits : \delta(M(\mu K\pi), M(\mu K)), p_T(K^-) > 4.0\text{GeV}/c,\ \frac{11\pi}{12} < \phi(K^-) \leq \frac{15\pi}{12}$

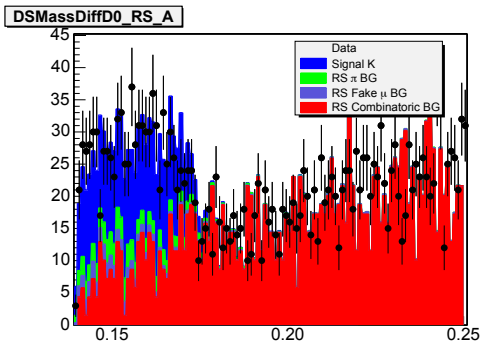

(a) $1.2 < M(\mu^+K^-) \leq 1.3$

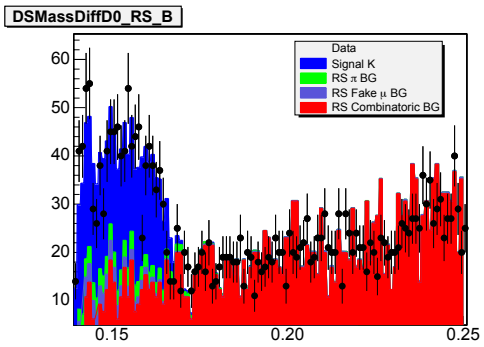

(b) $1.3 < M(\mu^+K^-) \leq 1.4$

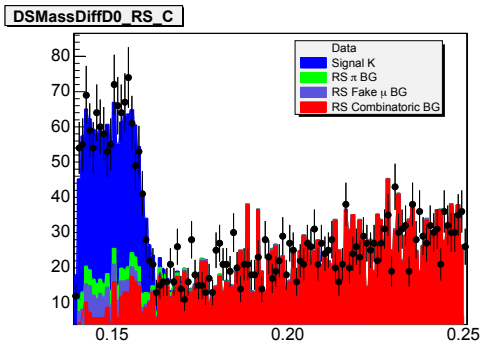

(c) $1.4 < M(\mu^+K^-) \leq 1.5$

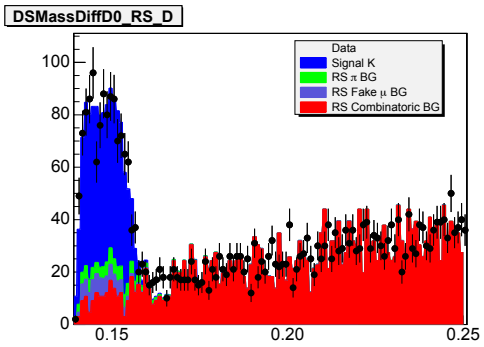

(d) $1.5 < M(\mu^+K^-) \leq 1.6$

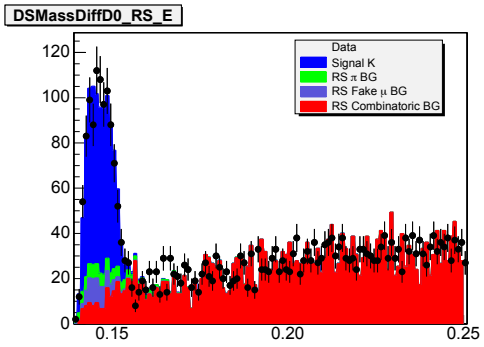

(e) $1.6 < M(\mu^+K^-) \leq 1.7$

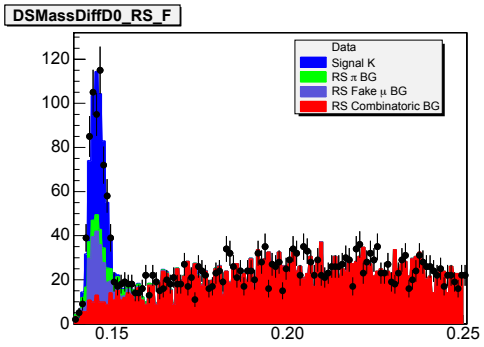

(f) $1.7 < M(\mu^+K^-) \leq 1.8$

Figure B.17: $D^{*+} Fits : \delta(M(\mu K\pi), M(\mu K)), p_T(K^-) > 4.0\text{GeV}/c,\ \frac{15\pi}{12} < \phi(K^-) \leq \frac{19\pi}{12}$

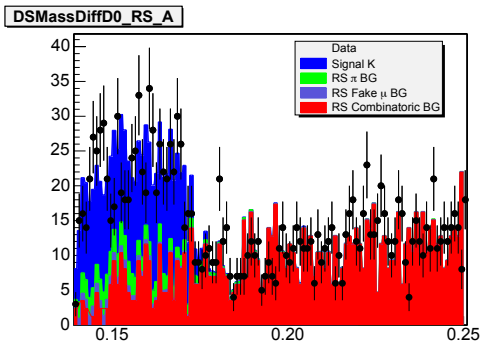

(a) $1.2 < M(\mu^+K^-) \leq 1.3$

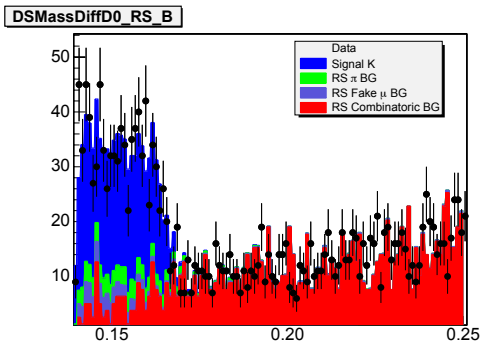

(b) $1.3 < M(\mu^+K^-) \leq 1.4$

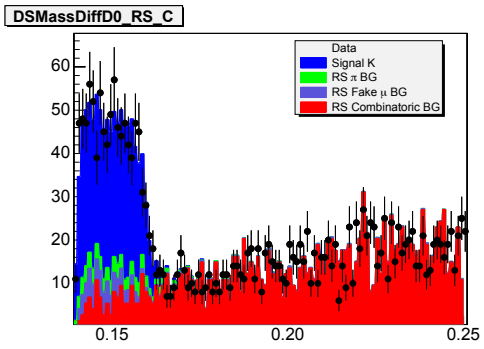

(c) $1.4 < M(\mu^+K^-) \leq 1.5$

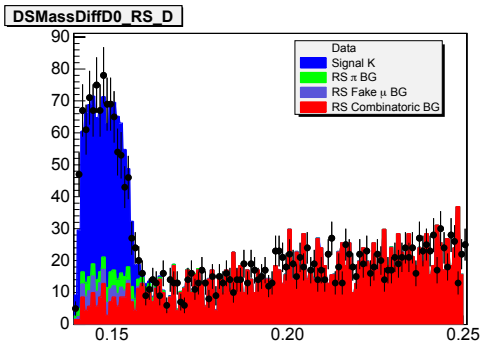

(d) $1.5 < M(\mu^+K^-) \leq 1.6$

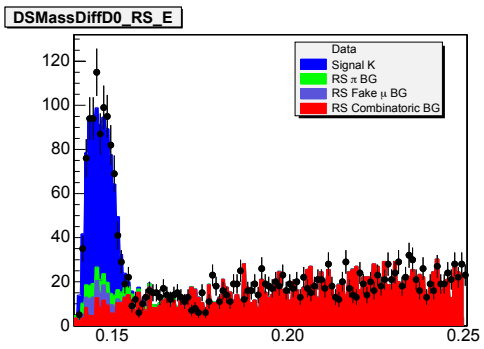

(e) $1.6 < M(\mu^+K^-) \leq 1.7$

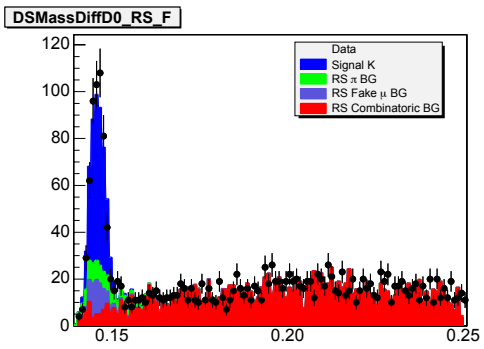

(f) $1.7 < M(\mu^+K^-) \leq 1.8$

Figure B.18: $D^{*+} Fits : \delta(M(\mu K\pi), M(\mu K)), p_T(K^-) > 4.0\text{GeV}/c,\ \frac{19\pi}{12} < \phi(K^-) \leq \frac{23\pi}{12}$

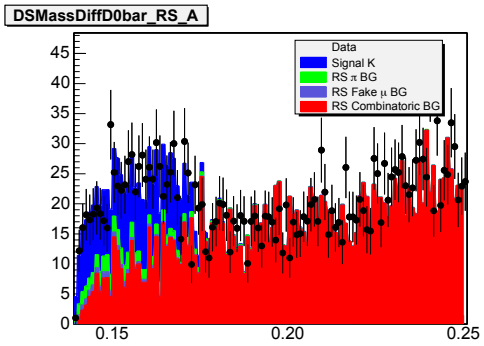

(a) $1.2 < M(\mu^+K^-) \leq 1.3$

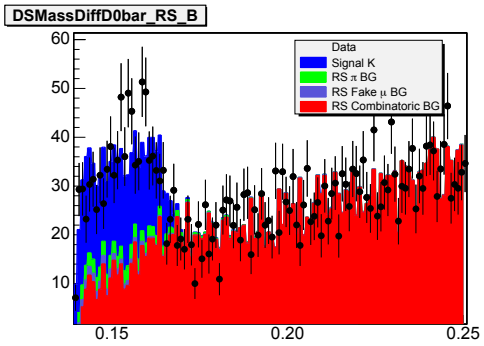

(b) $1.3 < M(\mu^+K^-) \leq 1.4$

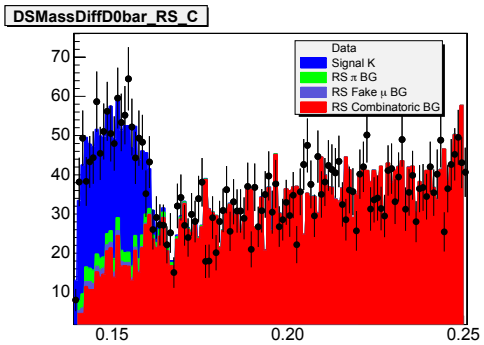

(c) $1.4 < M(\mu^+K^-) \leq 1.5$

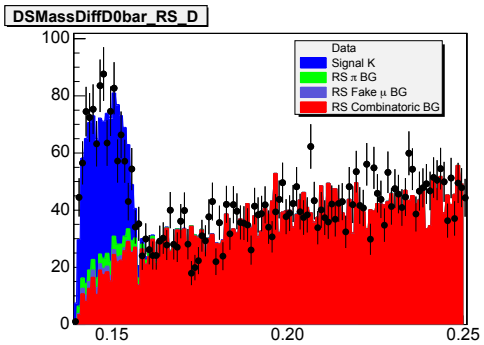

(d) $1.5 < M(\mu^+K^-) \leq 1.6$

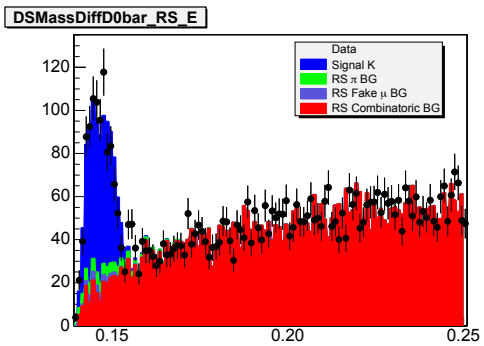

(e) $1.6 < M(\mu^+K^-) \leq 1.7$

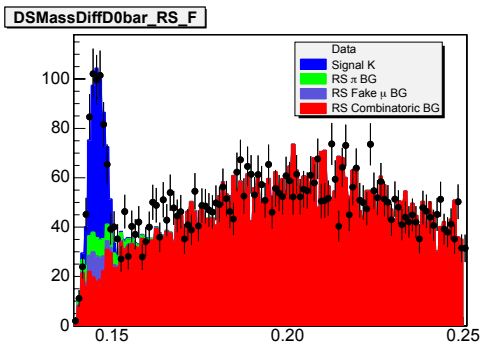

(f) $1.7 < M(\mu^+K^-) \leq 1.8$

Figure B.19: $D^{*-} Fits : \delta(M(\mu K\pi), M(\mu K)), 2.0\text{GeV}/c < p_T(K^-) \leq 3.0\text{GeV}/c, -\frac{\pi}{12} < \phi(K^-) \leq \frac{3\pi}{12}$

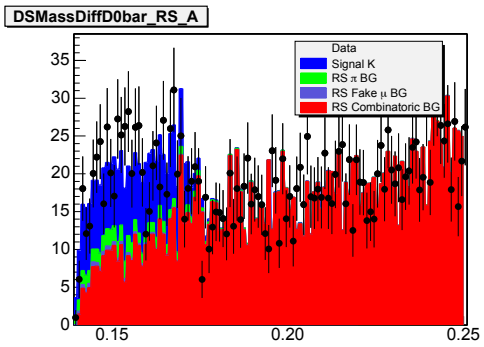

(a) $1.2 < M(\mu^+K^-) \leq 1.3$

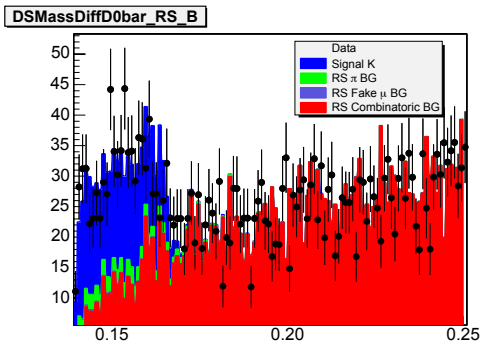

(b) $1.3 < M(\mu^+K^-) \leq 1.4$

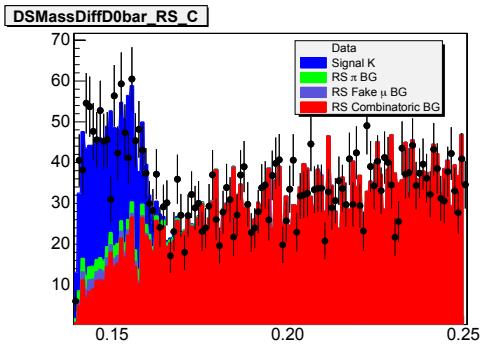

(c) $1.4 < M(\mu^+K^-) \leq 1.5$

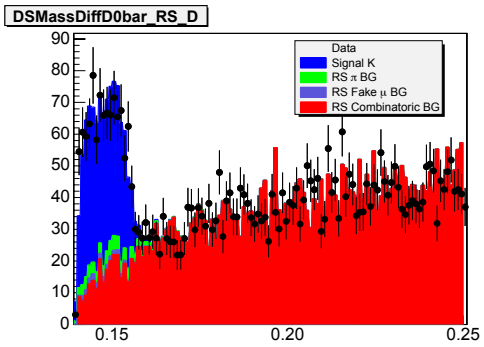

(d) $1.5 < M(\mu^+K^-) \leq 1.6$

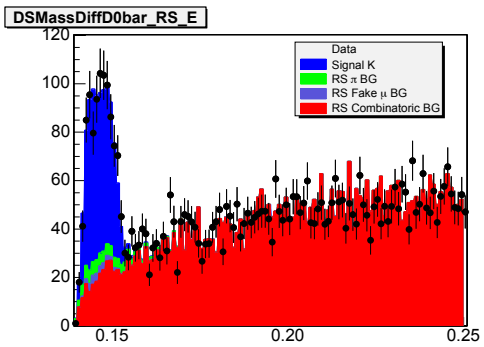

(e) $1.6 < M(\mu^+K^-) \leq 1.7$

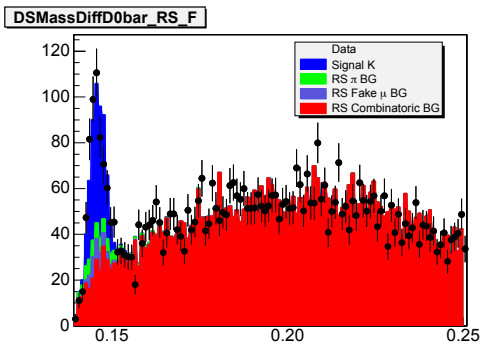

(f) $1.7 < M(\mu^+K^-) \leq 1.8$

Figure B.20: $D^{*-} Fits : \delta(M(\mu K\pi), M(\mu K)), 2.0\text{GeV}/c < p_T(K^-) \leq 3.0\text{GeV}/c$, $\frac{3\pi}{12} < \phi(K^-) \leq \frac{7\pi}{12}$

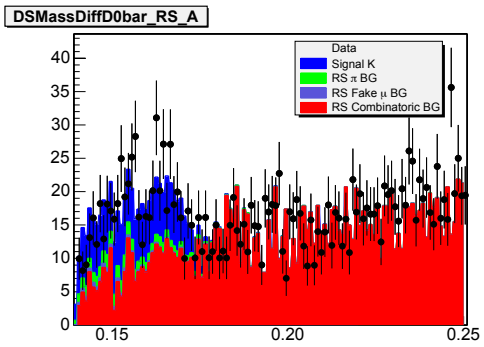

(a) $1.2 < M(\mu^+K^-) \leq 1.3$

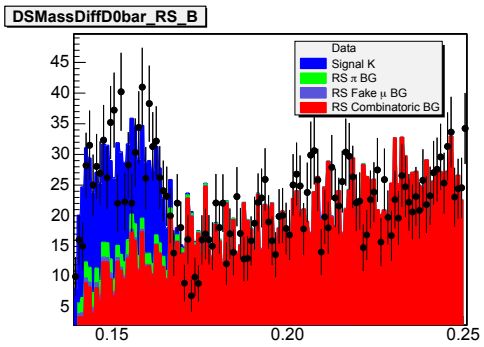

(b) $1.3 < M(\mu^+K^-) \leq 1.4$

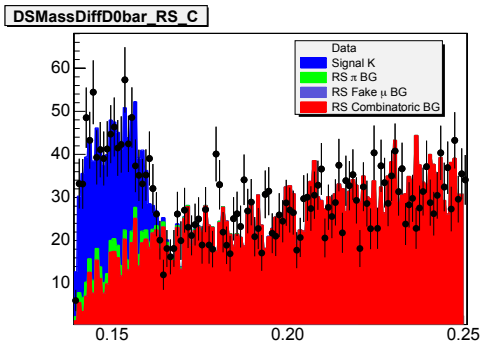

(c) $1.4 < M(\mu^+K^-) \leq 1.5$

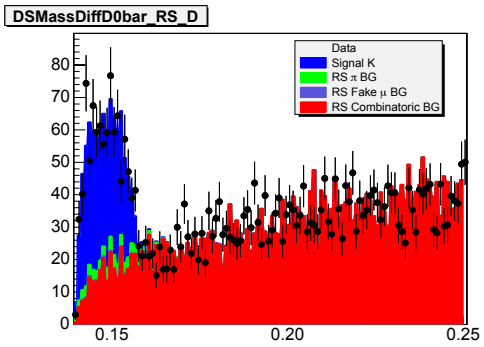

(d) $1.5 < M(\mu^+K^-) \leq 1.6$

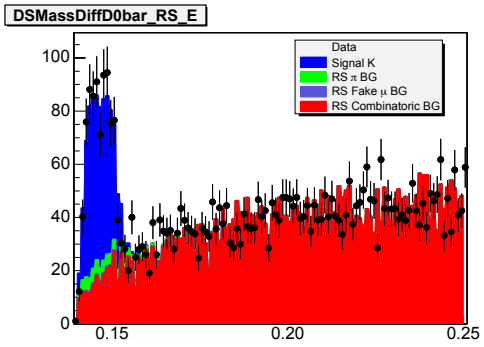

(e) $1.6 < M(\mu^+K^-) \leq 1.7$

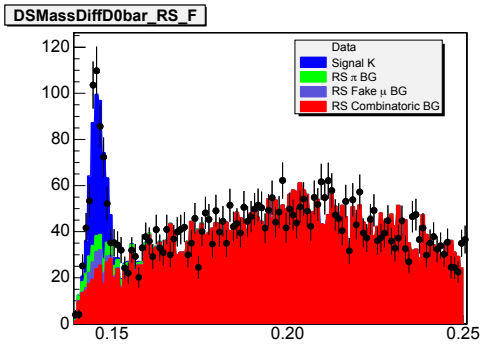

(f) $1.7 < M(\mu^+K^-) \leq 1.8$

Figure B.21: $D^{*-} Fits : \delta(M(\mu K\pi), M(\mu K)), 2.0\text{GeV}/c < p_T(K^-) \leq 3.0\text{GeV}/c$, $\frac{7\pi}{12} < \phi(K^-) \leq \frac{11\pi}{12}$

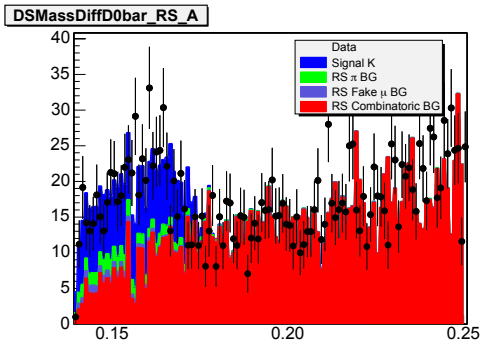

(a) $1.2 < M(\mu^+K^-) \leq 1.3$

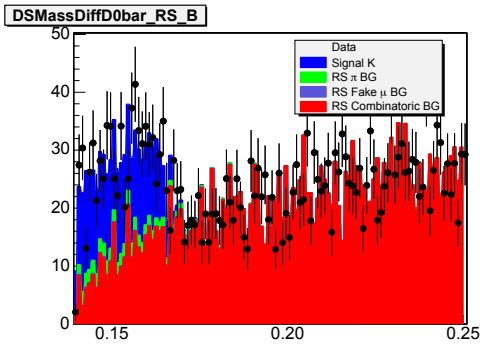

(b) $1.3 < M(\mu^+K^-) \leq 1.4$

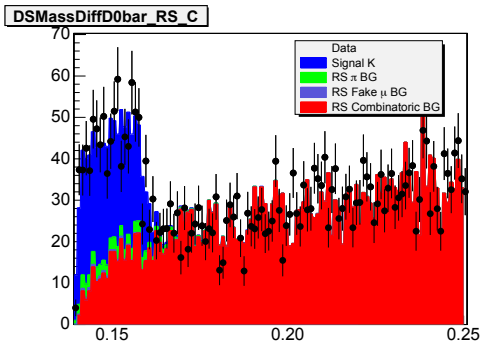

(c) $1.4 < M(\mu^+K^-) \leq 1.5$

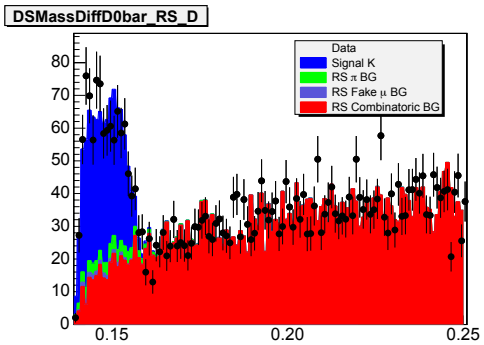

(d) $1.5 < M(\mu^+K^-) \leq 1.6$

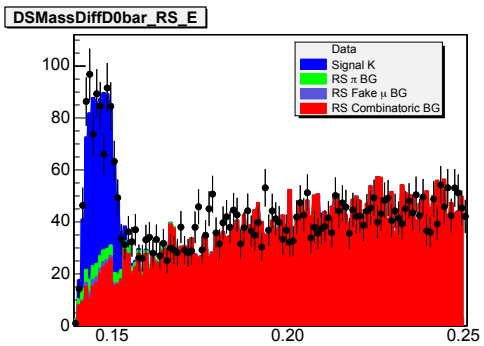

(e) $1.6 < M(\mu^+K^-) \leq 1.7$

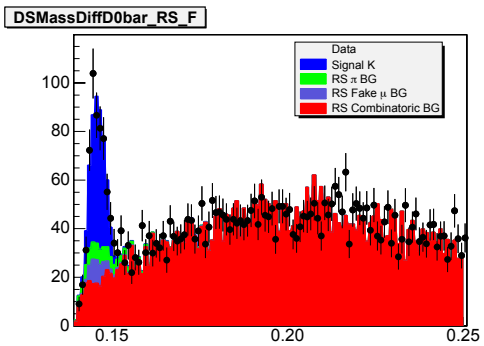

(f) $1.7 < M(\mu^+K^-) \leq 1.8$

Figure B.22: $D^{*-} Fits : \delta(M(\mu K\pi), M(\mu K)), 2.0\text{GeV}/c < p_T(K^-) \leq 3.0\text{GeV}/c$, $\frac{11\pi}{12} < \phi(K^-) \leq \frac{15\pi}{12}$

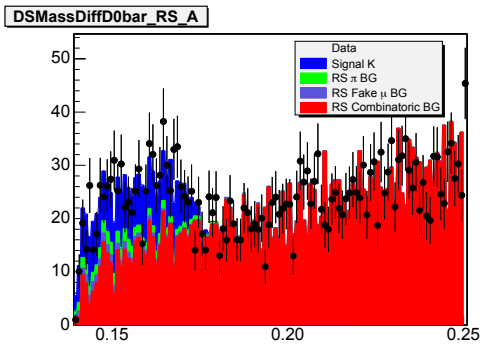

(a) $1.2 < M(\mu^+K^-) \leq 1.3$

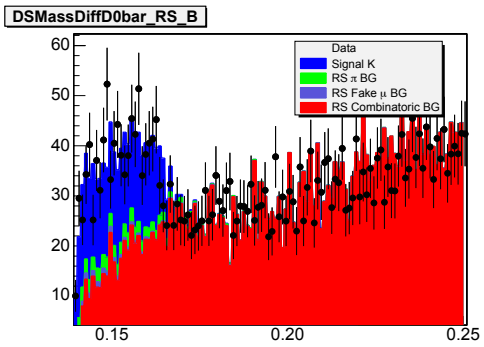

(b) $1.3 < M(\mu^+K^-) \leq 1.4$

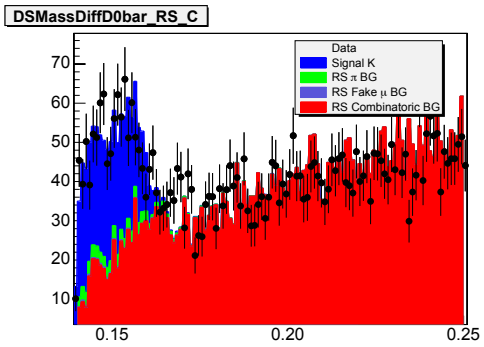

(c) $1.4 < M(\mu^+K^-) \leq 1.5$

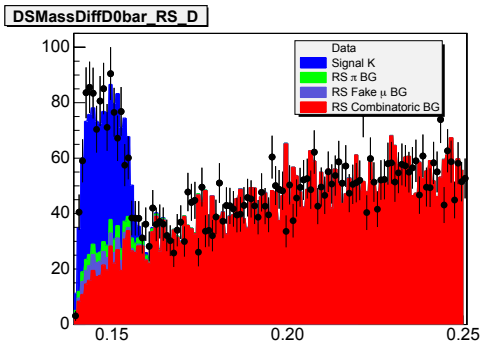

(d) $1.5 < M(\mu^+K^-) \leq 1.6$

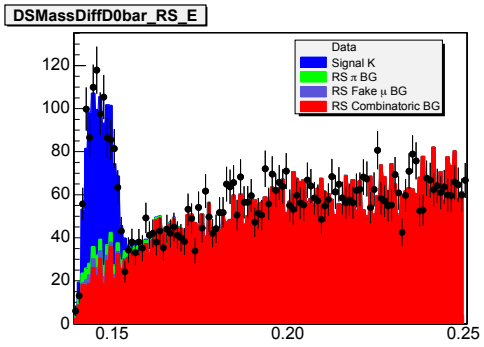

(e) $1.6 < M(\mu^+K^-) \leq 1.7$

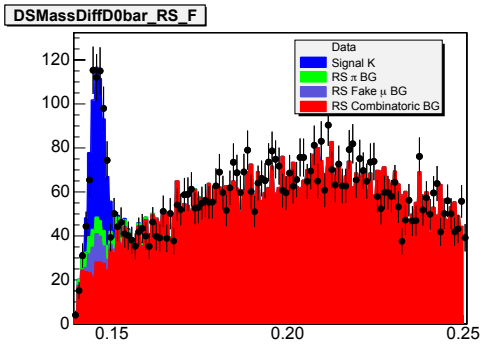

(f) $1.7 < M(\mu^+K^-) \leq 1.8$

Figure B.23: $D^{*-} Fits : \delta(M(\mu K\pi), M(\mu K)), 2.0\text{GeV}/c < p_T(K^-) \leq 3.0\text{GeV}/c$, $\frac{15\pi}{12} < \phi(K^-) \leq \frac{19\pi}{12}$

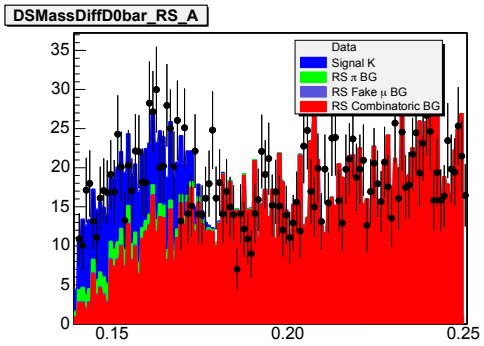

(a) $1.2 < M(\mu^+K^-) \leq 1.3$

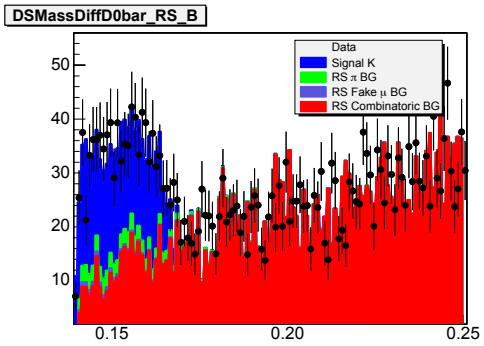

(b) $1.3 < M(\mu^+K^-) \leq 1.4$

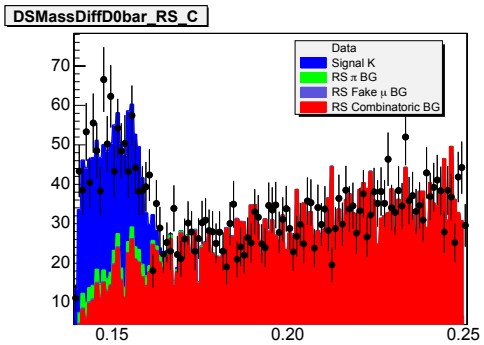

(c) $1.4 < M(\mu^+K^-) \leq 1.5$

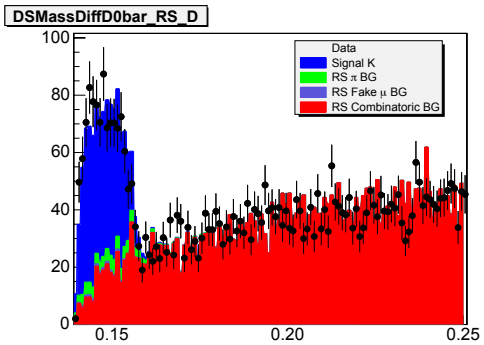

(d) $1.5 < M(\mu^+K^-) \leq 1.6$

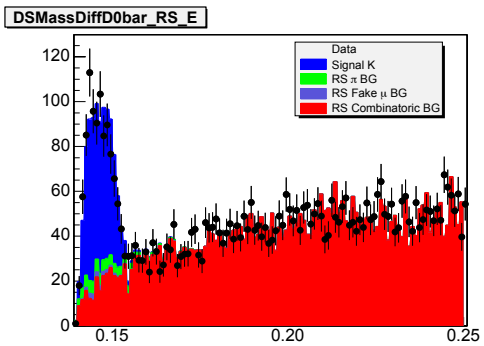

(e) $1.6 < M(\mu^+K^-) \leq 1.7$

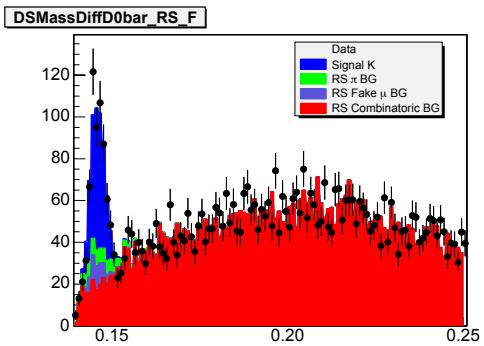

(f) $1.7 < M(\mu^+K^-) \leq 1.8$

Figure B.24: $D^{*-} Fits : \delta(M(\mu K\pi), M(\mu K)), 2.0\text{GeV}/c < p_T(K^-) \leq 3.0\text{GeV}/c$, $\frac{19\pi}{12} < \phi(K^-) \leq \frac{23\pi}{12}$

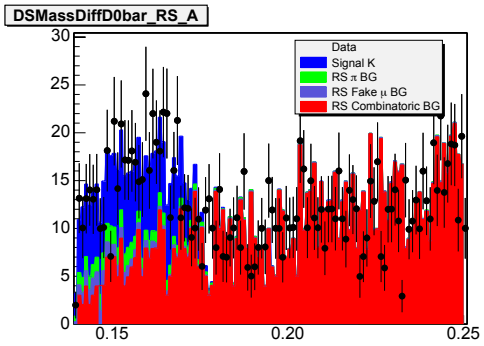

(a) $1.2 < M(\mu^+K^-) \leq 1.3$

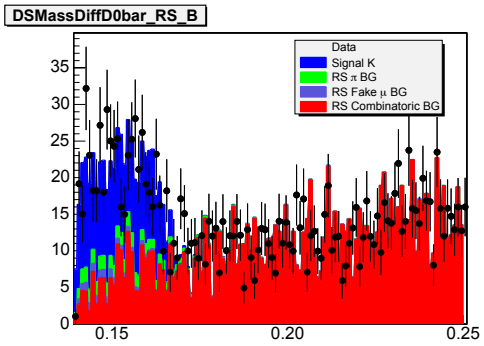

(b) $1.3 < M(\mu^+K^-) \leq 1.4$

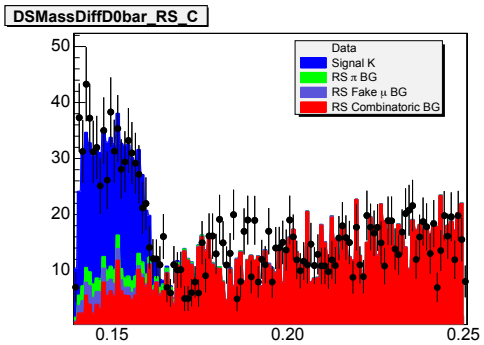

(c) $1.4 < M(\mu^+K^-) \leq 1.5$

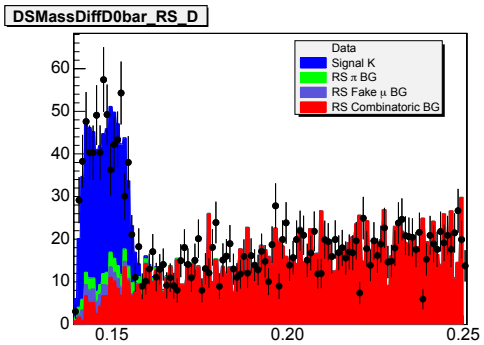

(d) $1.5 < M(\mu^+K^-) \leq 1.6$

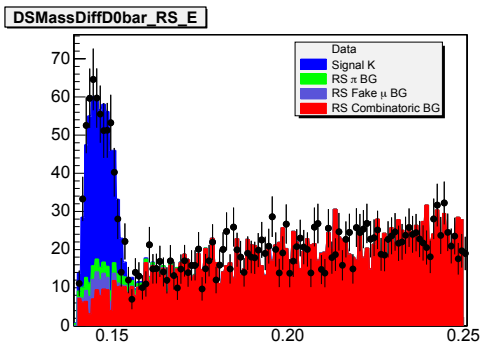

(e) $1.6 < M(\mu^+K^-) \leq 1.7$

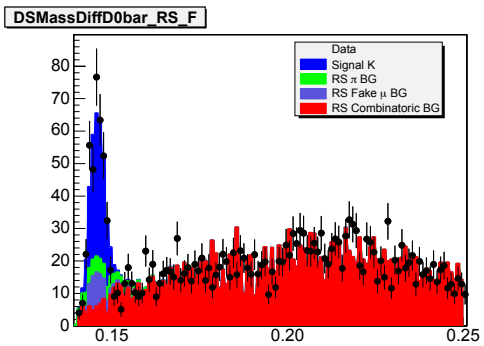

(f) $1.7 < M(\mu^+K^-) \leq 1.8$

Figure B.25: $D^{*-} Fits : \delta(M(\mu K\pi), M(\mu K)), 3.0\text{GeV}/c < p_T(K^-) \leq 4.0\text{GeV}/c, -\frac{\pi}{12} < \phi(K^-) \leq \frac{3\pi}{12}$

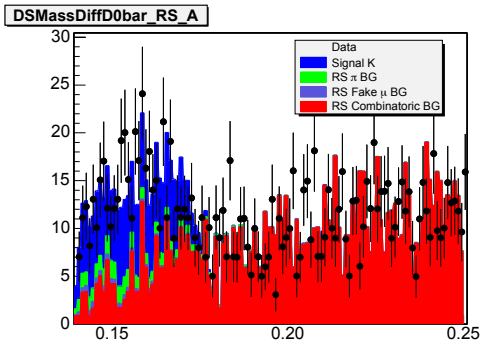

(a) $1.2 < M(\mu^+K^-) \leq 1.3$

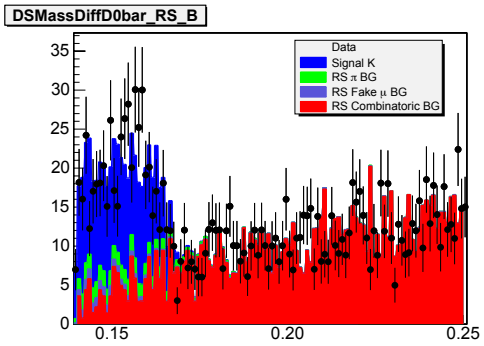

(b) $1.3 < M(\mu^+K^-) \leq 1.4$

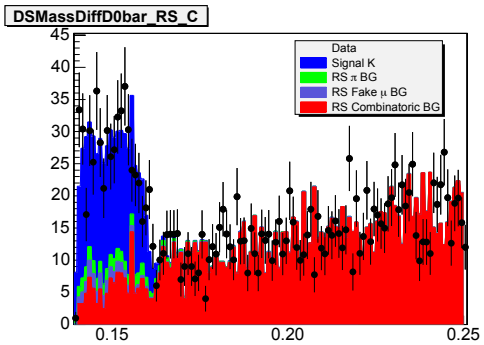

(c) $1.4 < M(\mu^+K^-) \leq 1.5$

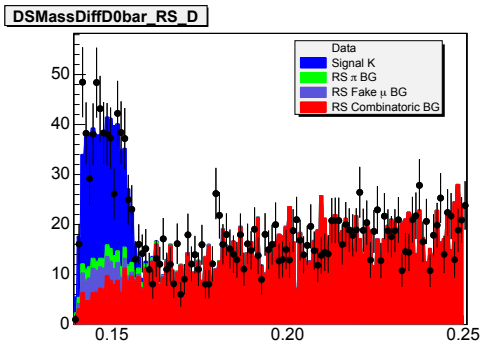

(d) $1.5 < M(\mu^+K^-) \leq 1.6$

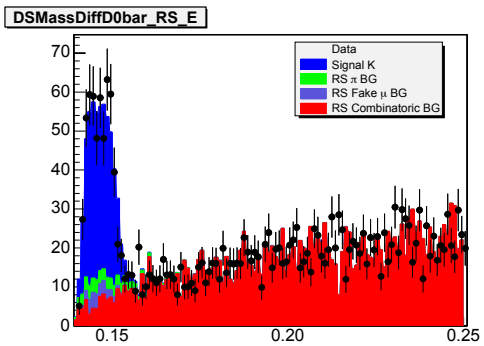

(e) $1.6 < M(\mu^+K^-) \leq 1.7$

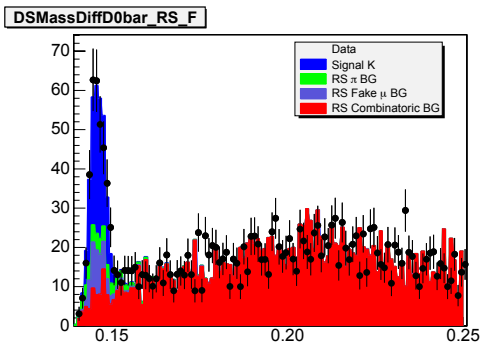

(f) $1.7 < M(\mu^+K^-) \leq 1.8$

Figure B.26: $D^{*-} Fits : \delta(M(\mu K\pi), M(\mu K)), 3.0\text{GeV}/c < p_T(K^-) \leq 4.0\text{GeV}/c$, $\frac{3\pi}{12} < \phi(K^-) \leq \frac{7\pi}{12}$

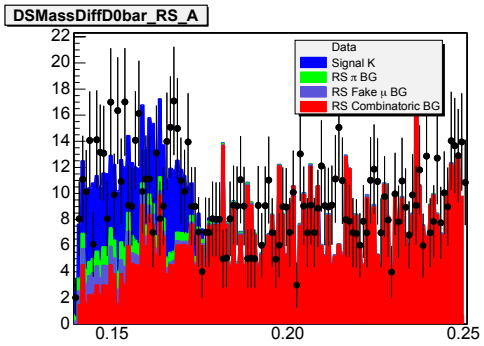

(a) $1.2 < M(\mu^+K^-) \leq 1.3$

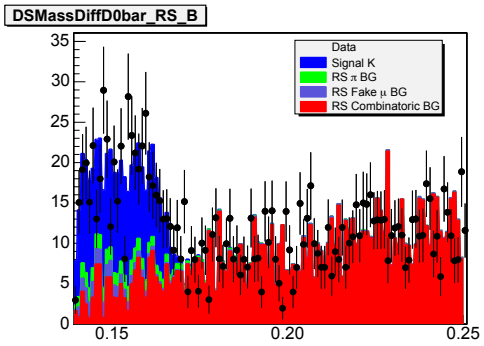

(b) $1.3 < M(\mu^+K^-) \leq 1.4$

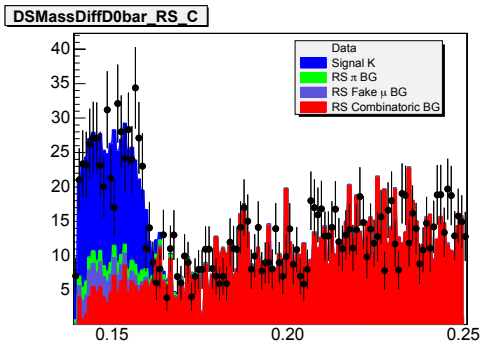

(c) $1.4 < M(\mu^+K^-) \leq 1.5$

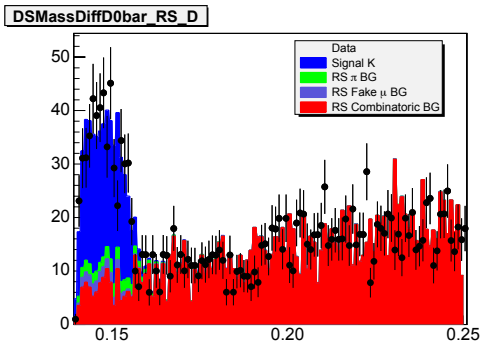

(d) $1.5 < M(\mu^+K^-) \leq 1.6$

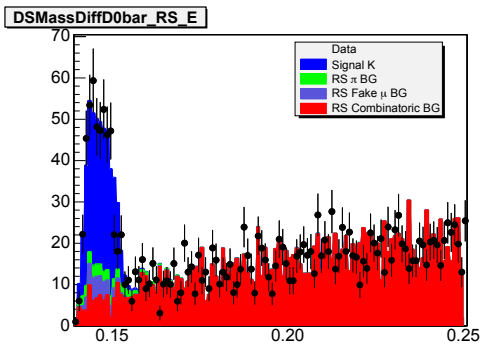

(e) $1.6 < M(\mu^+K^-) \leq 1.7$

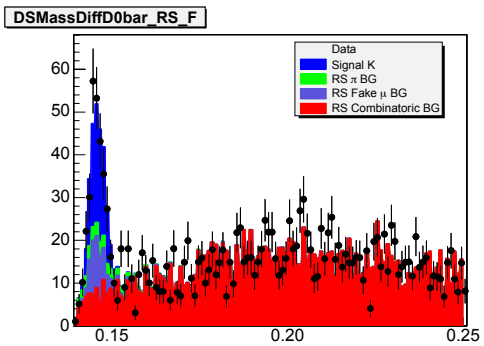

(f) $1.7 < M(\mu^+K^-) \leq 1.8$

Figure B.27: $D^{*-} Fits : \delta(M(\mu K\pi), M(\mu K)), 3.0\text{GeV}/c < p_T(K^-) \leq 4.0\text{GeV}/c$, $\frac{7\pi}{12} < \phi(K^-) \leq \frac{11\pi}{12}$

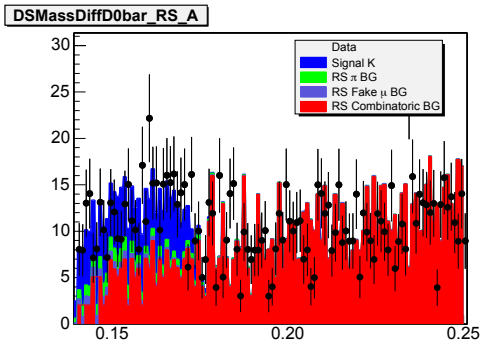

(a) $1.2 < M(\mu^+K^-) \leq 1.3$

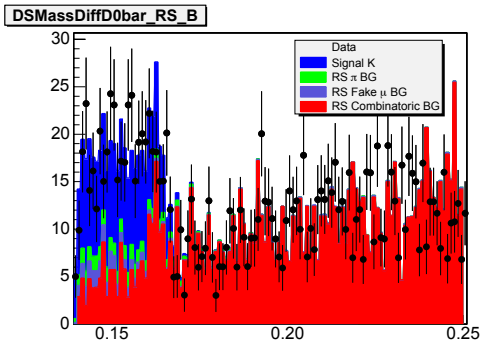

(b) $1.3 < M(\mu^+K^-) \leq 1.4$

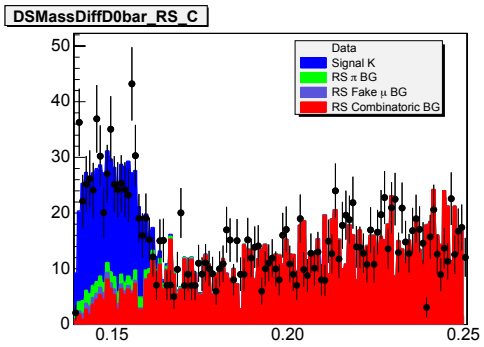

(c) $1.4 < M(\mu^+K^-) \leq 1.5$

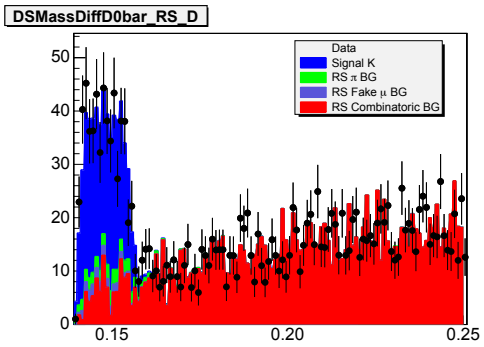

(d) $1.5 < M(\mu^+K^-) \leq 1.6$

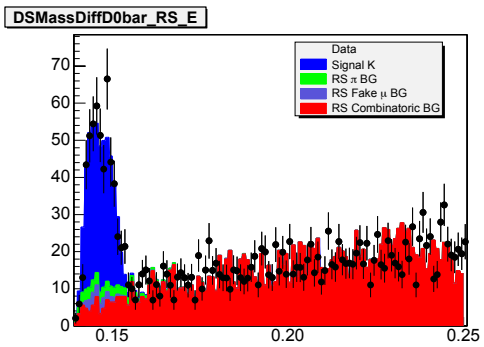

(e) $1.6 < M(\mu^+K^-) \leq 1.7$

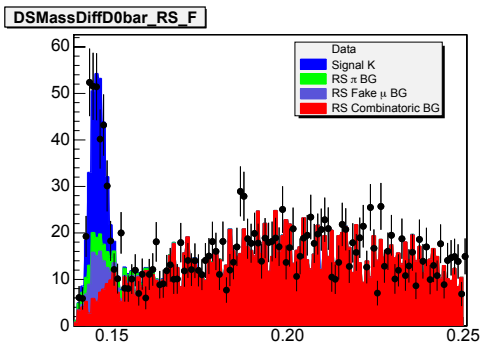

(f) $1.7 < M(\mu^+K^-) \leq 1.8$

Figure B.28: $D^{*-} Fits : \delta(M(\mu K\pi), M(\mu K)), 3.0\text{GeV}/c < p_T(K^-) \leq 4.0\text{GeV}/c,\ \frac{11\pi}{12} < \phi(K^-) \leq \frac{15\pi}{12}$

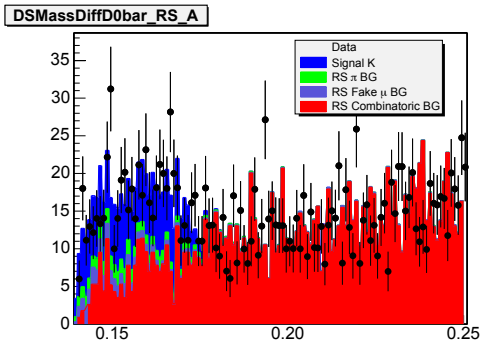

(a) $1.2 < M(\mu^+K^-) \leq 1.3$

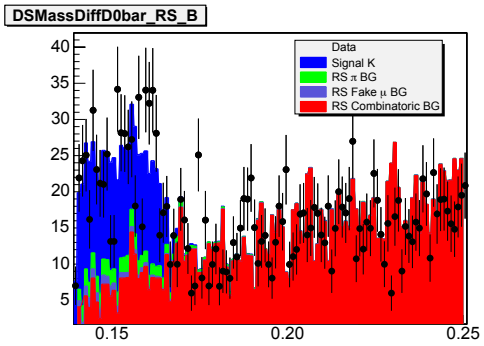

(b) $1.3 < M(\mu^+K^-) \leq 1.4$

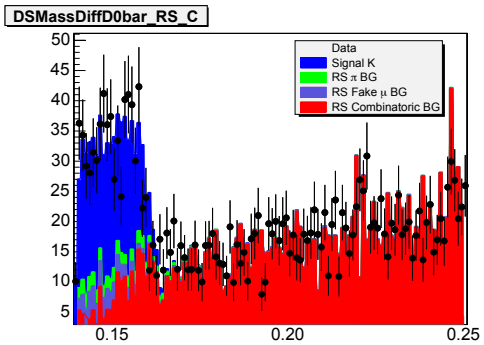

(c) $1.4 < M(\mu^+K^-) \leq 1.5$

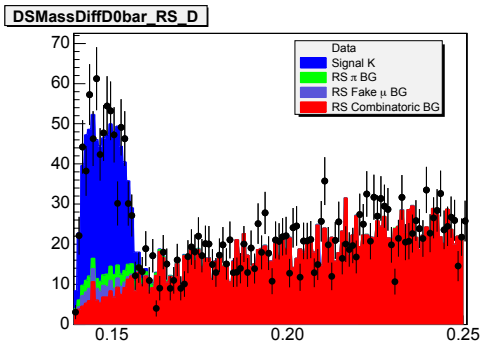

(d) $1.5 < M(\mu^+K^-) \leq 1.6$

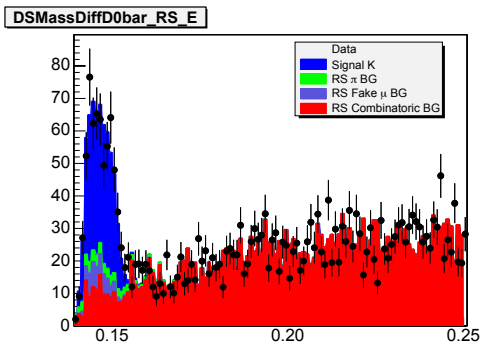

(e) $1.6 < M(\mu^+K^-) \leq 1.7$

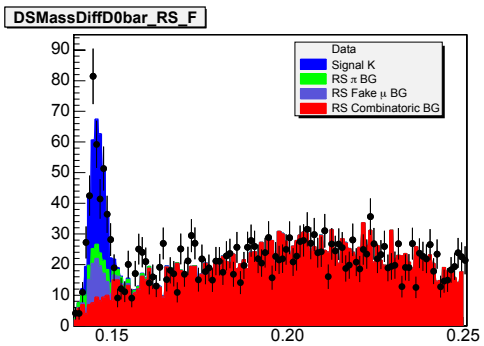

(f) $1.7 < M(\mu^+K^-) \leq 1.8$

Figure B.29: $D^{*-} Fits : \delta(M(\mu K\pi), M(\mu K)), 3.0\text{GeV}/c < p_T(K^-) \leq 4.0\text{GeV}/c$, $\frac{15\pi}{12} < \phi(K^-) \leq \frac{19\pi}{12}$

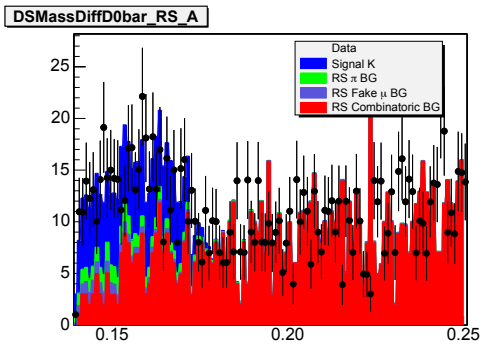

(a) $1.2 < M(\mu^+K^-) \leq 1.3$

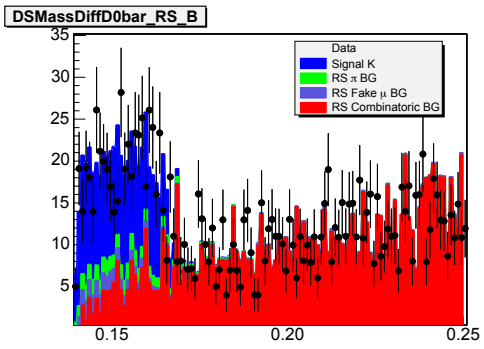

(b) $1.3 < M(\mu^+K^-) \leq 1.4$

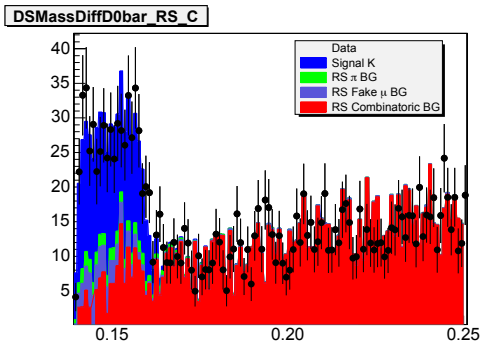

(c) $1.4 < M(\mu^+K^-) \leq 1.5$

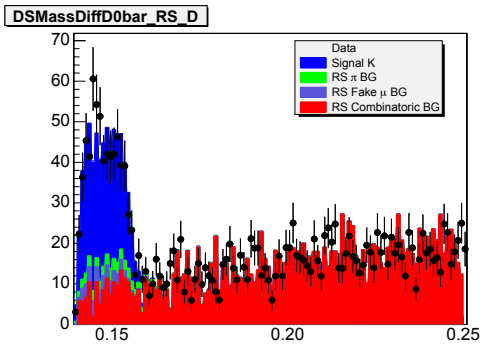

(d) $1.5 < M(\mu^+K^-) \leq 1.6$

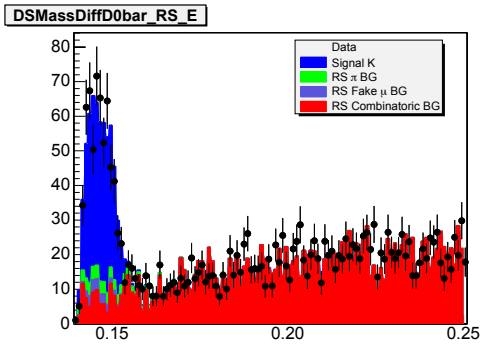

(e) $1.6 < M(\mu^+K^-) \leq 1.7$

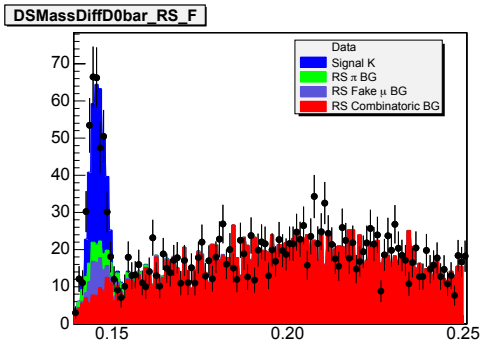

(f) $1.7 < M(\mu^+K^-) \leq 1.8$

Figure B.30: $D^{*-} Fits : \delta(M(\mu K\pi), M(\mu K)), 3.0\text{GeV}/c < p_T(K^-) \leq 4.0\text{GeV}/c$, $\frac{19\pi}{12} < \phi(K^-) \leq \frac{23\pi}{12}$

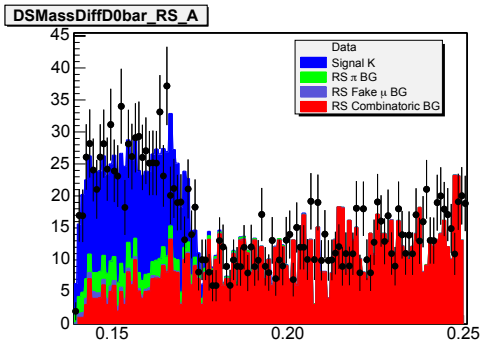

(a) $1.2 < M(\mu^+K^-) \leq 1.3$

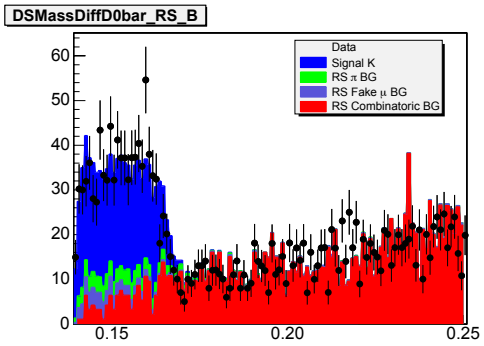

(b) $1.3 < M(\mu^+K^-) \leq 1.4$

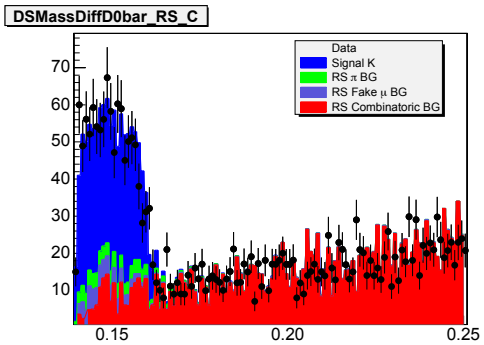

(c) $1.4 < M(\mu^+K^-) \leq 1.5$

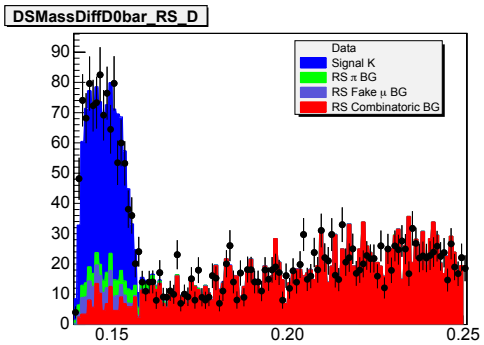

(d) $1.5 < M(\mu^+K^-) \leq 1.6$

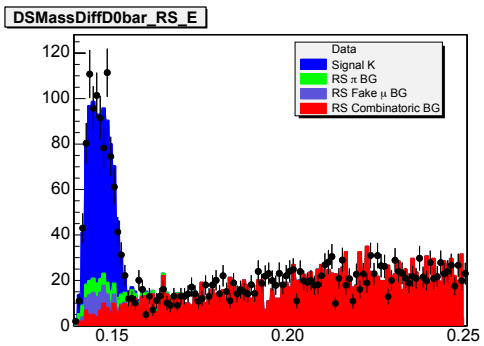

(e) $1.6 < M(\mu^+K^-) \leq 1.7$

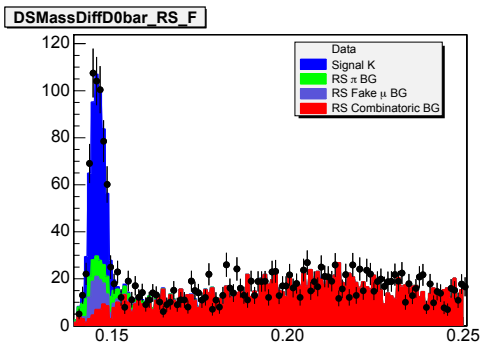

(f) $1.7 < M(\mu^+K^-) \leq 1.8$

Figure B.31: $D^{*-} Fits : \delta(M(\mu K\pi), M(\mu K)), p_T(K^-) > 4.0\text{GeV}/c, -\frac{\pi}{12} < \phi(K^-) \leq \frac{3\pi}{12}$

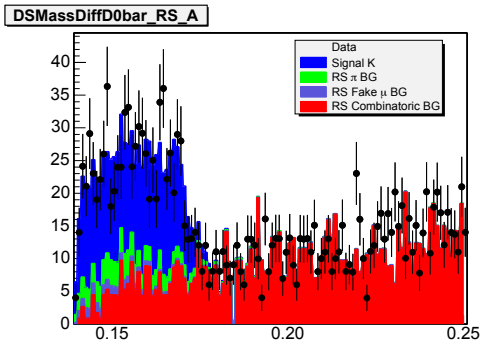

(a) $1.2 < M(\mu^+K^-) \leq 1.3$

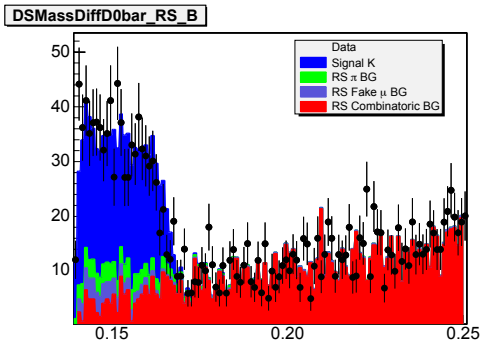

(b) $1.3 < M(\mu^+K^-) \leq 1.4$

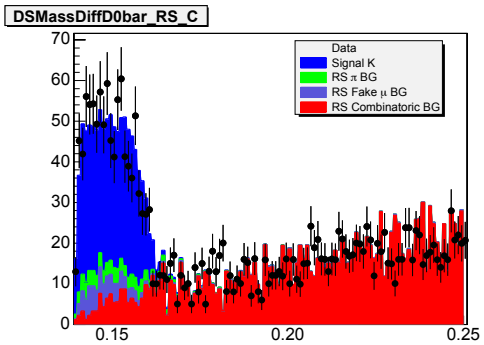

(c) $1.4 < M(\mu^+K^-) \leq 1.5$

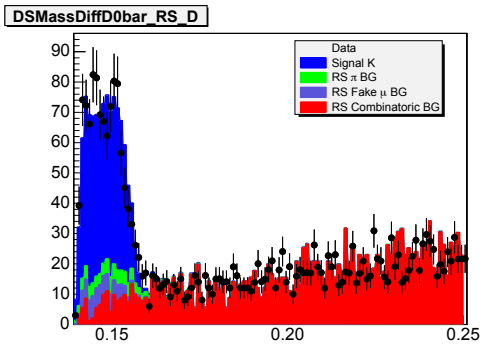

(d) $1.5 < M(\mu^+K^-) \leq 1.6$

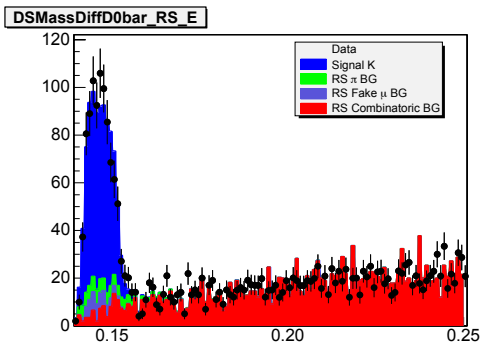

(e) $1.6 < M(\mu^+K^-) \leq 1.7$

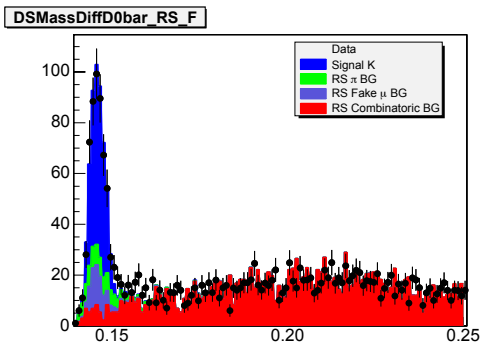

(f) $1.7 < M(\mu^+K^-) \leq 1.8$

Figure B.32: $D^{*-} Fits : \delta(M(\mu K\pi), M(\mu K)), p_T(K^-) > 4.0\text{GeV}/c,\ \frac{3\pi}{12} < \phi(K^-) \leq \frac{7\pi}{12}$

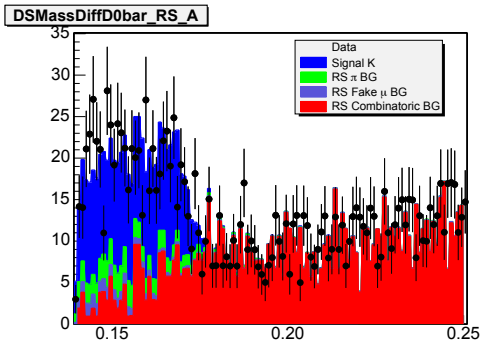

(a) $1.2 < M(\mu^+K^-) \leq 1.3$

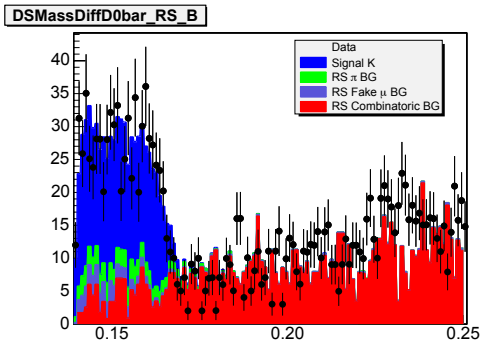

(b) $1.3 < M(\mu^+K^-) \leq 1.4$

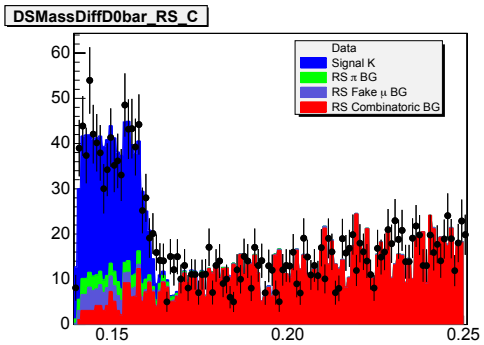

(c) $1.4 < M(\mu^+K^-) \leq 1.5$

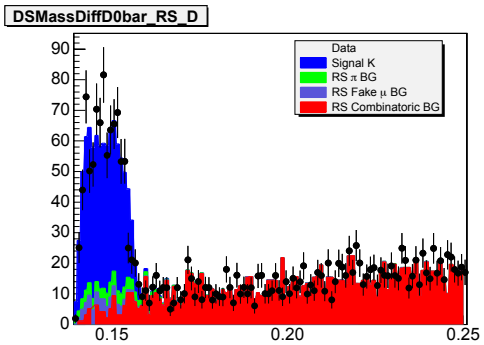

(d) $1.5 < M(\mu^+K^-) \leq 1.6$

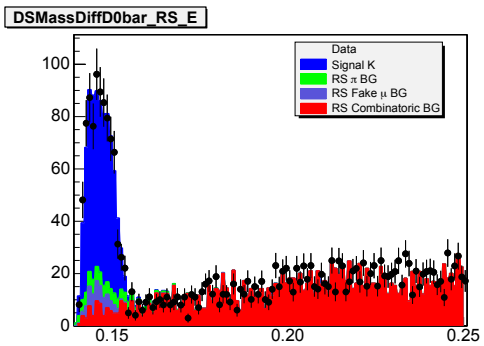

(e) $1.6 < M(\mu^+K^-) \leq 1.7$

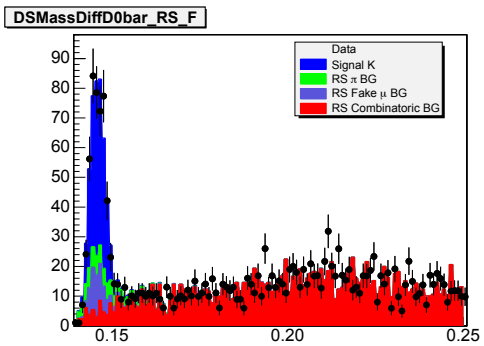

(f) $1.7 < M(\mu^+K^-) \leq 1.8$

Figure B.33: $D^{*-} Fits : \delta(M(\mu K\pi), M(\mu K)), p_T(K^-) > 4.0\text{GeV}/c,\ \frac{7\pi}{12} < \phi(K^-) \leq \frac{11\pi}{12}$

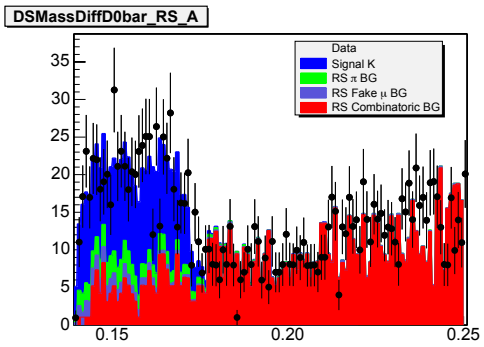

(a) $1.2 < M(\mu^+K^-) \leq 1.3$

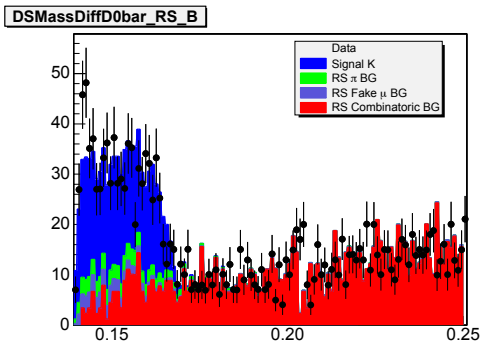

(b) $1.3 < M(\mu^+K^-) \leq 1.4$

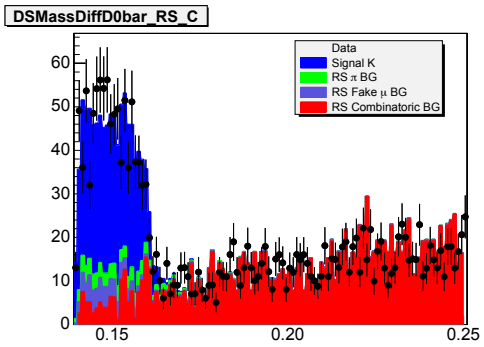

(c) $1.4 < M(\mu^+K^-) \leq 1.5$

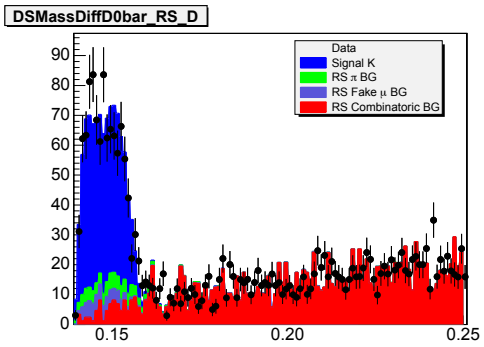

(d) $1.5 < M(\mu^+K^-) \leq 1.6$

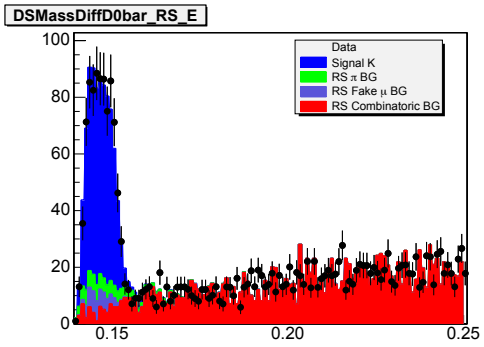

(e) $1.6 < M(\mu^+K^-) \leq 1.7$

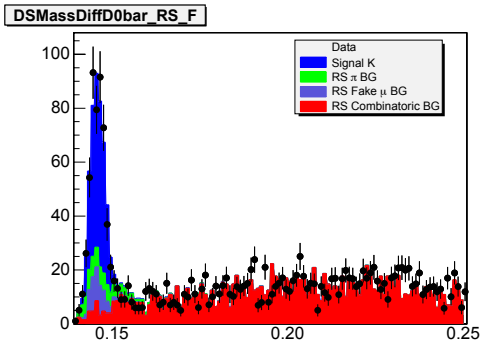

(f) $1.7 < M(\mu^+K^-) \leq 1.8$

Figure B.34: $D^{*-} Fits : \delta(M(\mu K\pi), M(\mu K)), p_T(K^-) > 4.0\text{GeV}/c,\ \frac{11\pi}{12} < \phi(K^-) \leq \frac{15\pi}{12}$

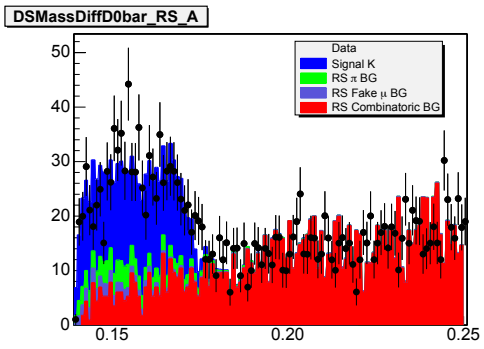

(a) $1.2 < M(\mu^+K^-) \leq 1.3$

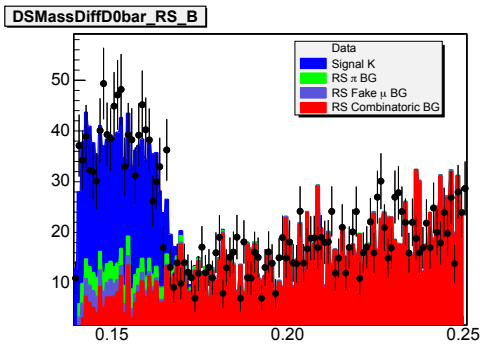

(b) $1.3 < M(\mu^+K^-) \leq 1.4$

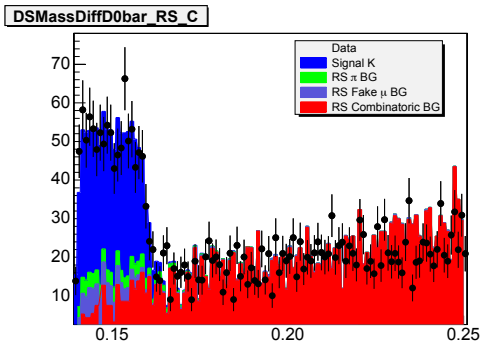

(c) $1.4 < M(\mu^+K^-) \leq 1.5$

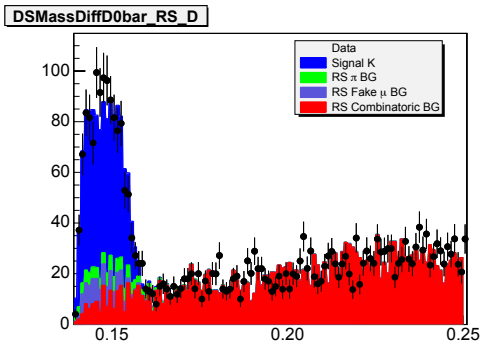

(d) $1.5 < M(\mu^+K^-) \leq 1.6$

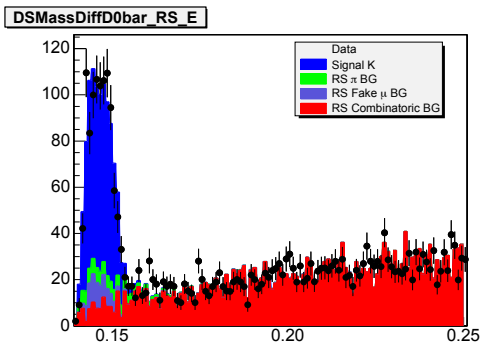

(e) $1.6 < M(\mu^+K^-) \leq 1.7$

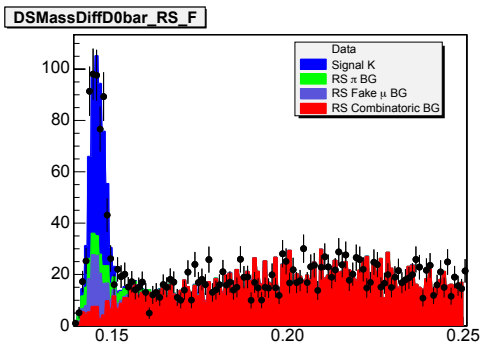

(f) $1.7 < M(\mu^+K^-) \leq 1.8$

Figure B.35: $D^{*-} Fits : \delta(M(\mu K\pi), M(\mu K)), p_T(K^-) > 4.0\text{GeV}/c,\ \frac{15\pi}{12} < \phi(K^-) \leq \frac{19\pi}{12}$

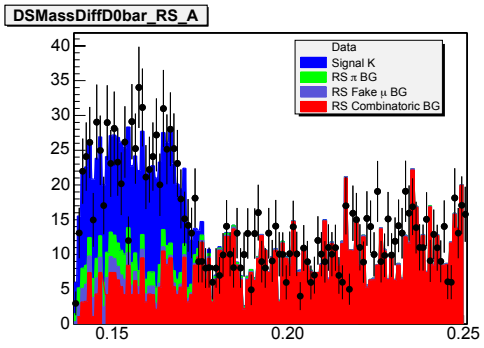

(a) $1.2 < M(\mu^+K^-) \leq 1.3$

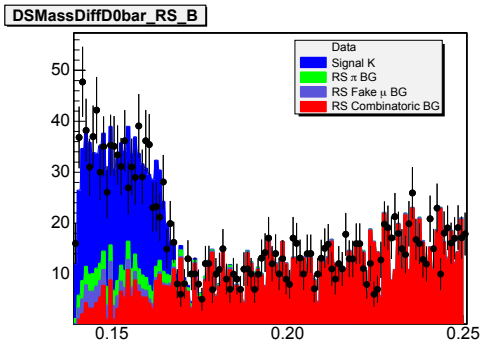

(b) $1.3 < M(\mu^+K^-) \leq 1.4$

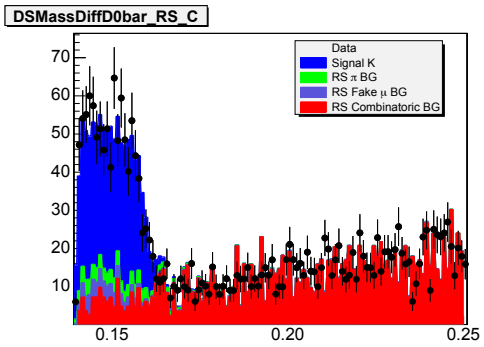

(c) $1.4 < M(\mu^+K^-) \leq 1.5$

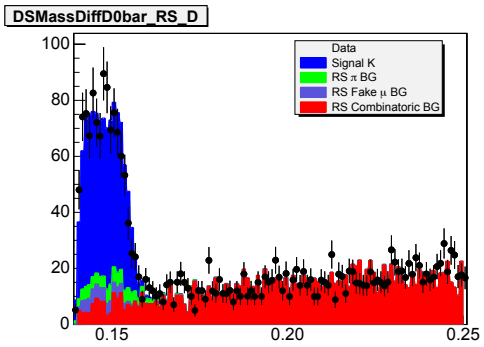

(d) $1.5 < M(\mu^+K^-) \leq 1.6$

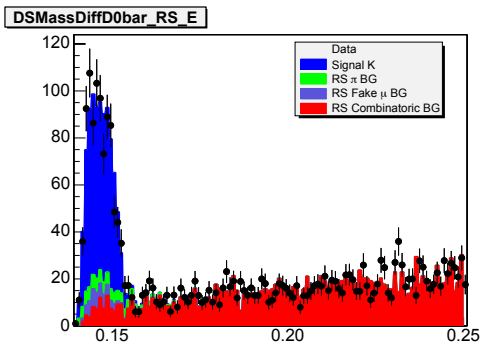

(e) $1.6 < M(\mu^+K^-) \leq 1.7$

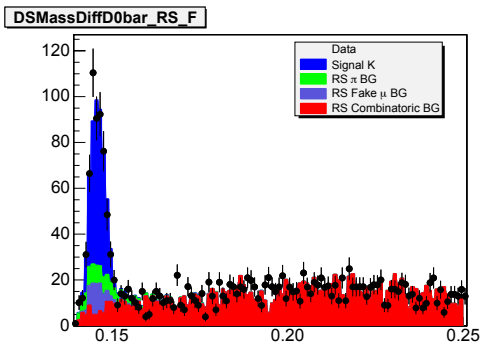

(f) $1.7 < M(\mu^+K^-) \leq 1.8$

Figure B.36: $D^{*-} Fits : \delta(M(\mu K\pi), M(\mu K)), p_T(K^-) > 4.0\text{GeV}/c,\ \frac{19\pi}{12} < \phi(K^-) \leq \frac{23\pi}{12}$

B.3 WS Fits

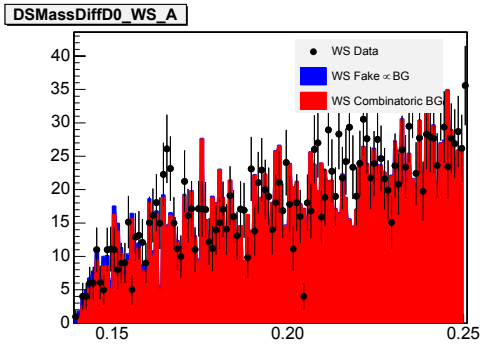

(a) $1.2 < M(\mu^+K^-) \leq 1.3$

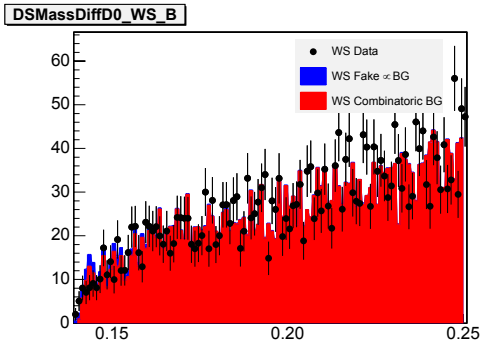

(b) $1.3 < M(\mu^+K^-) \leq 1.4$

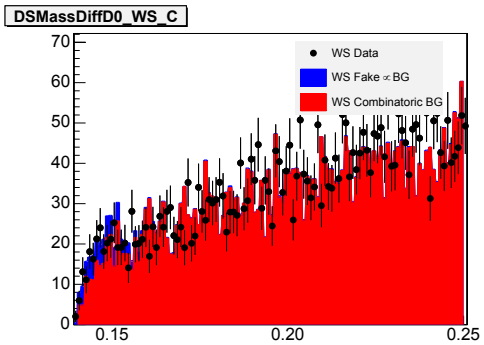

(c) $1.4 < M(\mu^+K^-) \leq 1.5$

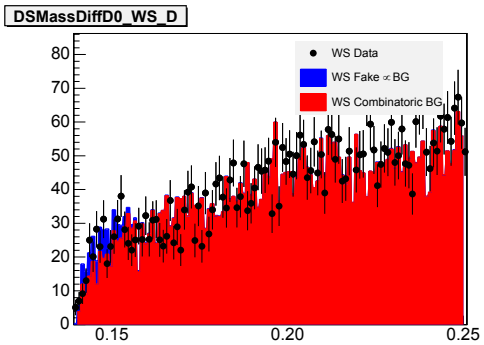

(d) $1.5 < M(\mu^+K^-) \leq 1.6$

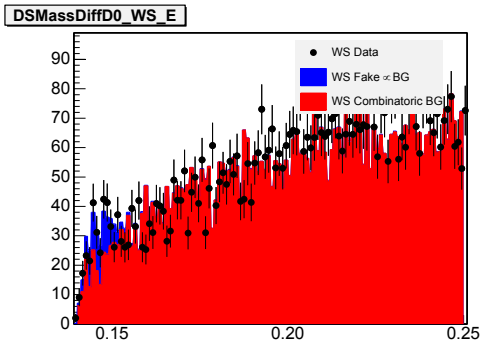

(e) $1.6 < M(\mu^+K^-) \leq 1.7$

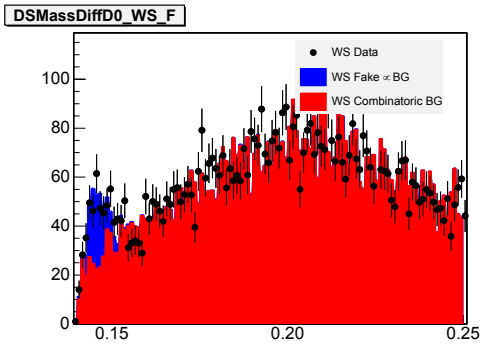

(f) $1.7 < M(\mu^+K^-) \leq 1.8$

Figure B.37: $D^{*+} Fits : \delta(M(\mu K\pi), M(\mu K)), 2.0\text{GeV}/c < p_T(K^-) \leq 3.0\text{GeV}/c, -\frac{\pi}{12} < \phi(K^-) \leq \frac{3\pi}{12}$

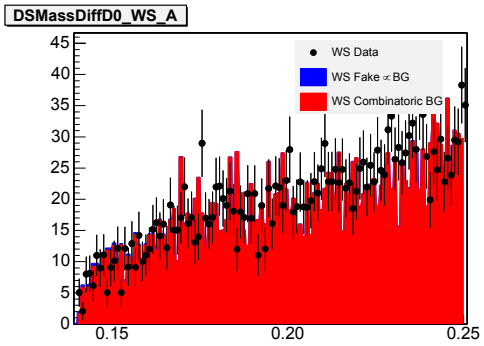

(a) $1.2 < M(\mu^+K^-) \leq 1.3$

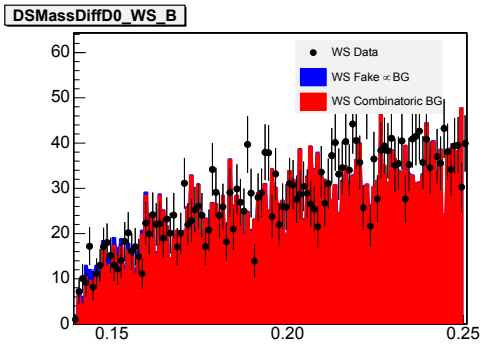

(b) $1.3 < M(\mu^+K^-) \leq 1.4$

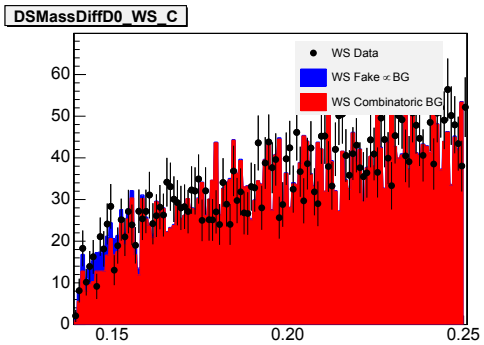

(c) $1.4 < M(\mu^+K^-) \leq 1.5$

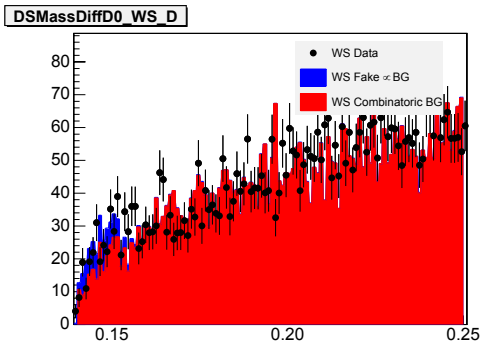

(d) $1.5 < M(\mu^+K^-) \leq 1.6$

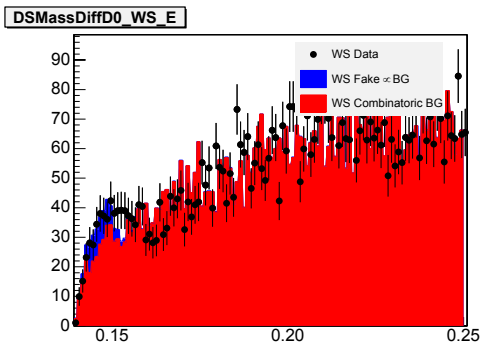

(e) $1.6 < M(\mu^+K^-) \leq 1.7$

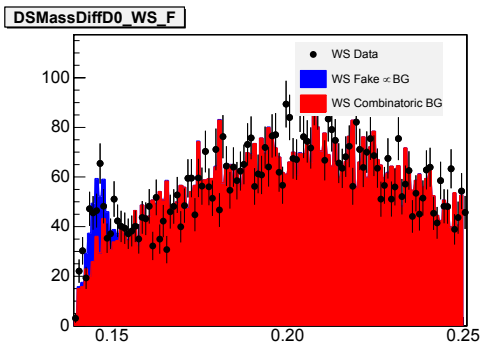

(f) $1.7 < M(\mu^+K^-) \leq 1.8$

Figure B.38: $D^{*+} Fits : \delta(M(\mu K\pi), M(\mu K)), 2.0\text{GeV}/c < p_T(K^-) \leq 3.0\text{GeV}/c$, $\frac{3\pi}{12} < \phi(K^-) \leq \frac{7\pi}{12}$

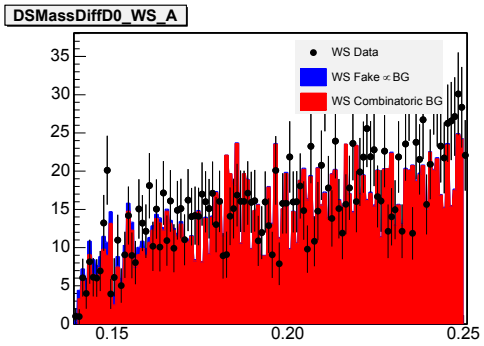

(a) $1.2 < M(\mu^+K^-) \leq 1.3$

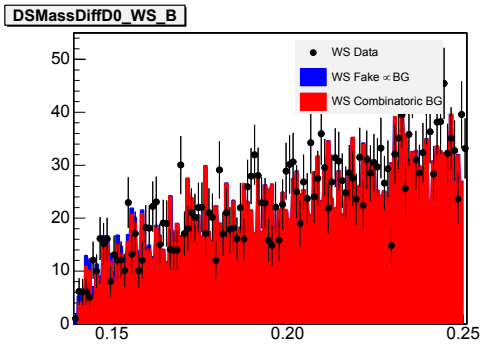

(b) $1.3 < M(\mu^+K^-) \leq 1.4$

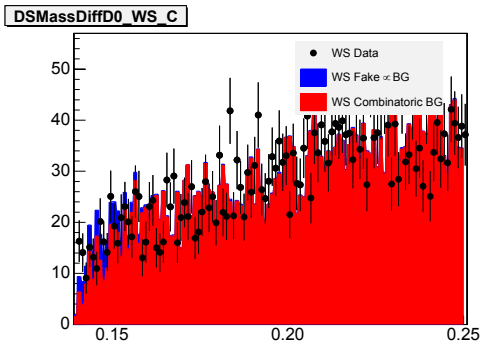

(c) $1.4 < M(\mu^+K^-) \leq 1.5$

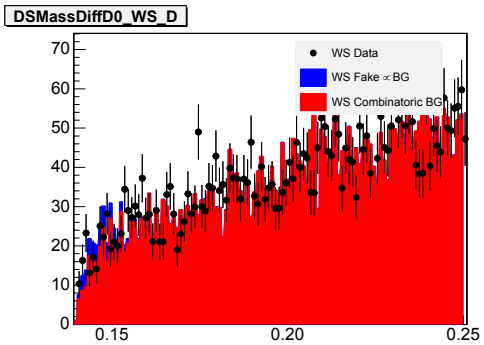

(d) $1.5 < M(\mu^+K^-) \leq 1.6$

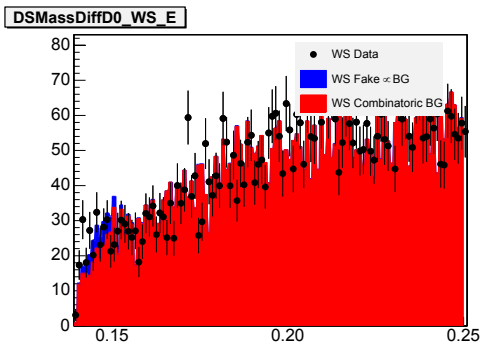

(e) $1.6 < M(\mu^+K^-) \leq 1.7$

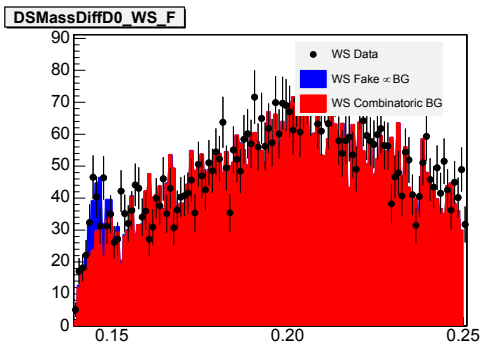

(f) $1.7 < M(\mu^+K^-) \leq 1.8$

Figure B.39: $D^{*+} Fits : \delta(M(\mu K\pi), M(\mu K)), 2.0\text{GeV}/c < p_T(K^-) \leq 3.0\text{GeV}/c$, $\frac{7\pi}{12} < \phi(K^-) \leq \frac{11\pi}{12}$

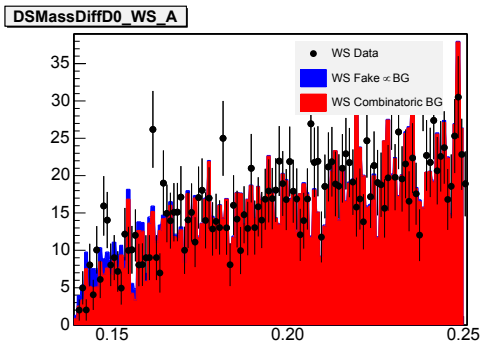

(a) $1.2 < M(\mu^+K^-) \leq 1.3$

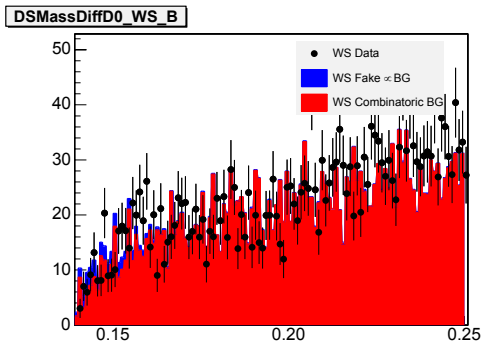

(b) $1.3 < M(\mu^+K^-) \leq 1.4$

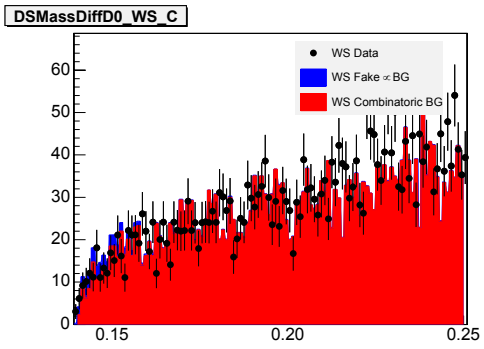

(c) $1.4 < M(\mu^+K^-) \leq 1.5$

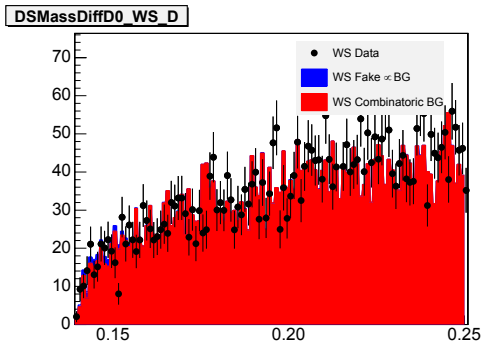

(d) $1.5 < M(\mu^+K^-) \leq 1.6$

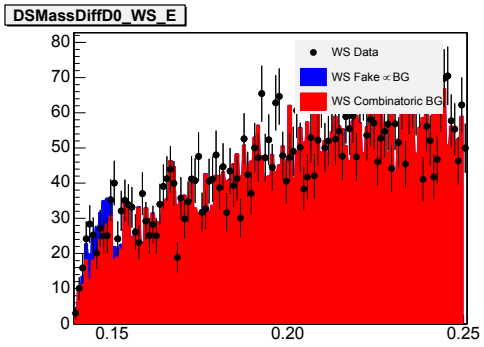

(e) $1.6 < M(\mu^+K^-) \leq 1.7$

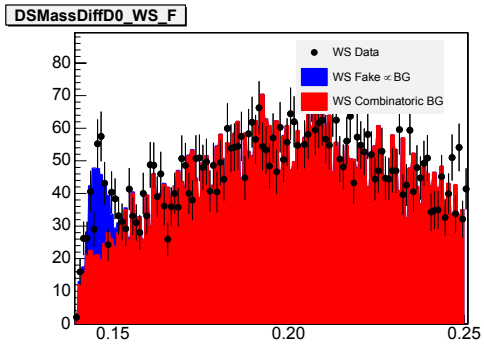

(f) $1.7 < M(\mu^+K^-) \leq 1.8$

Figure B.40: $D^{*+} Fits : \delta(M(\mu K\pi), M(\mu K)), 2.0\text{GeV}/c < p_T(K^-) \leq 3.0\text{GeV}/c$, $\frac{11\pi}{12} < \phi(K^-) \leq \frac{15\pi}{12}$

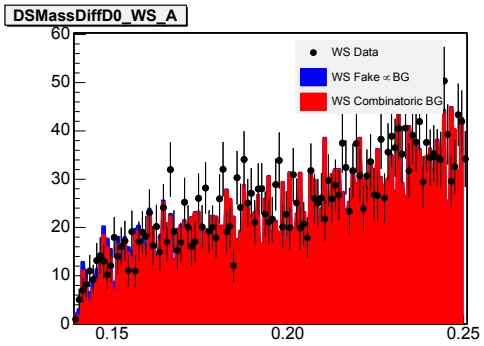

(a) $1.2 < M(\mu^+K^-) \leq 1.3$

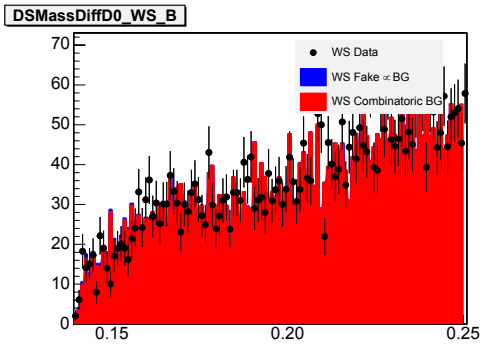

(b) $1.3 < M(\mu^+K^-) \leq 1.4$

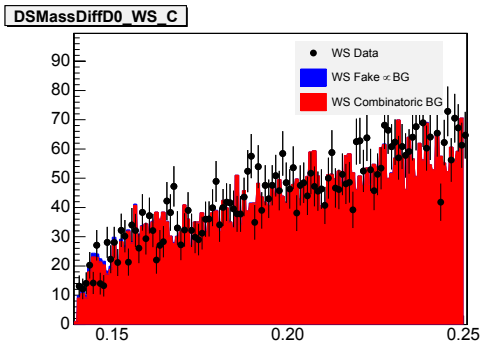

(c) $1.4 < M(\mu^+K^-) \leq 1.5$

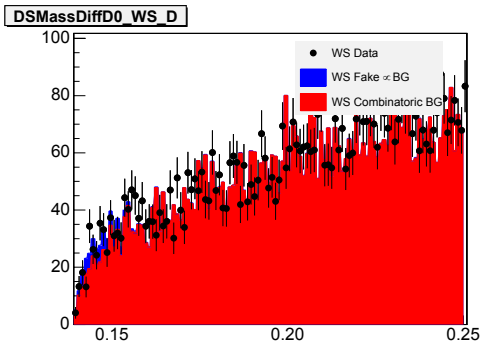

(d) $1.5 < M(\mu^+K^-) \leq 1.6$

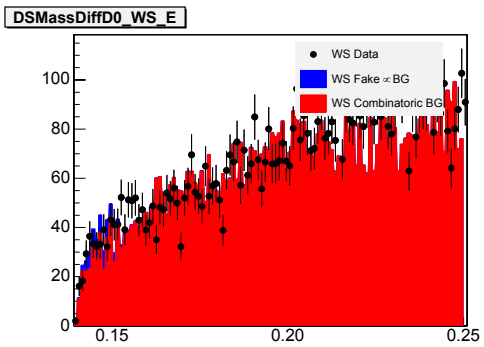

(e) $1.6 < M(\mu^+K^-) \leq 1.7$

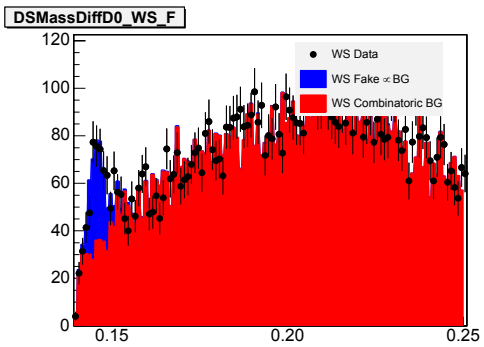

(f) $1.7 < M(\mu^+K^-) \leq 1.8$

Figure B.41: $D^{*+} Fits : \delta(M(\mu K\pi), M(\mu K)), 2.0\text{GeV}/c < p_T(K^-) \leq 3.0\text{GeV}/c$, $\frac{15\pi}{12} < \phi(K^-) \leq \frac{19\pi}{12}$

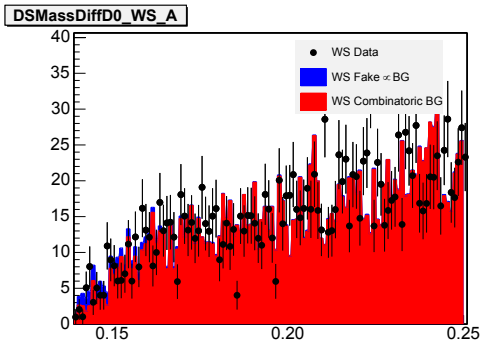

(a) $1.2 < M(\mu^+K^-) \leq 1.3$

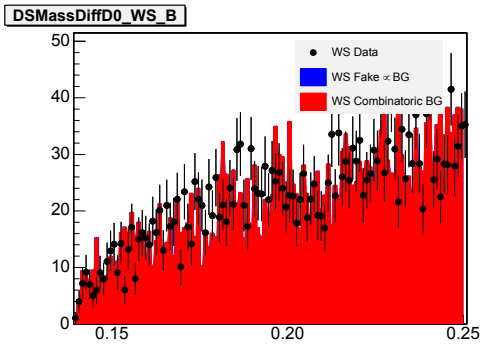

(b) $1.3 < M(\mu^+K^-) \leq 1.4$

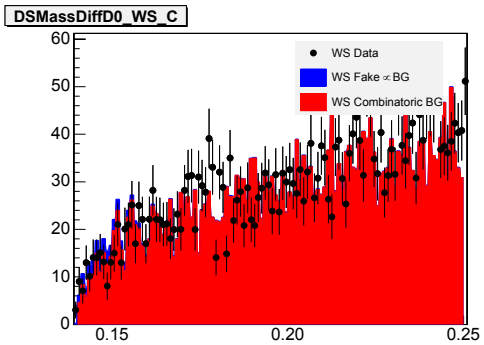

(c) $1.4 < M(\mu^+K^-) \leq 1.5$

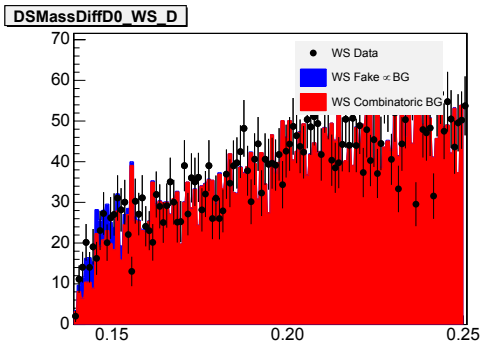

(d) $1.5 < M(\mu^+K^-) \leq 1.6$

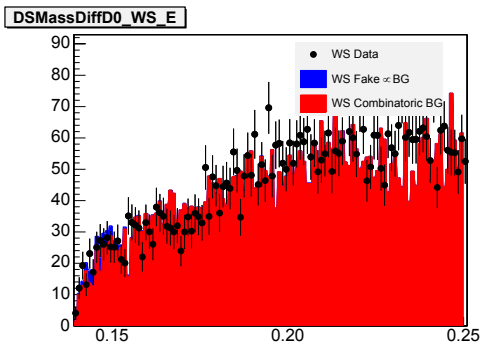

(e) $1.6 < M(\mu^+K^-) \leq 1.7$

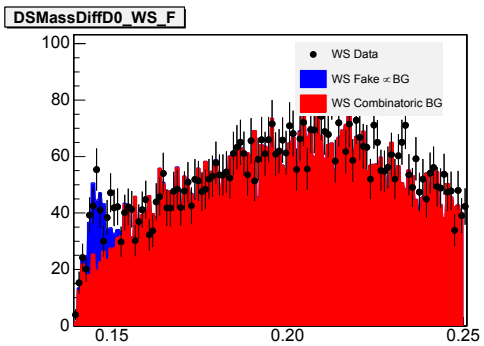

(f) $1.7 < M(\mu^+K^-) \leq 1.8$

Figure B.42: $D^{*+} Fits : \delta(M(\mu K\pi), M(\mu K)), 2.0\text{GeV}/c < p_T(K^-) \leq 3.0\text{GeV}/c$, $\frac{19\pi}{12} < \phi(K^-) \leq \frac{23\pi}{12}$

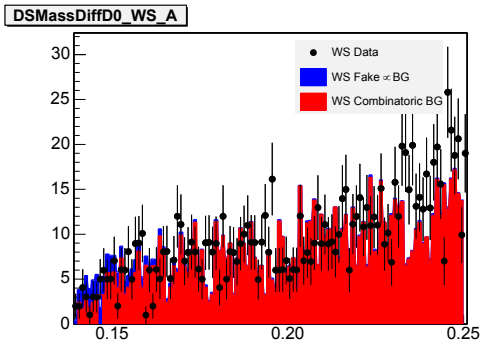

(a) $1.2 < M(\mu^+K^-) \leq 1.3$

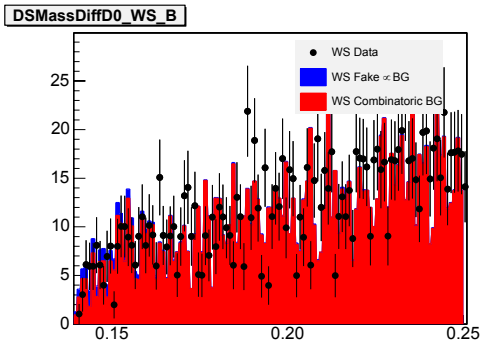

(b) $1.3 < M(\mu^+K^-) \leq 1.4$

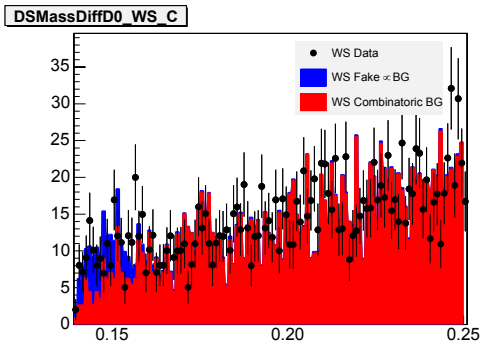

(c) $1.4 < M(\mu^+K^-) \leq 1.5$

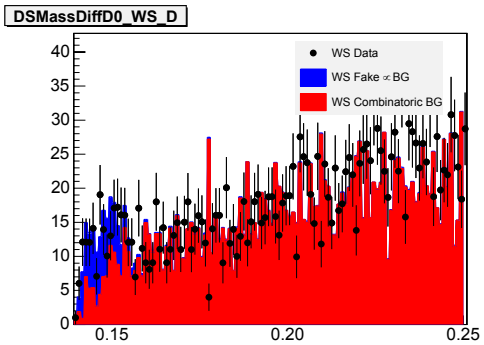

(d) $1.5 < M(\mu^+K^-) \leq 1.6$

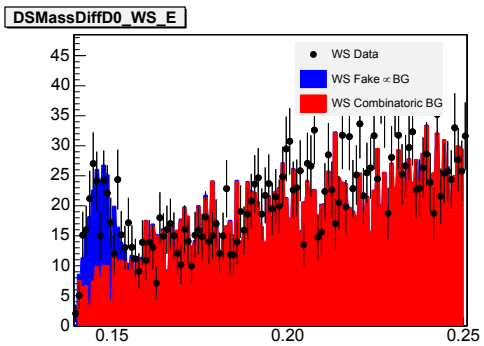

(e) $1.6 < M(\mu^+K^-) \leq 1.7$

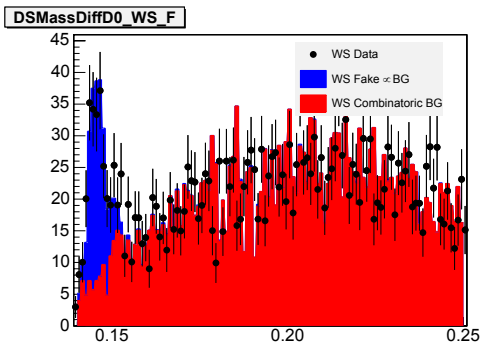

(f) $1.7 < M(\mu^+K^-) \leq 1.8$

Figure B.43: $D^{*+} Fits : \delta(M(\mu K\pi), M(\mu K)), 3.0\text{GeV}/c < p_T(K^-) \leq 4.0\text{GeV}/c, -\frac{\pi}{12} < \phi(K^-) \leq \frac{3\pi}{12}$

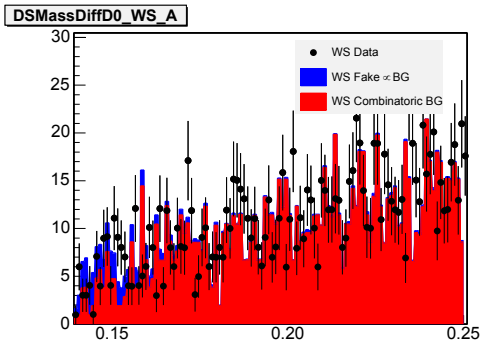

(a) $1.2 < M(\mu^+K^-) \leq 1.3$

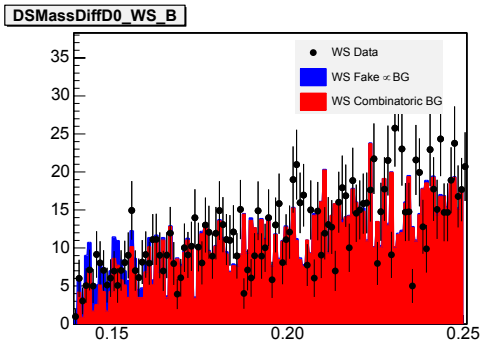

(b) $1.3 < M(\mu^+K^-) \leq 1.4$

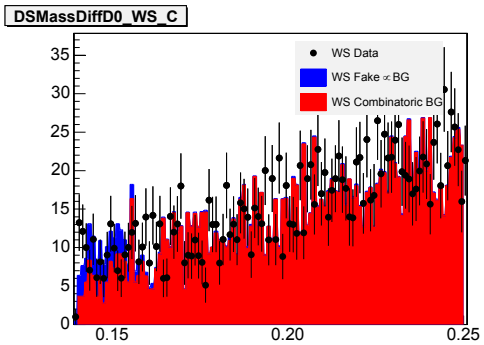

(c) $1.4 < M(\mu^+K^-) \leq 1.5$

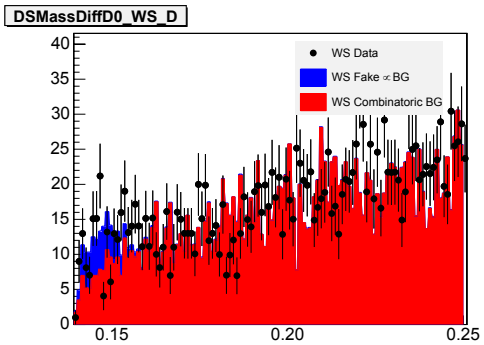

(d) $1.5 < M(\mu^+K^-) \leq 1.6$

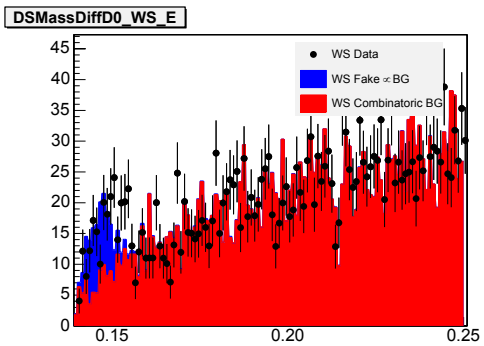

(e) $1.6 < M(\mu^+K^-) \leq 1.7$

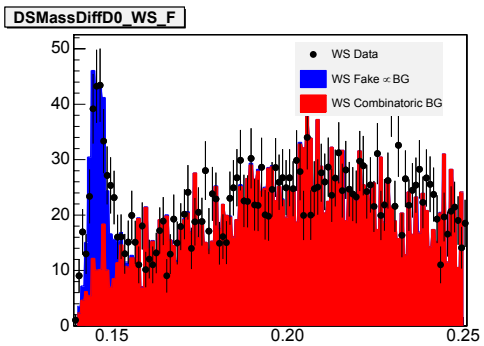

(f) $1.7 < M(\mu^+K^-) \leq 1.8$

Figure B.44: $D^{*+} Fits : \delta(M(\mu K\pi), M(\mu K)), 3.0\text{GeV}/c < p_T(K^-) \leq 4.0\text{GeV}/c,\ \frac{3\pi}{12} < \phi(K^-) \leq \frac{7\pi}{12}$

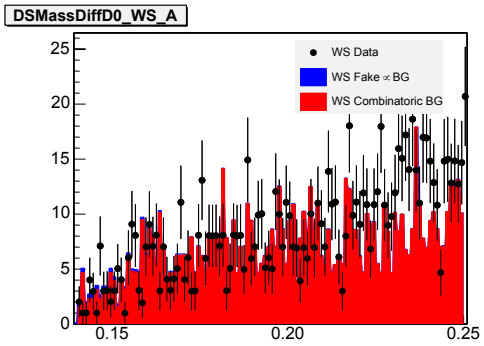

(a) $1.2 < M(\mu^+K^-) \leq 1.3$

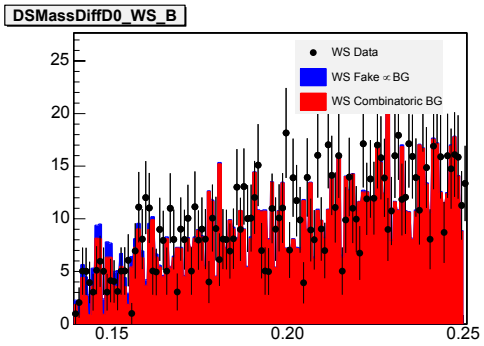

(b) $1.3 < M(\mu^+K^-) \leq 1.4$

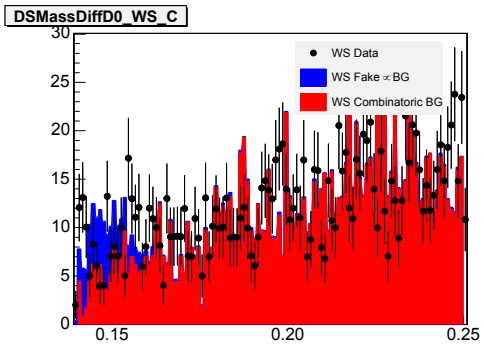

(c) $1.4 < M(\mu^+K^-) \leq 1.5$

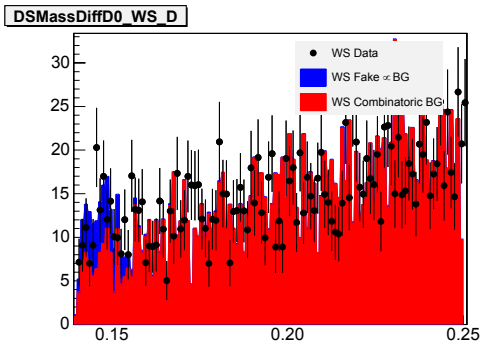

(d) $1.5 < M(\mu^+K^-) \leq 1.6$

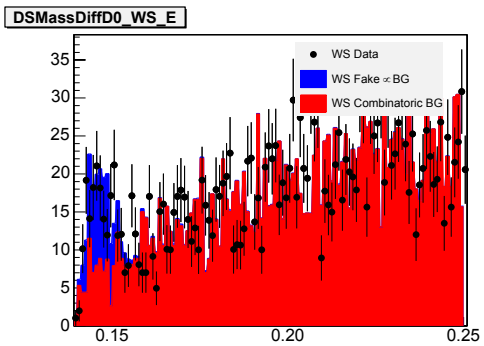

(e) $1.6 < M(\mu^+K^-) \leq 1.7$

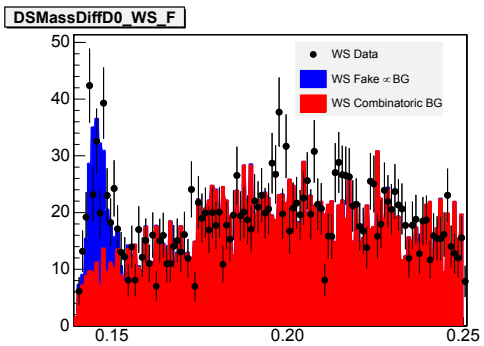

(f) $1.7 < M(\mu^+K^-) \leq 1.8$

Figure B.45: $D^{*+} Fits : \delta(M(\mu K\pi), M(\mu K)), 3.0\text{GeV}/c < p_T(K^-) \leq 4.0\text{GeV}/c$, $\frac{7\pi}{12} < \phi(K^-) \leq \frac{11\pi}{12}$

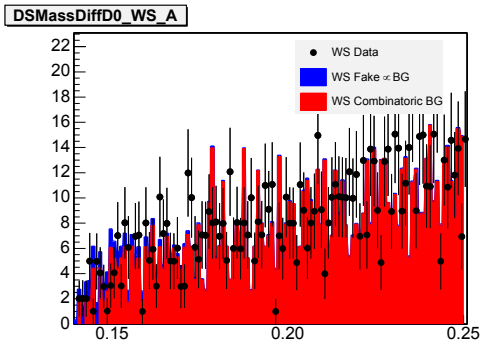

(a) $1.2 < M(\mu^+K^-) \leq 1.3$

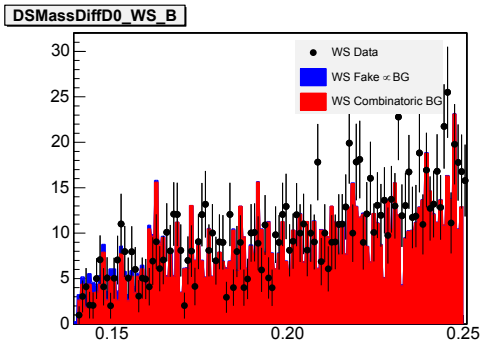

(b) $1.3 < M(\mu^+K^-) \leq 1.4$

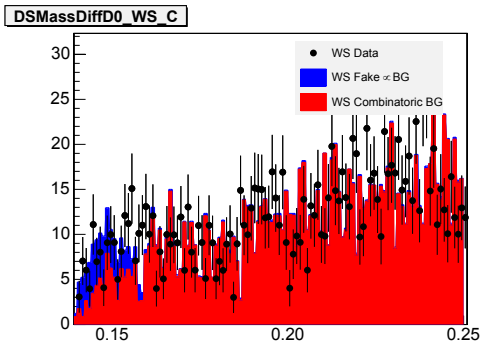

(c) $1.4 < M(\mu^+K^-) \leq 1.5$

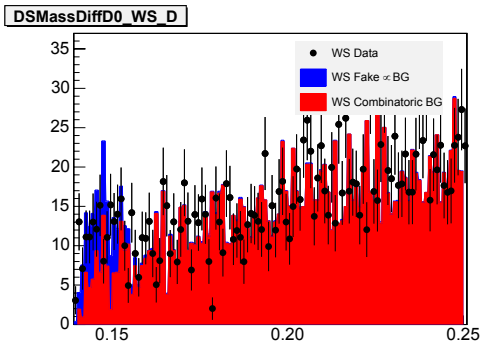

(d) $1.5 < M(\mu^+K^-) \leq 1.6$

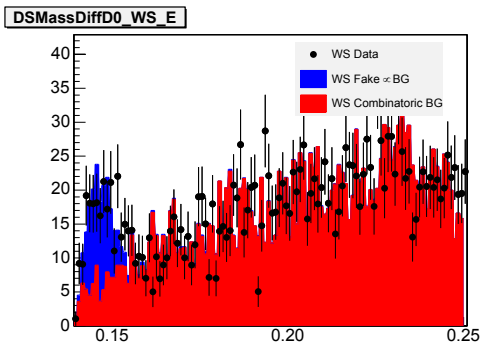

(e) $1.6 < M(\mu^+K^-) \leq 1.7$

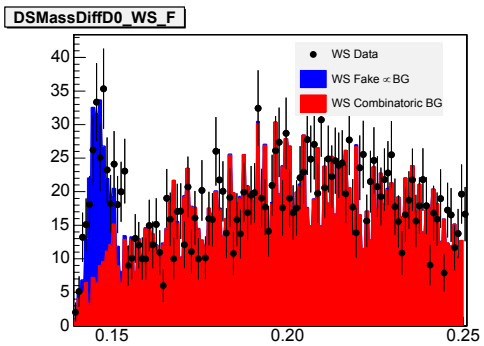

(f) $1.7 < M(\mu^+K^-) \leq 1.8$

Figure B.46: $D^{*+} Fits : \delta(M(\mu K\pi), M(\mu K)), 3.0\text{GeV}/c < p_T(K^-) \leq 4.0\text{GeV}/c$, $\frac{11\pi}{12} < \phi(K^-) \leq \frac{15\pi}{12}$

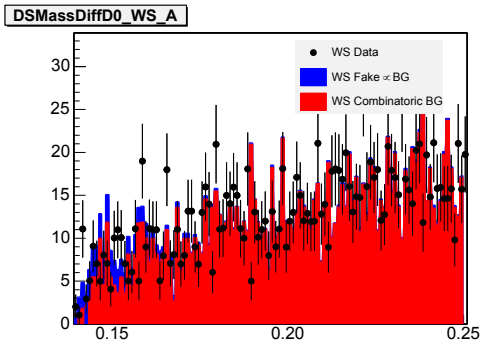

(a) $1.2 < M(\mu^+K^-) \leq 1.3$

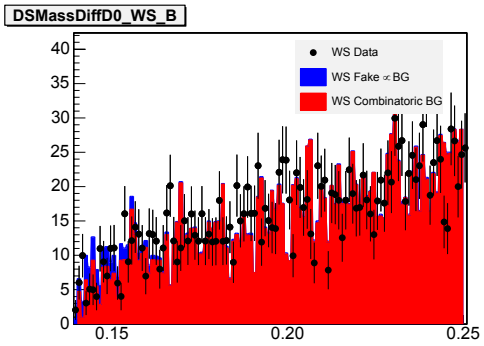

(b) $1.3 < M(\mu^+K^-) \leq 1.4$

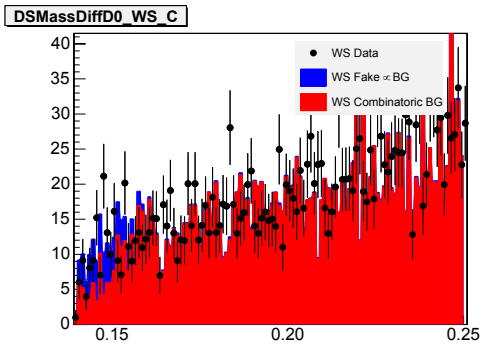

(c) $1.4 < M(\mu^+K^-) \leq 1.5$

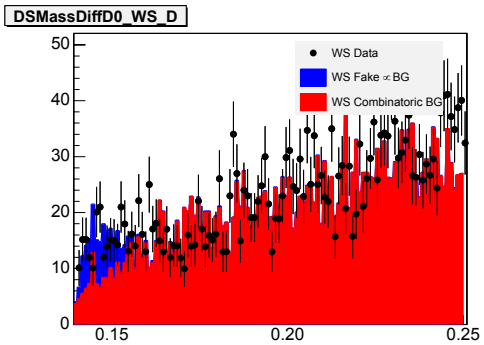

(d) $1.5 < M(\mu^+K^-) \leq 1.6$

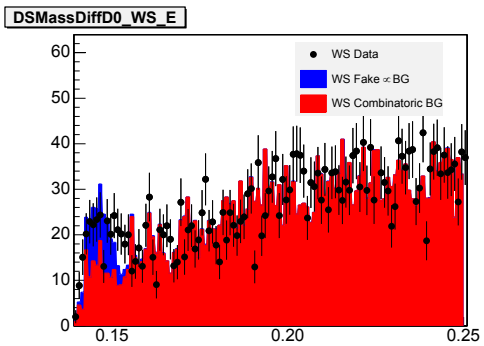

(e) $1.6 < M(\mu^+K^-) \leq 1.7$

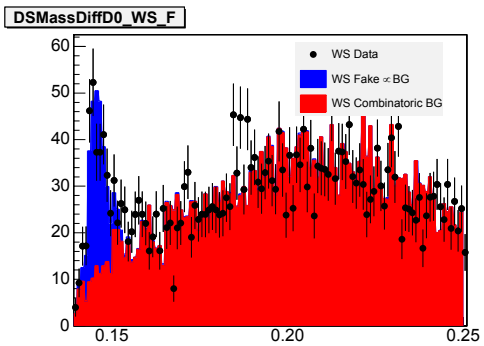

(f) $1.7 < M(\mu^+K^-) \leq 1.8$

Figure B.47: $D^{*+} Fits : \delta(M(\mu K\pi), M(\mu K)), 3.0\text{GeV}/c < p_T(K^-) \leq 4.0\text{GeV}/c$, $\frac{15\pi}{12} < \phi(K^-) \leq \frac{19\pi}{12}$

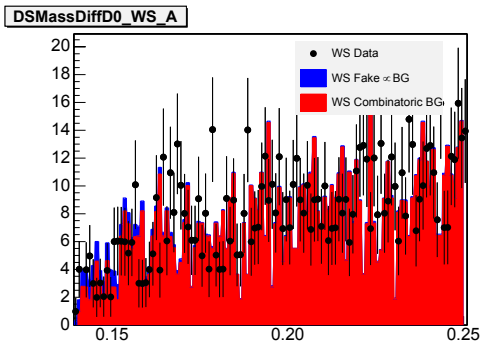

(a) $1.2 < M(\mu^+K^-) \leq 1.3$

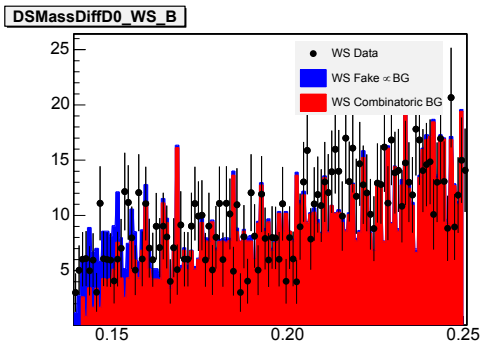

(b) $1.3 < M(\mu^+K^-) \leq 1.4$

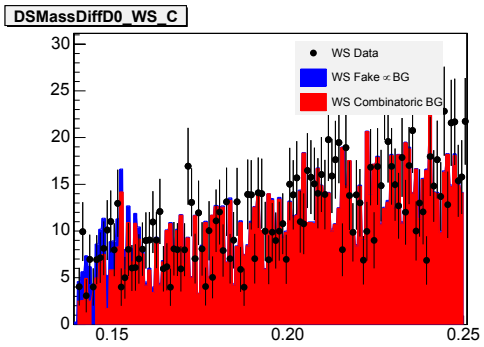

(c) $1.4 < M(\mu^+K^-) \leq 1.5$

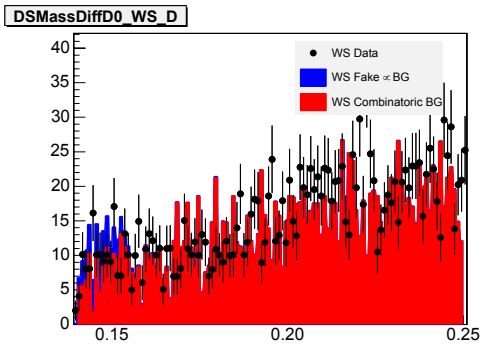

(d) $1.5 < M(\mu^+K^-) \leq 1.6$

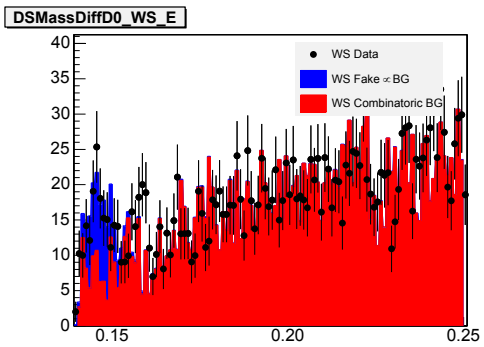

(e) $1.6 < M(\mu^+K^-) \leq 1.7$

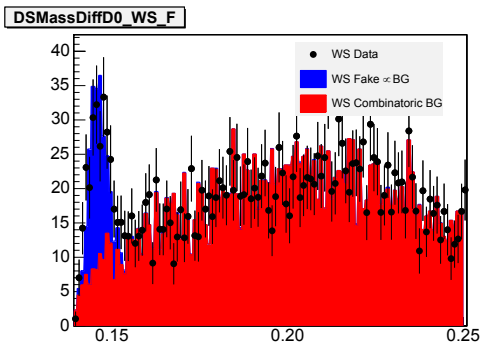

(f) $1.7 < M(\mu^+K^-) \leq 1.8$

Figure B.48: $D^{*+} Fits : \delta(M(\mu K\pi), M(\mu K)), 3.0\text{GeV}/c < p_T(K^-) \leq 4.0\text{GeV}/c$, $\frac{19\pi}{12} < \phi(K^-) \leq \frac{23\pi}{12}$

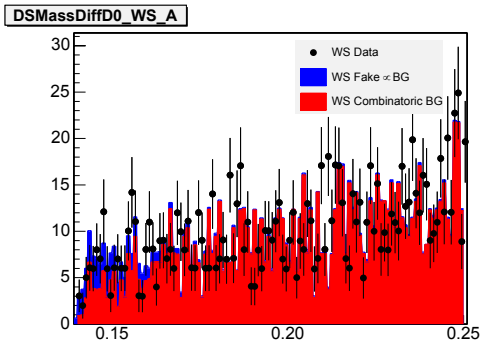

(a) $1.2 < M(\mu^+K^-) \leq 1.3$

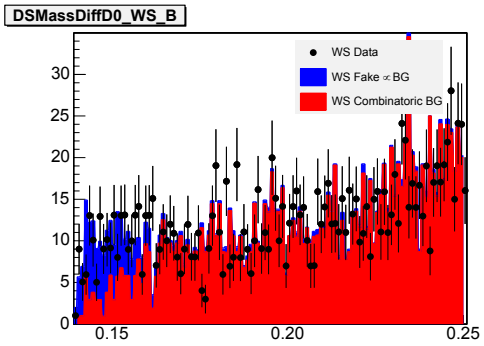

(b) $1.3 < M(\mu^+K^-) \leq 1.4$

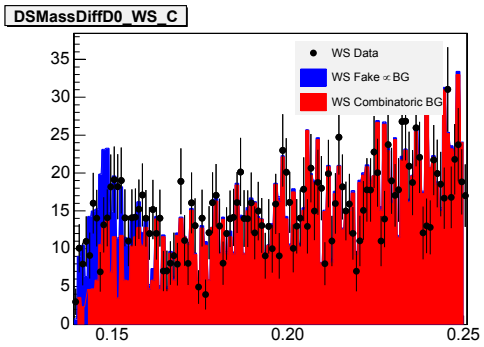

(c) $1.4 < M(\mu^+K^-) \leq 1.5$

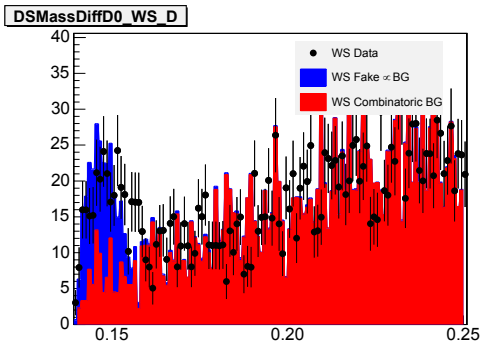

(d) $1.5 < M(\mu^+K^-) \leq 1.6$

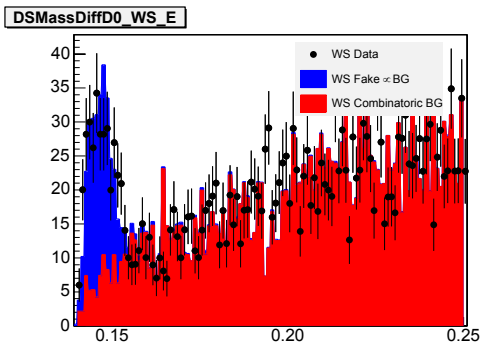

(e) $1.6 < M(\mu^+K^-) \leq 1.7$

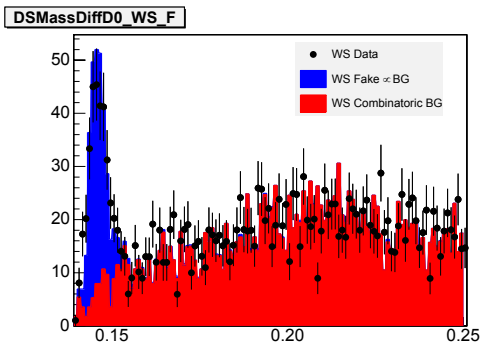

(f) $1.7 < M(\mu^+K^-) \leq 1.8$

Figure B.49: $D^{*+}Fits : \delta(M(\mu K\pi), M(\mu K)), p_T(K^-) > 4.0\text{GeV}/c, -\frac{\pi}{12} < \phi(K^-) \leq \frac{3\pi}{12}$

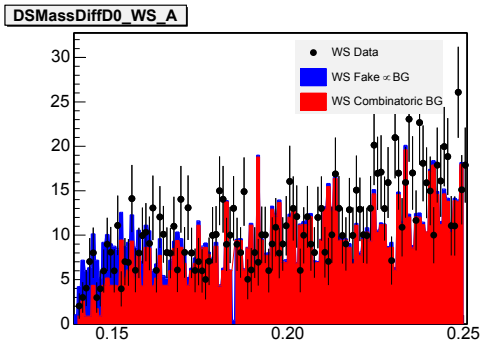

(a) $1.2 < M(\mu^+K^-) \leq 1.3$

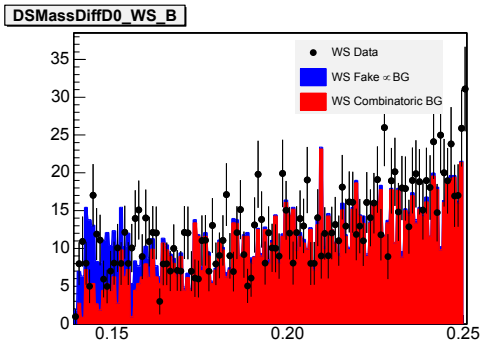

(b) $1.3 < M(\mu^+K^-) \leq 1.4$

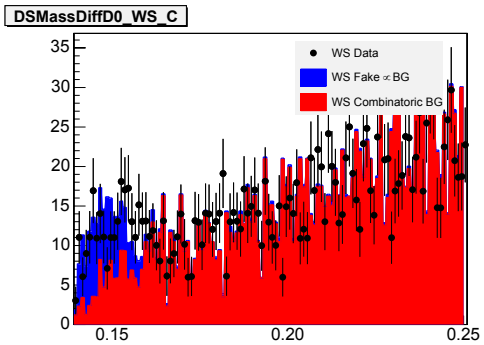

(c) $1.4 < M(\mu^+K^-) \leq 1.5$

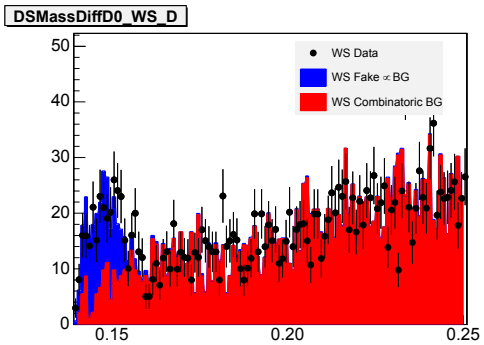

(d) $1.5 < M(\mu^+K^-) \leq 1.6$

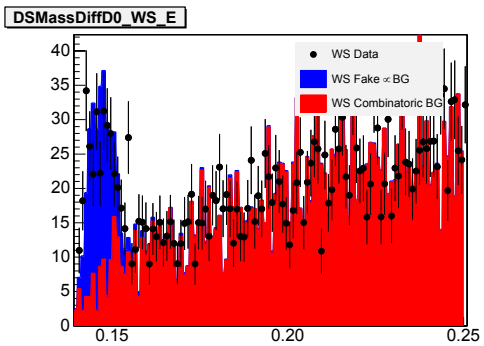

(e) $1.6 < M(\mu^+K^-) \leq 1.7$

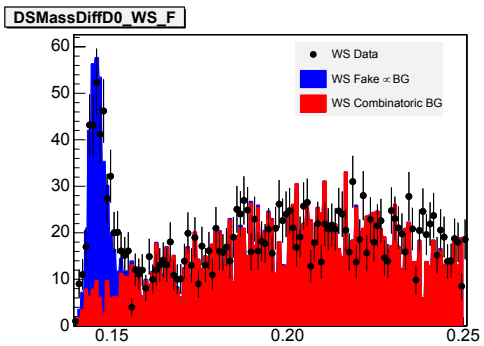

(f) $1.7 < M(\mu^+K^-) \leq 1.8$

Figure B.50: $D^{*+} Fits : \delta(M(\mu K\pi), M(\mu K)), p_T(K^-) > 4.0\text{GeV}/c,\ \frac{3\pi}{12} < \phi(K^-) \leq \frac{7\pi}{12}$

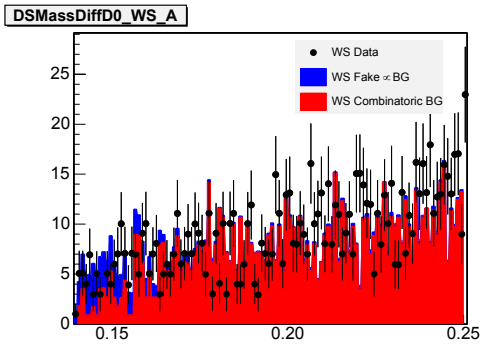

(a) $1.2 < M(\mu^+K^-) \leq 1.3$

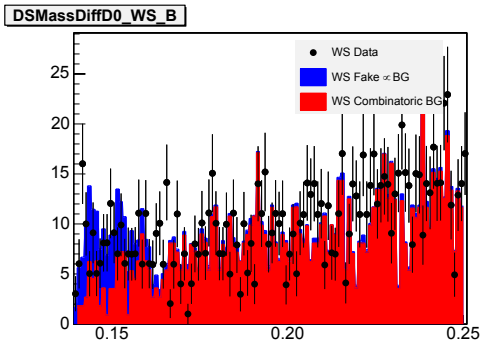

(b) $1.3 < M(\mu^+K^-) \leq 1.4$

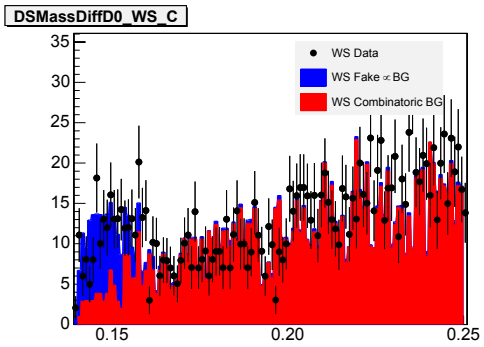

(c) $1.4 < M(\mu^+K^-) \leq 1.5$

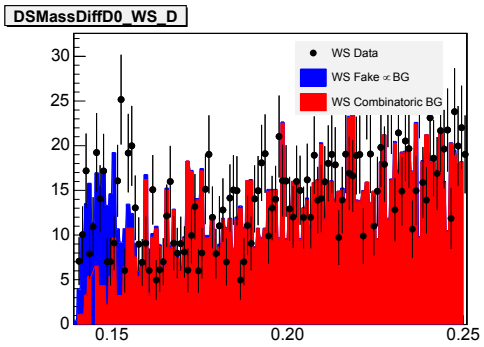

(d) $1.5 < M(\mu^+K^-) \leq 1.6$

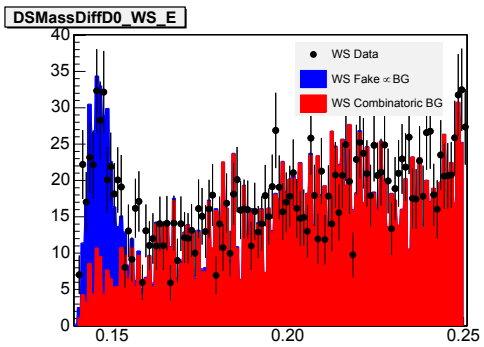

(e) $1.6 < M(\mu^+K^-) \leq 1.7$

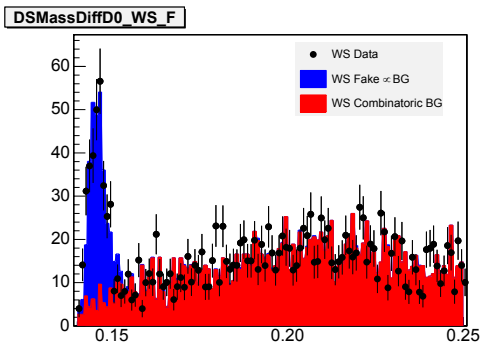

(f) $1.7 < M(\mu^+K^-) \leq 1.8$

Figure B.51: $D^{*+} Fits : \delta(M(\mu K\pi), M(\mu K)), p_T(K^-) > 4.0\text{GeV}/c,\ \frac{7\pi}{12} < \phi(K^-) \leq \frac{11\pi}{12}$

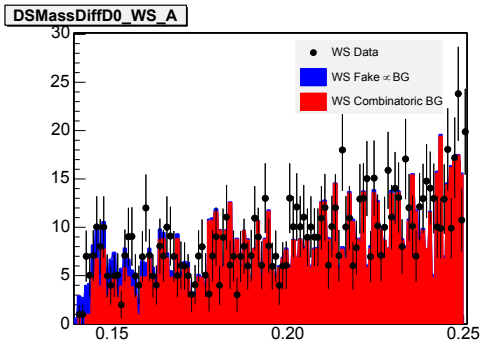

(a) $1.2 < M(\mu^+K^-) \leq 1.3$

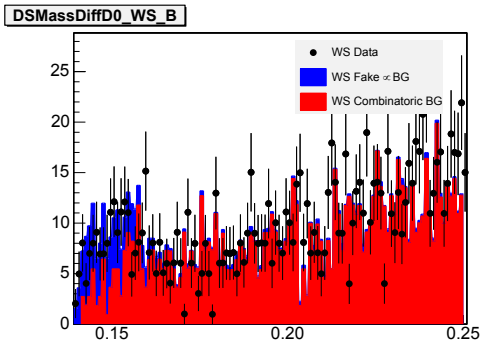

(b) $1.3 < M(\mu^+K^-) \leq 1.4$

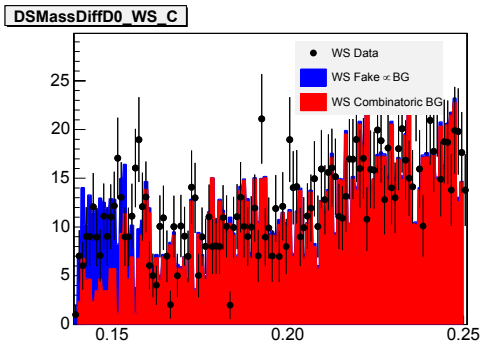

(c) $1.4 < M(\mu^+K^-) \leq 1.5$

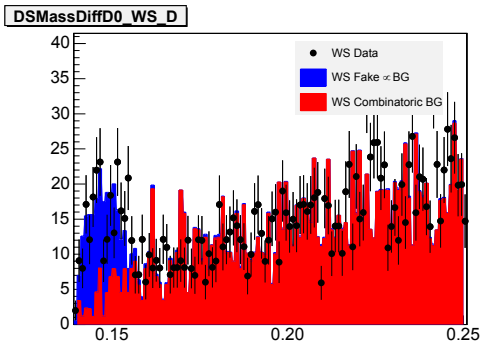

(d) $1.5 < M(\mu^+K^-) \leq 1.6$

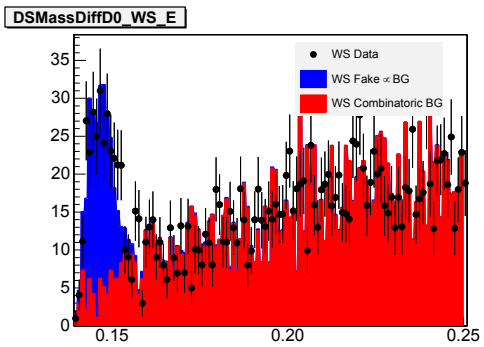

(e) $1.6 < M(\mu^+K^-) \leq 1.7$

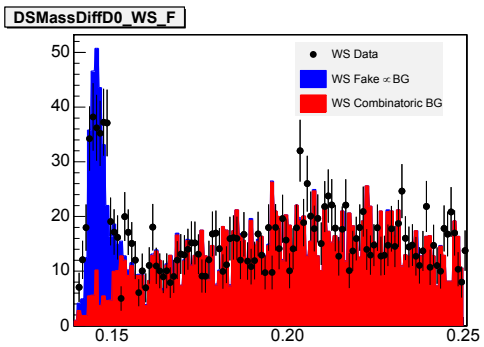

(f) $1.7 < M(\mu^+K^-) \leq 1.8$

Figure B.52: $D^{*+} Fits : \delta(M(\mu K\pi), M(\mu K)), p_T(K^-) > 4.0\text{GeV}/c,\ \frac{11\pi}{12} < \phi(K^-) \leq \frac{15\pi}{12}$

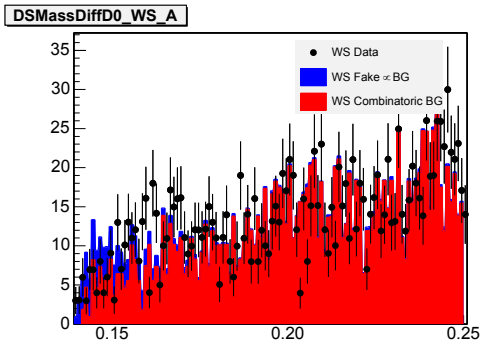

(a) $1.2 < M(\mu^+K^-) \leq 1.3$

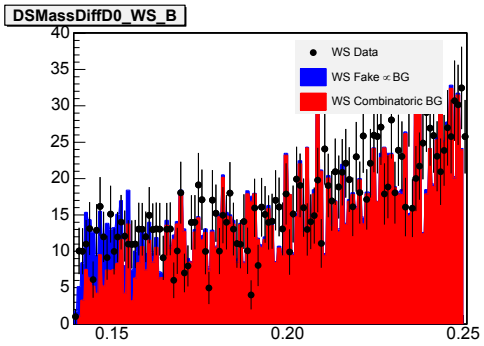

(b) $1.3 < M(\mu^+K^-) \leq 1.4$

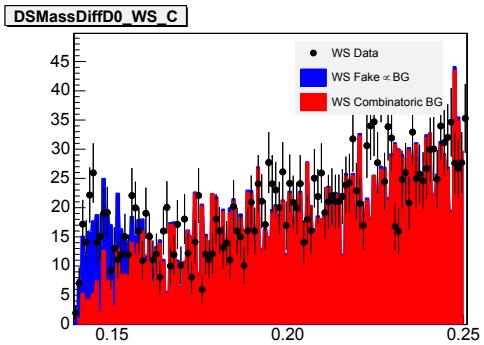

(c) $1.4 < M(\mu^+K^-) \leq 1.5$

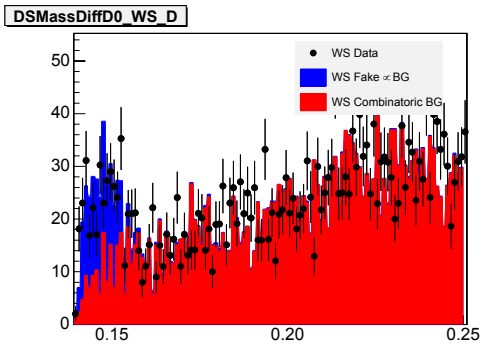

(d) $1.5 < M(\mu^+K^-) \leq 1.6$

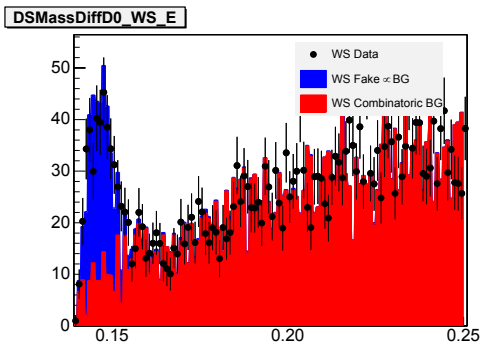

(e) $1.6 < M(\mu^+K^-) \leq 1.7$

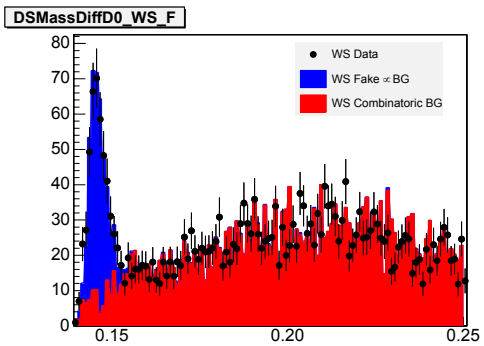

(f) $1.7 < M(\mu^+K^-) \leq 1.8$

Figure B.53: $D^{*+} Fits : \delta(M(\mu K\pi), M(\mu K)), p_T(K^-) > 4.0\text{GeV}/c,\ \frac{15\pi}{12} < \phi(K^-) \leq \frac{19\pi}{12}$

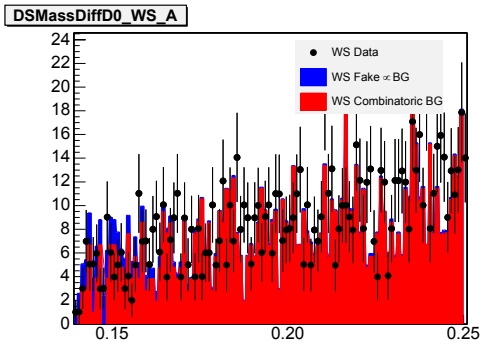

(a) $1.2 < M(\mu^+K^-) \leq 1.3$

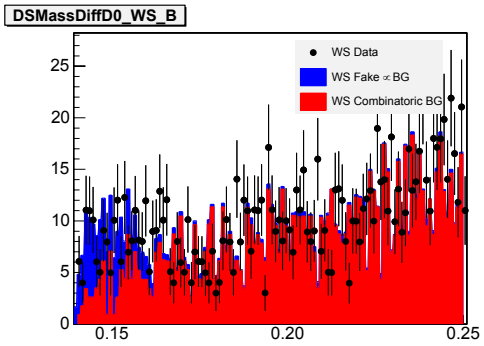

(b) $1.3 < M(\mu^+K^-) \leq 1.4$

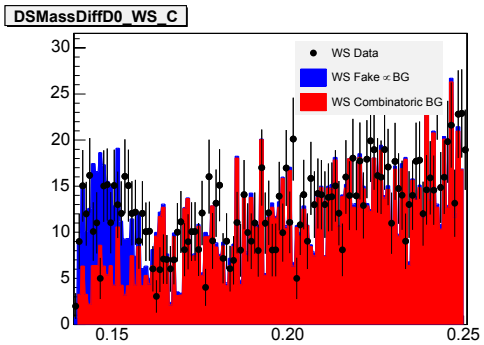

(c) $1.4 < M(\mu^+K^-) \leq 1.5$

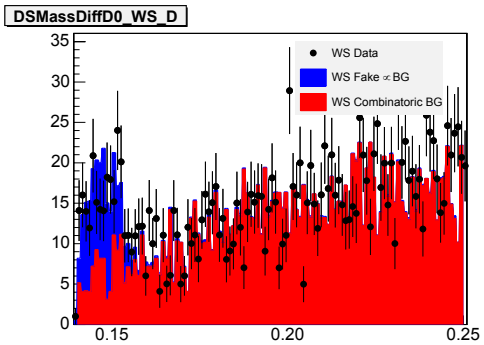

(d) $1.5 < M(\mu^+K^-) \leq 1.6$

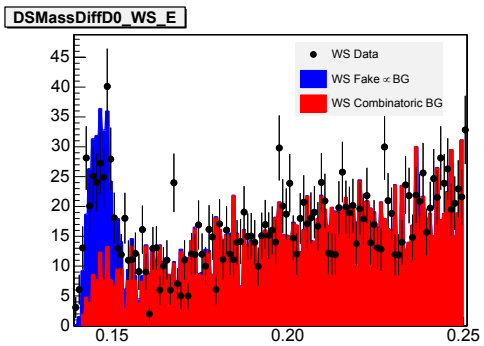

(e) $1.6 < M(\mu^+K^-) \leq 1.7$

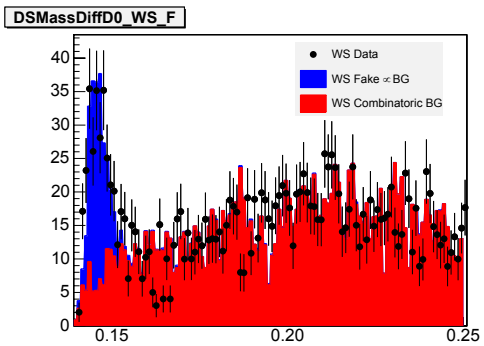

(f) $1.7 < M(\mu^+K^-) \leq 1.8$

Figure B.54: $D^{*+} Fits : \delta(M(\mu K\pi), M(\mu K)), p_T(K^-) > 4.0\text{GeV}/c,\ \frac{19\pi}{12} < \phi(K^-) \leq \frac{23\pi}{12}$

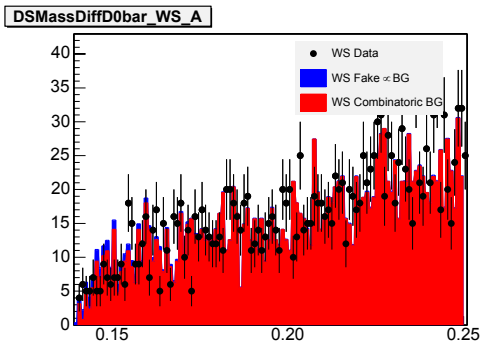

(a) $1.2 < M(\mu^+K^-) \leq 1.3$

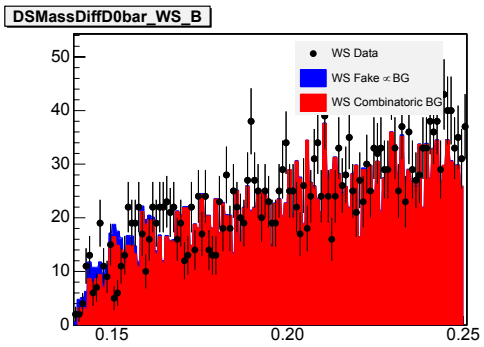

(b) $1.3 < M(\mu^+K^-) \leq 1.4$

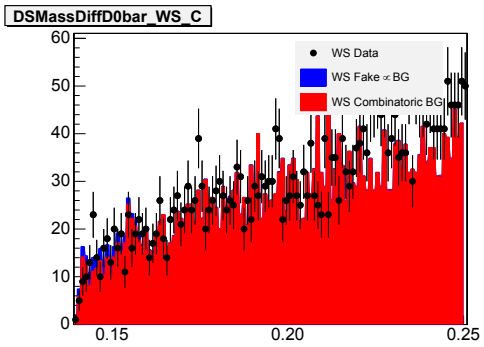

(c) $1.4 < M(\mu^+K^-) \leq 1.5$

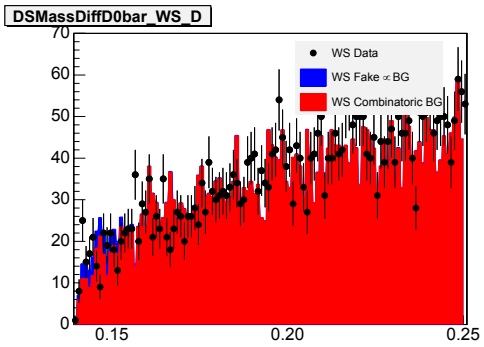

(d) $1.5 < M(\mu^+K^-) \leq 1.6$

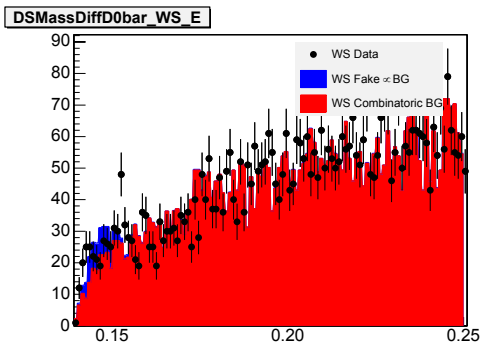

(e) $1.6 < M(\mu^+K^-) \leq 1.7$

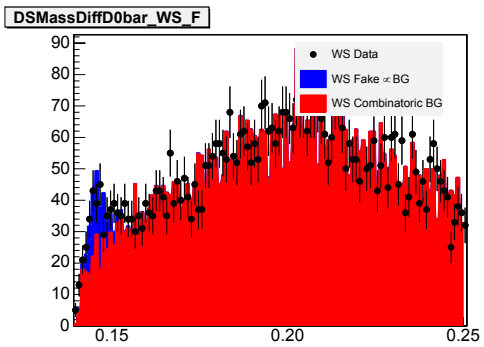

(f) $1.7 < M(\mu^+K^-) \leq 1.8$

Figure B.55: $D^{*-} Fits : \delta(M(\mu K\pi), M(\mu K)), 2.0\text{GeV}/c < p_T(K^-) \leq 3.0\text{GeV}/c, -\frac{\pi}{12} < \phi(K^-) \leq \frac{3\pi}{12}$

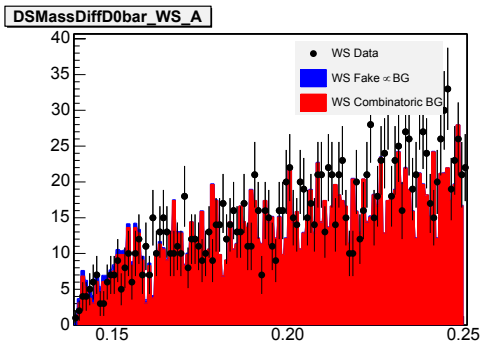

(a) $1.2 < M(\mu^+K^-) \leq 1.3$

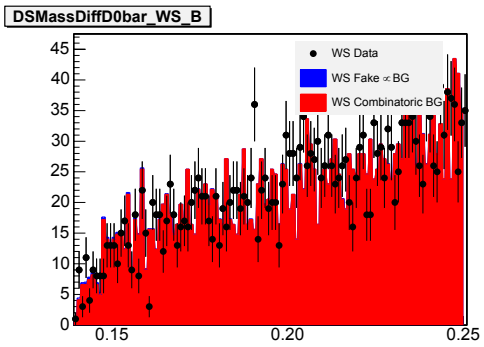

(b) $1.3 < M(\mu^+K^-) \leq 1.4$

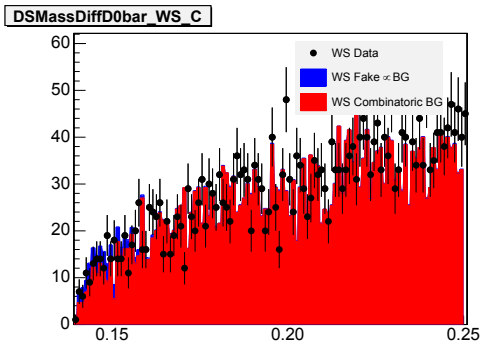

(c) $1.4 < M(\mu^+K^-) \leq 1.5$

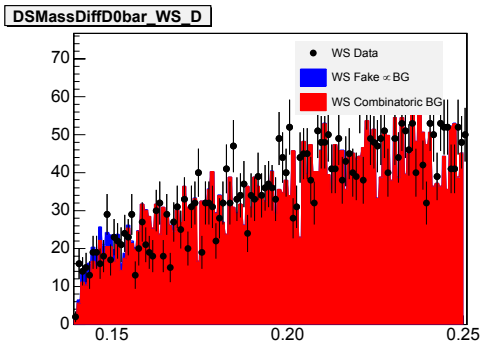

(d) $1.5 < M(\mu^+K^-) \leq 1.6$

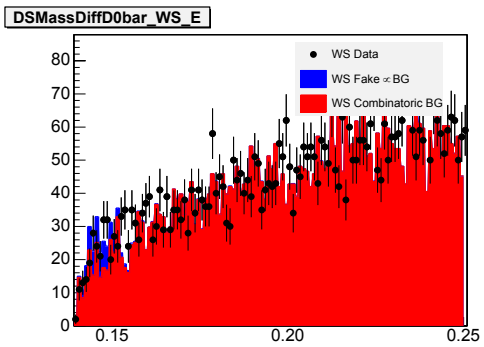

(e) $1.6 < M(\mu^+K^-) \leq 1.7$

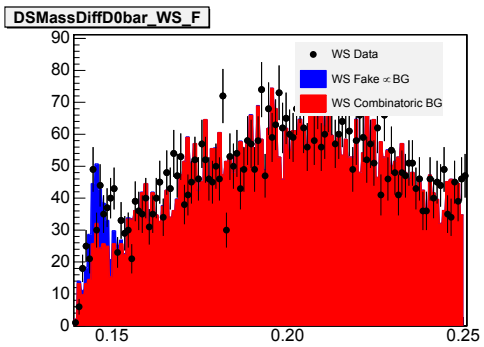

(f) $1.7 < M(\mu^+K^-) \leq 1.8$

Figure B.56: $D^{*-} Fits : \delta(M(\mu K\pi), M(\mu K)), 2.0\text{GeV}/c < p_T(K^-) \leq 3.0\text{GeV}/c$, $\frac{3\pi}{12} < \phi(K^-) \leq \frac{7\pi}{12}$

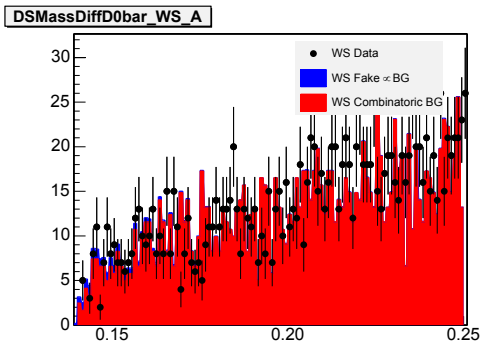

(a) $1.2 < M(\mu^+K^-) \leq 1.3$

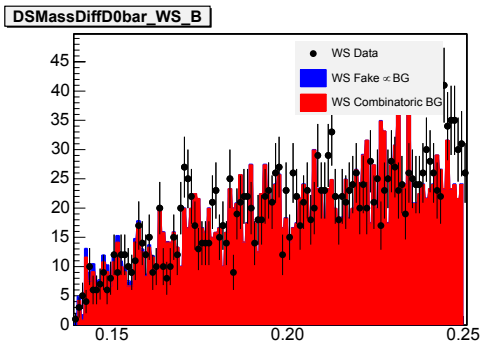

(b) $1.3 < M(\mu^+K^-) \leq 1.4$

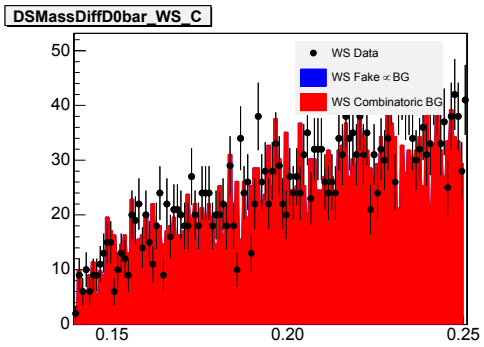

(c) $1.4 < M(\mu^+K^-) \leq 1.5$

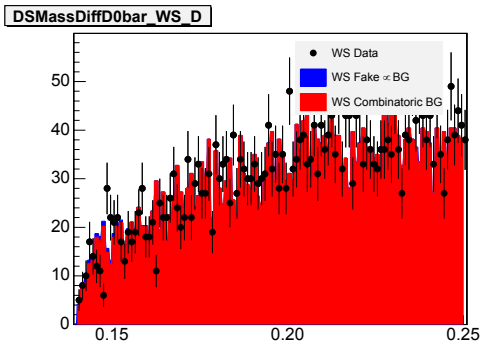

(d) $1.5 < M(\mu^+K^-) \leq 1.6$

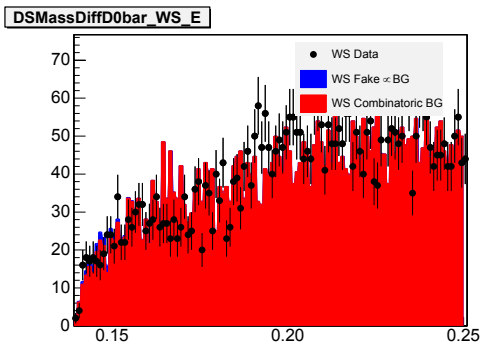

(e) $1.6 < M(\mu^+K^-) \leq 1.7$

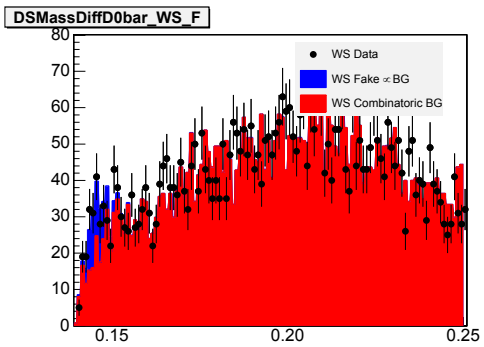

(f) $1.7 < M(\mu^+K^-) \leq 1.8$

Figure B.57: $D^{*-} Fits : \delta(M(\mu K\pi), M(\mu K)), 2.0\text{GeV}/c < p_T(K^-) \leq 3.0\text{GeV}/c$, $\frac{7\pi}{12} < \phi(K^-) \leq \frac{11\pi}{12}$

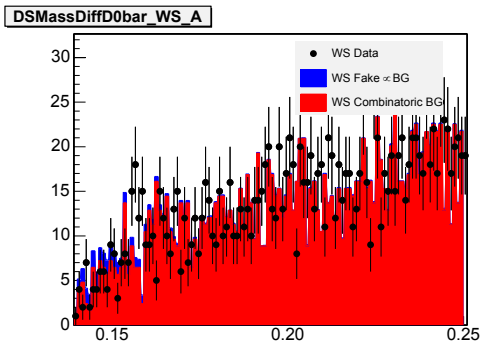

(a) $1.2 < M(\mu^+K^-) \leq 1.3$

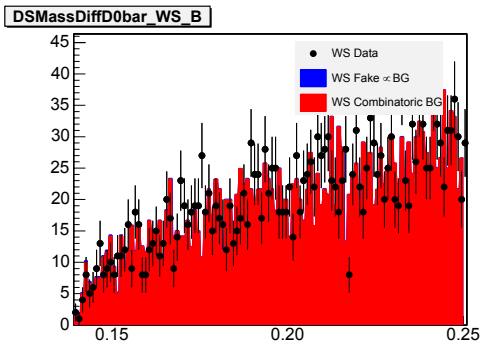

(b) $1.3 < M(\mu^+K^-) \leq 1.4$

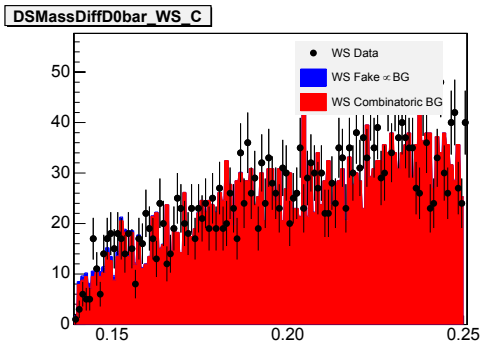

(c) $1.4 < M(\mu^+K^-) \leq 1.5$

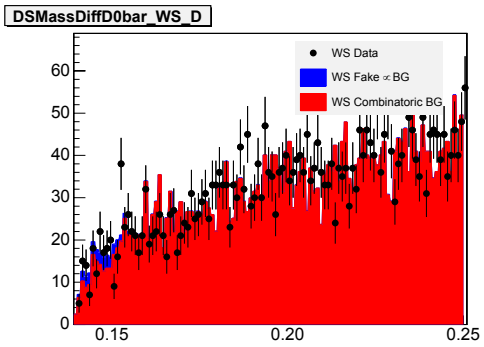

(d) $1.5 < M(\mu^+K^-) \leq 1.6$

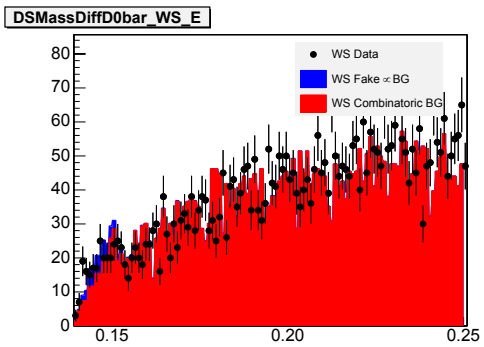

(e) $1.6 < M(\mu^+K^-) \leq 1.7$

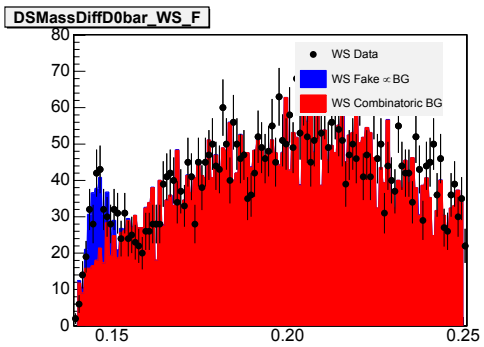

(f) $1.7 < M(\mu^+K^-) \leq 1.8$

Figure B.58: $D^{*-} Fits : \delta(M(\mu K\pi), M(\mu K)), 2.0\text{GeV}/c < p_T(K^-) \leq 3.0\text{GeV}/c,\ \frac{11\pi}{12} < \phi(K^-) \leq \frac{15\pi}{12}$

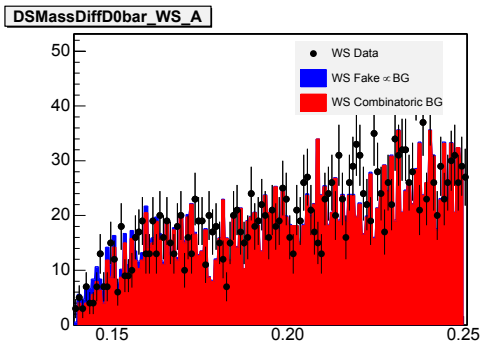

(a) $1.2 < M(\mu^+K^-) \leq 1.3$

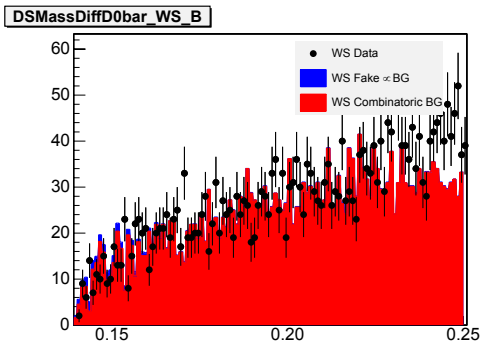

(b) $1.3 < M(\mu^+K^-) \leq 1.4$

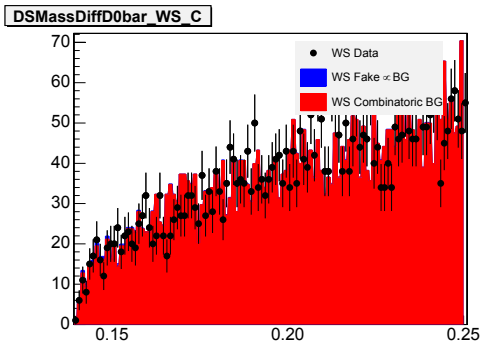

(c) $1.4 < M(\mu^+K^-) \leq 1.5$

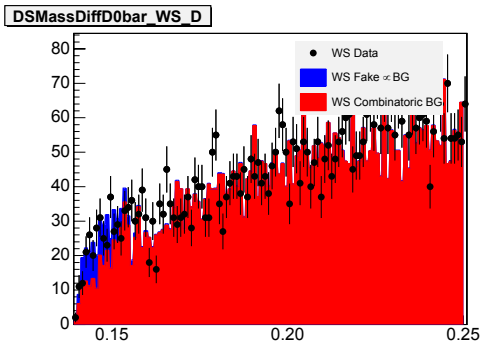

(d) $1.5 < M(\mu^+K^-) \leq 1.6$

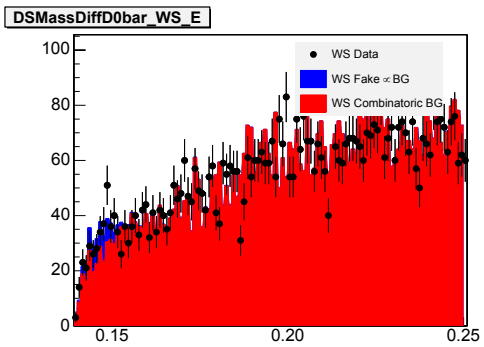

(e) $1.6 < M(\mu^+K^-) \leq 1.7$

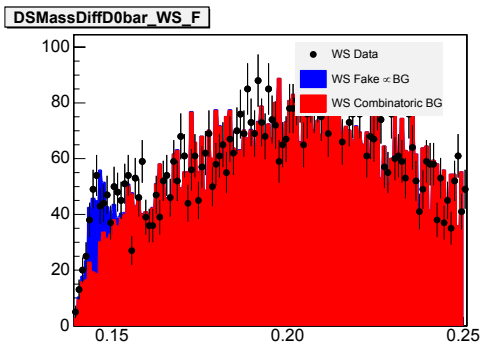

(f) $1.7 < M(\mu^+K^-) \leq 1.8$

Figure B.59: $D^{*-} Fits : \delta(M(\mu K\pi), M(\mu K)), 2.0\text{GeV}/c < p_T(K^-) \leq 3.0\text{GeV}/c$, $\frac{15\pi}{12} < \phi(K^-) \leq \frac{19\pi}{12}$

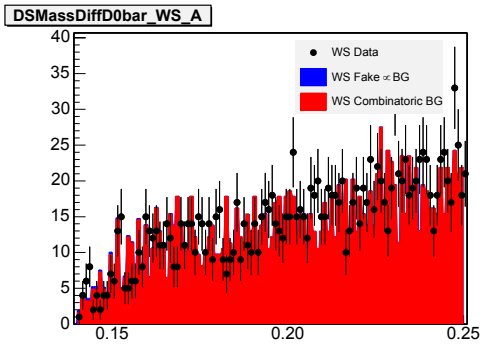

(a) $1.2 < M(\mu^+K^-) \leq 1.3$

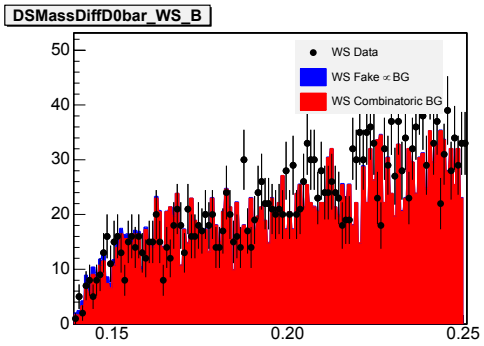

(b) $1.3 < M(\mu^+K^-) \leq 1.4$

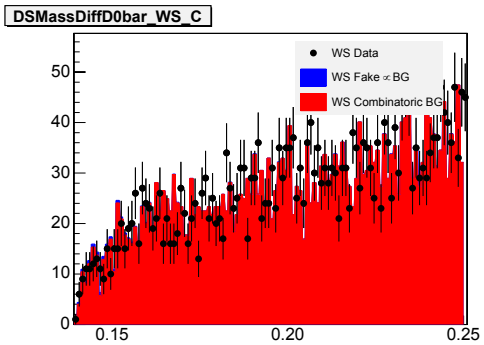

(c) $1.4 < M(\mu^+K^-) \leq 1.5$

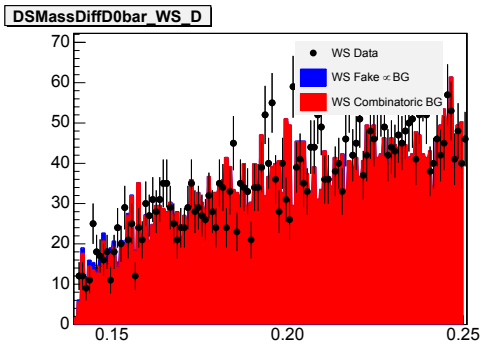

(d) $1.5 < M(\mu^+K^-) \leq 1.6$

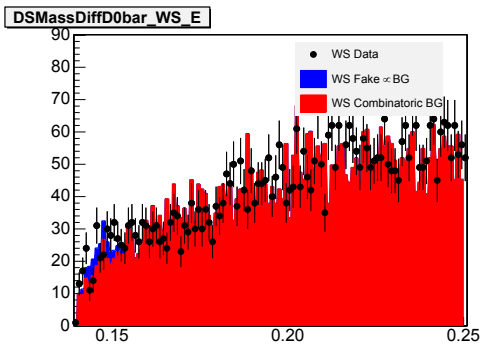

(e) $1.6 < M(\mu^+K^-) \leq 1.7$

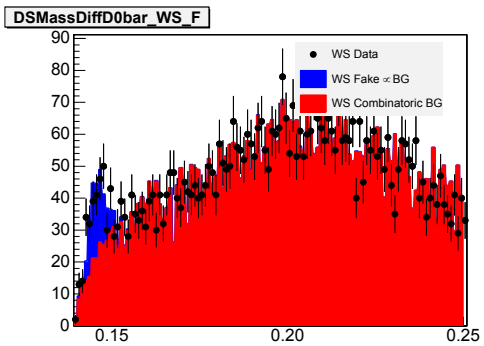

(f) $1.7 < M(\mu^+K^-) \leq 1.8$

Figure B.60: $D^{*-} Fits : \delta(M(\mu K\pi), M(\mu K)), 2.0\text{GeV}/c < p_T(K^-) \leq 3.0\text{GeV}/c$, $\frac{19\pi}{12} < \phi(K^-) \leq \frac{23\pi}{12}$

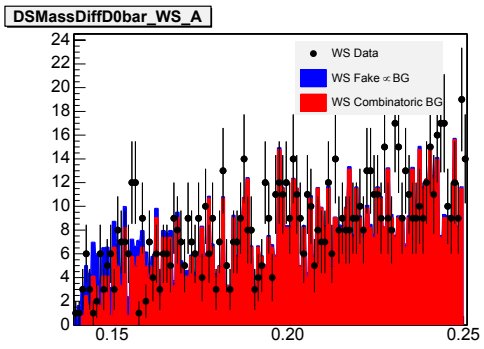

(a) $1.2 < M(\mu^+K^-) \leq 1.3$

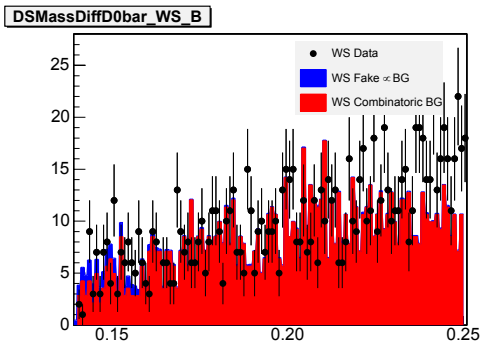

(b) $1.3 < M(\mu^+K^-) \leq 1.4$

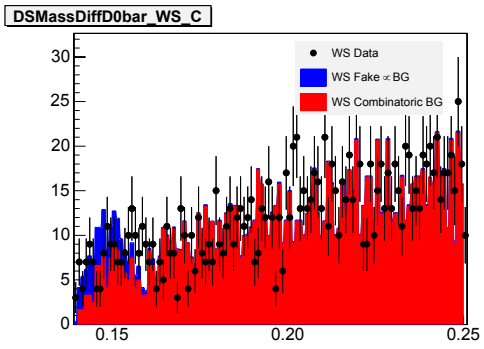

(c) $1.4 < M(\mu^+K^-) \leq 1.5$

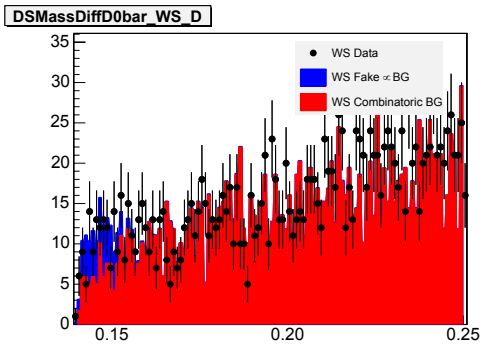

(d) $1.5 < M(\mu^+K^-) \leq 1.6$

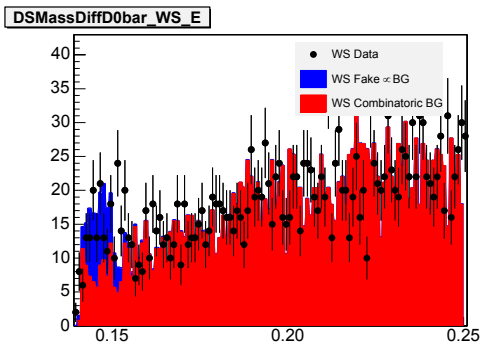

(e) $1.6 < M(\mu^+K^-) \leq 1.7$

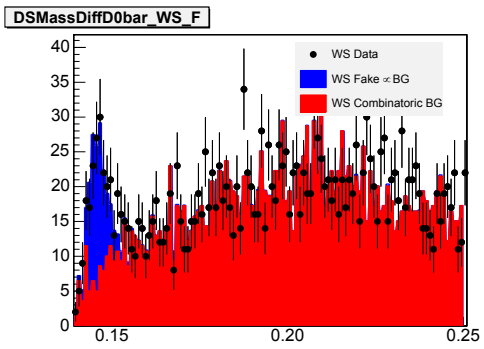

(f) $1.7 < M(\mu^+K^-) \leq 1.8$

Figure B.61: $D^{*-} Fits : \delta(M(\mu K\pi), M(\mu K)), 3.0\text{GeV}/c < p_T(K^-) \leq 4.0\text{GeV}/c, -\frac{\pi}{12} < \phi(K^-) \leq \frac{3\pi}{12}$

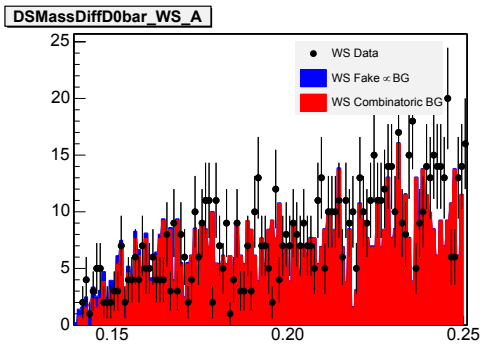

(a) $1.2 < M(\mu^+K^-) \leq 1.3$

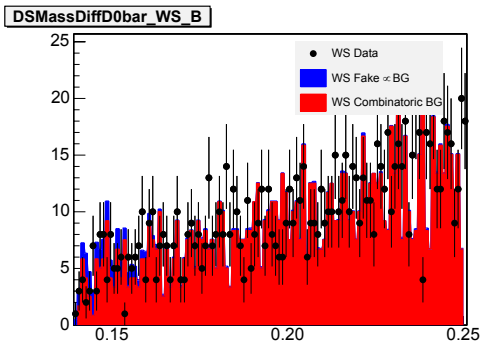

(b) $1.3 < M(\mu^+K^-) \leq 1.4$

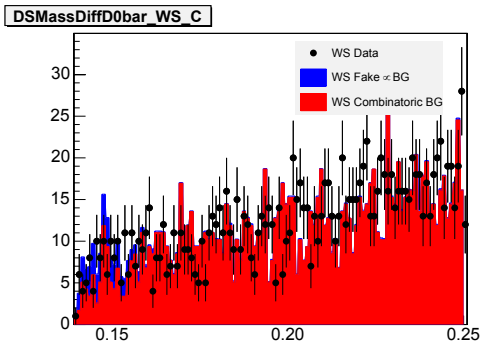

(c) $1.4 < M(\mu^+K^-) \leq 1.5$

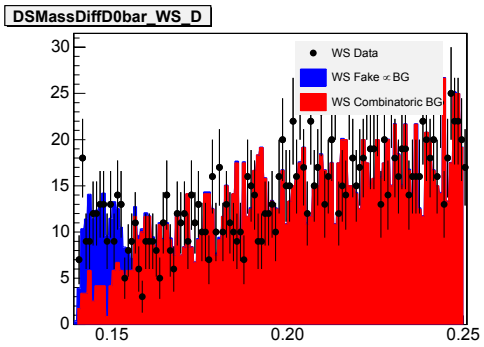

(d) $1.5 < M(\mu^+K^-) \leq 1.6$

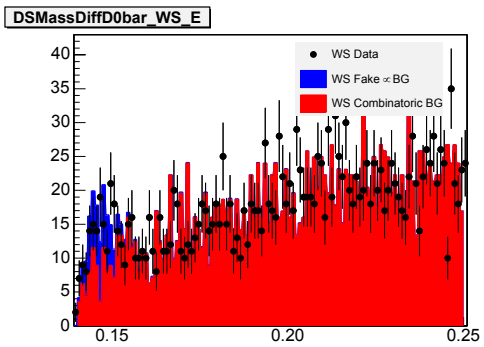

(e) $1.6 < M(\mu^+K^-) \leq 1.7$

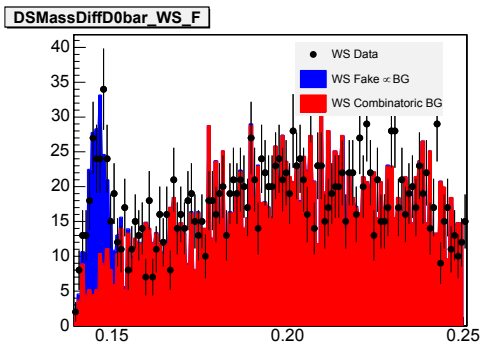

(f) $1.7 < M(\mu^+K^-) \leq 1.8$

Figure B.62: $D^{*-} Fits : \delta(M(\mu K\pi), M(\mu K)), 3.0\text{GeV}/c < p_T(K^-) \leq 4.0\text{GeV}/c$, $\frac{3\pi}{12} < \phi(K^-) \leq \frac{7\pi}{12}$

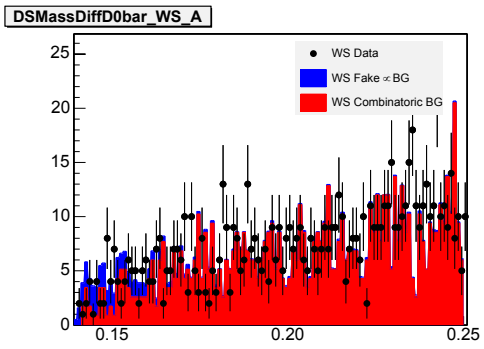

(a) $1.2 < M(\mu^+K^-) \leq 1.3$

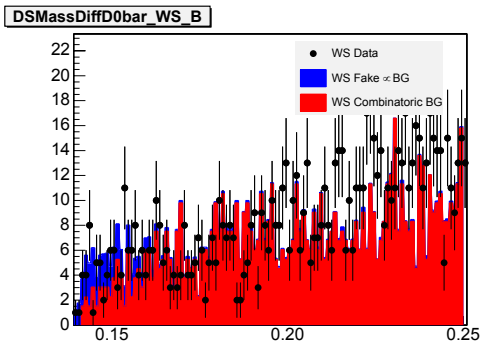

(b) $1.3 < M(\mu^+K^-) \leq 1.4$

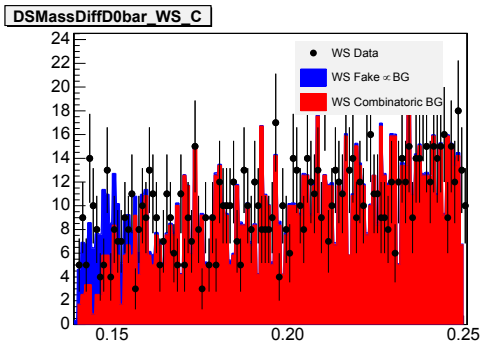

(c) $1.4 < M(\mu^+K^-) \leq 1.5$

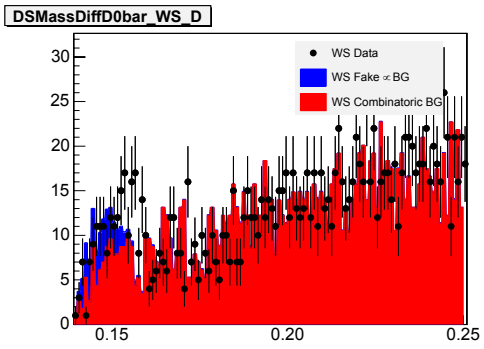

(d) $1.5 < M(\mu^+K^-) \leq 1.6$

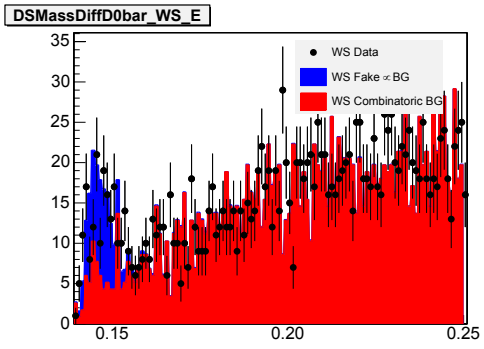

(e) $1.6 < M(\mu^+K^-) \leq 1.7$

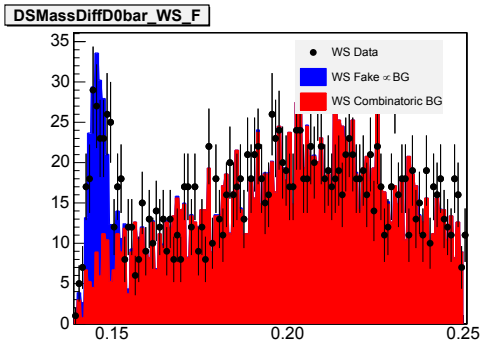

(f) $1.7 < M(\mu^+K^-) \leq 1.8$

Figure B.63: $D^{*-} Fits : \delta(M(\mu K\pi), M(\mu K)), 3.0\text{GeV}/c < p_T(K^-) \leq 4.0\text{GeV}/c$, $\frac{7\pi}{12} < \phi(K^-) \leq \frac{11\pi}{12}$

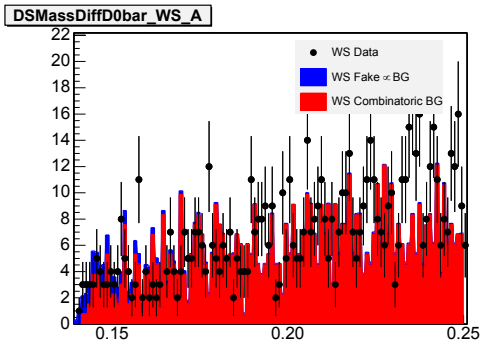

(a) $1.2 < M(\mu^+K^-) \leq 1.3$

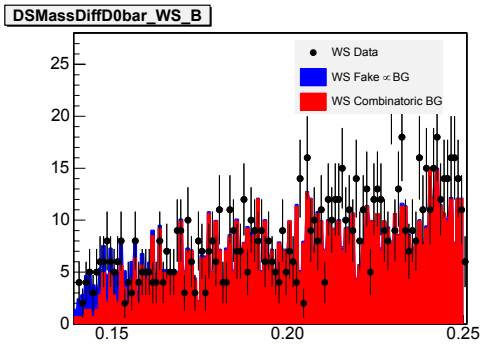

(b) $1.3 < M(\mu^+K^-) \leq 1.4$

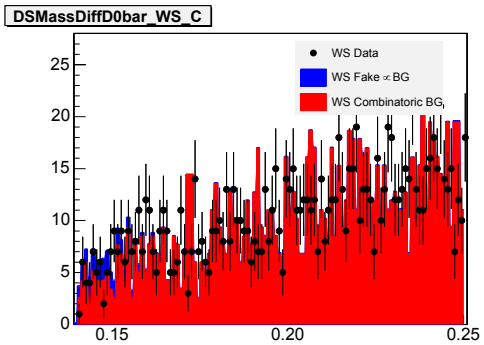

(c) $1.4 < M(\mu^+K^-) \leq 1.5$

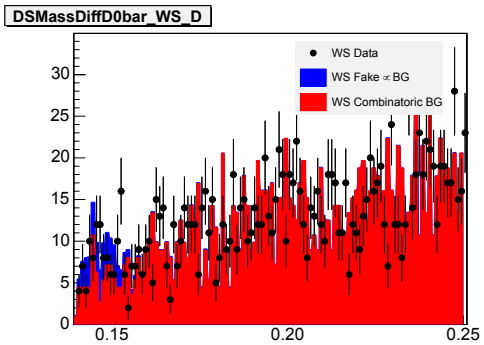

(d) $1.5 < M(\mu^+K^-) \leq 1.6$

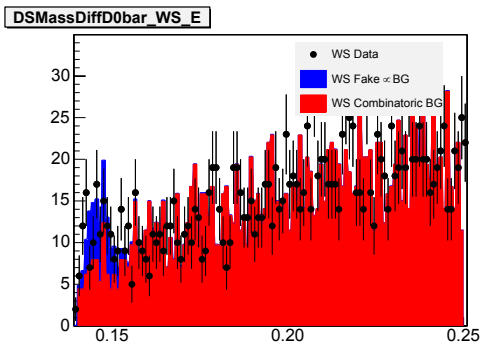

(e) $1.6 < M(\mu^+K^-) \leq 1.7$

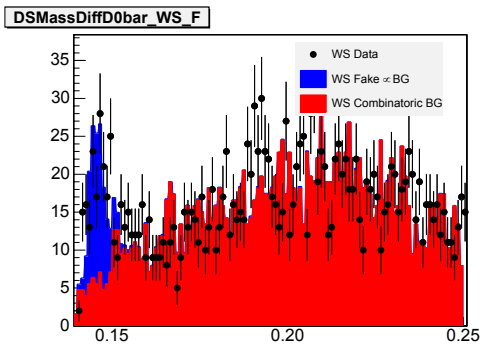

(f) $1.7 < M(\mu^+K^-) \leq 1.8$

Figure B.64: $D^{*-} Fits : \delta(M(\mu K\pi), M(\mu K)), 3.0\text{GeV}/c < p_T(K^-) \leq 4.0\text{GeV}/c$, $\frac{11\pi}{12} < \phi(K^-) \leq \frac{15\pi}{12}$

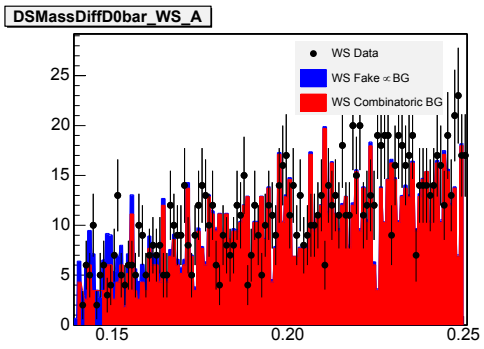

(a) $1.2 < M(\mu^+K^-) \leq 1.3$

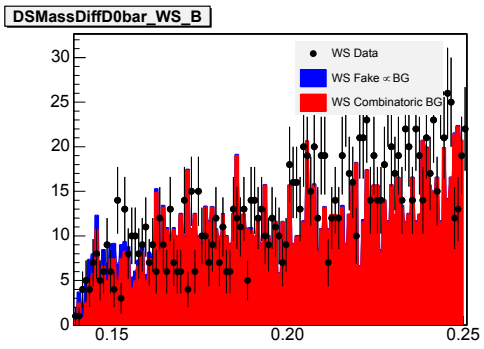

(b) $1.3 < M(\mu^+K^-) \leq 1.4$

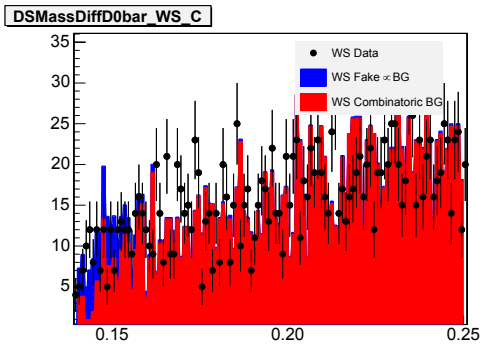

(c) $1.4 < M(\mu^+K^-) \leq 1.5$

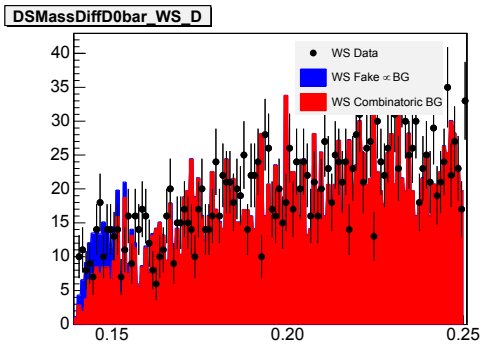

(d) $1.5 < M(\mu^+K^-) \leq 1.6$

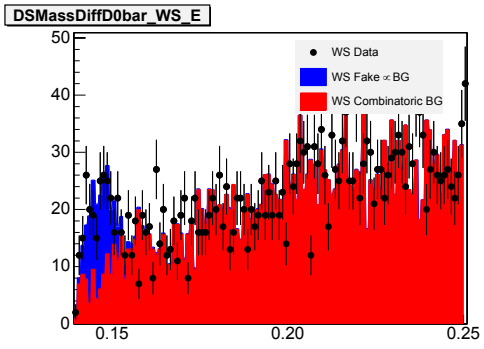

(e) $1.6 < M(\mu^+K^-) \leq 1.7$

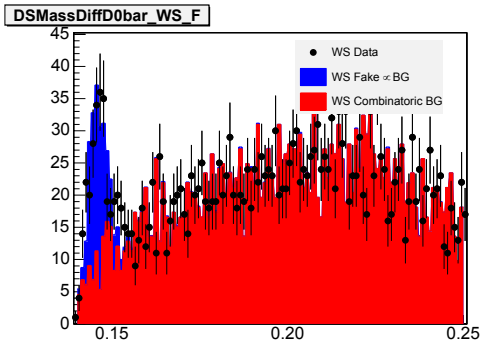

(f) $1.7 < M(\mu^+K^-) \leq 1.8$

Figure B.65: $D^{*-} Fits : \delta(M(\mu K\pi), M(\mu K)), 3.0\text{GeV}/c < p_T(K^-) \leq 4.0\text{GeV}/c$, $\frac{15\pi}{12} < \phi(K^-) \leq \frac{19\pi}{12}$

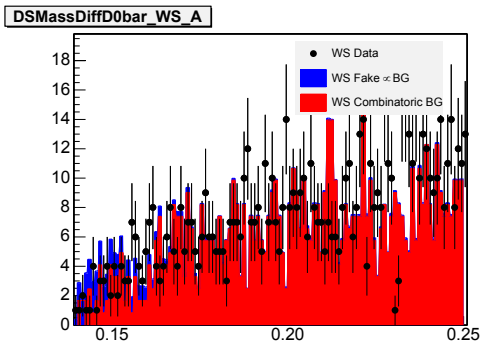

(a) $1.2 < M(\mu^+K^-) \leq 1.3$

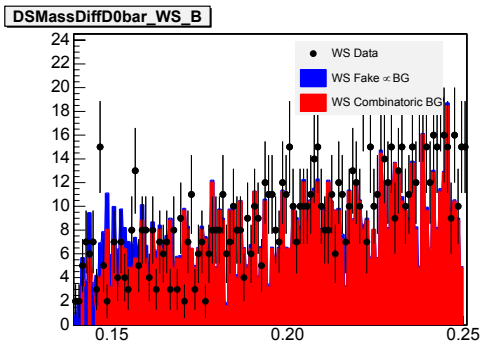

(b) $1.3 < M(\mu^+K^-) \leq 1.4$

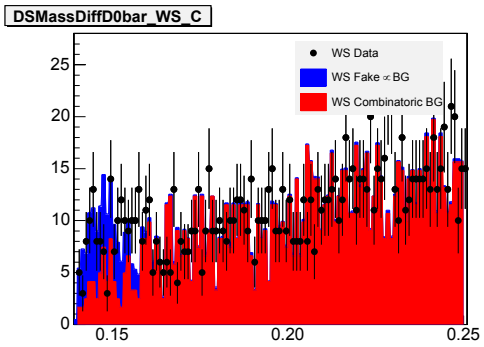

(c) $1.4 < M(\mu^+K^-) \leq 1.5$

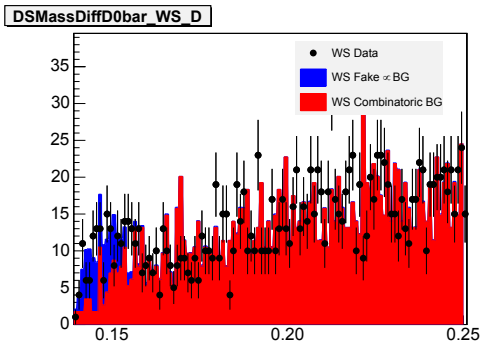

(d) $1.5 < M(\mu^+K^-) \leq 1.6$

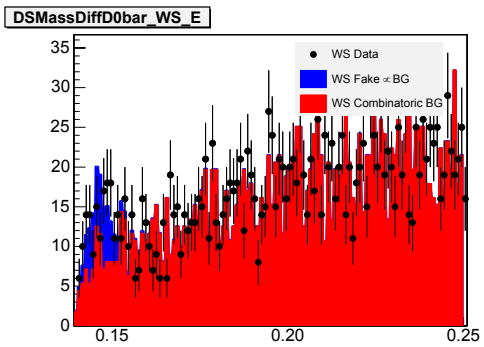

(e) $1.6 < M(\mu^+K^-) \leq 1.7$

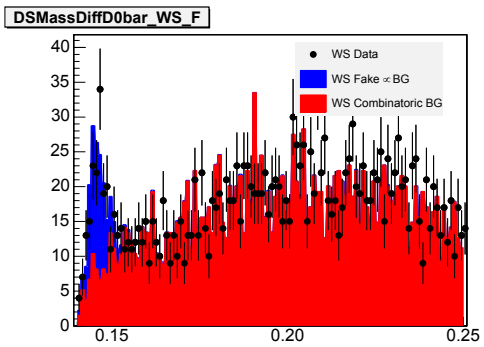

(f) $1.7 < M(\mu^+K^-) \leq 1.8$

Figure B.66: $D^{*-} Fits : \delta(M(\mu K\pi), M(\mu K)), 3.0\text{GeV}/c < p_T(K^-) \leq 4.0\text{GeV}/c$, $\frac{19\pi}{12} < \phi(K^-) \leq \frac{23\pi}{12}$

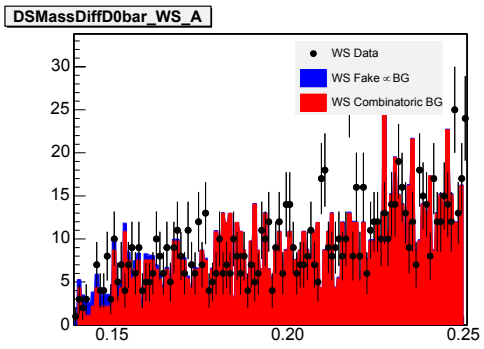

(a) $1.2 < M(\mu^+K^-) \leq 1.3$

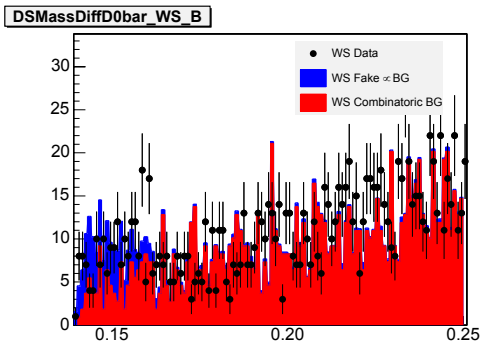

(b) $1.3 < M(\mu^+K^-) \leq 1.4$

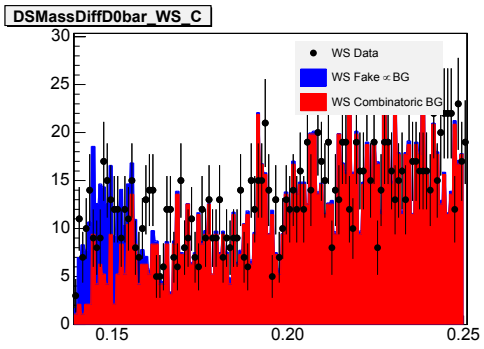

(c) $1.4 < M(\mu^+K^-) \leq 1.5$

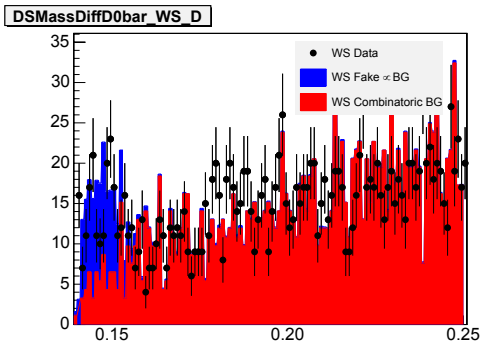

(d) $1.5 < M(\mu^+K^-) \leq 1.6$

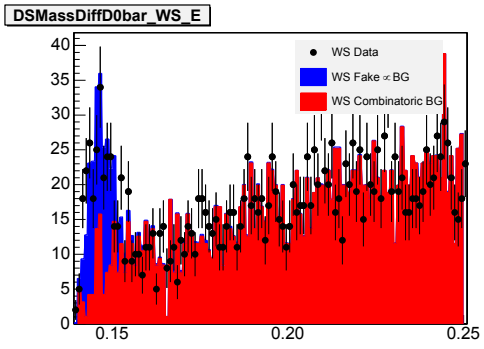

(e) $1.6 < M(\mu^+K^-) \leq 1.7$

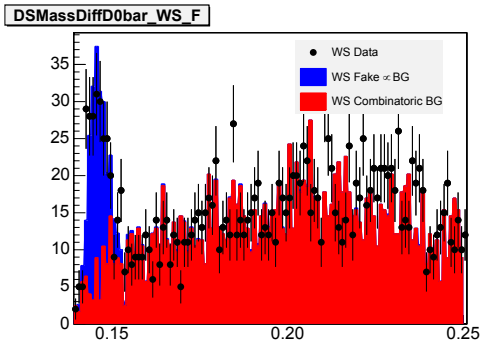

(f) $1.7 < M(\mu^+K^-) \leq 1.8$

Figure B.67: $D^{*-} Fits : \delta(M(\mu K\pi), M(\mu K)), p_T(K^-) > 4.0\text{GeV}/c, -\frac{\pi}{12} < \phi(K^-) \leq \frac{3\pi}{12}$

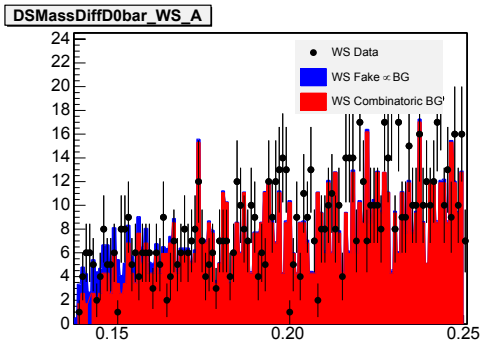

(a) $1.2 < M(\mu^+K^-) \leq 1.3$

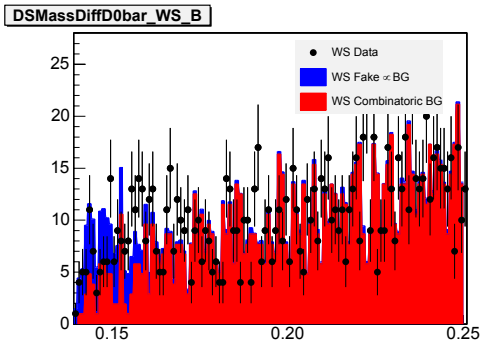

(b) $1.3 < M(\mu^+K^-) \leq 1.4$

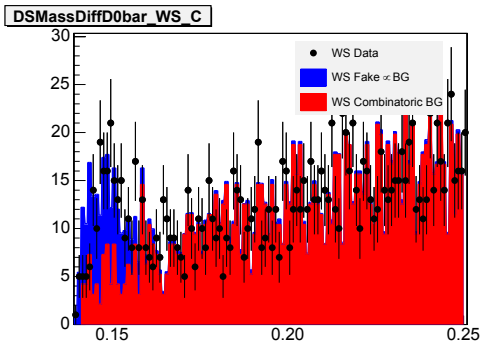

(c) $1.4 < M(\mu^+K^-) \leq 1.5$

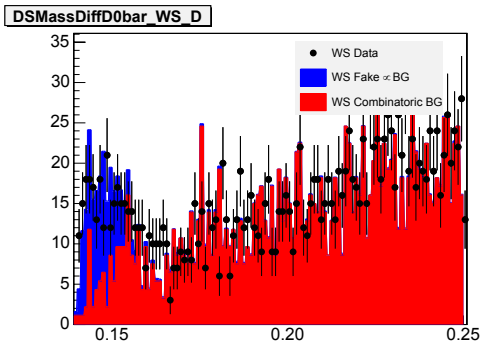

(d) $1.5 < M(\mu^+K^-) \leq 1.6$

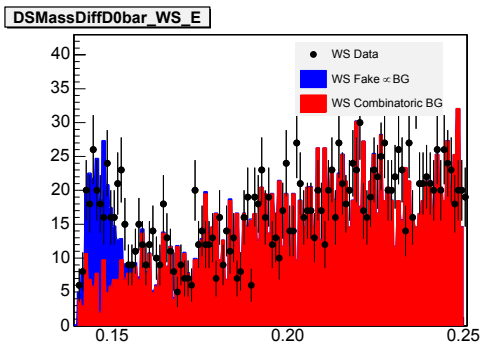

(e) $1.6 < M(\mu^+K^-) \leq 1.7$

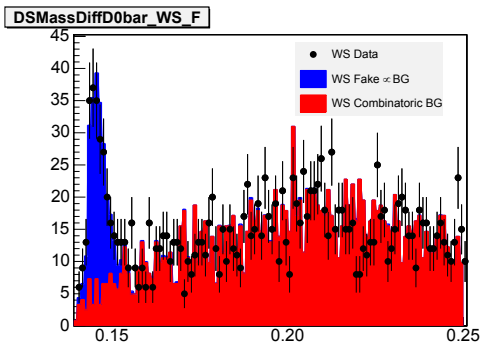

(f) $1.7 < M(\mu^+K^-) \leq 1.8$

Figure B.68: $D^{*-} Fits : \delta(M(\mu K\pi), M(\mu K)), p_T(K^-) > 4.0\text{GeV}/c,\ \frac{3\pi}{12} < \phi(K^-) \leq \frac{7\pi}{12}$

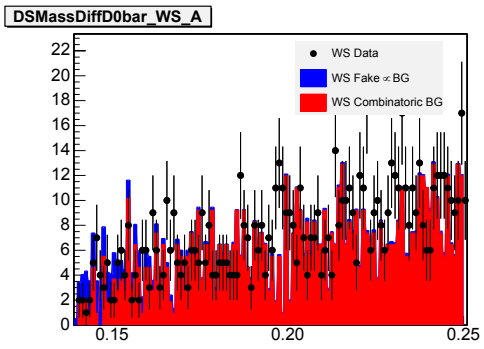

(a) $1.2 < M(\mu^+K^-) \leq 1.3$

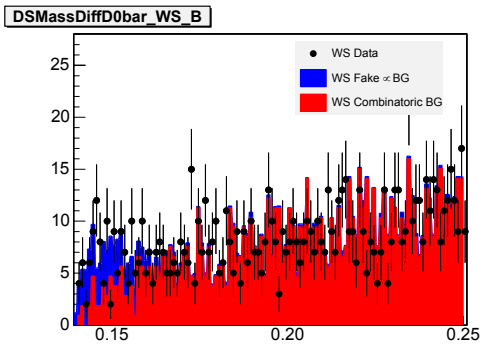

(b) $1.3 < M(\mu^+K^-) \leq 1.4$

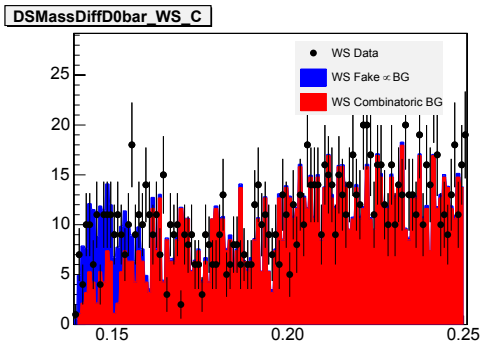

(c) $1.4 < M(\mu^+K^-) \leq 1.5$

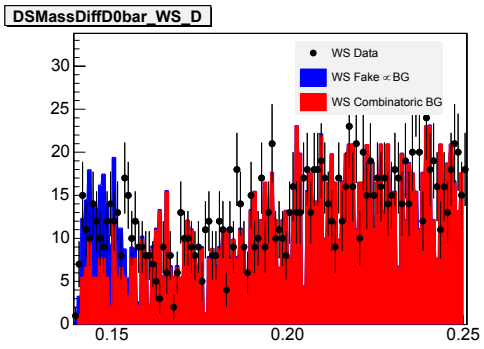

(d) $1.5 < M(\mu^+K^-) \leq 1.6$

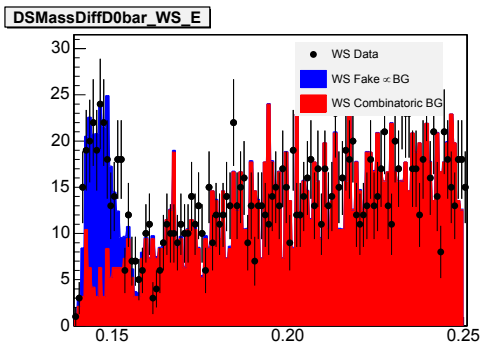

(e) $1.6 < M(\mu^+K^-) \leq 1.7$

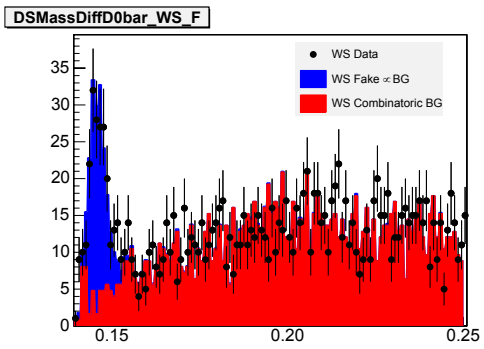

(f) $1.7 < M(\mu^+K^-) \leq 1.8$

Figure B.69: $D^{*-} Fits : \delta(M(\mu K\pi), M(\mu K)), p_T(K^-) > 4.0\text{GeV}/c,\ \frac{7\pi}{12} < \phi(K^-) \leq \frac{11\pi}{12}$

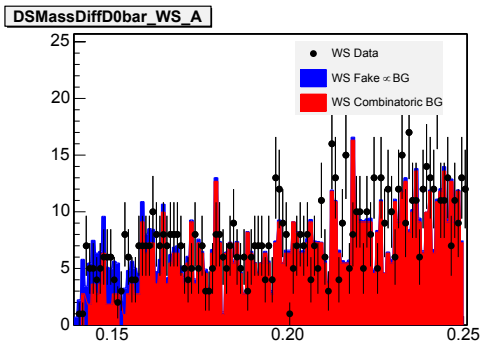

(a) $1.2 < M(\mu^+K^-) \leq 1.3$

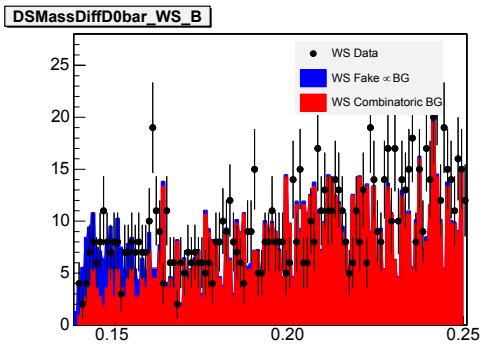

(b) $1.3 < M(\mu^+K^-) \leq 1.4$

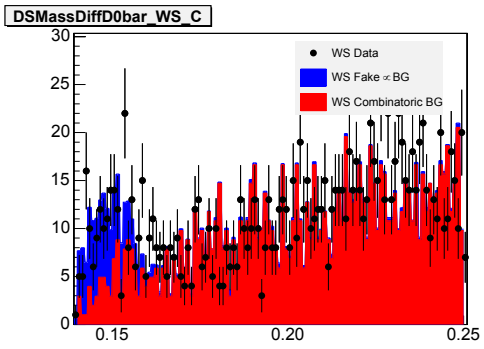

(c) $1.4 < M(\mu^+K^-) \leq 1.5$

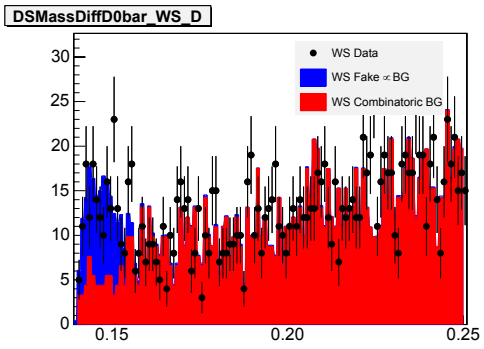

(d) $1.5 < M(\mu^+K^-) \leq 1.6$

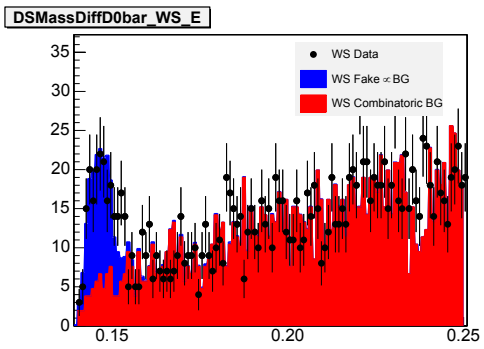

(e) $1.6 < M(\mu^+K^-) \leq 1.7$

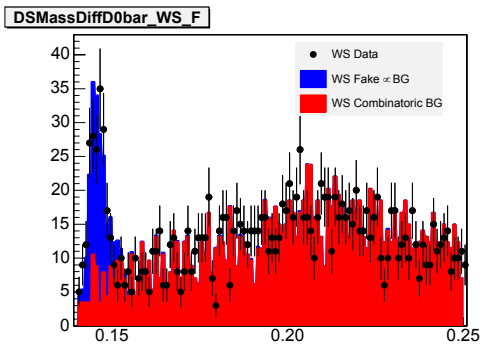

(f) $1.7 < M(\mu^+K^-) \leq 1.8$

Figure B.70: $D^{*-} Fits : \delta(M(\mu K\pi), M(\mu K)), p_T(K^-) > 4.0\text{GeV}/c,\ \frac{11\pi}{12} < \phi(K^-) \leq \frac{15\pi}{12}$

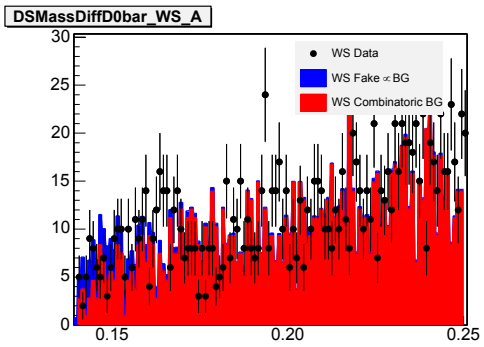

(a) $1.2 < M(\mu^+K^-) \leq 1.3$

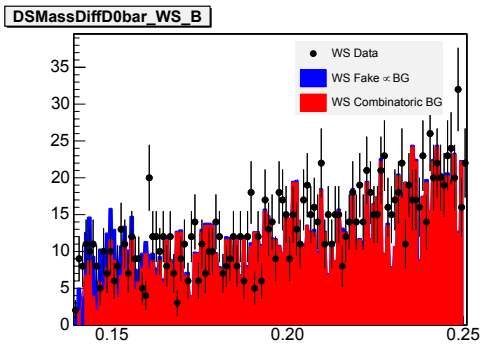

(b) $1.3 < M(\mu^+K^-) \leq 1.4$

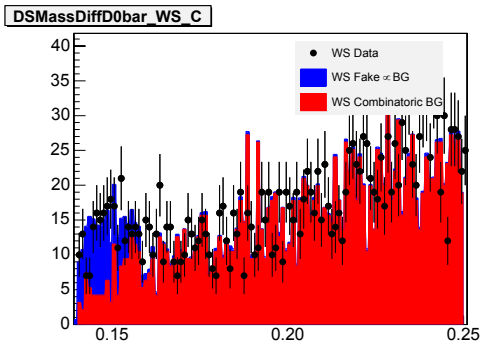

(c) $1.4 < M(\mu^+K^-) \leq 1.5$

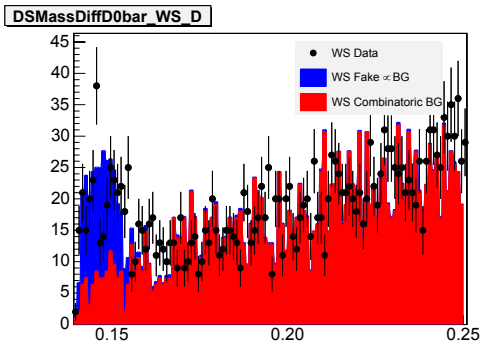

(d) $1.5 < M(\mu^+K^-) \leq 1.6$

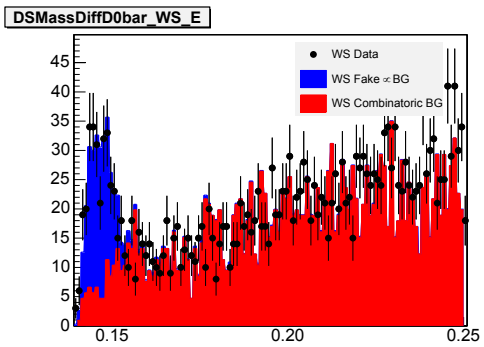

(e) $1.6 < M(\mu^+K^-) \leq 1.7$

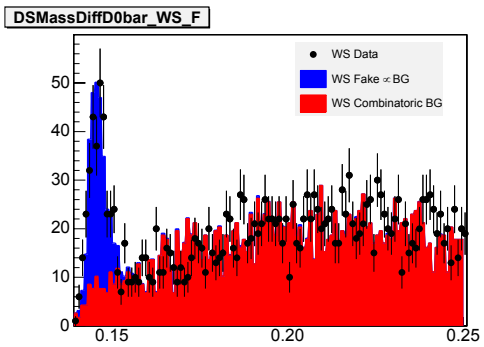

(f) $1.7 < M(\mu^+K^-) \leq 1.8$

Figure B.71: $D^{*-} Fits : \delta(M(\mu K\pi), M(\mu K)), p_T(K^-) > 4.0\text{GeV}/c,\ \frac{15\pi}{12} < \phi(K^-) \leq \frac{19\pi}{12}$

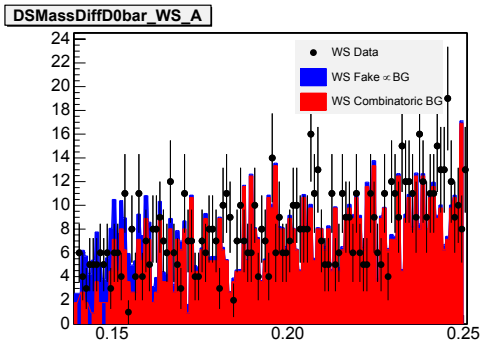

(a) $1.2 < M(\mu^+K^-) \leq 1.3$

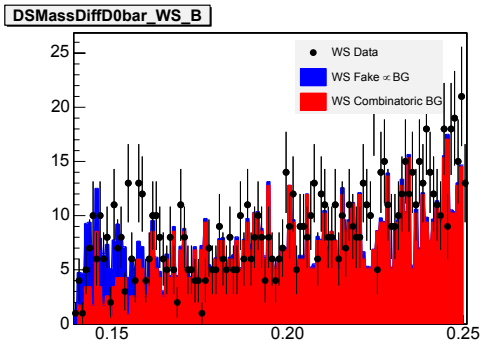

(b) $1.3 < M(\mu^+K^-) \leq 1.4$

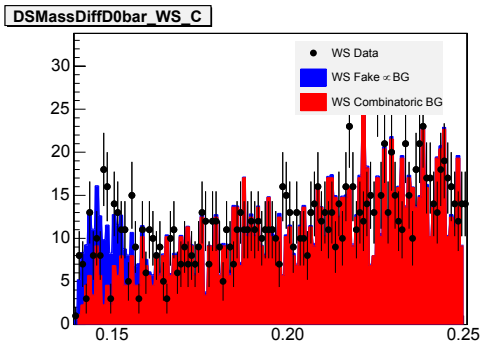

(c) $1.4 < M(\mu^+K^-) \leq 1.5$

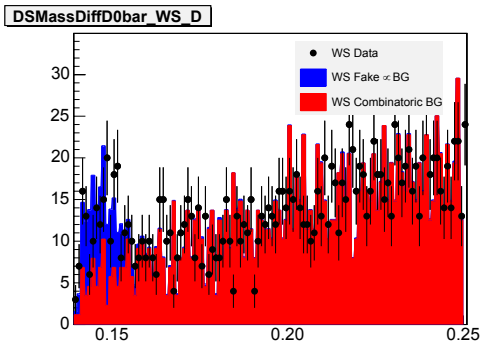

(d) $1.5 < M(\mu^+K^-) \leq 1.6$

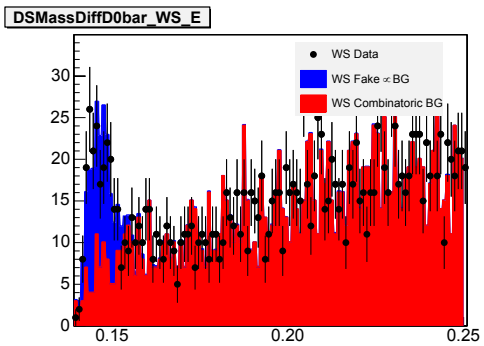

(e) $1.6 < M(\mu^+K^-) \leq 1.7$

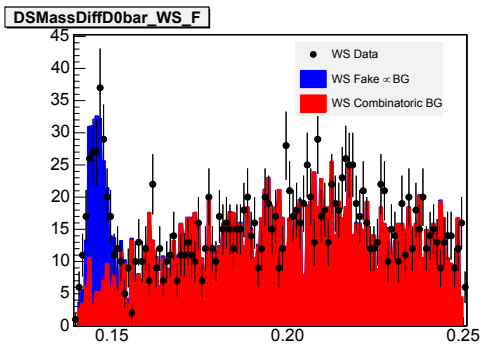

(f) $1.7 < M(\mu^+K^-) \leq 1.8$

Figure B.72: $D^{*-} Fits : \delta(M(\mu K\pi), M(\mu K)), p_T(K^-) > 4.0\text{GeV}/c,\ \frac{19\pi}{12} < \phi(K^-) \leq \frac{23\pi}{12}$

Appendix C

Monte Carlo Decay Tables

The decay table used to determine the branching fraction for the muonic $D^{*+} \to D^0\pi^+$ decays in the Monte Carlo simulations is shown in Table C.1.

Table C.1: Muonic D^{*+} MC Decay Table

D^0 Daughters	Branching Fraction
$K^{*-}\mu^+\nu_\mu$	0.0214
$K^-\mu^+\nu_\mu$	0.0340
$K_1^-\mu^+\nu_\mu$	0.0014
$K_2^{*-}\mu^+\nu_\mu$	0.0015
$\pi^-\mu^+\nu_\mu$	0.0034
$\rho^-\mu^+\nu_\mu$	0.0022
$\bar{K}^0\pi^-\mu^+\nu_\mu$	0.0011
$K^-\pi^0\mu^+\nu_{mu}$	0.0006

Glossary

ASDQ Amplifier Shaper Discriminator with Charge (Q) Encoding. 29–32

bunch A group of protons or anti-protons that are isolated in space in the accelerator. 17–20

Cabibbo-suppressed Suppression of a process due to intergenerational coupling. 43, 44, 47, 48

CDF The Collider Detector at Fermilab, the experiment on the Tevatron which was used to collect the data for this thesis.. 17, 20–25, 27, 57

CEM Central Electromagnetic Calorimeter. 25

CERN European Organization for Nuclear Research. Laboratory of the same name is the location of the LHC. 17

CES Central Strip Detector. 34

CHA Central Hadronic Calorimeter. 25

CLC Cherenkov Luminosity Counters. 26

CMP Central Muon uPgrade. 27

CMU Central Muon Detector. 27

CMX Central Muon Extension. 27

COT Central Outer Tracker, the main tracking volume at CDF. 23–25, 27, 28

CP Charge Parity. 4, 5, 8–10, 15, 16, 41, 42, 54, 57, 58, 78

CPT Charge Parity Time. 4

ISL Intermediate Silicon Layer. 22

L00 Layer 00, the innermost layer of the silicon vertex detector. Resides immediately outside the beam pipe. 22

LHC Large Hadron Collider, a 14 TeV pp collider at CERN. 17

Linac Linear Accelerator. 17, 18

MC Monte Carlo, event simulation. 41, 44–46, 60, 62–67, 74, 75

PEM Plug Electromagnetic Calorimeter. 25

PHA Plug Hadronic Calorimeter. 25

RS Right Sign candidate. In this analysis, RS refers to either a $\mu^+K^-\pi^+$ candidate or a $\mu^-K^+\pi^-$ candidate.. 60

SM The Standard Model of Particle Physics. 9, 10

SS Same Sign candidate. In this analysis, SS refers to either a $\mu^+K^+\pi^+$ candidate or a $\mu^-K^-\pi^-$ candidate.. 60

SVX II Silicon Vertex Detector, Run II Upgrade. 22, 23

Tevatron The $p\bar{p}$ collider at the Fermilab National Accelerator Laboratory with center of mass energy of 1.96TeV. 15

TOF Time of Flight Detector. 25

TRACER TRigger And Clock + Event Readout Module. Provides interface between front end crates and the rest of the CDF system.. 32

WHA Wall Hadronic Calorimeter. 25

WS Wrong Sign candidate. In this analysis, RS refers to either a $\mu^+K^-\pi^-$ candidate or a $\mu^-K^+\pi^+$ candidate.. 60

References

[1] S.W. Herb et al., Phys. Rev. Lett. 39 (1977) 252.

[2] W.S. Hou, M. Nagashima and A. Soddu, (2006), hep-ph/0605080.

[3] J. Thomson, The Electrician 39 104.

[4] P.A.M. Dirac, Royal Society of London Proceedings Series A 114 (1927) 243.

[5] C.D. Anderson, Physical Review 43 (1933) 491.

[6] M. Gell-Mann, Phys. Rev. 125 (1962) 1067.

[7] M. Gell-Mann, Phys. Lett. 8 (1964) 214.

[8] V.E. Barnes et al., Physical Review Letters 12 (1964) 204.

[9] M. Breidenbach et al., Phys. Rev. Lett. 23 (1969) 935.

[10] S.L. Glashow, J. Iliopoulos and L. Maiani, Phys. Rev. D 2 (1970) 1285.

[11] D.J. Gross and F. Wilczek, Phys. Rev. Lett. 30 (1973) 1343.

[12] L.L. Chau and W.Y. Keung, Phys. Rev. Lett. 53 (1984) 1802.

[13] L. Wolfenstein, Phys. Rev. Lett. 51 (1983) 1945.

[14] C. Amsler et al., Journal of Physics G 33 (2006) 1+.

[15] W. Bernreuther, Cp violation and baryogenesis, CP Violation in Particle, Nuclear and Astrophysics, edited by M. Beyer, , Lecture Notes in Physics Vol. 591, pp. 237–293, Springer Berlin / Heidelberg, 2002, 10.1007/3-540-47895-7_7.

[16] P. Huet and E. Sather, Phys. Rev. D 51 (1995) 379.

[17] J.H. Christenson et al., Phys. Rev. Lett. 13 (1964) 138.

[18] Y.H. Ahn, H.Y. Cheng and S. Oh, Wolfenstein parametrization at higher order: Seeming discrepancies and their resolution, 2011, arXiv:1106.0935.

[19] Belle, K. Sakai et al., Phys. Rev. D82 (2010) 091104, 1008.2567.

[20] D0, V.M. Abazov et al., Phys. Rev. Lett. 100 (2008) 211802, 0802.3299.

[21] E.J. Thomson et al., IEEE Trans. Nucl. Sci. 49 (2002) 1063.

[22] R. Downing et al., Nucl.Instrum.Meth. A570 (2007) 36, physics/0606247.

[23] P. Nason, S. Dawson and R.K. Ellis, Nuclear Physics B 303 (1988) 607 .

[24] CDF Collaboration, D. Acosta et al., Phys.Rev. D71 (2005) 032001, hep-ex/0412071.

[25] D.L. For, The evtgen event generator package.

[26] R. Brun et al., CERN-DD-78-2-REV and CERN-DD-78-2.

[27] T.C. Collaboration, 10296 (2010).

[28] CDF Collaboration, T. Aaltonen et al., Phys.Rev. D77 (2008) 072004, 0710.1895.

[29] C.P. Marino, (2007), Ph.D. Thesis (advisor: Kevin Pitts).